

***IN VIVO* IMAGING TO CHARACTERIZE DYNAMIC TISSUE RESPONSES AFTER
NEURAL ELECTRODE IMPLANTATION**

by

James Regis Eles

B.S., University of Rochester, 2012

Submitted to the Graduate Faculty of
Swanson School of Engineering in partial fulfillment
of the requirements for the degree of
Doctor of Philosophy

University of Pittsburgh

2019

UNIVERSITY OF PITTSBURGH
SWANSON SCHOOL OF ENGINEERING

This dissertation was presented

by

James Regis Eles

It was defended on

August 29, 2018

and approved by

Aaron Batista, Ph.D., Associate Professor
Department of Bioengineering

Takashi Kozai, Ph.D., Assistant Professor
Department of Bioengineering

Kacey G. Marra, Ph.D., Associate Professor
Departments of Plastic Surgery

Alberto Vazquez, Ph.D., Associate Professor
Departments of Radiology

Dissertation Director: Xinyan Tracy Cui, Ph.D., Professor
Department of Bioengineering

Copyright © by James R. Eles

2019

***IN VIVO* IMAGING TO CHARACTERIZE DYNAMIC TISSUE RESPONSES AFTER NEURAL ELECTRODE IMPLANTATION**

James Regis Eles, Ph.D.

University of Pittsburgh, 2019

Implantable neural electrodes are promising technologies to restore motor, sensory, and cognitive function in many neural pathologies through brain-computer interfacing (BCI). Many BCI applications require electrode implantation within neural tissue to resolve and/or modulate the physiological activity of individual neurons via electrical recording and stimulation. This invasive implantation leads to acute and long-term deterioration of both the electrode device as well as the neurons surrounding the device. Ultimately, damage to the electrode and neural tissue results in electrode recording failure within the first years after implantation.

Many strategies to improve BCI longevity focus on mitigating tissue damage through improving neuronal survival or reducing inflammatory activity around implants. Despite incremental improvements, electrode failure persists as an obstacle to wide-spread clinical deployment of BCIs. This can be partly attributed to an incomplete understanding of the biological correlates of recording performance. These correlates have largely been identified through post-mortem histological staining, which cannot capture dynamic changes in cellular physiology and morphology.

In the following dissertation, we use longitudinal two-photon *in vivo* imaging to quantify how neurons, microglia, and meningeal immune cells are affected by an intracortical electrode during and after implantation in mouse cortex. We go beyond conventional histological

techniques to show the time-course of neuronal injury and microglial recruitment after implantation. Neuronal injury occurs instantaneously, with prolonged, high calcium levels evident in neurons within 100 μm of implants. Microglial activation occurs within minutes of implantation and subsequent microglial encapsulation of electrodes can be modulated by bioactive surface coatings. Within the first day post-implant, there is high trafficking of peripheral immune cells through venules at the surface of the brain as well as along the electrode's shank at the surface of the brain. Over the next month, calcium activity in neurons increases while the collagenous meningeal tissues at the surface of the brain thicken. We further show that meningeal thickening can have profound implications for devices implanted into non-human primates as well. In sum, these results define new potential therapeutic targets and windows that could improve the longevity of implantable neural electrodes.

TABLE OF CONTENTS

PREFACE.....	XVI
1.0 INTRODUCTION.....	1
1.1 NEURAL INTERFACES: CLINICAL USE AND FAILURE MODES	1
1.1.1 Use and design of electrodes for neural interface applications	1
1.1.2 Biological failure modes of neural electrodes: the CNS response.....	4
1.1.3 Biological failure modes of neural electrodes: Meningeal encapsulation and ejection.....	10
1.2 DISPARITY BETWEEN NEURAL ELECTRODE PERFORMANCE AND HISTOLOGICAL MARKERS OF TISSUE HEALTH	12
1.3 <i>IN VIVO</i> IMAGING TO DETERMINE THE BIOLOGICAL MECHANISMS AND TIME COURSE OF ELECTRODE FAILURE 	13
1.4 DISSERTATION ORGANIZATION.....	15
2.0 <i>IN VIVO</i> IMAGING OF NEURONAL CALCIUM DURING AND AFTER NEURAL ELECTRODE IMPLANTATION: SPATIAL AND TEMPORAL MAPPING OF DAMAGE AND RECOVERY	18
2.1 ABSTRACT.....	18
2.2 INTRODUCTION	19
2.3 MATERIALS AND METHODS.....	21

2.3.1	Experimental model and subject details.....	21
2.3.2	Surgery and propidium iodide administration.....	22
2.3.3	Two-photon and fluorescence microscope imaging.....	24
2.3.4	Acute studies—cell counting and distance measurement	26
2.3.5	Acute studies—GCaMP intensity measurements.....	27
2.3.6	Acute studies—morphological analyses.....	27
2.3.7	Chronic studies	29
2.4	RESULTS	30
2.4.1	Neural probe insertion causes abnormal and long-lasting elevated calcium levels in neurons within 150µm of the device	31
2.4.2	Effect of dura resection on implantation-related calcium elevation.....	35
2.4.3	Neuronal sub-cellular compartments are morphologically deformed following neural electrode insertion	38
2.4.4	Sustained elevated calcium levels in neuronal sub-cellular compartments at 1h and 3h post-insert	40
2.4.5	Cells with membrane damage at 3-6h post-insert are geographically distinct from GCaMP(+) cells activated during electrode implantation	47
2.4.6	Increasing GCaMP activity within 150 µm of the electrode array over 28d post-insert	48
2.5	DISCUSSION	51
2.5.1	Mechanical deformation of cells may underlie high calcium levels in neuron cell bodies and neurites	52
2.5.2	Axonal transport disruption after mechanical deformation and Ca ⁺⁺ influx	55

2.5.3	Normal Ca ⁺⁺ activity increases over the first month post-insertion	56
2.5.4	Beyond implantation trauma: other sources of mechanical injury	57
2.5.5	Future directions: new therapeutic avenues	61
2.6	CONCLUSION	62
2.7	ACKNOWLEDGMENTS.....	62
3.0	NEUROADHESIVE L1 COATING ATTENUATES ACUTE MICROGLIAL ATTACHMENT TO NEURAL ELECTRODES AS REVEALED BY LIVE TWO-PHOTON MICROSCOPY	63
3.1	ABSTRACT.....	63
3.2	INTRODUCTION	64
3.3	MATERIALS AND METHODS.....	67
3.3.1	Neural probes and L1 protein immobilization.....	67
3.3.2	Surgery and probe insertion.....	68
3.3.3	Two-photon imaging.....	69
3.3.4	Data and statistical analysis.....	71
3.4	RESULTS	75
3.4.1	Microglia process extension velocity is unaffected by the L1 coating	76
3.4.2	Immediate and sustained inhibition of microglial surface coverage of the probe with the L1 coating	78
3.4.3	Changes in microglia activation at 6 h with L1 coating.....	82
3.5	DISCUSSION.....	86
3.5.1	Microglial process extension and probe surface coverage.....	86

3.5.2	Possible mechanisms of the L1-coating effect	89
3.5.3	Long-term effects of L1 coatings and future directions.....	94
3.6	CONCLUSION	95
3.7	ACKNOWLEDGMENTS.....	96
4.0	MENINGEAL INFLAMMATORY RESPONSE AND FIBROUS TISSUE GROWTH AROUND INTRACORTICAL IMPLANTS: AN IN VIVO TWO-PHOTON IMAGING STUDY.....	97
4.1	ABSTRACT.....	97
4.2	INTRODUCTION	98
4.3	MATERIALS AND METHODS	102
4.3.1	Animals and surgery	102
4.3.2	Hydrogel preparation and validation	103
4.3.3	<i>In vivo</i> two-photon imaging	103
4.3.4	Non-human primate explant analysis.....	104
4.3.5	Cell velocity analysis.....	105
4.3.6	Cell density analysis	106
4.3.7	Blood vessel trafficking analysis.....	107
4.3.8	Meningeal thickness analysis.....	108
4.4	RESULTS	109
4.4.1	A migratory window for rapid CX3CR1(+) cell movement along electrode shanks in the meninges	109
4.4.2	Variable meningeal CX3CR1(+) cell densities around the implant over the first month	112

4.4.3	Robust CX3CR1(+) cell trafficking through venules at \leq 1dpi decreases by 2-4 dpi	113
4.4.4	Meningeal collagen-I thickens over the first month post-implant, regardless of sealant.....	116
4.4.5	Implants in saline-filled craniotomies become buried in meningeal tissue by 14dpi.....	117
4.4.6	Material dependent response: meningeal CX3CR1(+) cells migrate within a hydrogel sealant	120
4.5	DISCUSSION.....	123
4.5.1	The meningeal inflammation timeline	123
4.5.2	Disambiguating effects of implant, sealant, and craniotomy.....	125
4.5.3	Relevance for fibrous implant ejection in higher order animals.....	127
4.5.4	Mitigation strategies and future directions	129
4.6	CONCLUSIONS.....	130
4.7	ACKNOWLEDGMENTS.....	130
5.0	HISTOLOGICAL EVALUATION OF A CHRONICALLY-IMPLANTED ELECTROCORTICOGRAPHIC ELECTRODE GRID IN A NON-HUMAN PRIMATE.....	131
5.1	NOTE ON AUTHORSHIP	131
5.2	ABSTRACT.....	131
5.3	INTRODUCTION	132
5.4	MATERIALS AND METHODS.....	135
5.4.1	ECoG grid implantation surgery	135
5.4.2	Neural recording and task control.....	136

5.4.3	Hand control task	136
5.4.4	Electrical impedance measurement	137
5.4.5	RMS amplitude analysis	138
5.4.6	Explant	138
5.4.7	Immunohistochemistry	141
5.4.8	Confocal imaging	142
5.4.9	Collagen-I imaging	143
5.5	RESULTS	145
5.5.1	Cortical architecture	145
5.5.2	Fibrous encapsulation	150
5.5.3	Physiological recordings	154
5.6	DISCUSSION.....	160
5.6.1	Histological findings	160
5.6.2	ECoG recording quality	164
5.6.3	Implications and future directions.....	165
5.7	ACKNOWLEDGMENTS.....	166
6.0	CONCLUSION	168
6.1	SUMMARY OF RESULTS	168
6.2	FUTURE DIRECTIONS.....	170
6.2.1	Directions to further understand and modulate the CNS tissue response	170

6.2.2	Directions to further understand and modulate the meningeal response	172
APPENDIX A		175
BIBLIOGRAPHY		184

LIST OF FIGURES

Figure 1-1 Placement of different types of electrode devices.....	2
Figure 1-2 Anatomy of penetrating intraneural electrode devices.....	3
Figure 2-1 Electrode array implantation causes neuronal Ca ⁺⁺ elevation within 150 μm of the device.	32
Figure 2-2 Widespread, long-lasting high Ca ⁺⁺ levels following electrode implantation.....	34
Figure 2-3 Electrode array insertion after partial or full durotomy of AAV-Syn-GCaMP6f animals resulted in cortical spreading depression (CSD) activity.	37
Figure 2-4 Neurons activated by electrode implantation are morphologically deformed.	39
Figure 2-5 Projections of time-series of GCaMP activity shows persistent, high Ca ⁺⁺ concentrations in “blebs” at tissue-electrode interface.	42
Figure 2-6 Comparison of GCaMP intensity in the same region before and after implantation. .	44
Figure 2-7 High Ca ⁺⁺ levels in neurite and soma sub-cellular compartments at the tissue-electrode interfaces persists through at least 3h post-insertion.....	45
Figure 2-8 Cells with membrane dysfunction at 3-6h post-insert are geographically distinct from cells with high Ca ⁺⁺ levels during device insertion.....	48
Figure 2-9 Chronic neural Ca ⁺⁺ activity surrounding a neural electrode increases after implantation.	50
Figure 2-10 Gas evolution during stimulation alters resting state network activity.	60
Figure 3-1 Experimental set-up.	71

Figure 3-2 Microglial process extension velocity is unaffected by L1 coating.....	77
Figure 3-3 L1 prevents microglial surface coverage of neural probes over the first 79 min post-implant.	79
Figure 3-4 L1 coating continues to prevent microglial surface coverage through 6 h post-implant.	80
Figure 3-5 Decreases in the % of tissue with microglial signal adjacent to L1 coated probes.....	82
Figure 3-6 L1 coating alters morphological features at 6 h post implant.	85
Figure 3-7 Partial L1 coatings show localized L1 effect.	93
Figure 4-1 In vivo imaging of meningeal response to chronically implanted electrode arrays..	101
Figure 4-2 Meningeal CX3CR1(+) cells migrate along the electrode’s surface during the first days post-implant.	111
Figure 4-3 Meningeal CX3CR1(+) cell densities fluctuate, but are stable, over the first month post implant.....	113
Figure 4-4 CX3CR1(+) cell trafficking through pial venules during the first 4 dpi.....	115
Figure 4-5 The meninges thicken over the first month post-implant.....	117
Figure 4-6 Without the silicone sealant to fix the devices in place, electrodes were buried under the meninges by 14 dpi.	119
Figure 4-7 Validation of PEG/PEI hydrogel biocompatibility.	120
Figure 4-8 <i>In situ</i> forming PEG/PEI hydrogels elicit a unique meningeal inflammatory response.	122
Figure 4-9 <i>Ex vivo</i> imaging of fibrous encapsulation of Utah array platform implanted in a rhesus macaque for 2.5 years.	128
Figure 5-1 Gross anatomical disposition at implant and explant.....	140
Figure 5-2 Long-term ECoG grid implantation causes minimal changes in cortical cytoarchitecture.....	146

Figure 5-3 Chronic implantation yields higher microglial density with no change in cell morphology.	148
Figure 5-4 Wide-field image of implant margin.....	149
Figure 5-5 Second-harmonic imaging of fibrous encapsulation reveals fibrous, cell-sparse region and cell dense regions in both dorsal and ventral aspects of encapsulation.	152
Figure 5-6 Immunohistochemical staining of encapsulation tissue.....	154
Figure 5-7 ECoG signal modulation during 8-target center-out reach tasks.	155
Figure 5-8 Directional modulation of ECoG signals during reaching.....	157
Figure 5-9 Electrode impedance and RMS amplitude of electrophysiological recordings.	159
Figure A6-1 FITC Albumin release from PEDOT-CNT film.	177
Figure A6-2 Fold increase of DNA signal after electrically stimulated release from PEDOT-CNT films.	178
Figure A6-3 Transfection of HAPI cells through electrically released GFP-Plasmid from PEDOT-CNT films.	180
Figure A6-4 Resveratrol release from a PEG-PEI Gel into PBS.....	182
Figure A6-5 Viability of stimulated HAPI cells after treatment with released resveratrol.	183

PREFACE

This work would not have been possible without mentors who very graciously provided support and countless hours of their time to teach me about neural engineering, how to ask the right questions, and how to plan and execute quality experiments. Thank you to my advisor, Dr. Tracy Cui, and my other key mentors Dr. Takashi Kozai and Dr. Alberto Vazquez. Thank you to my Dissertation Committee, and especially Dr. Kacey Marra and Dr. Aaron Batista, for your invaluable input. This dissertation has also hugely benefitted from my lab mates in Dr. Cui's lab—Nicholas Alba, Cassi Weaver, Noah Snyder, Kasey Catt, Jeff Du, Christi Kolarcik, Mitch Taylor, Bin Cao, Asiyeh Golabchi, Patrick Cody, Sally Zheng, Emma Yang, Kevin Woeppel, Bingchen Wu, and, most of all, Xia Li. Thank you all for being excellent colleagues and making science fun!

The broader University of Pittsburgh Department of Bioengineering and Center for Neural Basis of Cognition community has provided incredible support. Thank you to our leadership, faculty, and to Nick Mance for everything. Our department is home of a very dedicated chapter of the Biomedical Engineering Society, which has been a central pillar of our community. Thank you for making this department a warm and welcoming place.

Finally, I would like to thank my family, friends, and my partner, Dr. Eileen Wong for filling these past few years with many, many great memories. None of this would be possible without you!

1.0 INTRODUCTION

1.1 NEURAL INTERFACES: CLINICAL USE AND FAILURE MODES

1.1.1 Use and design of electrodes for neural interface applications

Implantable neural electrodes have been used since the early 20th century to understand the electrical activity and connections of the brain [1]. From these original studies, electrical stimulation was quickly identified as having high potential for therapeutic use and has subsequently been adapted for treating deafness [2], blindness [3], chronic pain [4], and Parkinson's disease [5]. After the discovery that extracellular motor cortex neuronal recordings can predict motor behavior [6], implantable electrodes have also been conceived of as a way to interface with and control computers and robotic limbs as brain-computer interfaces (BCI) [7]. BCI technologies have since been translated to the clinical environment [8-11].

There are a variety of designs for BCI neural electrodes that have tradeoffs between invasiveness and spatiotemporal resolution (Figure 1-1) [12, 13]. Electroencephalogram (EEG) electrodes are non-invasive placed on the patient's scalp, but have low spatial and temporal resolution. Electrocorticography (ECoG) electrodes are invasive, requiring implantation epi- or sub-durally under the skull. As part of a BCI, they can achieve at least 3 degrees of freedom in controlling a robotic arm under human control [14]. Penetrating intracortical electrode arrays are

the most invasive, requiring traumatic insertion through the cortex. These electrodes have the highest spatial and temporal resolution, enabling electrophysiological recording from individual neurons. BCIs with intracortical electrode arrays can achieve at least 10 degrees of freedom in control of robotic limbs [15]. Because of their ability to resolve individual neurons and control BCIs, intracortical electrodes are the most widely used for BCI research and development.

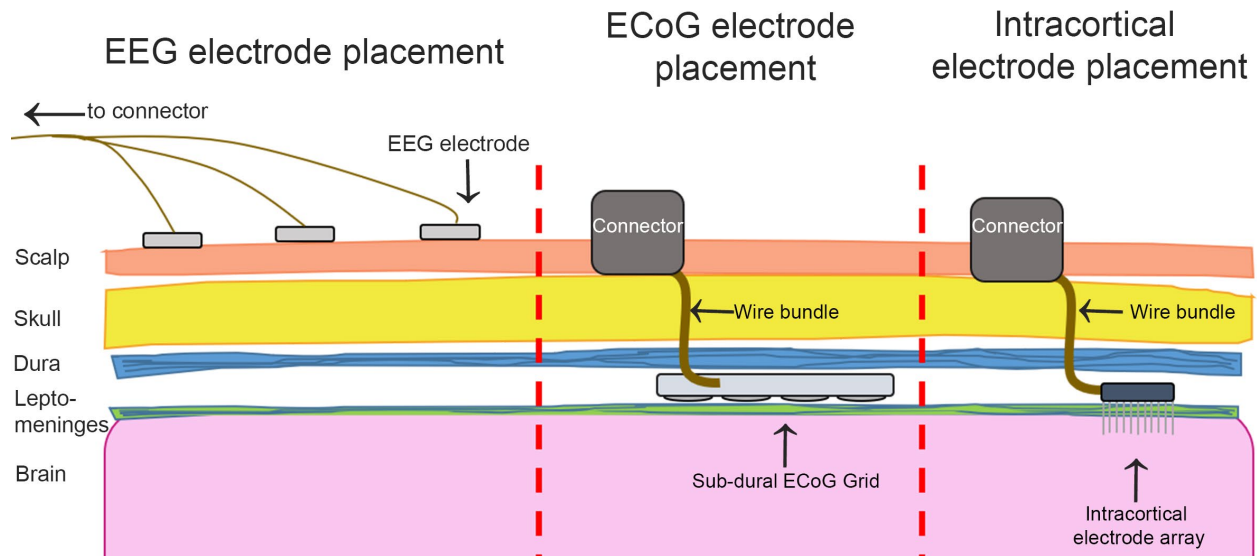


Figure 1-1 Placement of different types of electrode devices.

EEG electrodes (*left*) are the least invasive device, being placed on the patient’s scalp. ECoG electrodes (*middle*) are more invasive, requiring a craniotomy for electrodes to be placed epi- or sub- durally (dura mater shown in blue). Intracortical electrodes (*right*) are the most invasive, requiring penetrating of the brain’s cortex.

The simplest design for an intracortical electrode is an insulated wire with an exposed, conductive tip (Figure 1-2). The electrode site is inserted into the brain and placed within 140 μm of neurons of interest in order to resolve extracellular activity for individual neurons [16]. Single-electrode devices can also be fabricated by depositing conductive traces and electrode sites on silicon substrate that has been patterned or etched into a needle. To survey larger neural populations, multi-electrode arrays are made by joining several single electrode needles (referred to as “shanks”) on a platform [17] or by depositing multiple electrode sites along an electrode shank [18, 19].

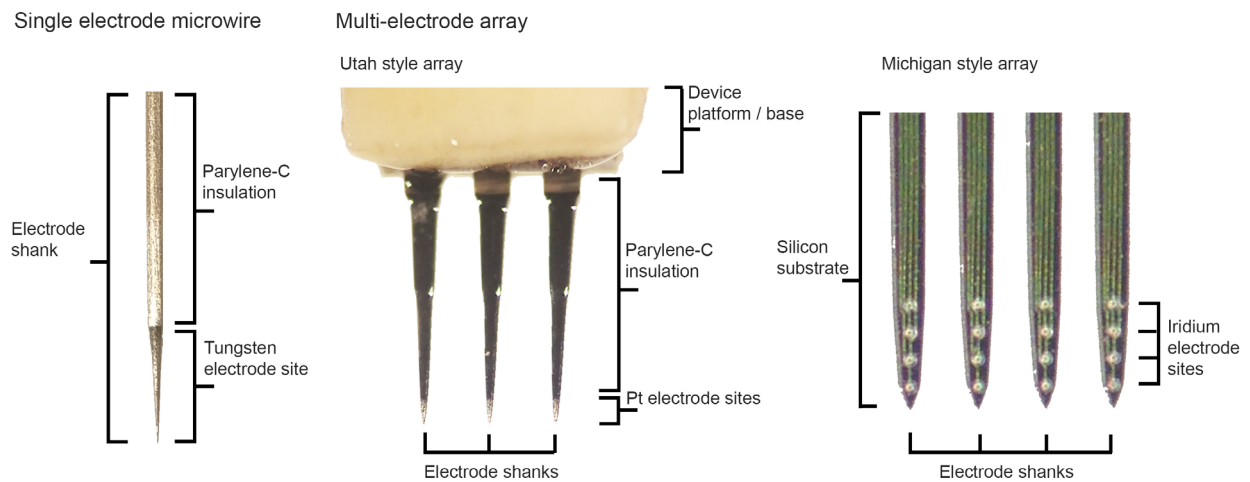


Figure 1-2 Anatomy of penetrating intraneural electrode devices.

The simplest electrode is an insulated wire with an exposed conductive tip at the end (*left*). This is a single-shank, single-electrode device. Multielectrode arrays can be made by joining multiple electrode shanks at a platform or base (Utah style device, *middle*). Alternatively, multiple electrode sites can be deposited along electrode shank, with the ability to still join multiple shanks to a platform (Michigan style device, *right*).

1.1.2 Biological failure modes of neural electrodes: the CNS response

After implantation, electrode arrays suffer progressive decline in recording quality and eventually fail to record single unit activity in mice [20], rats [21], cats [22, 23], and non-human primates [24-27] on the order of months to years after insertion. This inevitable decline in performance is hallmarked by high variability in how and when devices fail [22, 27, 28]. Barring implant loss due to mechanical breakage of the percutaneous connector or wiring, devices are typically thought to either fail due to poor tissue integration in the central nervous system (CNS) that results in damage to neural tissue surrounding implanted devices and progressive material degradation of the device or due to poor integration of the device with the meningeal tissue at the surface of the brain that results in fibrous encapsulation and ejection of the electrode device.

The CNS response to implantation occurs within the brain. Neural electrode implantation is an inherently traumatic process. During insertion, electrodes are pushed into the surface of the brain until the tissue tears and the electrode inserts into the cortex [29]. This requires electrodes to apply a force sufficient to break the leptomenigeal and cortical surface tissues [30]. The high penetration force can injure and kill neurons [31-35] and can rupture and drag blood vessels at the insertion site [36-38] leading to hypoperfusion and vascular leakage within the brain [37, 39, 40]. While insertion damage can be minimized by modulating insertion speed, electrode tip shape, electrode size, and the density of electrode shanks [30, 36, 41-46], the damaging effects of implantation persist to some degree. Insertion can also strain and buckle the implanted device [47, 48], which can lead to damage of electrode sites, traces, and insulation [49]. These effects of acute insertion may explain immediate drop in neuronal density around devices [35, 50, 51] as well as poor recording performance immediately after implantation [20, 27, 52]. The initial drop in neural density due to implantation can be partly confirmed by “stab wound” studies, in which

electrodes are inserted and immediately removed to isolate the implantation effects. Some studies show that a stab wound alone results in a 25-50% drop in neuronal density 2-16 weeks after surgery [53], while others report that there is a higher density of neurons around the stab wound site after 2-16 weeks [35, 54]. The increase in density is likely on account of the hollow electrode tracks left by the stab wound. As the tissue remodels after injury, the electrode tracks could be “filled in” by the surrounding parenchyma, which would appear as denser neuronal tissue.

After the mechanical impact and vascular damage of insertion, the electrode device can be fouled by cell debris and plasma proteins that are usually barred from the brain by the blood brain barrier [37, 55, 56]. Plasma proteins such as IgG [57], fibrinogen [58], and albumin [59, 60] can exacerbate inflammation by activating microglia and astrocytes, and can also have direct, damaging effects on neurons [61]. This may explain microglia become activated and extend processes toward the electrode device in the first minutes after implantation [40]. Blood-brain barrier leakage can persist for at least 3 months after electrode implantation [37, 53, 62-66]. Over the next day after implant, microglia will begin to migrate and aggregate at the tissue-electrode interface, beginning the formation of the glial scar [67, 68]. Over the next weeks, microglia and astrocytes form a compact glial scar (typically extending no more than 200 μm from the insertion site) around the device [51, 54, 69]. There is also high influx of inflammatory cells (macrophages and lymphocytes) and fibroblasts to the scar region from outside of the brain [50, 66, 70-72]. Peripheral macrophages may comprise as much as 60% of the macrophage population at the tissue electrode interface and remain there for at least 3 months after implantation [50].

There are multiple “triggers” that control the development and extent of the glial scar. While the mechanical impact of insertion appears to be the start of glial scar formation, stab

wound studies agree that the chronic presence of a neural electrode leads to significantly greater neuron loss and reactive microglial and astrocyte density around implanted devices [35, 53, 54]. Nonetheless, all implanted electrodes and even stab wounds elicit some degree of neuronal damage and glial scarring. Through varying electrode design parameters that provides insight as to what controls the extent of the damage. The critical design parameters are electrode size and shape, fixation and material properties, and surface chemistry. For size, electrodes with lower cross-sectional areas tend to have greater neuronal densities and generate less glial scarring at the tissue-electrode interface [51, 73, 74]. This may reflect reduced tissue damage upon implantation [30, 36], but also may be benefited by macrophage adhesion dynamics. Macrophages in the periphery have different response for fibers of different diameters, with fibers with cross-sectional areas $< 30 \mu\text{m}^2$ eliciting significantly less macrophage adhesion and encapsulation than larger fibers [75, 76]. Devices of this size are difficult to fabricate to maintain sufficient electrical properties for implantation and single-unit recording (material strength, electrode electrochemical surface area, insulation thickness), but microfabrication technologies are beginning to approach these limits. Carbon fiber and SU-8 based electrodes with $58.1 \mu\text{m}^2$ and $50 \mu\text{m}^2$ cross-sectional areas respectively are able to record single neuronal action potentials over months with limited glial scarring or neural loss [48, 55, 77]. As these technologies continue to improve, size may play a smaller role in electrode longevity. Related to size, the shape of the electrode is also a critical factor. Devices with edges generate more mechanical strain than smooth devices, and may explain why round electrodes tend to have less glial reaction than planar devices [49, 64]. The number and spacing of electrode shanks in a device's shape will also play a key role. A greater number of shanks increases the probability of vascular damage upon implantation [37, 38, 78]. The ideal spacing between shanks is relatively unexplored, but shanks

that are greater than 1 mm apart from one another seem to generate independent tissue reactions [79], while shanks spaced $< 600 \mu\text{m}$ from one another have progressively worse glial scarring outcomes [26, 35, 46]. Notably, the interaction effects between electrode size and shape, and especially on shank count and spacing, is largely unexplored. It is likely that these factors will need to be optimized together in order to improve tissue-electrode integration.

Another set of factors that govern the degree of tissue response is the fixation and material properties of a device. These both relate to the micromotion of the brain relative to an implanted electrode. The brain floats in a bath of cerebral spinal fluid in the skull, and as a person's heart beats or they breathe or move, the brain also moves. Most commercially available electrodes are made of silicon or metal and are fixed to the skull for mechanical support (also called "anchoring"). This means that as brain moves it pushes into the stiff electrode and creates mechanical strain [49, 80-82]. The incident strain is thought to activate microglia and astrocytes, perturb neurons, increase blood brain barrier leakage, and create cracking and fracturing of electrode components. Many research groups have experimentally tested this by either implanting flexible or soft devices or allowing standard rigid devices to float on the surface of the brain by not fixing them to the skull (unanchored). Indeed, flexible devices tend to elicit less inflammatory tissue response and blood-brain barrier leakage than rigid devices [45, 77, 83-87]. Due to the softness of these devices, they often require some sort of shuttle for insertion, which may generate additional tissue damage [83, 88, 89]. Despite this, flexible devices seem to perform well. While reduction of micromotion is one explanation for why these devices improve integration, non-flexible devices with soft coatings can also modulate microglial activation and migration [90, 91]. These are exciting findings, as these devices with rigid bulk properties are easier to insert than fully soft and flexible devices. Micromotion related damage can also be

controlled by an “unanchored” fixation that allow devices to float on the surface of the brain. These devices also have reduced glial scarring and blood brain barrier disruption with improved neuronal survival, suggesting that micromotion is indeed an instigator of tissue reaction [64, 70, 72, 73].

A final potential trigger for glial scarring is surface chemistry. Protein fouling and subsequent microglial attachment after electrode insertion represent the beginning of glial scar formation. The extent of molecular and cellular fouling can be controlled by device’s surface chemistry, and so plays a significant role in the extent of long-term glial scarring [46, 55, 92-94]. Most basically, fouling can be controlled through modulating the hydrophobicity of the device’s surface. Hydrophilic or zwitterionic self-assembled monolayer coatings tend to prevent protein and cell attachment by maintaining a “hydrated layer” between the surface of the device and the surrounding tissue [55, 94-98]. While these coatings provide a temporary reprieve from fouling, they do not prevent cellular adhesion indefinitely as the coating suffers oxidative or mechanical damage over time [93, 98, 99]. Macroscopic gel coatings can be effective, but expand the cross-sectional area of the device and will further swell if a hydrogel material [100-103]. Bioactive coatings consist of cell adhesion molecules, enzymes, or enzyme mimics to the surface of devices. They can lead to short and long-term improvements to tissue integration by deterring macrophage and astrocyte attachment and, for certain coatings, improve neural attachment [95, 104-109]. These coatings will be explored in Chapter 3 of this dissertation.

While the above triggers can modulate the scale of the glial scar, the reactive cellular lesion can still have a number of deleterious effects on the tissue-electrode interface. Firstly, it can act as a high electrical impedance barrier that separates the electrode sites from the neuronal population [27, 110-113]. While the electrical impedance of neural electrodes come from

multiple sources and has varied effects on neural recording quality, there is little doubt that scar tissue formation can increase electrical impedance [110-112]. More consequential to the long-term viability of electrodes, glial scar tissue has upregulation of pro-inflammatory macrophage markers as well as secretions of pro-inflammatory, neurotoxic cytokines (TNF and MCP-1) [54, 63, 94] and reactive oxidative species [109, 114]. This persistent inflammatory environment may be responsible for neuronal apoptosis [20] as well as modulation of neural activity [115] and loss of myelin around the implant [116]. Gliotransmission from glial scar cells may also be responsible for altering ion channel expression in neurons around the implanted electrode, which modulates neuronal excitability [117, 118]. Finally, the hot, salty, and oxidative environment of the glial scar in conjunction with micromotion can lead to material degradation of the electrode as well [21, 49, 119-121]. Over long periods of time, this environment leads to cracking and breakage of electrical traces and electrical sites and deterioration of the insulation [21, 27, 46, 49, 113, 121, 122]. In fact, there are currently no dielectric materials used *in vivo* that are expected to withstand the harsh environment for more than 10 years [120, 123]. Ultimately, it is believed that a combination of the insulating glial scar, neurodegeneration and neuromodulation, and material damage that leads to device recording failure.

While recording failure is expected to occur within months of implantation for rodents, studies in non-human primates suggest that electrodes can still record single neuronal units for up to 7-8 years after implantation [25, 27, 113]. There is evidence that there is a similar or slower progression in the clinical BCI population [11, 124]. This is perhaps not surprising given the large differences in the immune systems between mice and humans [125]. For clinical patients and higher-order preclinical models, there are other biological failure modes that may manifest just as frequently but more rapidly than the CNS tissue response related failure.

1.1.3 Biological failure modes of neural electrodes: Meningeal encapsulation and ejection

As is shown in Figure 1-2, the intraneural and ECoG electrodes have components that reside in the meningeal tissues at the surface of the brain. The meninges consist of 3 tissue layers. Most dorsally, there is the thick, collagenous dura mater that surrounds and protects the brain. Under the dura are the two leptomeninges layers: the arachnoid layer and pia mater. Cerebral spinal fluid fills the sub-arachnoid space between these layers and provides buoyancy and mechanical cushioning for the brain [126]. The arteries and veins of the brain run parallel to the surface of the brain in the pia and penetrate orthogonally into the brain to provide circulation [127, 128]. In addition to providing mechanical support to the brain and harboring vasculature, the meninges are critical in neural development [129, 130], repair after CNS injury [131-134], immunogenic antigen presentation and response during infection [135], and brain waste disposal [136].

Neural electrodes are typically implanted through the dura in mice, which is very thin (~20 μm thick, see Chapter 4) [20]. Larger animals typically have thicker dura (>300 μm in rhesus macaque, see Chapter 5) that must be removed prior to insertion [27]. For either of these implantation scenarios, the damage involved in the surgical procedures is implicated in meningeal inflammation. After craniotomy [137, 138], hemorrhage [133, 134], or mechanical trauma [132] in the meninges, there is inflammatory mobilization to the tissue and the ultimately the meninges thicken as collagen synthesis is upregulated. Ultimately, meningeal integrity must be maintained for the tissue to execute its critical protective functions and maintain cerebral spina fluid pressure [138, 139].

In fact, intracortical electrodes implanted in rats [52, 65], cats [23], and non-human primates [27, 113] can become progressively encapsulated in meningeal tissue after device insertion. For the studies involving cats and non-human primates, the dura is reflected and

replaced after implantation. In these studies, collagen that is continuous with both the dura and arachnoid layers appears to grow to surround the electrode platform. As collagen continues to proliferate, the electrodes appear to be lifted out or ejected from the cortex, leading to electrode failure [23, 113].

In a study of 78 10x10 Utah arrays implanted into non-human primates, 53% of biological device failures was due to meningeal encapsulation and ejection of electrode devices [27]. Similar rates or greater rates of meningeal encapsulation have been reported in rat [52, 65] and cat [23]. Most encapsulation appears within the first year of encapsulation. Interestingly, meningeal encapsulation also occurs with non-penetrating, epi-dural [140, 141] and sub-dural [142] ECoG grids implanted in rats, suggesting that the encapsulation is triggered by the presence of foreign bodies in the meninges and not necessarily a product of durotomy or intracranial implantation. Further, there are few reports of meningeal encapsulation of devices without a large, meningeal-dwelling 2D platform like in the Utah array. The meningeal encapsulation of small-platform devices may be under-reported, as it would likely not lead to device ejection without a large platform for collagen to “grip”. This may highlight the importance of electrode platform design in overcoming the meningeal encapsulation problem. Beyond these studies, there is little known about the triggers for meningeal encapsulation and ejection. It is possible that fibroblasts in the meninges are upregulating collagen-I synthesis due to the mechanical strain generated by the presence of chronic implants [143] or by the presence of activated macrophage [144, 145]. There is a great need to expand research on the mechanisms of meningeal encapsulation to design the next generation of implantable neural technologies.

1.2 DISPARITY BETWEEN NEURAL ELECTRODE PERFORMANCE AND HISTOLOGICAL MARKERS OF TISSUE HEALTH

Much of the theory of biological sources of electrode failure is built upon post-mortem histological and molecular analysis. To understand the progression of the tissue reaction to implanted electrodes, multiple cohorts of animals are used with discrete end-points that, in aggregate, can provide insight about the changing biology around implanted electrodes. There are intrinsic limitations in this approach. There is a great degree of variability in both the recording performance as well as the histological disposition even amongst adjacent electrode shanks in the same device [22, 23, 27, 122]. This variability is compounded in studies with different cohorts for different time points. Ultimately, this creates a high burden on performing statistical tests for histology around implanted neural devices.

Additionally, there are limits to the information gained from post-mortem antibody stains. While many dyes and antibodies can reveal if a certain cell-type is present, it gives only a limited understanding of dynamic cell behaviors. A concrete example of this is the NeuN antibody that labels neuronal nuclei and is used in many studies to determine neuronal density around chronically implanted electrodes [146]. While it reliably labels neurons, it does not convey information about activity of that neuron. As a result, there are many examples of electrode sites that show little material damage and are surrounded by many NeuN(+) neurons but fail to record electrophysiological activity [20, 122]. In these situations, it is possible that the neurons around the device are quiescent or suppressed in some way. This can be partly addressed by activity based stains like c-Fos, but these typically are only sensitive to very high firing events in neurons and would not capture subtle dynamic changes in neural activity [147]. Antibodies directed to neuron ion channels, transporters, and receptors can suggest the excitability of a

neuron [117, 118]. Another possibility is that some of the silent neuron's neurites were damaged upon implantation and so has fewer inputs. This could potentially be revealed by ultrastructural analysis through transmission electron microscopy [148]. Similarly, dynamic behaviors of microglia [56, 58, 149-151] and astrocytes [152] would not be captured by static or activity-based antibody stains for these cells.

A final drawback to post-mortem histology is the potential to create artifacts during tissue sectioning [153]. While there are image processing solutions to generate 3D reconstructions from serially sectioned tissue, sectioning and reconstruction still creates additional sources of error generation and variability in the treatment of individual slices [154].

These limitations in post-mortem histological analysis of the tissue-electrode interface could be hindering discovery of new biological mechanisms of electrode failure. In turn, this could be a bottleneck in the development of next-generation electrode technologies and therapeutics that could improve the lifespan of BCIs.

1.3 *IN VIVO* IMAGING TO DETERMINE THE BIOLOGICAL MECHANISMS AND TIME COURSE OF ELECTRODE FAILURE

In vivo imaging—also called intravital imaging—provides the means to overcome the limitations of post-mortem histology by monitoring molecular, cellular, and organ anatomy and physiology in the same animals over time. Modalities for *in vivo* imaging vary in their depth of penetration, spatiotemporal resolution, and ability to use targeted contrast agents. Based on these parameters as well as the location and optical properties of the organ of interest, *in vivo* imaging ranges

widely in invasiveness [155]. The invasiveness of imaging must be balanced with the desired duration of imaging in order to avoid complications or mortality.

In the realm of monitoring the tissue response to electrodes with *in vivo* imaging, several techniques have been pursued. Magnetic resonance imaging could provide non-invasive monitoring of neural activity around implants, but are complicated by heating and imaging artifacts around metal components of devices [156-158]. Optical coherence imaging can be used to monitor vasculature and tissue density, but requires either a cranial window or an implantable optical coherence tomography fiber to achieve sufficient imaging resolution [159, 160]. Optical coherence techniques are further limited in that they cannot use targeted contrast agents to image specific cell types. Brightfield and fluorescence mesoscale imaging through cranial windows can take advantage of using fluorescent labels to image specific cell types, cellular activity, and vasculature [140, 141]. Traditional light microscopy, however, suffers from poor axial resolution that prevents precise localization of cells. Multi-photon imaging stands out as having the most potential to image the tissue-electrode interface over long periods of time. Multi-photon imaging uses femtosecond pulses of infrared wavelength lasers to excite fluorophores in tissue. Due to the higher wavelength and flux of the multi-photon laser, two-photon and three-photon laser scanning microscopy can image deeper into tissue with less light scattering and higher axial resolution [161, 162]. Additionally, due to the lower energy of infrared photons, phototoxicity is drastically reduced for multi-photon microscopy compared to traditional single-photon scanning laser microscopy. While deep multi-photon imaging of brain tissue also requires removal or thinning of the skull [163, 164], the major advantage is that it can be used with genetically-modified or dye-injected animals that have fluorescent molecules localized to specific cell types. This allows longitudinal tracking of specific cell populations. These methods are particularly

powerful in conjunction with injected or genetically expressed voltage or calcium sensitive molecules that can be used to report dynamic changes in cellular physiology over time.

Kozai et al initially adapted two-photon microscopy for imaging acute damage to vasculature [37] and the subsequent microglial, oligodendrocyte, and NG2 cell responses [40, 68, 122, 165] during neural electrode implantation. These experiments were later expanded to chronic implantation scenarios, lasting 3 months post implantation [62]. These experiments have shown the extent to which vascular damage can affect tissue damage after implantation. They have also shown that microglia and NG2 cell responses to implantation are rapid, with microglial activation and polarization toward the implant occurring immediately after insertion, and both microglial and NG2 cell migration toward the device within the first days post implant. These are findings that would be very difficult to obtain from post-mortem histology, and highlight the need for longitudinal imaging to better understand the tissue response to chronically implanted electrode devices.

1.4 DISSERTATION ORGANIZATION

In order to design next generation neural electrodes with greater longevity, the root causes of electrode failure must be understood. The following dissertation primarily uses *in vivo* imaging to answer critical questions that have eluded studies that rely on post-mortem histology. We seek to answer 3 major questions: how does electrode implantation damage neurons? How does surface chemistry alter the initial microglial response to implanted electrodes? How does meningeal inflammation and encapsulation develop over time? By answering these questions, we

believe that we have identified novel targets that future devices and implantation strategies can exploit to improve long-term device performance.

In Chapters 2 and 3, we focus on the acute CNS response to intracranial electrodes. In Chapter 2, we investigate the mechanisms of neuronal damage during and after electrode implantation with two-photon microscopy in mice with transgenic expression of a fluorescent calcium indicator in neurons. We analyze imaging data to quantify disruption in neuronal calcium levels, which is an important indicator of health and damage of neurons. The viability of neurons is also investigated with *in vivo* stains for membrane permeability. Calcium activity over the next month is monitored to determine if there is any improvement or decline in calcium activity after implantation. The results from this chapter can reveal high resolution changes in neuronal health after implant that may suggest novel therapies to improve electrode performance.

Chapter 3 shifts focus to investigating the microglial response to acute electrode implantation. In our previous work, we used two-photon microscopy of mice with transgenic expression of green fluorescent protein (GFP) to demonstrate that microglia have an immediate response to electrode implantation, extending endfeet processes toward the device. In this chapter, we expand upon that work to question if this microglial response can be modulated with bioactive surface coatings. Specifically, we implant electrodes with a self-assembled monolayer coating of L1 cell adhesion molecule, which mediates neuron-neuron adhesion in the healthy brain. We quantify the ensuing microglial response, determining if the L1-coated device can elicit changes in microglial process extension and encapsulation behaviors within the first 6 hours of implantation. This chapter seeks to both evaluate an experimental coating that could improve long-term electrode performance as well as provide basic mechanistic insight regarding microglial interactions with surfaces.

The final two chapters examine the meningeal response to implanted electrodes. Chapter 4 describes longitudinal imaging of meningeal inflammation around implanted electrode devices. Using two-photon imaging of GFP-labeled leukocytes in the meninges of transgenic mice, we quantify meningeal cell migration through blood vessels and on implanted electrodes for the first month after implantation. We also image meningeal collagen to track meningeal thickness over this time. This is the first targeted study to understand the mechanisms of meningeal encapsulation of implanted electrodes, and seeks to identify potential therapeutic routes to prevent device ejection.

Chapter 5 provides a detailed post-mortem examination of the CNS and meningeal tissue response to an ECoG electrode grid that was implanted in a non-human primate for 666 days. We use antibody staining to determine how chronic implantation affected cortical tissue and to identify different cell types that dwell in meningeal encapsulation tissue. These results are correlated with end-point electrophysiology during reaching tasks and longitudinal electrical impedance spectroscopy to determine how the manifestation of meningeal encapsulation affected device performance. Chapter 5 ultimately provides valuable insight about device safety for ECoG grids, and also interrogates the mechanisms of meningeal encapsulation.

2.0 *IN VIVO* IMAGING OF NEURONAL CALCIUM DURING AND AFTER NEURAL ELECTRODE IMPLANTATION: SPATIAL AND TEMPORAL MAPPING OF DAMAGE AND RECOVERY

2.1 ABSTRACT

Implantable electrode devices enable long-term electrophysiological recordings for brain-computer interfaces and basic neuroscience research. Implantation of these devices, however, leads to neuronal damage and progressive neural degeneration that can lead to device failure. The present study uses *in vivo* two-photon microscopy to study the calcium activity and morphology of neurons before, during, and one month after electrode implantation to determine how implantation trauma injures neurons. We show that implantation leads to sustained, high calcium levels in neurons within 150 μ m of the electrode interface. These neurons are morphologically distorted and mechanoporated after implantation, suggesting that calcium influx is related to mechanical trauma. Further, calcium-laden neurites develop signs of axonal injury at 1-3h post-insert. Over the first month after implantation, neuronal calcium activity increases, suggesting that neurons may be recovering. By defining the mechanisms of neuron damage after electrode implantation, our results suggest new directions for therapies to improve electrode longevity. This chapter has been reprinted from work published in *Biomaterials* [166].

2.2 INTRODUCTION

Intracortical electrode arrays are necessary tools for recording extracellular action potentials from single neurons in brain-computer interface and basic neuroscience applications [12, 167-170]. Implantation of these devices, however, is an inherently traumatic process that can result in immediate vascular and neural tissue damage, acute and chronic inflammatory glial responses, and progressive local neurodegeneration [35, 50, 53, 54, 171-174]. Neuron loss within the effective recording distance of electrode devices (electrode sites can resolve single neuron activity within 50-140 μm [13, 16, 175]) is thought to lead to progressive failure of a device's recording quality in rodent [20, 176], cat[23], and primate models [25, 27]. These biocompatibility issues must be surmounted before brain-computer interface technologies can have widespread clinical translation.

One major challenge to biocompatibility is acute tissue damage due to surgical insertion of electrode arrays. Post-mortem studies of stab wounds and acute implantations (1 and 24h) reveal that there is immediate neuronal cell death following implantation, and that the most rapid drop in neuronal cell density relative to healthy brain tissue occurs within the first 2 weeks post-insert [35, 50, 53]. Other post-mortem studies have begun to suggest that acute implantation can result in changes to the phenotype and activity of surviving neurons [117]. Namely, neurons within 100 μm of the electrode initially show increases in excitatory neuron markers (VGLUT1, 3 days post-insert) and later show increases in inhibitory cell markers (VGAT, 1 month post-insert) [28, 117, 118]. One explanation for these findings is that the inflammatory environment surrounding the implanted electrode modulates neural activity. This is corroborated by experiments detailing the rapid response of microglia following electrode implantation and

knowledge of neuromodulatory inflammatory species secreted by these reactive microglia [40, 54, 64, 165, 177]. An alternative, unstudied explanation is that neuron activity is affected by sub-cellular, sub-lethal neuronal damage during implantation that may physically alter the synaptic connectivity of neurons [28].

In the present study, we use longitudinal, *in vivo* imaging of neuron morphology and neuron calcium (Ca^{++}) activity to quantitatively map the effect of acute electrode implantation on neuron activity and health. We hypothesize that the mechanical trauma of electrode implantation can physically deform neuron cell bodies and neurites, leading to altered calcium activity and neurite degeneration. Calcium activity surrounding implanted electrodes is a particularly important read-out, as transient high calcium levels are associated with action potentials and burst firing during healthy neuron behavior [178], while high-concentration and prolonged calcium build-up in neuronal somas and neurites is associated with neurite degeneration and excitotoxic cell death [179-182].

We ultimately show that both neuronal somas and neurites within the effective recording distance are mechanically distorted during implantation. Both of these cellular compartments exhibit prolonged high calcium levels during implantation, following which neurites show early signs of degradation. Despite this, only a limited subset of cells that exhibited prolonged high calcium levels had membrane disruption by the end of the 3-6h experiment. By day 2 post-insert, cells within the affected region appear to be largely quiescent, but demonstrated recovery over the first 28 days post-insert. Overall, these results identify a previously unreported damage pattern that may point to new therapeutic targets to prevent neural electrode performance decline.

2.3 MATERIALS AND METHODS

2.3.1 Experimental model and subject details

All experiments used a mouse model for neural electrode implantation. All mice were adult (> 8 weeks), male, 25-30g, and single-housed in room temperature with a 12h light/ 12h dark circadian cycle. Studies involving imaging of calcium transients in neurons during acute neural electrode implantation (\leq 6h post-insert) were performed with C57BL/6J-Tg(Thy1-GCaMP6s)GP4.3Dkim/J (Jackson Laboratories, Bar Harbor, ME; RRID: IMSR_JAX:024275), which express the calcium sensitive protein GCaMP in the neurons under the thymus cell antigen 1 (Thy-1) promoter, with positive expression in pyramidal neurons in Layers II/III and V of cortex (n = 5 animals) [178]. For chronic studies of Ca⁺⁺ transients in neurons following neural electrode implantation (1-28d post-insert), C57BL/6J mice (RRID: IMSR_JAX:000664) injected with AAV-Syn-GCaMP6f obtained from the University of Pennsylvania Viral Vector Core were used. Based on pilot studies, we noted that the AAV-Syn-GCaMP6f model showed a higher proportion of GCaMP expressing neurons. Injection into motor, somatosensory, and visual cortices (<1 μ L per site) was performed with a micro-pipette and pressure injector. Animals were allowed to recover for >2 weeks prior to neural probe implantation and imaging to allow for adequate GCaMP expression (n = 8 animals implanted, with 4 additional discounted from chronic imaging studies due to premature death, surgical complication, or poor cranial window visibility)). To study neurite morphology following acute neural electrode implantation, Tg(Cnp-EGFP*)1Qrlu/J (n = 3 animals) and B6.Cg-Tg(Thy1-YFP)16Jrs/J mice (n = 4 animals; Jackson Laboratories, Bar Harbor, ME; respectively: RRID: IMSR_JAX:026105, 003709) were used [183, 184]. Respectively, these mice have GFP expression in oligodendrocytes and myelinated

axons under control of the 2',3'-cyclic nucleotide 3' phosphodiesterase (CNP) promoter or YFP expression in layer V neurons and their neurite arborization that project upwards to in cortical layers I-III.

2.3.2 Surgery and propidium iodide administration

Implants for acute experiments and chronic imaging experiments were non-functional 16-channel, 4-shank planar silicon electrodes with 125 μm shank-spacing (NeuroNexus, Ann Arbor, MI). Shanks were 3 mm long, 15 μm thick, and tapered from 55 μm wide to a point. All procedures and experimental protocols were approved by the University of Pittsburgh, Division of Laboratory Animal Resources and Institutional Animal Care and Use Committee in accordance with the standards for humane animal care as set by the Animal Welfare Act and the National Institutes of Health Guide for the Care and Use of Laboratory Animals. For all surgeries, animals were anesthetized with intraperitoneal (IP) injections of 75 mg kg⁻¹ ketamine and 10 mg kg⁻¹ xylazine and head-fixed by ear bars. Depth of anesthesia was assessed by heart rate, respiratory rate, and toe-pinch reflex. For surgeries lasting longer than 1h and throughout acute experiments, animals received additional IP injections of 45 mg kg⁻¹ h⁻¹ ketamine. Each animal's scalp was shaved, cleaned with ethanol and betadine (for survival surgeries), and resected with scissors. After removing periosteum from the exposed skull, a layer of veterinary cyanoacrylate was applied to the skull (Vetbond, 3M). A high-speed dental drill was used to create 5x5 mm craniotomy on one (for chronic preparations) or two (for acute preparations) hemispheres.

Acute surgeries were conducted for experiments lasting 3-6 hours. As previously described [40, 177], following craniotomy, a dental cement well (Composite Flowable; Henry

Schein, NY, USA) was placed around the exposed skull, and the animal was positioned under a two-photon microscope objective. The electrode array was stereotaxically targeted to motor or visual cortex at a 30-35° angle, avoiding large pial vasculature. Electrode array implantation to a depth of 250-350 μm (Layer II/III) was completed at a speed of 200 $\mu\text{m s}^{-1}$ with an oil hydraulic microdrive (MO-81, Narishige, Japan). The insertion speed was selected to model with widely used implantation protocols, as well as to minimize tissue dimpling during insertion [36, 41, 177]. Because imaging occurred during implantation and continuously for 30 minutes post-implantation, it was not possible to cement the device to the skull for these acute studies. Any motion related damage associated with this conformation was limited by ear head fixation. Prior to implantation, animals received an IP injection of sulforhodamine 101 (SR101, 0.05mL, 1 mg mL⁻¹) as a transient vascular contrast agent. Animals were maintained in an anesthetic plane throughout the duration of the acute experiment (3-6h). At the conclusion of the experiment, propidium iodide (PI, 1 mg mL⁻¹ in saline) was topically applied to the cortex for 20-30min to label cells with disrupted cell membranes (n = 3 of 4 acutely implanted transgenic GCaMP animals) [132]. PI was washed off with saline and animals were imaged while still anesthetized. All animals were euthanized afterwards.

Chronic surgeries and accompanying viral injections were carried out for experiments with multiple days of data collection. Through preliminary studies (not shown), we qualitatively determined that viral injection of Syn-GCaMP6f showed more Ca⁺⁺ activity in neurites when compared to transgenically expressed Thy1-GCaMP6. Denser labeling is preferred for power spectral density analysis, but can prohibit counting and morphological analyses if labeled cells are too densely packed. Therefore, viral injections were performed for chronic imaging studies that revolved around power spectral density analysis, while transgenic animals were used for the

other studies. We performed AAV-Syn-GCaMP6f (University of Pennsylvania Viral Vector Core) injections after craniotomy of C57BL6/J mice (8 animals were implanted, though $n = 4$ for chronic imaging studies due to premature death, surgical complications, or poor cranial window visibility). Injection was performed in aseptic conditions at multiple locations in visual, somatosensory, and motor cortices. Injection was completed with a micromanipulator, 5-10 μm diameter glass pipette, and micro-injector (Toohey Company, Fairfield, NJ, USA). Vasculature was avoided during injection and negligible bleeding was observed during or after injection. Following injection, the craniotomy was sealed with glass coverslips that were secured with dental cement. Headplates (W12mm \times D19mm \times 1mm) were affixed to the mouse skull with dental cement and cyanoacrylate to be used in awake recording (Narishige, Japan). After 2-4 weeks after injection—or after GCaMP expression was observed to be stable—animals were anesthetized, the cover glass was removed from the skull, and neural electrode arrays were inserted into a region of cortex with abundant GCaMP expression—within 500 μm of the injection site—at a 30-35° angle at a speed of 200 $\mu\text{m s}^{-1}$ as previously described [62]. Following insertion, electrode arrays were anchored to the mouse's skull with dental composite. For 3 animals, we noted that a thick fibrous layer of tissue had grown over the craniotomy between virus injection and neural electrode implantation. This tissue was fully or partially removed before implantation. The craniotomy was then sealed with silicone elastomer (Kwik-Sil, World Precision Instruments, Sarasota, FL) and a clean glass coverslip.

2.3.3 Two-photon and fluorescence microscope imaging

During acute implantation (pre-insertion, during insertion, and at 1-6h post-insertion) and at 1, 2, 4, 7, 14, 21, and 28 days post-insert for chronic preparations, animals were imaged by a scanning

two-photon microscope system consisting of a Bruker scan head (Madison, WI) and a laser tuned to 920nm with 100fs pulses at a frequency of 80Mhz (Mai Tai DS or Insight DS+; Spectra-Physics, Menlo Park, CA). The laser power was maintained between 20-40 mW. Emitted light was collected through a 16X, 0.8 NA objective lens (Nikon Instruments, Melville, NY) and detected with photomultiplier tubes (Hamamatsu Photonics KK, Hamamatsu, Shizuoka, Japan). Z-stack images were collected with a size of either 1024×1024 or 512×512 pixels with a resolution of $0.4\text{-}1.6 \mu\text{m pixel}^{-1}$ and a Z step size of $2\text{-}3 \mu\text{m}$ for high-resolution stacks or $10\text{-}25\mu\text{m}$ for stacks collected during electrode insertion. Z-stack images were collected every 1-2 min for the first 25-30min post implant. Time series images of GCaMP activity were typically acquired with an optical zoom of 2-3X at a frame rate of 3-4Hz at a resolution of $1\text{-}1.5\mu\text{m pixel}^{-1}$ for 1-3 min. Animals received IP injections of SR101 prior to imaging.

For animals with a chronic preparation, on each day of two-photon imaging as well as during probe insertion, GCaMP activity was also imaged through an MVX-10 epifluorescence microscope (Olympus, Tokyo, Japan) and a CCD camera with exposure time of 48.5 ms (CoolSnap HQ2; Photometrics, Princeton, NJ). GCaMP was excited using a white light source (Sola II, Lumencor, Inc; Beaverton, OR) and a 470 ± 20 nm fluorescence excitation filter. The fluorescence emission (525 ± 25 nm) was imaged over a field-of-view of $4\times 4 \text{ mm}^2$ at a frame rate of 10-20 Hz for 3-5min. All chronic imaging time-points were performed with awake animals that were head-fixed by headplate on a custom frame.

One additional animal was included in this study that was implanted with a functional 16-channel, 4-shank planar silicon electrodes with $125 \mu\text{m}$ shank-spacing (NeuroNexus, Ann Arbor, MI) in order to characterize the effect of high-amplitude electrical stimulation on tissue deformation. At one month post-implantation, electrical stimulation was applied to a 703 cm^2

irridium electrode site using a current isolator box (AMPI) as previously described [170, 185]. The stimulus parameter consisted of a charge balanced asymmetric cathodic leading electrical rectangular pulse with a width of 50 μs and a trailing anodic pulse width of 250 μs using a k value of 0.55 at 130 Hz. On a separate electrode site, a “rejuvenation” protocol was carried out as previously published using a monopolar 4s 1.5V DC bias [186, 187]. The stainless steel bone screw in the contralateral calvarium was used as the ground. GCaMP activity was imaged with the two-photon microscope at 3 Hz.

2.3.4 Acute studies—cell counting and distance measurement

Z-stacks from acute studies were analyzed to determine the number of GCaMP active cells following implantation as a function of distance from the probe’s surface and time post-insert. Cells were counted manually based on elliptical morphology, with major axis length between 10-20 μm (average major axis length of measured cells: $12.69 \pm 0.42\mu\text{m}$). Cells included both cells with GCaMP signal excluded and included within the nucleus. A sample of counted neurons were measured post-hoc to confirm that their fluorescence intensity was >2X that of local background signal. Distance of a GCaMP active neuron or PI(+) cell from the probe’s surface was determined by manually defining a 2D mask to outline the electrode array’s footprint in ImageJ (National Institutes of Health). Because the electrode array is implanted at a 30-35°, the 2D mask was digitally rotated using the “Interactive Stack Rotation” tool in ImageJ to align with the array[188]. A distance transform was then created with the 3D mask using the “bwdist” function in Matlab (MathWorks, Boston, MA). Positions of manually counted cells were cross referenced with the distance transform to determine the distance between each cell and the nearest-contact point of the electrode array. Statistical differences in the number of activated

neurons as a function of distance (bins of 10 μ m) and time (bins of 1-1.6 minutes) were determined by non-repeated measures (Matlab) or one-way repeated measures ANOVA analysis (SPSS Statistics, IBM), respectively, both of which using Tukey's post-hoc test ($p < 0.05$). Statistical differences between counts of GCaMP active cells and PI(+) cells as a function of distance were determined by two-way ANOVA with Tukey's post-hoc tests ($p < 0.05$, Matlab). Images of GCaMP active cells at 0 min post-insert and PI(+) cells 3-6h post implant from the same animal were manually aligned in ImageJ using the electrode array as a stable land-mark.

2.3.5 Acute studies—GCaMP intensity measurements

The fluorescence intensity of GCaMP of neurites in cortical Layer I was tracked from 1-2 minutes pre-insertion, to 27.2 min post-insertion ($n = 5$ animals). Average fluorescence intensities within 150x68 μ m regions of interest were measured at the tissue-electrode interface and in a control region that was >350 μ m from the device. Fluorescence was calculated as F/F_0 , where F_0 is the average fluorescence of an ROI pre-insertion and F is the average fluorescence of an ROI at a given time-point post-insert. Insertion site and control region fluorescences were compared by two-way repeated measures ANOVA with Tukey's post-hoc tests (significance: $p < 0.05$; SPSS Statistics, IBM).

2.3.6 Acute studies—morphological analyses

Z-stack images were also used to determine cell morphology. Cell somas of GCaMP active cells during peak activation (immediately after probe insertion) were manually traced and ellipses were fitted to the trace in ImageJ. The length of the major (b) and minor (a) axes of the fitted

ellipses were used to calculate cell shape strain index (CSSI; Equation 2-1; Figure 2-2a) as previously described [83]:

$$CSSI = \frac{\Delta L}{L_0} = \frac{(b-a)}{\frac{(b+a)}{2}} \quad (2-1)$$

CSSI assumes that, on average, a cell without strain is a circle with a mean diameter of L_0 , while a strained cell becomes ellipsoid that can be represented by ΔL . Histograms of CSSI were generated with a bin size of 0.1 and statistically compared before and after insertion with two-way ANOVA with a two-sample Kolmogorov-Smirnov test (significance: $p < 0.01$).

Changes to neurite morphology were assessed with CNP-GFP and Thy1-GCaMP animals. Z-stacks from CNP-GFP mice were also analyzed for neurite orientation changes after neural electrode implantation. Neurite orientation was measured by performing a morphological opening operation with a line structuring element with a length of 25 pixels (optimized experimentally) at 11 different angles (15 to 180°, 15° intervals) on each image ('imopen' function in Matlab). Because 0° and 180° both represent horizontal lines, we included only 180° in our structuring element library to omit redundant filters. Neurite angle was determined to be the angle of the structuring element with the highest opening operation response for each pixel whose intensity was above a threshold value (Otsu's thresholding method). Histograms of neurite orientation were calculated for regions of interest (50 x 75 μm rectangles) at the tissue-electrode interface in Layer I or in distant, healthy tissue regions (> 350 μm from the implant). Histograms between groups were compared with a two-sample Kolmogorov-Smirnov test (significance: $p < 0.01$).

In Thy1-GCaMP animals, neurite “blebbing” was tracked. Blebs are swollen, hypertrophic spherical bodies (2-8 μm diameter, distinct from synaptic boutons which are < 2 μm diameter) that develop along degenerating neurites following trauma [33, 181, 189, 190]. Blebs were automatically counted along Z-stacks in regions of interest that bounded the footprint of the electrode device and the tissue above the device. Blebs were also counted in distant regions from the implantation site (> 350 μm) to be used as controls. Both regions of interest were tracked at 1h and 3h post-insert. Automated bleb counting was performed via the Particle Analyzer function in ImageJ. Prior to using the Particle Analyzer, Z-stacks were first prepared by background subtraction (defined by $\bar{x} + 2\sigma$ of the Z-stack slice with the highest mean pixel intensity, where \bar{x} is the mean pixel intensity and σ is the pixel standard deviation), filtering with a 1-pixel radius median filter, and then binarized based on the ImageJ IsoData threshold variant method [191]. In order to avoid re-counting blebs along the Z-stack, every 4th slice (or every 8 μm) was analyzed. Particles with radii between 2-8 μm were then counted. Changes in the density of blebs (blebs per 10 μm^2) over time and between implantation region and distant regions were compared with repeated measures two-way ANOVAs with Tukey’s post-hoc tests (significance: $p < 0.05$). The distribution of bleb diameter was also quantified and compared between implant and distant regions at both time points with a two-sample Kolmogorov-Smirnov test (significance: $p < 0.05$).

2.3.7 Chronic studies

During electrode insertion, epifluorescence microscope imaging revealed a subset of AAV-Syn-GCaMP6f animals that exhibited GCaMP activity that spread out from the implantation site across an expansive region of transduced cortex. The speed and duration of this Ca^{++} wave was

quantified by tracking the margin of the Ca^{++} wave in 3-4 regions of interest on the cortex and averaging the velocity ($\mu\text{m/s}$) and duration (s) of Ca^{++} wave in these ROIs.

Following initial insertion imaging, macroscope and two-photon microscope time-series images were collected from days 2, 7, and 28 post-insert ($n = 4$ animals, with 4 additional animals removed from longitudinal studies due to premature death, surgical complication, or poor visibility through the cranial window). Power spectral density (PSD) of dF/F_0 GCaMP signal, where F_0 is the mean GCaMP intensity over time, from 2.5-5 min macroscope recordings was calculated for each pixel from 0.1-10Hz after computing the Fast-Fourier Transform for each series (Matlab) [192, 193]. The sum of PSD over the 0.1-1.2Hz frequency band was calculated, and the average value within a $600 \times 600 \mu\text{m}$ ROI around the implant was taken at each time point. This band was selected as it contains the majority of GCaMP6 activity in the 4.3 subtype [178]. Values over time were statistically compared by one-way ANOVA with Tukey's post-hoc tests (significance: $p < 0.05$).

2.4 RESULTS

Previous studies have shown that neural probe implantation incurs neuronal cell death within 1h post-insert, but the mechanisms are unclear, including if there is other sub-lethal damage to neurons. In order to explore these unknowns, we implanted non-functional 4-shank silicon planar electrodes in to the cortex of mice with transgenically ($n = 5$ animals) or virally ($n = 4$ animals, with 4 additional animals removed from longitudinal studies due to premature death, surgical complication, or poor visibility through the cranial window) expressed calcium sensitive protein GCaMP in neurons to visualize changes in activity and morphology following neural probe

implantation. Morphological changes were also assessed in mice with transgenically expressed GFP in oligodendrocytes and myelinated neurites (n = 3 animals) and mice with YFP or GCaMP expressed in cortical neurons (n = 4 animals). Cell membrane damage was tracked with the cell-impermeant dye propidium iodide (PI) (in a subset of acutely prepared transgenic Thy1-GCaMP animals, n = 3 animals). Changes were tracked acutely (up to 6h post insert) and chronically (from day 1 to 28 post insert) with two-photon microscopy and epifluorescence macroscopy.

2.4.1 Neural probe insertion causes abnormal and long-lasting elevated calcium levels in neurons within 150 μ m of the device

While observing neural probe insertion into the cortex of transgenic Thy1-GCaMP mice with an epifluorescence macroscope, we noted a visible increase in GCaMP activity around the implantation site (Figure 2-1a). By generating traces of average fluorescence intensity at the insertion site before and after insertion (Figure 2-1b), the dynamics of the insertion-related Ca^{++} activity are elaborated. Activity peaks roughly 4.1s post-insert, begins to drop by 8s, and stabilizes by 42s. Over the 54.1s imaging window, Ca^{++} signal did not return to pre-insertion baseline.

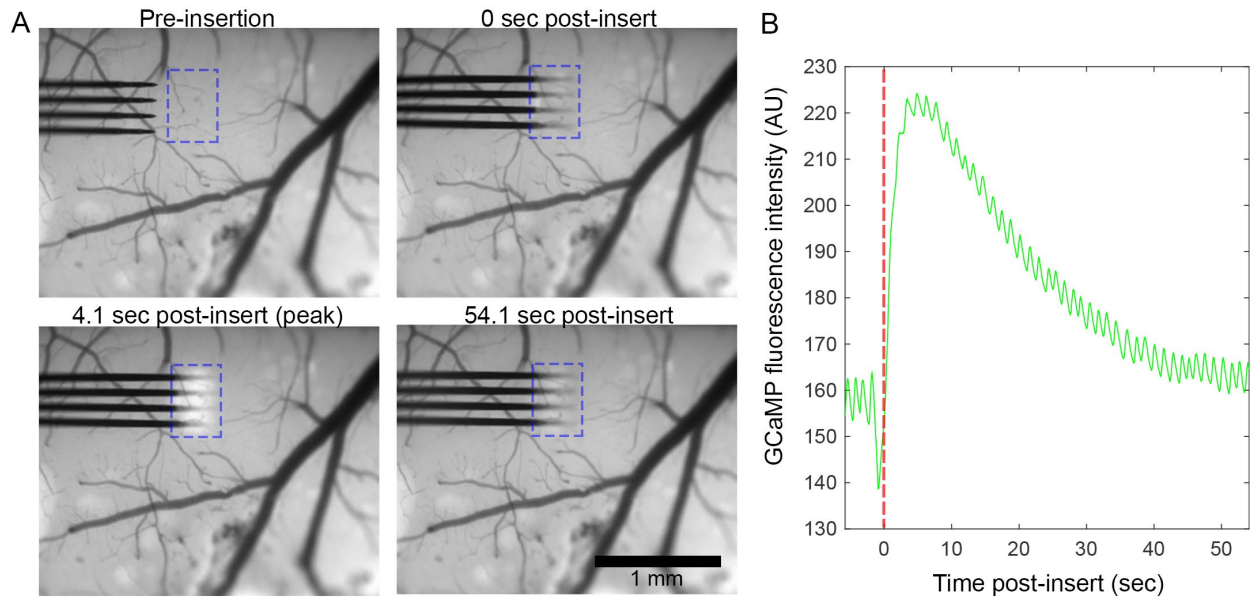


Figure 2-1 Electrode array implantation causes neuronal Ca^{++} elevation within $150\ \mu\text{m}$ of the device.

(A) Epifluorescence macroscope imaging of array implantation into the cortex of transgenic Thy-1-GCaMP6 animals reveals a visible increase in neuronal Ca^{++} in the vicinity of the implant site (outlined by a blue dotted box). (B) Traces of Ca^{++} signal within the dotted blue box in panel (A) show that Ca^{++} signal peaks by 4.1s post-insert, returns towards baseline by 19.4s, and begins to plateau above by 42s.

In order to resolve Ca^{++} dynamics during electrode insertion with sufficient X, Y, and Z resolution to study single cells and cellular processes, neural electrode insertion and the subsequent 25-30min post-insertion were imaged by two-photon. 3D Z-stacks of the implantation site were imaged every 1-2min with a Z-step size of 10-25 μm . This enabled visualization of the entire implantation site from the meninges through Layer II/III of cortex with sufficient temporal resolution to capture broad changes in Ca^{++} activity. In accordance with macroscope imaging, GCaMP activity peaked immediately after insertion, and fell to relative silence in the minutes that followed (Figure 2-2A). During peak activation (0 min post-insert),

activated neurons were largely confined within 150 μm of the implant, with significantly more active neurons between 0-70 μm from the probe compared to >120 μm from the implant (Figure 2-2B; one-way ANOVA shows significant difference across distance, $p < 0.0001$; all significant bin comparisons $p < 0.05$ in Tukey's post-hoc tests). Peak activation lasted for the first 2 min post-insertion, which had significantly more activated cells within 200 μm of the electrode than either pre-insertion or 6-25min post-insertion (Figure 2-2C; one-way ANOVA shows significant difference across time, $p < 0.0001$; significant bin comparisons $p < 0.05$ in Tukey's post-hoc tests). Further, there was no difference between the number of neurons between pre-insertion and 6-25 min post-insertion, suggesting that activity returned to baseline. Finally, the duration of GCaMP transients of cells that were depolarized during implantation were much longer than reported values for normal GCaMP6 activity (half-decay time for fluorescence in GCaMP6 4.3 = 360 ± 300 ms), with 42% of GCaMP transients lasting more than 1 min (Figure 2-2D) [178]. Due to temporal resolution limitations, we were only able to sample GCaMP activity every 1-2 min, however, sustained GCaMP activity was only considered if fluorescence activity was sustained and uninterrupted between time points.

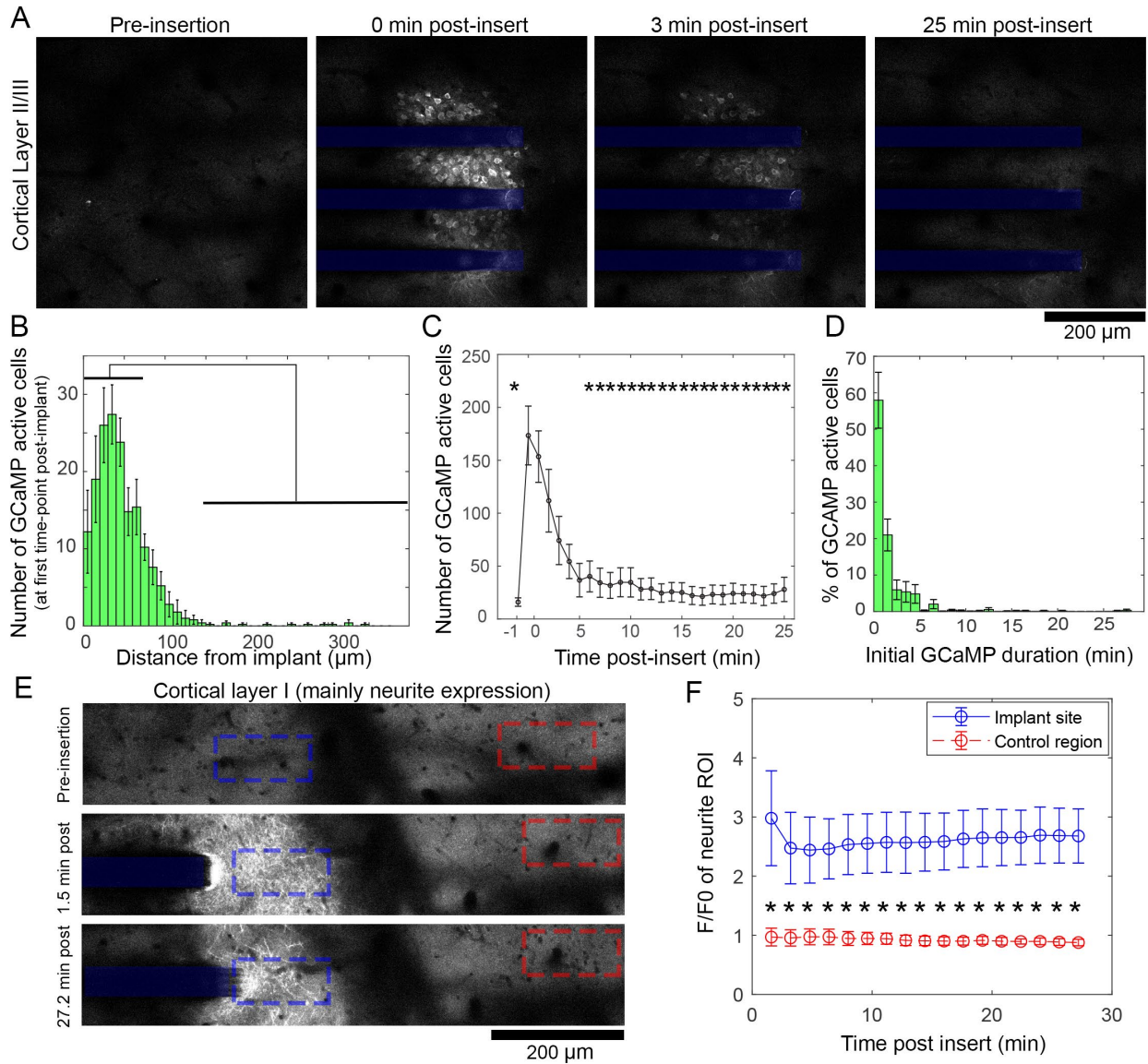


Figure 2-2 Widespread, long-lasting high Ca^{++} levels following electrode implantation.

(A) Two-photon microscopy of electrode implantation into cortical layer II/III of Thy-1-GCaMP animals shows that neuronal soma Ca^{++} elevation occurs following implantation, and subsides by 25 min post-insert.

(B) Quantification of the number of neurons activated in the minute post-implantation as a function of distance from the electrode shows that there are significantly more neurons activated between 0-70 μm compared to >120 μm from the implant (indicated by black bars, $p < 0.05$, $n = 5$ animals).

(C) The number of active cells dwindles rapidly after implant, with significantly more activated cells at 1-2min post-insert

compared to pre-insertion (-1 min) as well as 6-25min (* indicate significant difference compared to 1 and 2 min post-insertion, $p < 0.05$, $n = 5$ animals). Importantly, there was no difference in number of cells between pre-implant and 6-25 mins post-insert, suggesting activity returned to baseline. (D) Measuring the duration of GCaMP transients shows 42% of cells initially activated post-insert had influx longer than 1min, suggesting pathological activation ($n = 5$ animals). (E) Imaging of superficial cortical layer I, which predominately hosts GCaMP(+) neurites, shows similar widespread Ca^{++} elevation after implantation. High Ca^{++} levels in these neurites lasts for the duration of the initial imaging window (27.2 min). (F) There is a significant group-wise difference between the insertion site (blue) calcium and those of a distant control region (red, $>350\mu\text{m}$ from implant) (repeated measures 2-way ANOVA $p < 0.0001$). All data presented as mean \pm SEM.

GCaMP(+) neurites in cortical layer I also showed high Ca^{++} levels over the first 27.2 min post-insert (Figure 2-2E). In contrast to neuron cell bodies, which had elevated Ca^{++} levels within the first minutes post-insert, neurite fluorescence was sustained through the initial 27.2 min compared to distant regions $>350\mu\text{m}$ from the implantation site. Tracing the average fluorescence intensity in ROIs at the implantation site (Figure 2-2E-F, blue) vs. ROIs at distant regions (red), there was a sustained statistically significant increase in GCaMP intensity at the implantation site (repeated measures two-way ANOVA, $p < 0.0001$).

2.4.2 Effect of dura resection on implantation-related calcium elevation

Animals that were injected with AAV-Syn GCaMP6f virus and prepared for chronic imaging studies were implanted under a fluorescence microscope. A subset of these animals (3 out of 8 implanted animals) could not be successfully implanted without removal of a dense fibrous tissue over the surface of the brain that formed after virus injection surgery. These animals

exhibited a wave of GCaMP activity after implantation that extended across the extent of the transduced cortex, far beyond the site of mechanical insertion impact (Figure 2-3A). The Ca^{++} wave had a velocity of $39.45 \pm 10.52 \mu\text{m/s}$ (mean \pm SEM; Figure 2-3B) and a duration of $87.35 \pm 30.62 \text{ s}$ (mean \pm SEM; Figure 2-3C), which is consistent with reported values for cortical spreading depression (CSD) [194]. Virus injected animals without durotomy exhibited calcium elevation similar to transgenic animals (Figure 2-1).

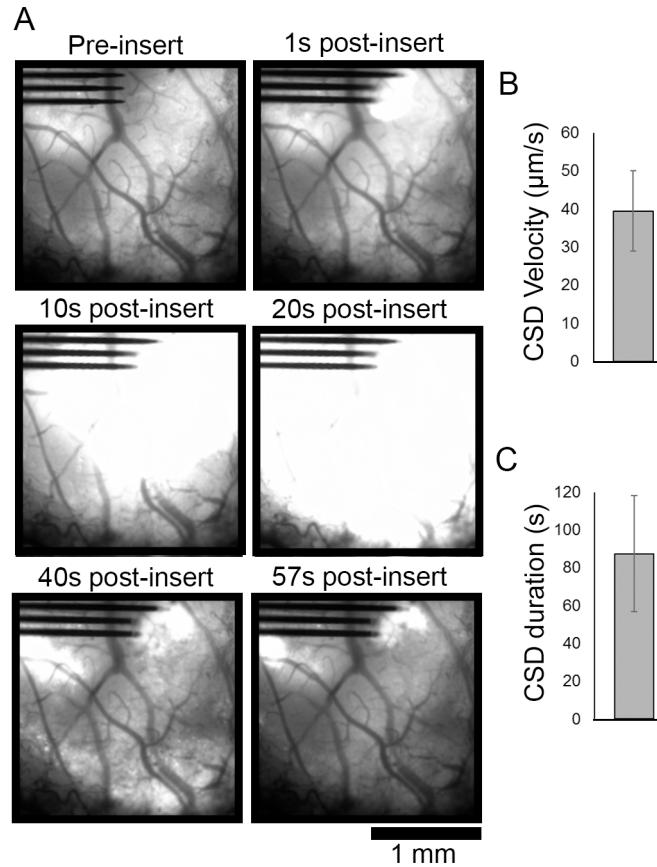


Figure 2-3 Electrode array insertion after partial or full durotomy of AAV-Syn-GCaMP6f animals resulted in cortical spreading depression (CSD) activity.

(A) Fluorescence macroscopy imaging of a subset ($n = 3$ of 8 implanted animals) of animals that transduced with GCaMP under control of synapsin promoter via AAV vector injection developed significant fibrosis under their cranial windows. After resection of the fibrous tissue, probe implantation created fast-moving GCaMP activity consistent with CSD that spreads across the transduced region of cortex that resolved by 57s post-insert. **(B)** CSD velocity was measured to be average $39.45 \pm 10.52 \mu\text{m/s}$ and **(C)** duration was on average $87.35 \pm 30.62 \text{ s}$ (mean \pm SEM, $n = 3$ animals).

2.4.3 Neuronal sub-cellular compartments are morphologically deformed following neural electrode insertion

Noting that neuronal deformation can cause abnormal neural activity [195, 196], we quantified the morphology of GCaMP active cells in transgenic Thy1-GCaMP animals during peak activation following neural electrode insertion. The mechanical strain of these cells were quantified by a Cell Shape Strain Index (CSSI) [83], which captures how much a cell deviates from a perfect circle by fitting an ellipse to a cell's perimeter (Figure 2-4A; bottom: example average CSSI values are shown, with lower values indicating less strain and high values indicating more cellular strain). We noted that on average, cells were more strained after implantation compared with the same tissue prior to implantation (Figure 2-4B, cells with CSSI > 0.3 are indicated with red *). These changes were quantified by comparing distributions of CSSI before (138 neurons from 4 animals) and after implant (472 neurons from 4 animals). Despite unmatched sample sizes, there was a statistically significant difference between distributions of CSSI (Figure 2-4C; Kolmogorov-Smirnov test, $p < 0.0001$).

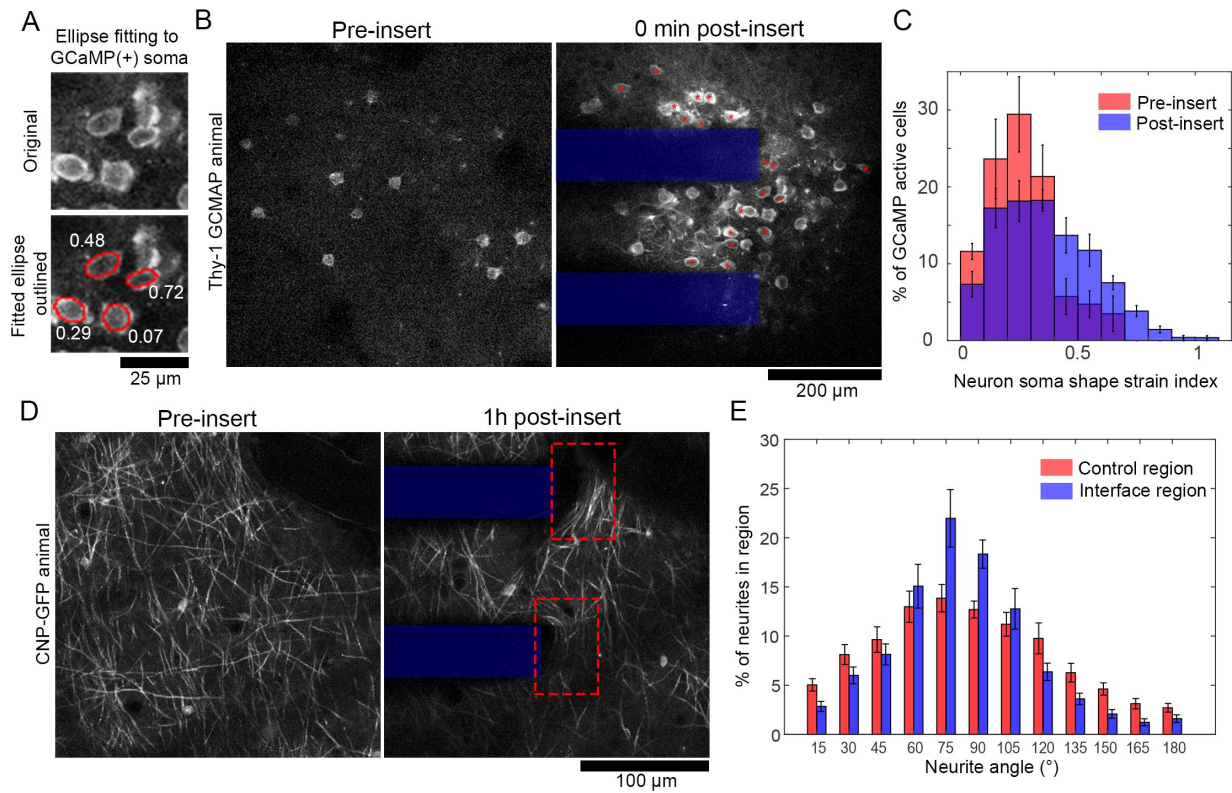


Figure 2-4 Neurons activated by electrode implantation are morphologically deformed.

(A) Neuron soma morphology is measured by manual tracing cells and ellipse fitting (bottom, red traces). Neuron soma shape strain index (white text) measures the extent of ellipsoid deformation of a cell body. (B) Images of GCaMP(+) neuron somas before and after insertion. Red * indicate cells with a neuron soma shape strain index > 0.3 . (C) Histograms of neuron soma shape strain index pre (red) and immediately post (blue) probe insertion. There is a significant difference between the group-wise distributions (Komogorov-Smirnov test, $p < 0.0001$). (D) Transgenic animals with GFP expressed in oligodendrocytes under control of the CNP promotor show myelinated axons in layer I of cortex. After insertion (right), axons at the electrode-tissue interface (dotted red box) appear stretched perpendicular to the direction of insertion. (D) Each pixel with neurite signal was binned according to its orientation angle by morphological filtering. ROIs were $50 \times 75 \mu$ m boxes around either the electrode-tissue interface or tissue $> 350 \mu$ m from the interface. Histograms of neurite orientation reveal significantly group-wise differences in distribution (Komogorov-Smirnov test, $p < 0.0001$). All data presented as mean \pm SEM.

Deformation of neurites was also explored with transgenic CNP-GFP mice, with GFP expression in oligodendrocytes and myelinated neurites. Qualitatively, we noted that CNP(+) neurites appeared to be aligned across the face of the electrode after insertion (Figure 2-4D). This was quantitatively defined by determining neurite orientation through morphological opening operations with line structuring elements angled between 0-180° in 15° intervals. The neurite angle was selected to be the angle of the structuring element with the maximal morphological opening response. Comparing the distribution of neurite angles in regions of interest at the tissue-electrode interface to regions of interest in distant tissue (> 350 μm from the electrode), there was a statistically significant difference between neurite angle distributions (Figure 2-4E; Kolmogorov-Sminov test, $p < 0.0001$).

2.4.4 Sustained elevated calcium levels in neuronal sub-cellular compartments at 1h and 3h post-insert

The Ca^{++} event that had started during implantation continued through at least the first hours post-insert in the neurite and soma sub-cellular compartments of transgenic Thy1-GCaMP animals. In the neurites of cortical layer I, Ca^{++} -laden spherical bodies formed by 1h post-insert and continued to develop through at least 3h post-insert in Thy1-GCaMP animals (Figure 2-7A). These elements were consistent with previous descriptions of axonal ‘blebs’, which are 2-8 μm in diameter with high calcium concentration [33, 181, 189, 190]. Automated particle analysis was used to estimate the density of blebs (in units of blebs / 10μm² of tissue) in cortical layer I of Thy1-GCaMP mice at 1h and 3h post-insert at the implantation site as well as in tissue > 350 μm from the implantation site (Figure 2-7B, top). There was a significant group-wise difference between the implant site and distant regions for bleb density, but there was no effect of time

(repeated measures two-way ANOVA, $p < 0.001$). Tukey's post-hoc tests confirmed that there was significantly higher bleb density at the implantation site at 1h post insert, with a trending difference at 3h post-insert ($p < 0.05$ at 1h, $p = 0.064$ at 3h). The distribution of bleb diameters was also different between the implant site and distant regions at 1h and 3h post-implant, with a larger proportion of $>2.5\mu\text{m}$ diameter blebs at the implant site (Figure 2-7B, bottom; Kolomogorov-Smirnov test, $p < 0.0001$). Time-series images collected at 1h and 3h post-insert show that these blebs may still have fluctuations in calcium levels, but they showed sustained elevated calcium relative to background (Figure 2-5).

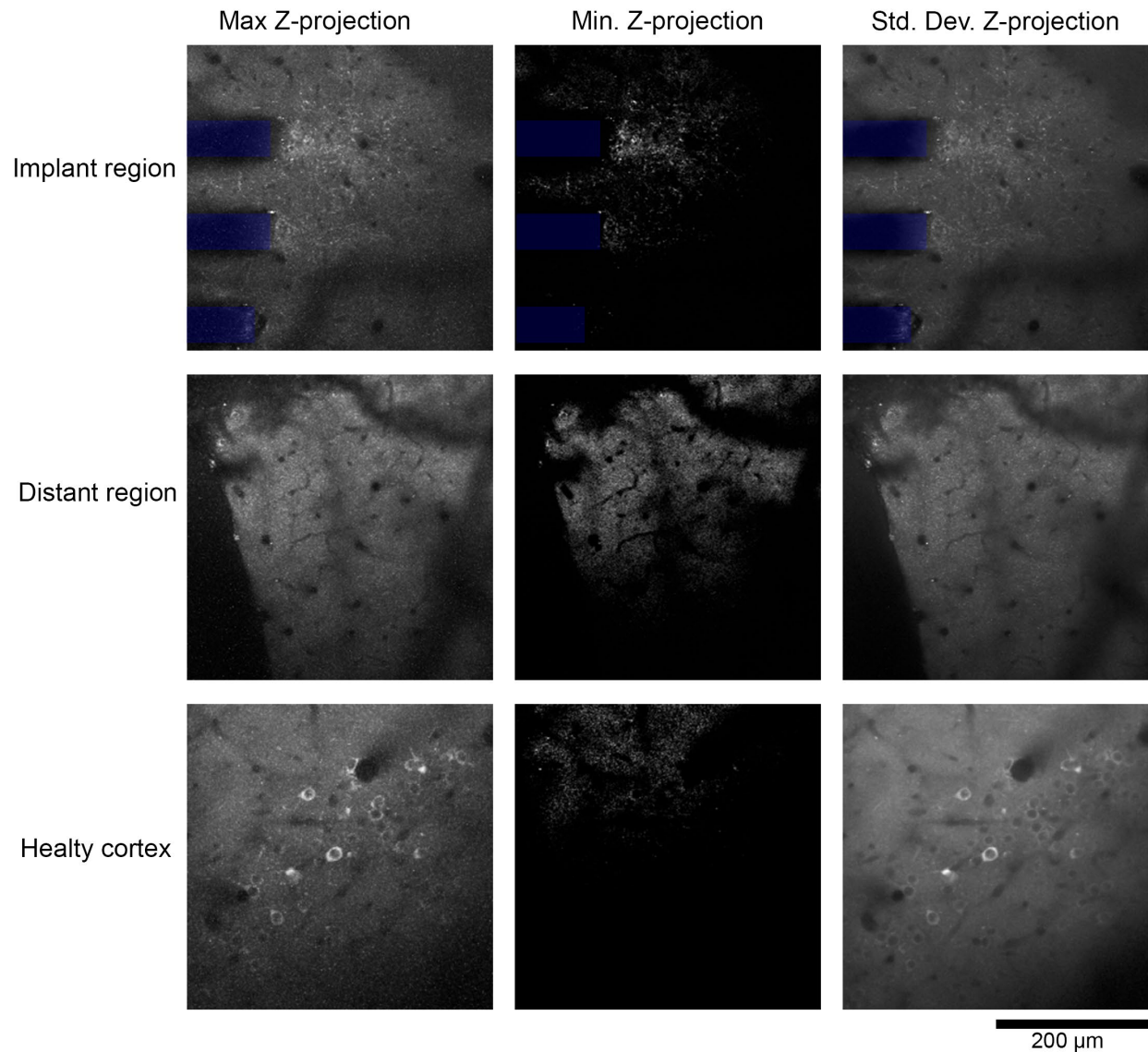


Figure 2-5 Projections of time-series of GCaMP activity shows persistent, high Ca^{++} concentrations in “blebs” at tissue-electrode interface.

The maximum projection (left) reveals the peak Ca^{++} signal throughout the imaging period, while the minimum projection (middle) shows the lowest Ca^{++} signal in the imaging period. The standard deviation projection shows Ca^{++} fluctuations through the imaging period. Ca^{++} signal in blebs at the implant region (left) are visible in all projections, indicating that Ca^{++} signal in blebs is fluctuating, but it is always higher than background. In distant regions (middle), there are elements that are greater than background, but these elements are not large enough to be considered “blebs”. In healthy cortex (bottom), there are several neurons

firing throughout the imaging period (max. and std. dev. projections), but they are not visible in the minimum projections. This indicates that in healthy GCaMP activity, when a neuron is no longer firing, it is no brighter than background.

In addition to differences in bleb density between the implant site and distant regions, we also qualitatively compared blebbing at the implant site before and after implantation (Figure 2-6). There were few blebs at the implant site prior to insertion, nor in the minutes that immediately followed insertion (Figure 2-6, middle; also, Figure 2-2B, where we elevated calcium levels in neurites after implantation, but without the beaded morphology typical of blebs). Rather, blebs appeared to form within the first hours after insertion.

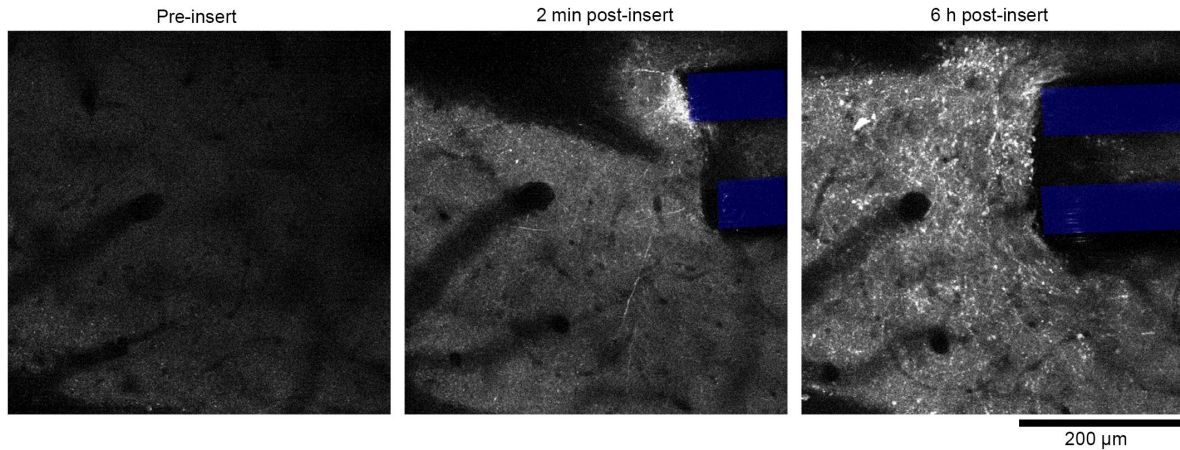


Figure 2-6 Comparison of GCaMP intensity in the same region before and after implantation.

Comparing between before (left), 2 min after implantation (middle; visible portions of electrodes indicated by blue boxes), and 6h after implantation (right) shows that axonal blebs are a negligible presence before implantation and immediately after implantation, but widely form in the hours that follow implantation.

In Thy1-GCaMP animals, blebs appeared mostly as isolated spheres that were disconnected from any neurite arborization. To determine if blebs were in fact isolated, we examined Thy1-YFP mice, which have YFP reporter expression to give a more stable and complete anatomical map of neurons (Figure 2-7C). While blebs formed in these animals on a similar time frame as the Thy1-GCaMP mice, they appeared to be connected to larger neurite structures. This suggests that the Ca^{++} -laden blebs in Thy1-GCaMP animals are not isolated, but rather highlight the discontinuous distribution of Ca^{++} in neurites in the vicinity of the tissue-electrode interface.

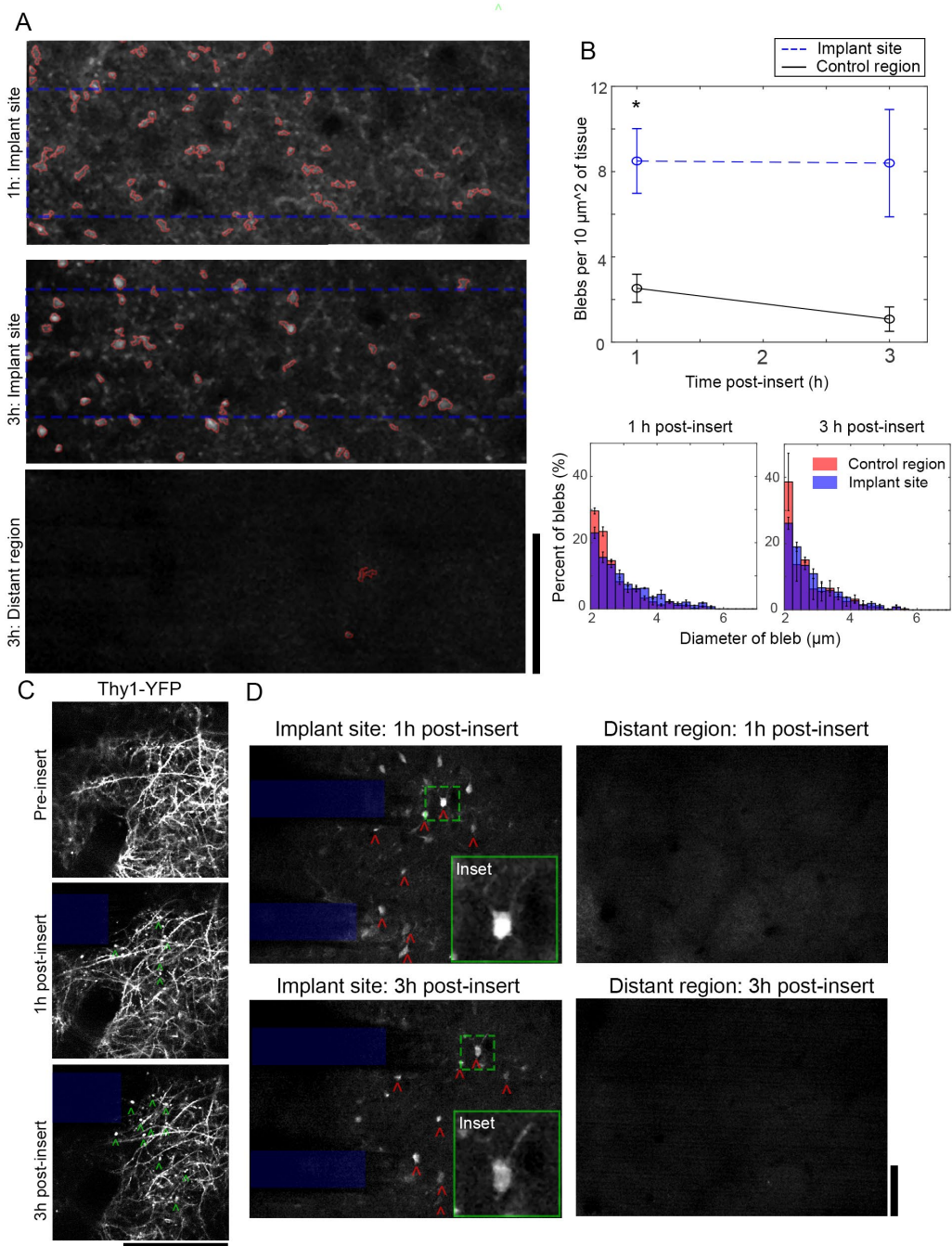


Figure 2-7 High Ca^{++} levels in neurite and soma sub-cellular compartments at the tissue-electrode interfaces persists through at least 3h post-insertion.

(A) In layer I, Ca^{++} -laden blebs in neurites were visible from 1-3h at the tissue-electrode interface (top), but not in distant cortical regions (bottom). Particle analysis was used to count blebs dorsal to the implanted

electrode (dotted blue rectangle). (B) Top: There is a statistically significant increase in bleb density at the implant site compared to distant tissues, with Tukey's post-tests confirming that there is a statistically significant increase at 1h and a trending increase at 3h post implant (repeated measures 2-way ANOVA, $p < 0.01$; Post-test for 1h: $p < 0.05$). Bottom: The distribution in diameter of blebs is significantly different between blebs at the implant site and distant region, with larger blebs prevalent at the implant site at both time-points (Kolmogorov-Smirnov test, $p < 0.00001$). Data presented as mean \pm SEM. (C) Observation of bleb development (green \wedge) in Thy-1 YFP animals confirmed that blebs formed within layer I neurites. (D) A sub-population of Ca^{++} -laden neurons with nuclear GCaMP inclusions (red \wedge) were tracked at 1-3h post-insertion in cortical layer II/III. These cells were only found within 150 μ m of the tissue-electrode interface (left), not in distant regions (right). Green dashed boxes indicate location of insets. Insets are 70x70 μ m; All scale bars = 100 μ m.

At 1-6h post-implant, there were few observable GCaMP transients in layer II/III neuronal somas at the tissue-electrode interface or in distant tissue $> 350\mu$ m from the implant (Figure 2-7D). This is possibly due to the systemic effects of the ketamine-xylazine anesthesia[197]. Nonetheless, 3 of 4 animals that were imaged at 3h post-insert had highly fluorescent GCaMP signals in neurons at the tissue-electrode interface, but not in distant regions (Figure 2-7D, red \wedge). These neurons were abnormal in that they had GCaMP signal in both the cytosol as well as the nucleus, where as normal GCaMP signal is confined to the cytosol (Figure 2-7D, Insets) [198]. This may suggest that the nuclear membrane in these cells has been compromised and can no longer exclude GCaMP from entering.

2.4.5 Cells with membrane damage at 3-6h post-insert are geographically distinct from GCaMP(+) cells activated during electrode implantation

Mechanical deformation of neurons can damage and disrupt their cell membranes [33, 34]. In order to test cell membrane permeability in the vicinity of implanted electrodes, we topically applied the cell-impermeant dye propidium iodide (PI) to the cortical surface at the end of acute implantation studies of transgenic Thy1-GCaMP animals (3-6h post-insert) (Figure 2-8A, left). PI enters cells to stain their nuclei if the cell and nuclear membranes have been damaged[199]. By aligning images PI(+) cells at 3-6h post implant to images GCaMP activity at peak activation post-insert, it was clear that PI(+) cells were more proximate to the implantation site than GCaMP active cells (Figure 2-8A, middle and right). The distributions of PI(+) and GCaMP active cells as a function of distance from the implantation site were statistically different (Figure 2-8B, two-way ANOVA, $p < 0.00005$) with Tukey's post-hoc tests indicating significantly more PI(+) cells than GCaMP active cells between 0-10 μ m from the probe's surface ($p < 0.001$), and significantly less PI(+) cells than GCaMP active cells between 20-50 μ m from the probe's surface ($p < 0.001$).

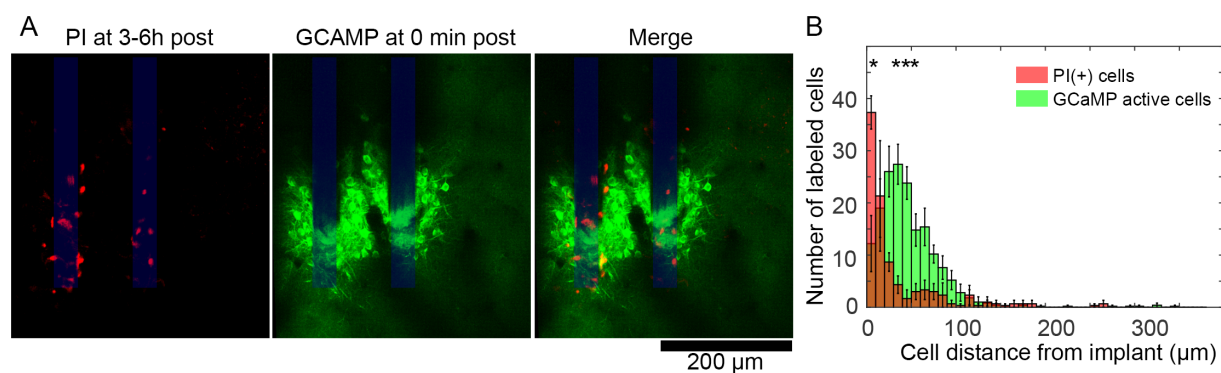


Figure 2-8 Cells with membrane dysfunction at 3-6h post-insert are geographically distinct from cells with high Ca^{++} levels during device insertion.

(A) At 3 or 6h post insertion, propidium iodide (PI) was topically applied over cortex to label cells with disrupted cell membranes (left). Images at these time points were aligned to images of transgenic Thy1-GCaMP6 activity at 0 min post-insert using the electrode shanks as a stable land mark (middle and right). PI(+) cells appear to be closer to the electrode-tissue interface than GCaMP active cells. (B) A histogram of PI(+) (red) and GCaMP(+) (green) cells as a function of distance from the neural probe show that PI(+) cells are geographically distinct from the GCaMP(+) cells, with statistically significant groupwise effects (2-way ANOVA, * indicate significant post-hoc tests, $p < 0.001$, $n = 4$ animals for GCaMP active cells; $n = 3$ animals for PI cells). Data presented as mean \pm SEM.

2.4.6 Increasing GCaMP activity within 150 μm of the electrode array over 28d post-insert

In order to study changes in Ca^{++} activity surrounding implanted electrodes in the early chronic phase post-insert, mice were injected with AAV-Syn-GCaMP6f virus (Figure 2-9). Viral injected animals were selected for chronic studies due to preliminary studies (not shown) indicating that

viral injected AAV-Syn-GCaMP6f animals had a greater proportion of GCaMP expressing neurons.

Following implantation, we estimated the degree of GCaMP activity in around the implant by quantifying the PSD over the 0.1-1.2Hz band (Figure 2-9A-C). Qualitatively, PSD increased from day 2 to day 28 post-insert (Figure 2-9A). Quantitative assessments of average 0.1-1.2Hz PSD within the 600x600 μ m ROI (Figure 2-9A, green dashed box) confirmed these observations, with PSD showing an increasing trend for all (4/4) animals over the first month post-insert (Figure 2-9B). Further, by quantifying the relative PSD fold-increases at days 7 and 28-35 post-insert compared to day 2, we identified statistically significant elevation in power at days 28-35 (Figure 2-9C; 1.72 ± 0.47 v. 3.18 ± 0.62 , mean \pm SEM; Student's t-test, $p < 0.05$, $n = 3$ of 4 animals, one animal excluded due to dural bleeding on Day 2). Two-photon microscopy was used to determine if the increase in PSD was also associated with an increase in dynamic calcium behavior in individual neurons. Standard deviation projections of time series images show that there are more active cells with time post-insert (Figure 2-9D, cells indicated by red). In these time-series, some axons which appeared to be stretched across the electrode's surface (as described in section 2.3.2) were able to exhibit GCaMP transients by 28d post-insert.

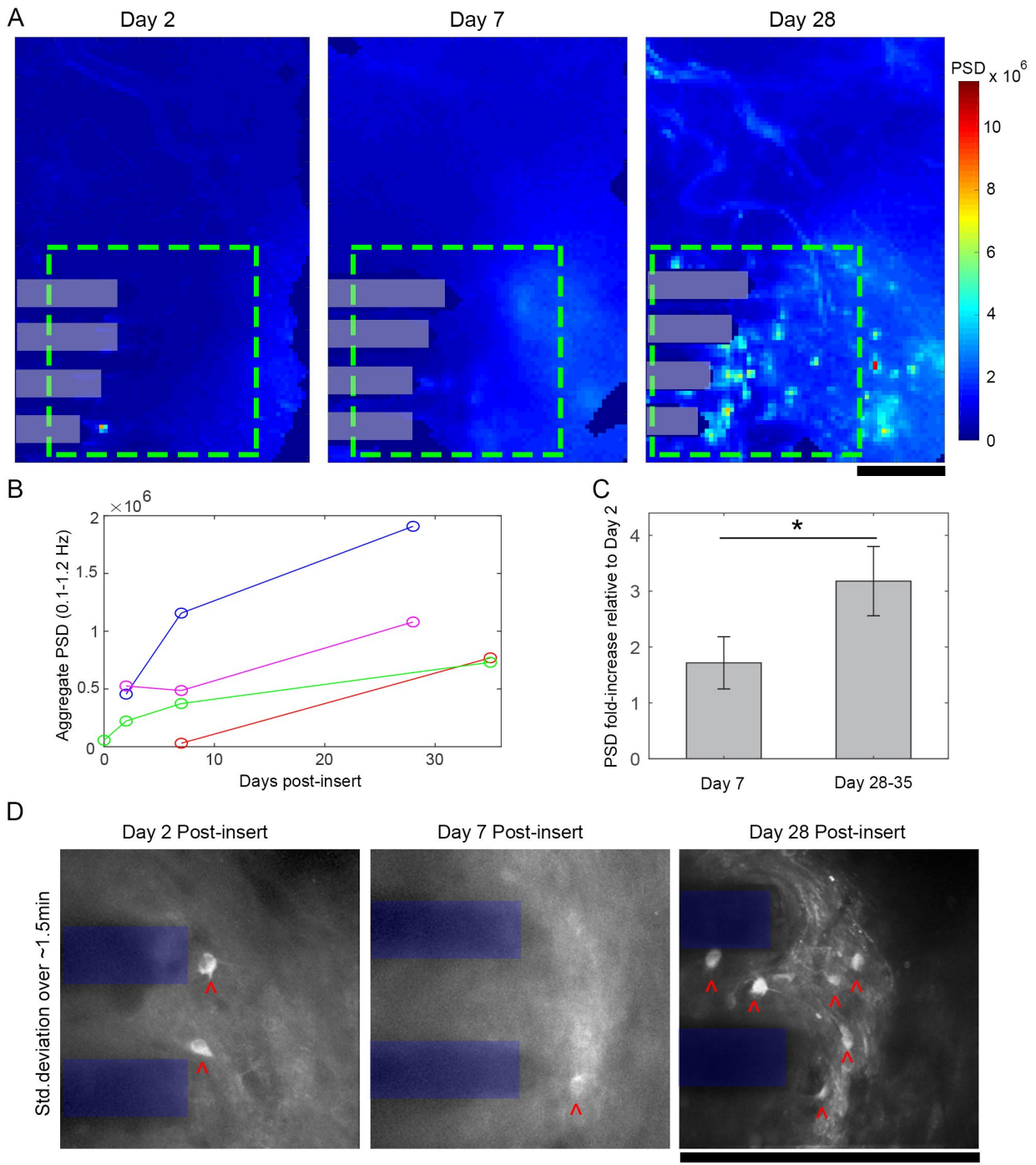


Figure 2-9 Chronic neural Ca⁺⁺ activity surrounding a neural electrode increases after implantation.

(A) Power spectral density (PSD) of 5 min epifluorescence macrocope recordings was summed for each pixel over 0.1-1.2Hz over 2-28 days post-insert. Power within a 600x600 μ m ROI (green dashed box) increased

progressively over time post-insert (electrode shanks in gray boxes). (B) PSD increased over time in 4/4 animals (C) Relative to aggregate PSD at Day 2 post-insert, there were fold-increases in PSD at day 7 and day 28-35 post –insert, with a statistically significant increase on relative PSD over time (Student’s T-test, $p < 0.05$; mean \pm SEM). (D) Standard deviation projections of two-photon image series within the same ROI (electrode shanks shown in blue) reveals increasing numbers of GCaMP active neurons (neuronal somas indicated by red ^) over time post-insert. All scale bars 250 μ m.

2.5 DISCUSSION

While high-yield, high-SNR neural recording can be obtained from implanted neural electrodes, reproducibility across implants remain high, due to the variability in implantation trauma. Furthermore, a uniform trend of decline in recording quality months to years post neural electrode implantation suggest that the initial trauma of acute implantation may also create the origin of the chronic inflammation and neurodegeneration [35, 40, 50, 53, 177]. Beyond this, it has long been believed—but not conclusively demonstrated—that electrode implantation will further damage neurite arborization without necessarily killing neurons. This dynamic tissue damage pattern has been largely unexplored [28], but could explain observed changes to neuron phenotype following implantation [117, 118]. In the present study, we hypothesized that electrode implantation will mechanically distort neurons, leading to abnormal calcium activity and axonal degeneration. Morphological measurements of neuronal soma shape and neurite orientation confirmed that neurons were in fact mechanically distorted. Imaging of calcium

before and after electrode insertion demonstrated that calcium levels increased after insertion, and persisted through at least 3h post-insert. Further, at 1-3h post-insert, neurites began to show signs of injury and possible degeneration. Despite this, a small population of cells demonstrated compromised membranes at 3-6h post-insert compared to the number of cells that initially expressed high calcium levels after implant. Over the first month post-insert, calcium activity in neurons surrounding the implanted devices increased, suggesting that cells recover after initial insult. Together, these findings allow for the following conclusions:

2.5.1 Mechanical deformation of cells may underlie high calcium levels in neuron cell bodies and neurites

Both neuronal soma and neurite sub-cellular compartments showed altered morphology after electrode implantation. The cell-shape strain index shows that neuron somas in the vicinity of the tissue-electrode interface were more elliptical than neurons in the same cortical region pre-insertion. This is likely due to the strain generated as the probe displaces tissue during insertion, as previously suggested [83, 172]. Changes in the distribution of neurite orientation at the tissue-electrode interface suggest that either neurites were stretched across the face of the device during insertion, or that neurites were pushed together during insertion. In either case, the orientation metric indicates that the neurites were mechanically distorted during probe entry. This suggests that the act of implantation mechanically distorted and strained neural tissue, as has previously been shown in implantations into *ex vivo* brain slices [36] as well as studies of *in vivo* brain dimpling during implantation [42]. Importantly, mechanical distortions of neuron somas and neurites has previously been shown to disrupt neuron membrane integrity [33, 34, 180], disrupt neurite cytoskeletal structure [181, 200, 201], and incur high cellular Ca^{++} influx [180-182]. One

limitation of these morphological analyses was our inability to track cell-shape strain index and neurite orientation of the same somas and neurites before and after implantation. This is due to the gross deformation in the Z-axis of the tissue during implantation (over 60 μ m deformations at points), which complicated cell tracking. To account for this, we sampled neurons in the same region (tracked by blood vessel landmarks) before and after implantation, which gives the best approximation of strain, but cannot give the actual cell strain. Future studies may address this by using cell labels with sparser expression that can make cell-tracking more viable or using advanced 3D imaging modalities.

In this work, Ca⁺⁺ flooded neurons and neurites at the tissue-electrode interface within 1 min of implantation. Importantly, over 42% of cells affected by this implantation-related Ca⁺⁺ influx showed elevated Ca⁺⁺ levels that lasted for over 1 min, which is > 90-1000X longer than action potential-related to single GCaMP6 4.3 transients [178]. Elevated Ca⁺⁺ after mechanical damage to neurons can come from opening Ca⁺⁺ channels and transporters [182, 202], mechanoporation [34, 180], or from release of intracellular calcium stores [181, 203]. The morphological results from this study show that many cells were in fact mechanically distorted after implantation, and propidium iodide staining at the end of experiments show that a subset of (non-neuron specific) cells had some degree of mechanoporation. While this may suggest that only a subset of cells that demonstrated abnormal Ca⁺⁺ levels, it is also possible that more cells were initially mechanoporated, but were able to self-repair by the time of propidium iodide infusion [34, 180]. Whether distortion of cells led to mechanoporation or not, mechanical deformation of neuron somas and neurites is still sufficient to cause release of intracellular Ca⁺⁺ stores and/or opening of voltage gated calcium channels and calcium transporters [181, 182, 202,

203]. These findings reinforce the importance of pursuing neural electrode footprints and insertion strategies that minimize mechanical strain and tissue distortion after implantation [204].

Unexpectedly, we found that removal of dura prior to implantation correlated with cortical spreading depolarizations (CSD) during implantation. CSDs are a global event that disrupts normal neural function, heightens the risk of neuronal injury and cell death, and is thought to underlie migraine pathology [205]. Because this phenomena was only observed in animals that had partial or full durotomy 2-4 weeks following AAV injection, we believe that the CSDs may have been related to this additional trauma. In this study, animals that developed thick fibrosis on the surface of the brain had previously received a craniotomy during the virus injection procedure [206, 207]. It is possible that fibrosis was related to the cover glass that remained on the surface of the brain between virus injection and implantation. Foreign bodies on the surface of the brain have previously been shown to incite fibrosis [62, 206]. Ultimately, this may suggest that repeated surgical interventions, epidural fibrosis, and/or duratomy could affect the nature of Ca^{++} activity following implantation. Alternatively, it is possible that CSDs were occurring in a larger subset of animals, but it is only apparent in some virus injected animals due to the virus's variable expression pattern [208]. Future studies should explore these potential mechanisms and consider the impact of CSDs in regeneration and degeneration following electrode array implantation.

While most electrode implantations are designed to be performed at 90° relative to the surface of the brain, electrode arrays in this study were implanted at $30\text{-}35^\circ$ in order to accommodate geometric constraints of the two-photon microscope objective for dynamic spatiotemporal imaging [40, 62, 165, 174, 177, 190]. The angled insertion may have resulted in more shearing of vertical axonal projections than a perpendicular insertion, which has been

suggested to generate more blebbing-type injury [33]. While this could also result in shearing damage penetrating arterioles and venules, we actively mapped and avoided these vessels during implantation as previously described [37]. Despite these concerns, we believe that even “perpendicular” implantations will still generate a distribution of local shear and compressive forces due to the natural variability in the angle of “vertical” axonal projections and the curvature of the brain. This is especially true of large, multi-shank arrays, which span large regions of brain curvature. With these considerations, the angled insertion of these experiments is still relevant for traditional “perpendicular” insertions.

2.5.2 Axonal transport disruption after mechanical deformation and Ca^{++} influx

Regardless of the mode of Ca^{++} entry, the prolonged high Ca^{++} levels observed after implantation suggests abnormal cell physiology and can jeopardize the health of the neurons. In addition to disrupting cellular ion balance, high concentrations of Ca^{++} can activate calcineurin and calpain, enzymes that can prevent neuronal Ca^{++} efflux and cause severe degradation of axonal cytoskeletal proteins [181, 203]. Mechanical deformation as well as calcium-activated calpain can cause disruption of microtubule structure, which is responsible for aggregation of axonal transport proteins and ions and the local swelling that defines blebs [181, 200]. This mechanism serves as a link between the current study’s observation of prolonged elevated Ca^{++} level and axonal blebbing. Our observation of blebs forming within the first hours post-insert is also consistent with other studies of mechanical trauma [180, 181]. Further, prolonged high Ca^{++} levels and axonal blebbing are known precursors to neuron cell death, neurite degeneration, and a loss of synaptic connectivity [33, 180, 202, 209]. Due to limitations of our acute preparation, it was not possible to track individual neurons for sufficient time to determine the fate of axons that

exhibited blebbing or neurons with severe, high Ca^{++} levels. Nonetheless, whether these axons ultimately repaired or degenerated, the presence of blebbing is sufficient to assert that neural electrode implantation caused some axonal transport interruption, with potential for neurite degeneration.

2.5.3 Normal Ca^{++} activity increases over the first month post-insertion

After the initial Ca^{++} influx after probe insertion, there was little GCaMP activity observed in the first hours, both adjacent to the implant as well as in distant regions from the implant. This is likely due to ketamine/xylazine anesthesia, which is known to suppress spontaneous activity, but would not prevent Ca^{++} influx from mechanical or electrical stimulation [180, 197, 210]. A cohort of GCaMP-virus injected animals was prepared with cranial windows to track awake, spontaneous GCaMP activity over the first month post-insert to overcome this limitation. We noted that from day 2 to day 28 post-insert, all animals showed an increase in PSD in calcium activity at the tissue-electrode interface, similar to previous reports [28]. Time-series videos of cells from this population confirmed that the Ca^{++} transients of these cells was $< 1\text{s}$, as has been reported for healthy, awake GCaMP6 4.3 subtype activity [178]. This is reminiscent of reports of neuronal suppression following TBI, followed by hyper-excitability at later time-points [211-213]. Noting our observations of axonal trauma following implant, a possible explanation for dynamic changes in neural activity may be on account of axon degeneration and regeneration. In tissue slice recordings following TBI, axotomized neurons show decreased excitability while intact neurons show an increase in excitability [209]. *In vitro* studies further corroborate this, showing that neurons lose a significant amount of connectivity and oscillatory behavior immediately following an impact [195, 202]. At later time-points, it is possible that

synaptogenesis has occurred, leading to increases in neuron Ca^{++} activity as suggested by molecular studies of the brain following traumatic brain injury [214]. This ultimately suggests that acute injury may have long-lived consequences, and may instigate changes to the functional connectivity of neurons at the tissue-electrode interface.

An alternative--and potentially parallel—explanation is that gliotransmission could be modulating neuronal activity at the tissue-electrode interface [117]. This theory suggests that glia could cause both neuron hyper-excitability as well as neuron suppression at later time points post-implant. While the current study shows an increase in cells with GCaMP signaling with time post-insert, it is possible that there is still a population of GCaMP expressing, but silent neurons that is unaccounted for. These explanations should be further explored with longitudinal studies with Thy1-YFP mice that can be used get a more complete depiction of neurite health over time.

2.5.4 Beyond implantation trauma: other sources of mechanical injury

The present work suggests that the mechanical trauma of electrode array implantation is correlated with sub-cellular neuronal damage. While implantation is the most significant source of tissue deformation and stress from a neural electrode, there are other sources of mechanical injury at the tissue-electrode interface. Brain micromotion during respiration, heartbeat, and movement creates stress at the tissue-electrode interface, however the force of electrode penetration is >10X the force generated by micromotion [215]. The current work observes aberrant Ca^{++} activity in neuron somas and neurites during implantation, but not during awake and anesthetized micromotion in acute or chronic experiments. This may suggest that the

potential contribution of micromotion to chronic neurodegeneration operates through different mechanisms than those suggested here.

Another potential source of tissue deformation is through aggressive electrical stimulation paradigms. It is well known that stimuli $>+1.5V$ are outside the water window and cause electrolysis of water into O_2 and H_2 gas as well as pH excursions [216-221]. While it has long been speculated that such gas evolution could create local pressure and deformation of tissue, there have been few publications that explore this *in vivo* [222]. Using the methods described in this work, we explored this theory with *in vivo* GCaMP imaging. We examined current-controlled stimulation through high impedance electrode sites (Figure 2-10A), which can lead to voltage excursions outside of the water window even when safe Shannon Criteria is used $k \ll 1.7$ ($k=0.55$) [216-221]. We also tested “rejuvenation” stimulation, which employs a 1.5V DC bias for 4 s which is hypothesized to perforate the glial scar encapsulating the electrode site to restore neural recording capabilities of failed recording sites (Figure 2-10B) [186, 187]. Imaging GCaMP activity around the implant during these strong stimuli reveals formation of large gas bubbles (110.35 μm diameter bubble for current-controlled stimulation, 37.14 μm for the “rejuvenation stimulation) that generate mechanical strain to the local tissue (Figure 2-10A-B). There is an initial depolarization of sparse and distributed population of neural depolarization [223]. However, as the stimulus continues, a gas bubble forms around the electrode site. The growing gas bubble, in turn, pushes the nearby tissue away generating mechanical strain. Neurons within 50 μm of the electrode site were displaced $9.05 \pm 1.12 \mu m$ (mean \pm SEM; $n = 11$ neurons) during current-controlled stimulation. Cell-shape strain index (see Methods section 3.3.6.) of these same neurons increased 0.18 ± 0.076 (mean \pm SEM). With the smaller gas bubble formed during “rejuvenation” stimulation, only one neuron was seen to be displaced (3.15 μm ;

CSSI change = 0.08). Neurons in this strained region for both stimulation paradigms are activated. Most noticeably, neurons that were spontaneously firing prior to the stimulus ceased all activity following the stimulus (Figure 2-10A-B, > arrows). Other neurons near the electrode that were not spontaneously firing before the stimulus showed robust spontaneous firing 2 minutes following the recovery from the stimulus (Figure 2-10A-B, v arrows). It is unclear if this altered neuronal activity is due to intense electrical stimulation, tissue deformation by the microbubble, release of O₂, H₂, and change of pH, though each of these factors has the ability to modulate neuronal activity [222, 224]. Future studies should examine how the native neural networks are disrupted from these strong stimulus pulses. The present work suggests that care needs to be taken in selecting stimulation parameters that do not disrupt the local functional neural network.

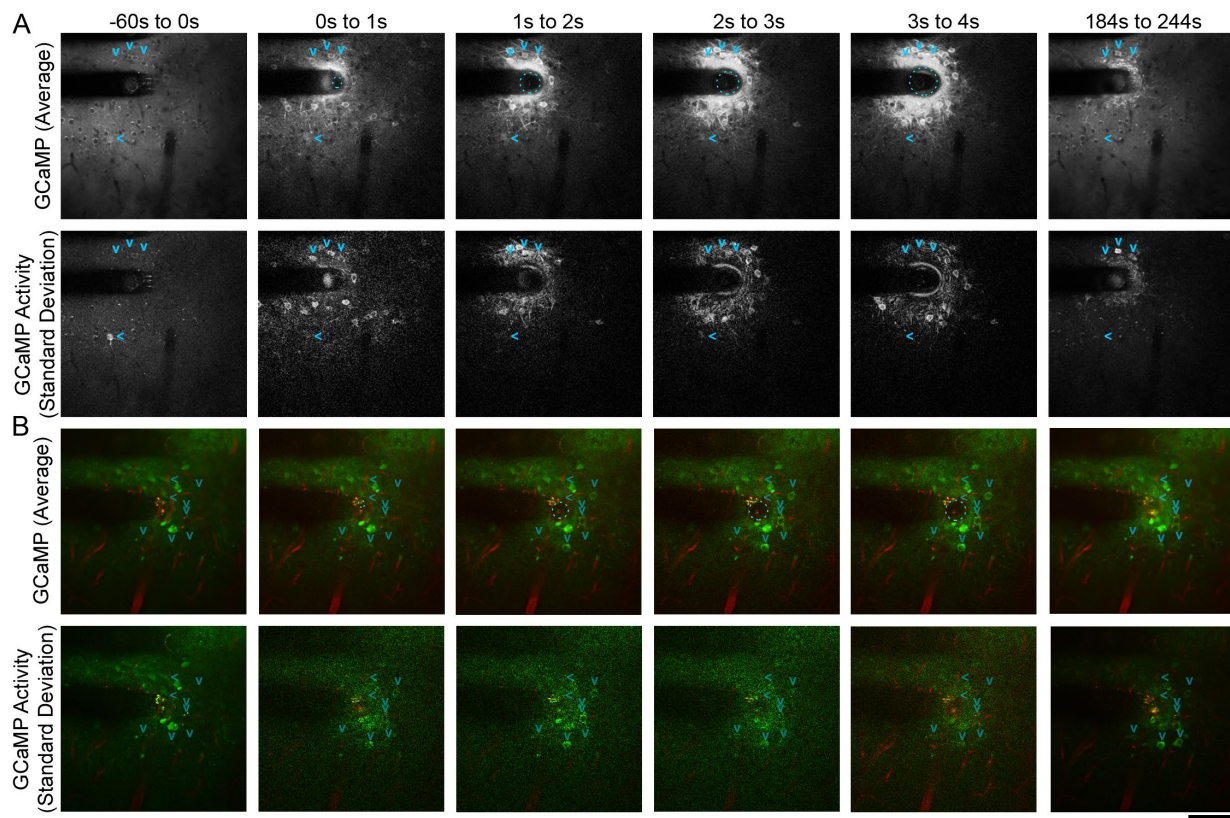


Figure 2-10 Gas evolution during stimulation alters resting state network activity.

Gas evolution can be caused by 130 Hz current-controlled charge balanced asymmetric electrical stimulation with a Shannon k value of 0.55 (A) as well as monopolar 4s +1.5V ‘Rejuvenation’ electrical stimulation(B). Average GCaMP activity (top) and standard deviation of activity (bottom) projections across frames in the designated time periods show evolution of a gas bubble during stimulation (cyan dashed circle). The gas bubble deformed neurons, which showed sustained Ca^{++} influx with oscillatory behavior (standard deviation projection). GCaMP signal reduced after stimulation (184s to 244s), but still remained elevated relative to surrounding tissue. Some neurons ($>$; right arrow) were spontaneously firing before the stimulus ceased activity following gas evolution. In addition, other neurons (v ; down arrows) that were quiescent prior to the stimulus began spontaneously firing following the gas evolution. Scale bar = 100 μ m.

2.5.5 Future directions: new therapeutic avenues

The above results identify three related mechanisms that may explain how the mechanical trauma of electrode implantation leads to neuron loss and neural signal decline: prolonged high intracellular Ca^{++} levels, mechanoporation, and axonal cytoskeletal injury. The true impact of these phenomena will not be understood until studies are conducted with controlled interventions that modulate these damage patterns. Potential interventions for high Ca^{++} levels could be pre-incubation with Ca^{++} chelators such as EGTA [180], blockade of Na^+ and Ca^{++} channels[182], or blocking the GluN2B subunit on NMDA receptors[202]. Mechanoporation can potentially be reduced by application of ‘membrane sealants’ such as polyethylene glycol [225, 226] or poloxamers [227]. Axonal cytoskeleton can be stabilized by selectively inhibiting the Ca^{++} activated protease calpain [180] or injection of the microtubule stabilizer paclitaxel [201]. One other strategy to address each of these issues is simply to reduce the mechanical trauma of implantation. This can be accomplished by altering the speed of insertion as well as the material, shape, and size of the device [204]. Reducing the overall volumetric footprint of the device reduces the tissue displacement during insertion resulting from the tissue accepting the probe’s volume [228-231].

While these strategies may spare many neurons and neurites from degeneration, the inherent trauma of neural electrode implantation is likely to still damage neural tissue. Therapies should also be focused on neural regeneration. Some approaches involve stem cell delivery to the implant site [67, 232] and encouraging neurite regrowth and neuronal survival through immobilized L1 cell adhesion molecule [104, 105, 177, 207], or neural protective drug release [233-238].

2.6 CONCLUSION

Using longitudinal, *in vivo* microscopy, we have for the first time identified sustained, high Ca^{++} levels in neuronal somas and neurites following electrode implantation. This is correlated with and potentially caused by mechanical distortion of somas and neurites as well as cell membrane disruption. Ca^{++} -laden neurites develop spherical ‘blebs’ over the first hours post-implant, suggesting disruption in axonal transport and axonal damage. We ultimately show that healthy Ca^{++} activity increases over the first month post-implant, suggesting that neurons are repairing and potentially rewiring following implantation trauma. These results ultimately identify early damage patterns after neural electrode implant that may be promising therapeutic avenues to improve the long-term viability of implantable neural technologies.

2.7 ACKNOWLEDGMENTS

This project was financially supported by NIH NINDS (Grant R01NS062019, 1R01NS094396, R01NS089688, 1R01094404). The authors would like to thank Vivek Jayaraman, Rex A. Kerr, Douglas S. Kim, Loren L. Looger and Karel Svoboda from the GENIE Project, Janelia Farm Research Campus (Howard Hughes Medical Institute) for generously allowing the use of GCaMP constructs. The authors would also like to thank Kip A. Ludwig for valuable discussions.

3.0 NEUROADHESIVE L1 COATING ATTENUATES ACUTE MICROGLIAL ATTACHMENT TO NEURAL ELECTRODES AS REVEALED BY LIVE TWO-PHOTON MICROSCOPY

3.1 ABSTRACT

Implantable neural electrode technologies for chronic neural recordings can restore functional control to paralysis and limb loss victims through brain-computer interfaces. These probes, however, have high failure rates partly due to the biological responses to the probe which generates an inflammatory scar and subsequent neuronal cell death. L1 is a neuronal specific cell adhesion molecule and has been shown to minimize glial scar formation and promote electrode-neuron integration when covalently attached to the surface of neural probes. In this work, the acute microglial response to L1-coated neural probes was evaluated *in vivo* by implanting coated devices into the cortex of mice with fluorescently labeled microglia, and tracking microglial dynamics with multi-photon microscopy for the ensuing 6 hours in order to understand L1's cellular mechanisms of action. Microglia became activated immediately after implantation, extending processes towards both L1-coated and uncoated control probes at similar velocities. After the processes made contact with the probes, microglial processes expanded to cover 47.7% of the control probes' surfaces. For L1-coated probes, however, there was a statistically significant 83% reduction in microglial surface coverage. This effect was sustained through the

experiment. At 6 hours post-implant, the radius of microglia activation was reduced for the L1 probes by 20%, shifting from 130.0 to 103.5 μm with the coating. Microglia as far as 270 μm from the implant site displayed significantly lower morphological characteristics of activation for the L1 group. These results suggest that the L1 surface treatment works in an acute setting by microglial mediated mechanisms. This chapter has been reprinted from work published in *Biomaterials* [177].

3.2 INTRODUCTION

Chronically implanted neural electrodes have emerged as basic neuroscience research tools and effective therapeutics [12, 167, 168, 239-241]. Specifically, microscale recording and stimulation electrodes have played a fundamental role in understanding and modulating the basic neural circuitry underlying complex neural networks [242-246]. In human clinical applications, implantable brain-computer interface devices have demonstrated great promise in the ability to restore functional motor control [8, 10]. However, the recording potential of implanted neural electrodes is limited by instability since the signal quality degrades over months to years [22, 25, 27, 245, 247]. The degradation of the signal quality over time is understood to be a combination of material failure and biological factors [92].

Material failures largely result from corrosion and delamination of the electrode sites [21, 248-253], cracks in the electrical traces [49, 84, 254], and delamination of insulation materials [21, 49, 92, 255, 256], all of which are exacerbated by perpetual strain caused by tissue micromotion during movement [49, 81, 82]. Biological failure modes of neural interfaces result from multiple sources that ultimately lead to meningeal cell invasion and fibrous encapsulation

[27, 206], insulting glial scar encapsulation, and neural degeneration [35, 54]. Electrode insertion is a traumatic process, and even insertions that avoid large pial arteries and veins will break capillaries in the cortex, causing blood-brain barrier disruption [37, 55, 92]. This leads to an influx of plasma proteins that adsorb onto the surface of microelectrodes [55, 92] and infiltration of inflammatory cells [50, 51, 67]. The combination of plasma proteins and cells, necrotic cell debris, and mechanical strain imposed by probe insertion causes an upregulation of proinflammatory cytokines that initiate the cascade of reactive tissue response [20, 40, 74, 92, 257]. Using two-photon microscopy, we have observed that nearby resident microglia immediately activate by retracting most of their processes while extending a few processes towards the probe in order to cover the surface of the implant with a lamellipodia sheath [40]. Over the following days, microglia and astrocytes aggregate at the surface of the implant to form an electrically insulating astroglial sheath [51, 54, 62, 67, 110]. Additionally, chronic inflammation leads to neural degeneration which presumably diminishes signal [20, 92, 251]. Lastly, failure is also fueled by the decrease in metabolic supply and neurotoxic waste product removal from loss of blood flow perfusion and increased metabolic consumption from inflammation [20, 40, 92].

To improve neural interface performance longevity, neural engineers have explored numerous intervention strategies. This includes changing the footprint of the probe or the probe's electrode sites [36, 48, 55, 74, 92, 228, 258, 259], altering recording site materials [228, 260-265], applying flexible geometries or soft materials [55, 84, 86, 88, 254, 266-268], creating dissolvable insertion shuttles for softer probe materials [88, 89], locally delivering anti-inflammatory or neuroprotective drugs [165, 234, 269-278], and modifying the probe's surface chemistry [55, 104, 105, 279].

One promising method involves covalently attaching L1 cell adhesion molecule (L1) to the surface of the probe. L1 is a transmembrane cell surface glycoprotein that functions through homophilic interactions with L1 molecules on other cells to mediate cell recognition and cell interactions [280, 281]. It has been shown to play a critical role in neuronal adhesion, axonal growth, neural migration, neural differentiation, and neuronal survival [282-290]. L1 is also implicated in improving regeneration following lesions in both the central and peripheral nervous systems [291-298]. Several studies have shown that L1 promotes neuronal cell attachment and growth while inhibiting glial and fibroblast cell attachment *in vitro* [95, 108, 299, 300]. In the context of neural implants, our group has shown that covalent attachment of brain tissue derived L1 to neural probes can reduce glial scarring, while simultaneously encouraging neuronal attachment to the probe's surface for at least 2 months post-implant [86, 104, 105]. While these studies suggest L1 can modify the behavior of glial scars, the mechanism behind this is unclear. In the present work, we use two-photon microscopy to study the dynamic microglial response to L1 coated microelectrodes for the first 6 h post-implant in living mice, as the first step to uncover the mechanisms. Compared to uncoated microelectrodes, there was significantly less microglial coverage of the L1 probes from 20 min – 6 h post-implant, despite similar degrees of microglial process extension toward both coated and control probes. This suggests that L1's mechanism for preventing glial attachment and scarring occurs rapidly after initial contact.

3.3 MATERIALS AND METHODS

3.3.1 Neural probes and L1 protein immobilization

All studies were performed using four-shank NeuroNexus 16-channel, 15 μm thick, 3mm long SOI silicon probes (NeuroNexus Technologies, Ann Arbor, MI) mounted on dummy boards.

For quantitative analysis, L1 immobilization was conducted along the entire shank of the probes ($n=7$), and all control probes ($n=7$) were pristine, uncoated arrays that were washed with ethanol and phosphate buffer solution. L1 immobilization on the silicon dioxide surface and iridium oxide electrode pads were carried out as previously described with minor modifications [95, 104]. Briefly, probes were cleaned and functionalized with either HNO_3 (Sigma Aldrich) or by serial washes in acetone, 50% (v/v) MeOH/ H_2O , and chloroform before oxygen plasma cleaning (30W) for one minute (Harrick Plasma, PDC-001) [301]. Probes were silanized by immersion in 2% (3-mercaptopropyl) trimethoxysilane (Sigma Aldrich) solution with 4-maleimidobutyric acid N-hydroxysuccinimide ester (2 mM, Sigma Aldrich) for 1 h. Finally, probes were fully immersed in a 100 $\mu\text{g}/\text{mL}$ solution of purified L1 protein (purified at our lab) for 1 h at 4°C , and stored in sterile 1X phosphate buffer solution (Sigma Aldrich) until implantation. In an additional validation experiment ($n = 1$), following silanization of the probe's full surface, the probe was dipped only $\sim 150 \mu\text{m}$ in the L1 solution. This half-coating design allowed for comparison between L1 and no L1 conditions on the same probe (Figure 3-7). The L1 modified probes were stored in saline for up to 1 h prior to implantation. Previous studies have shown that the L1 coating procedure yields a uniform 6.37 nm thick coating with 0.53 g cm^{-3} density and increased hydrophobicity (water contact angle: $69.8 \pm 1.7^\circ$ for L1 coated v. $27.3 \pm 1.4^\circ$ for unmodified control) [95].

3.3.2 Surgery and probe insertion

Surgical procedures were conducted as previously described with 14 adult CX3CR1-GFP transgenic mice with GFP expression in macrophages and microglia controlled by the CX3CR1 promoter (Jackson Laboratories, Bar Harbor, ME) [40]. A cocktail of intraperitoneally (IP) administered ketamine/xylazine (90/8 mg kg⁻¹) was used to induce anesthesia, with depth of anesthesia assessed by monitoring the toe-pinch response, breathing, and heart rate. After animals were secured in a stereotaxic frame, scalps were shaved, cleaned with 70% ethanol, and resected. Calvarial periosteum was scraped off with cotton swabs, and a thin layer of Vetbond (3M) was applied to dry the skull. A 1-1.5 mm tall well of light-curable cement (Composite Flowable; Henry Schein, NY, USA) was set around the margin of the exposed skull, following which a ~4-6mm craniotomy was performed with a high-speed dental drill over the visual cortex (V1 and V2; centered approximately 2-3.5 mm caudal to Bregma and 1-3mm lateral from midline). The craniotomy site was frequently washed with saline to remove bone fragments and prevent thermal damage of the underlying brain. A dental cement well was cured around the margin of the craniotomy to hold a saline immersion with the microscope objective. After the skull was thinned, it was carefully removed with fine-tip forceps. Following craniotomy, animals were placed under a two-photon microscope using a 16 x, 0.8 numerical aperture water immersion objective (Nikon Inc., Milville, NY). Probes were stereotaxically targeted within the V1/V2 portion of the craniotomy and inserted in a rostral direction into the cortex at a 30-35° angle and parallel to midline at 50-100µm s⁻¹ (oil hydraulic microdrive; MO-81, Narishige, Japan) to a final resting depth of 250-300 µm (layer II-III) beneath the surface of the brain (Figure 3-1). Major blood vessels were identified prior to insertion and avoided. All animals had a similar density of capillaries within the imaging window. Little or no bleeding was observed

during insertion, though some spontaneous bleeding was observed throughout the 6 h experiment. Immediately prior to imaging, sulforhodamine 101 (SR101) was injected IP as a vascular contrast agent (red; 0.02-0.04 cc; 1 mg ml⁻¹). Updates of SR101 (0.01 mg ml⁻¹) and ketamine (22.5 mg kg⁻¹) were administered approximately every 30 minutes to maintain vascular contrast and a deep anesthetic plane. Updates of ketamine and SR101 were given through an IP catheter line (Braintree Scientific, Inc., USA). Minimal edema was observed throughout the 6 h experiment. All procedures and experimental protocols were approved by the University of Pittsburgh, Division of Laboratory Animal Resources and Institutional Animal Care and Use Committee in accordance with the standards for humane animal care as set by the Animal Welfare Act and the National Institutes of Health Guide for the Care and Use of Laboratory Animals.

3.3.3 Two-photon imaging

In vivo imaging was conducted with a two-photon laser scanning microscope consisting of a scan head (Prairie Technologies, Madison, WI), a Ti:sapphire laser (Mai Tai DS; Spectra-Physics, Menlo Park, CA) tuned at a wavelength of 920 nm, and non-descanned photomultiplier tubes (Hamamatsu Photonics KK, Hamamatsu, Shizuoka, Japan) in whole-field detection mode to collect emitted light. Images were collected on Prairie View software. ZT stack images were collected every minute from one minute prior to 79 minutes after probe insertion, and then Z-stack images at 80 minutes post-implant and every hour from 2-6 h post-implant were collected. Sterile saline was held in the craniotomy site by a dental cement well. This allowed for brain

hydration and adequate water immersion for the microscope objective. Saline was replenished as it evaporated.

Both the initial ZT stack images and hourly Z stack images covered an area of 407.5 to 407.5 μm (1024×1024 pixels) at a scan rate of ~ 4.8 s/image, which gave sufficient resolution to track individual microglial processes. This image size allowed us to visualize 2-3 shanks at a time. Prior to probe insertion, continuous collection of 24 μm thick ZT-stacks (2 μm intervals between images; parameters set to maximize data collection at 1 minute intervals) focused on the lowest depths of the intended insertion site commenced. Following the first Z-stack scan, probes were inserted and ZT-stack collection continued through the first 79 minutes post implant. Following initial ZT-stack collection, Z-stacks capturing the full observable depth of the implanted cortex were taken at 80 minutes post-implant and every hour from 2-6 h post-implant.

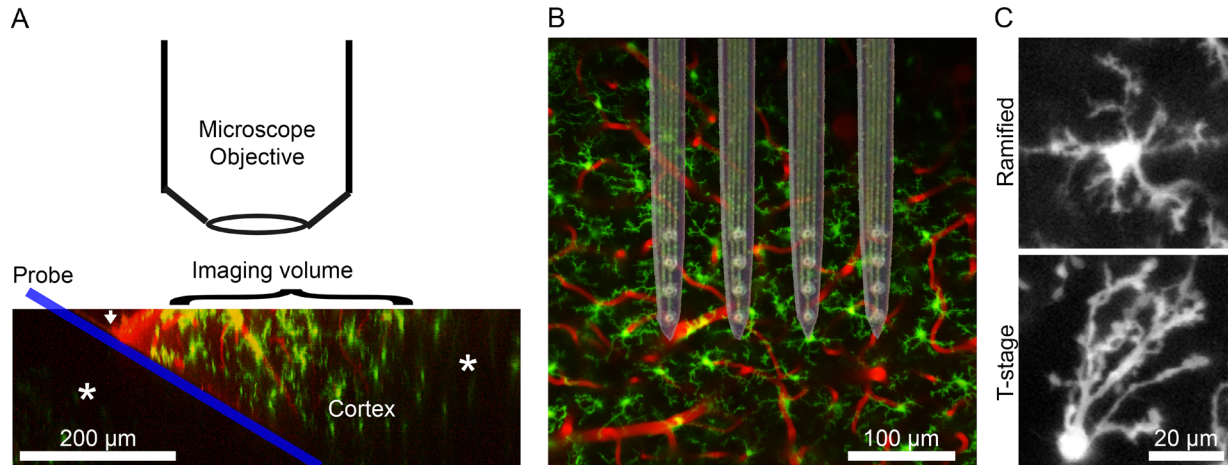


Figure 3-1 Experimental set-up.

(A) Following craniotomy, the probe (blue) is inserted into the cortex (Microglia in green; blood vessels in red) at a 30° angle. The white arrow indicates where the cortex is pierced. This allows the probe to be inserted without colliding with the microscope objective while maximizing the area of the probe that can be imaged. * denote darker regions due to being underneath either the probe, pial blood vessels. The image shown here is a side-projection of raw data made through a 3D reconstruction. (B) Raw data were images of cortex from a “bird’s-eye view”. Here, a bright-field image of the neural probes is superimposed over unimplanted cortex to demonstrate probe configuration and relative of cortex and implants. The implanted probes are 4-shank, silicon Michigan-style electrodes with Ir electrode sites. (C) Microglia are classified as ramified if processes extend equally in all directions or as “activated” transition stage (T-stage) if processes extend in one direction preferentially.

3.3.4 Data and statistical analysis

For each animal, ZT-stack images were analyzed to track individual microglial process positions over time and microglial surface coverage of the neural probes over time. Images with observable motion or drift from normal breathing, heartbeat, or tissue relaxation were corrected

with a custom-written MATLAB script (Math Works, Boston, MA) using a rigid-body translation algorithm based on cross-correlation as previously described [40]. Alternatively, the “StackReg” plugin for ImageJ was used for rigid-body corrections of large motions [302]. Animals or microglial processes were discounted for any time-points in which motion could not be corrected or if there was poor visibility due to dural bleeding. Microglia process migration toward the probe tracked by recording XY coordinates of processes using the ‘Measure’ function in ImageJ (National Institutes of Health). The determination of migration toward the probe or away from the probe was systemized by dividing each microglial cell body into a hemisphere facing the probe and a hemisphere facing away from the probe. The line between hemispheres was defined as the line parallel to the nearest probe edge and that went through the midpoint of microglial cell body (examples of line selection shown in Figure 3-6B). In order to negate any artefactual migration due tissue displacement upon probe insertion, measurements began after the probe’s entry. Time series movies were created with respect to the time stamps of individual frames. Microglial surface coverage of the probe and percent of tissue with microglial signal was determined by making a binary mask of a sum projection of each ZT-stack using the ImageJ Default variant of the IsoData threshold method [191]. An outline of the probe was manually defined by focusing on planes below the surface of the probe, where the profile of the probe appeared as dark shadow with high contrast between the edge of the probe and the fluorescence of the parenchyma. The dimensions of the probe outline were cross referenced with the dimensions of the device to ensure accuracy. Because there is likely disproportionate strain in tissue surrounding the tip of the probe due to micromotion, the first 30 μm of the probe from the tip was discounted from analyses [80]. Non-zero pixels were counted using the ‘Measure’

function, and divided by the area of the user-defined probe outline to derive the % surface coverage of the probe by microglial and the percent of tissue with microglial signal.

Z-stacks of the full observable depth of implanted cortex at 80 min and 2-6 h post-implant were analyzed to determine the extent of microglial surface coverage of the probe and the morphology of microglia surrounding the implant. For the quantification of microglial coverage of the probe, the Z-stacks were first digitally rotated 25-35° with Interactive Stack Rotation plugin for ImageJ in order to view the surface of the entire probe in one rotated Z plane [188]. The sum of Z-stack comprising the surface of the probe and the 20 µm above the probe were projected onto one image. Microglial surface coverage was then measured as described above.

For qualitative evaluation of the microglial reaction, Z-stacks were transformed from XY planes to XZ or YZ planes by linear interpolation (ImageJ; '3D Project' function). Average intensity or sum projections of reconstructed stacks allowed for analysis of specific regions of interest.

Changes in process velocity and microglial surface coverage of the probe with respect to time and changes in percent of tissue with microglial signal with respect to distance were modeled using a linear mixed effects model with random slopes and intercepts for each animal. To allow the model to fit nonlinear relationships, a restricted cubic spline basis was implemented with 4 knots placed at the 5th, 35th, 65th, and 95th percentiles of the data. Additional fixed effects included a categorical variable for group (L1 versus control) and the interaction between group and time. To test for any significant group-wise differences a likelihood ratio test was performed comparing two models: (1) the full model described above; and (2) a second model that excluded the group and group-by-time interaction predictors. Confidence intervals were

estimated using case bootstrapping with 1000 iterations. 95% confidence intervals were computed as 1.96 times the standard error of the model fits.

The 6 h post-implant Z-stacks were used to characterize microglia morphology. Microglia were classified as ramified (1) if processes extended in all directions without preference, or in the activated transitional stage (T-stage) (0) if processes were selectively extended toward the implant insertion site (Figure 3-1C) [40]. The determination of the direction that was toward the insertion site was made by the same hemispheric distinction described in the microglial velocity analysis description above. Microglia were binned by distance from the probe. From these values, a logistic regression was created to show the Bernolli Probability Distribution of microglia being in the ramified state (0 or 1) as a function of distance from the probe. Because probability distribution inherently accounts for error, there can be no additional calculation of error for this data.

Morphology was also used to assess the degree of microglial activation through a transitional stage morphology index (T-index) and a microglia directionality stage index (D-Index). The T-Index was calculated by measuring the length of the longest microglia process facing the probe (n) and the length of the longest process facing away from the probe (f). The D-Index was calculated by measuring the number of microglial processes projecting toward the probe (n) and away from the probe (f). n and f were then used to calculate respective index values through the following formula:

$$Index = \frac{(f-n)}{(f+n)} + 1 \quad (3-1)$$

For both indices, a value of 1 ($n = f$) indicates that a microglia extends processes in all directions without preference (ramified morphology). Index values < 1 indicate a preference in either process length (T-Index) or process number (D-Index) in the direction of the probe. Cells were binned by 30 μm distance intervals from the probe, which was selected to insure at least 10 samples per interval. To determine how microglial activation varied with distance from the probe, data was fitted to a custom MATLAB dual sigmoidal function. This model was previously optimized in studies of acute microglial reaction to different neural implants, and therefore allows for comparison between studies [40, 165]. The model has parameters for amplitude (a), shoulder location (d_1 and d_2 ; μm), and shoulder width (w_1 and w_2 ; μm):

$$y(d) = \frac{a}{1+e^{(d-d_1)/w_1}} + \frac{1-a}{1+e^{(d-d_2)/w_2}} \quad (3-2)$$

3.4 RESULTS

In order to characterize the dynamic interactions of microglia with L1-coated neural probes in the first 6 hours post-implantation, 7 probes with L1 protein immobilized along the full extent of all shanks and 7 pristine, uncoated control probes were implanted into the cortex of 14 CX3CR1-GFP reporter mice. Microglial dynamics were tracked in relation to the implanted probe with two-photon microscopy.

3.4.1 Microglia process extension velocity is unaffected by the L1 coating

Following craniotomy and vascular dye injection, we examined the surface of the brain with fluorescence microscopy for regions with low vascular density that would be suitable for imaging. Once a region was selected, we confirmed that there was no pre-existing microglial activation with two-photon microscopy, and inserted the probe. For both the control probes and L1 coated probe, microglial processes $\sim 175 \mu\text{m}$ from the probe extend toward the implant site immediately after insertion. In order to quantitatively compare process extension between groups, the velocities of individual microglia process end-feet (total processes varied between 12-21 depending on time-point with 5 animals for each group; 2 animals from each group were discounted due to movement artifacts) were tracked from 4 to 79 min post-implant (Figure 3-2A-B). Both control and L1 group microglia processes moved fastest within the first 30 min post-implant (between $0.5\text{-}1.5 \mu\text{m}/\text{min}$), and slowed to a near-stop by the first 60 min post-implant. There were no significant group-wise differences in velocity between the control and L1 groups in the likelihood ratio test. Additionally, there was no statistical difference in aggregate microglia process movement toward and away from the probe between 4-79 min post-implant velocity between the L1 and control groups (Figure 3-2C).

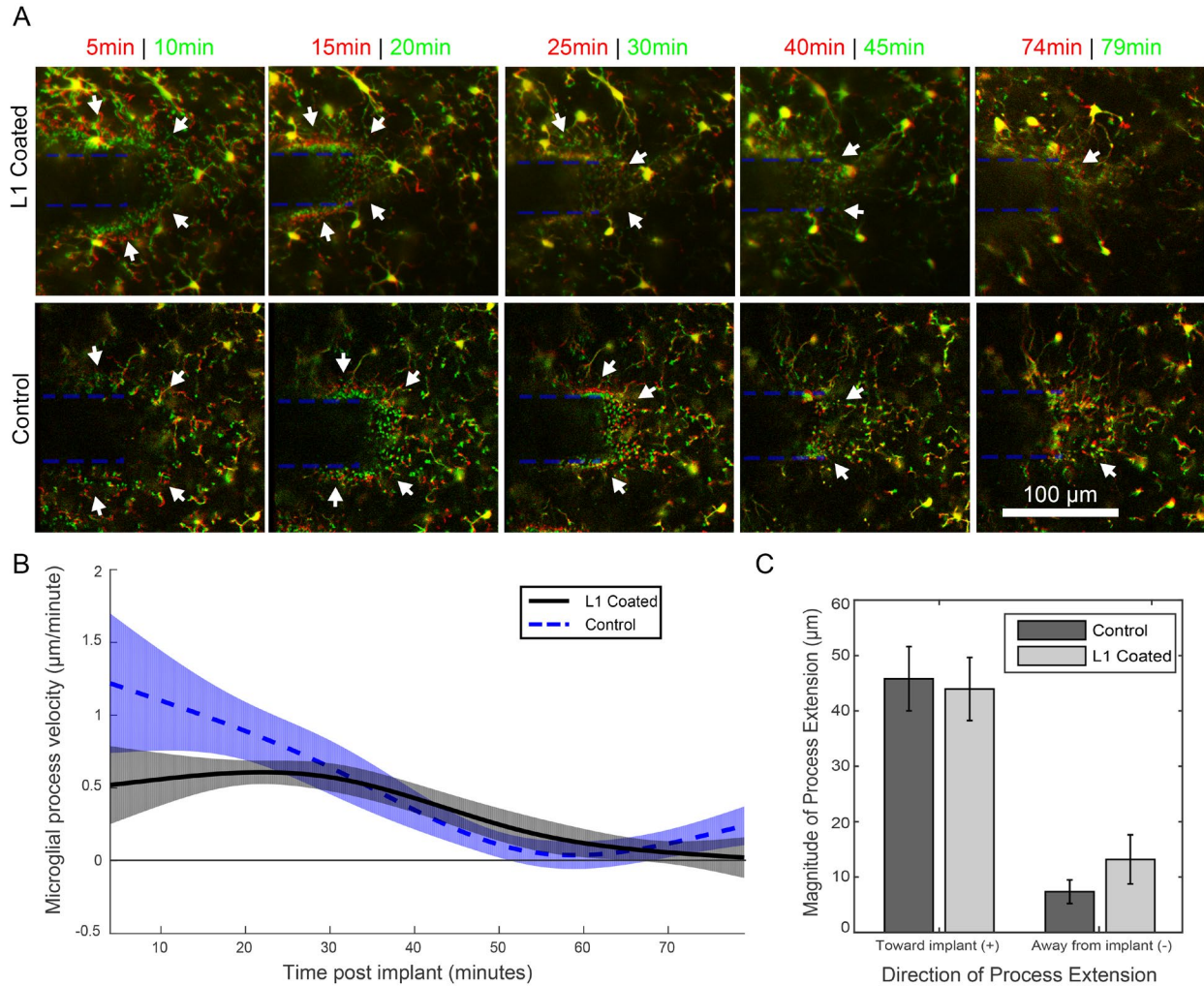


Figure 3-2 Microglial process extension velocity is unaffected by L1 coating.

(A) Process end-feet velocity and direction (toward (+) or away (-) from the probe, which is outlined in a blue dotted lines) are measured by comparing earlier time-point positions (red) to later (green). Yellow indicates features that did not move in that time interval. Arrows indicate the regions of advancing microglial processes, which can be identified by a layer of red processes followed by a layer of green processes. Forward progress dwindled at later time intervals (after 45 minutes). (B) Process velocity data was modeled with a linear mixed model for the L1 group (black, solid line) and the control group (blue, dotted line). Shaded regions are 95% confidence intervals. Likelihood ratio tests revealed no group-wise differences. (C) There were no significant differences in total movement toward or away from the neural probe between the L1 and control groups. Bar plot presented as mean \pm SEM.

3.4.2 Immediate and sustained inhibition of microglial surface coverage of the probe with the L1 coating

Once processes reached the edge or the face of the probe, the processes stopped migrating. However, once the process end-feet reached their destination, the microglia began covering the surface of the probe with lamellipodium sheaths. In order to characterize this microglial surface coverage, a threshold-based method was used to quantify the percent of the probe's face that was covered by processes between 4-79 min post-implant (Figure 3-3; n = 4 per group; 3 were discounted from each group due to movement artifacts or lack of visual clarity due to bleeding). There were significant group-wise-differences between the control and L1 coated probes (Likelihood ratio test, $p < 0.01$), with the 95% confidence intervals of groups diverging by 8 min post-implant, and remaining distinct for the remainder of the experiment. The face of L1 coated probes was less than 11% covered by microglia for the first 79 min post-implant. Coverage of control probes continued to increase, plateauing at 40-45% coverage by 30 min post-implant, and remaining statistically increased relative to L1 coated probes through the 79 minutes of imaging.

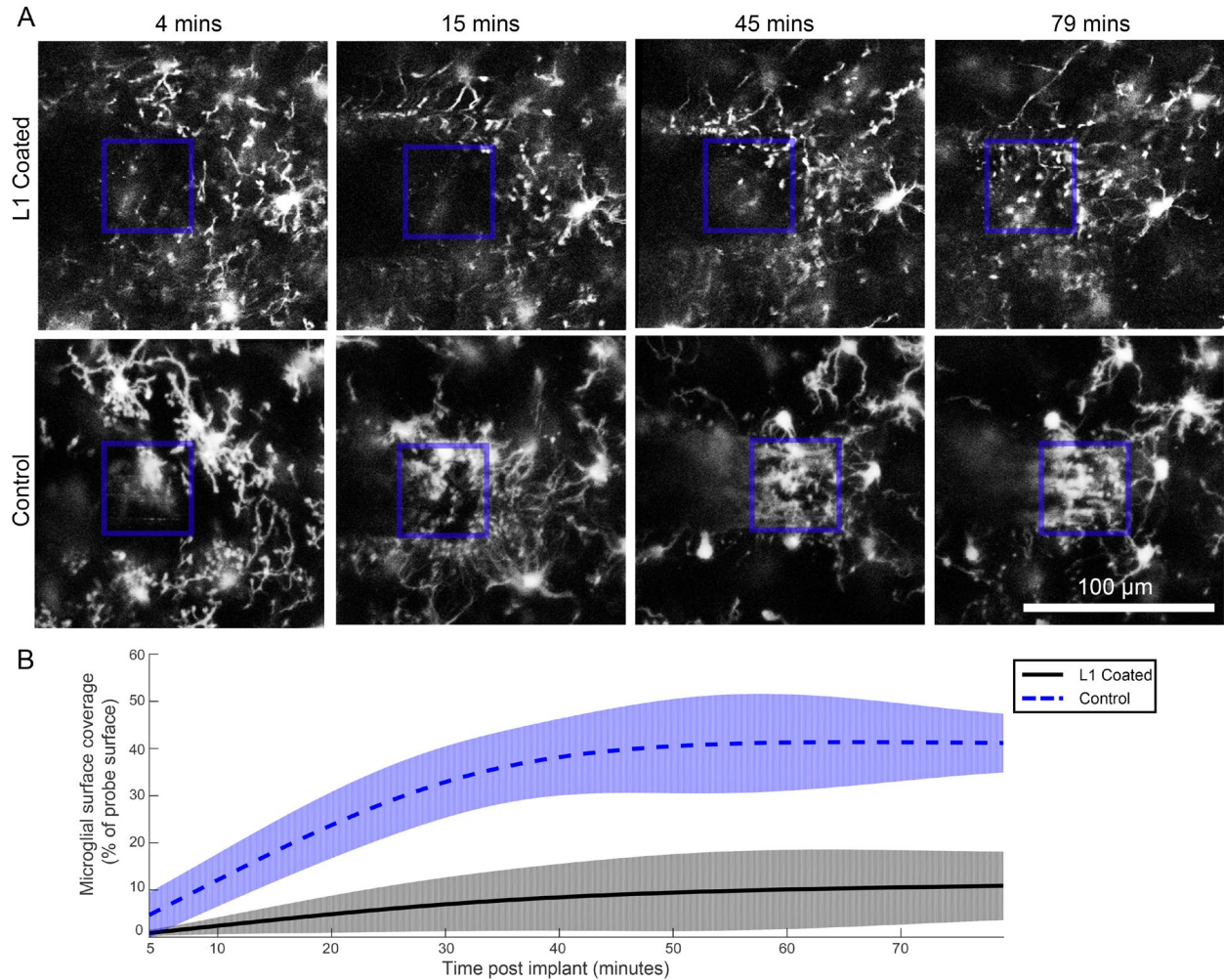


Figure 3-3 L1 prevents microglial surface coverage of neural probes over the first 79 min post-implant.

(A) An automated, threshold-based method quantified the percentage of probe faces covered by microglia processes. The aspect of the neural probe that was in focus is outlined in a blue box. **(B)** Coverage data was modeled with a linear mixed model for the L1 group (black, solid line) and control group (blue, dotted line). The likelihood ratio test revealed significant group wise differences ($p < 0.01$), with 95% confidence intervals (shaded aspects of traces) diverging by 8 min post-implant.

This effect of L1 coating preventing microglial surface coverage extended for hours (Figure 3-4). At both 2 h and 6 h post implant, there was significantly less microglial surface coverage of L1 coated probes compared to control probes (2 h: $8.2 \pm 2.4\%$ v. $47.7 \pm 3.4\%$, $p < 0.001$; 6 h: $6.2 \pm 2.4\%$ v. $35.8 \pm 6.9\%$, $p < 0.05$; both comparisons by Welch's t-tests). There was no statistical difference within the same coating groups between 2 and 6 h post-implant. This effect was qualitatively corroborated by a validation experiment ($n = 1$) in which the first $\sim 150\mu\text{m}$ from the tip of the probe was coated with L1, leaving the rest of the probe uncoated (Figure 3-7). At 3 h post-implant, there was an observable reduction in microglial surface coverage of the L1-coated portion of the probe.

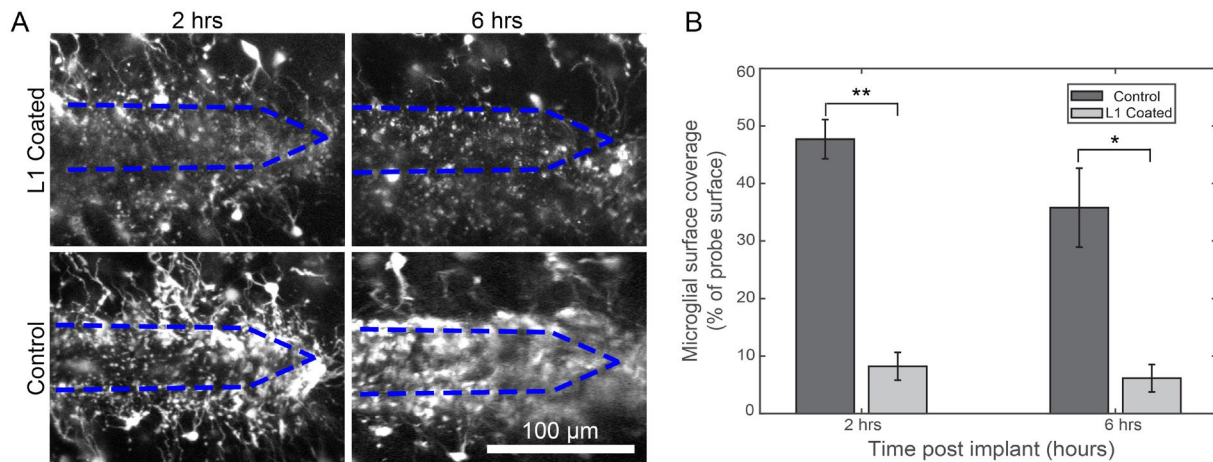


Figure 3-4 L1 coating continues to prevent microglial surface coverage through 6 h post-implant.

(A) 2D projections of probes at 2 and 6 h post-implant (B) The percentage of the probe's surface that was covered by microglia was significantly less for L1-coated probes compared to control probes at 2 h and 6 h post-implant (Welch's T-test; ** $p < 0.001$, * $p < 0.05$). Bar graph data presented as mean \pm SEM.

In order to determine how the amount microglial signal changed with Z-direction distance from the implant, thresholded side-projection images of 2 h post-implant Z stacks were rendered. Looking at the % of tissue with microglial signal after thresholding, there were significant group-wise differences between L1 and control probes (Figure 3-5; n =3 per group, reduced due to availability of sufficiently sized Z stacks; Likelihood ratio test, $p < 0.0001$). In particular, there was a deviation in 95% confidence intervals of groups within the first 20 μm of the probe surfaces, with a 92-57% reduction in microglial signal between 0-20 μm above the L1 coated probes (Figure 3-5B). Between 20-50 μm , however, the 95% confidence intervals converged for the groups, indicating that there was a similar amount of microglial signal in this region.

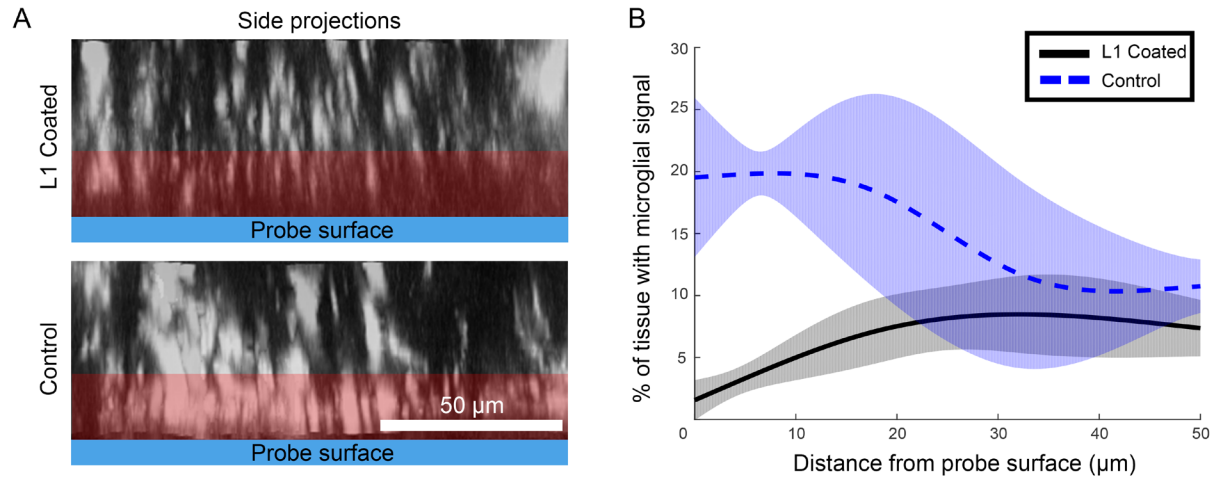


Figure 3-5 Decreases in the % of tissue with microglial signal adjacent to L1 coated probes.

(A) Side projections of Z stacks allow the microglial signal in the Z-direction above probes to be measured. The red region indicates where there are significant differences between groups. **(B)** % of tissue with microglial signal data was modeled with a linear mixed model for the L1 group (black, solid line) and control group (blue, dotted line). The likelihood ratio test revealed significant group wise differences ($p < 0.0001$), with 95% confidence intervals (shaded aspects of traces) diverging at 20 min post-implant.

3.4.3 Changes in microglia activation at 6 h with L1 coating

At 6 h post-implant, there were several differences in microglia morphology between control and L1 groups. Microglia morphology was evaluated ($n = 216$ microglia for the control group; 253 microglia for L1 group, each from 5 animals) and classified as either ramified (1) or transitional stage (T-stage; 0) (Figure 3-1 C), and plotted average values against distance from the probe's edge (Figure 3-6 A-B). Logistic regression was then used to model the data:

$$\text{Control: } \log(p/1-p) = -7.63x + 0.059 \quad (3-3)$$

$$L1: \log(p/1-p) = -5.06x + 0.059 \quad (3-4)$$

where p denotes the probability that a microglia at a given radius (x) is ramified. The distance from the probe at which 50% of microglia were ramified was determined to be 130.0 μm for the control group and 103.5 μm for the L1 group.

In order to explore differences in the degree of microglial activation between the control and L1 groups, two morphology indices were evaluated: 1) a T-stage morphology index (T-Index), which compares the length of the longest process extending toward the probe vs. the longest process extending away from the probe for each microglia, and 2) a directionality index (D-Index), which compares the number of processes facing toward the probe vs. the number of processes facing away from the probe for each microglia. For both indices, values closer to 0 indicate a stronger response toward the probe, whereas an index value of 1 indicates either ramified or no preferential response toward the probe. Two-shouldered sigmoidal functions were fit to the data of both indices using Equation 3-2 with parameters for relative amplitude (a), near shoulder ($d1$) and spread ($w1$), and far shoulder ($d2$) and spread ($w2$). For the T-index, control parameters were $a=0.65$, $d1=10.35 \mu\text{m}$, $w1=21.04 \mu\text{m}$, $d2=215.11 \mu\text{m}$, and $w2=5.00 \mu\text{m}$, and L1 parameters were $a=0.85$, $d1=58.63 \mu\text{m}$, $w1=23.94 \mu\text{m}$, $d2=146.25 \mu\text{m}$, and $w2=5.00 \mu\text{m}$ (Figure 3-5C). Comparing general trends of sigmoidal curves of the control and L1 group T-Indices, both groups had very low index values immediately adjacent to the probe, with few microglial processes protruding far away from the implantation site. Interestingly, the microglia between 30-60 μm from the L1 coated probes had a significantly lower T-index value compared to microglia around the control probes (Welch's T-test; $p < 0.001$). As noted in our previously published work, microglia between 60-210 μm from the control probes held at a 0.6 T-index.

Contrary to this, microglia in the same region around L1 coated probes had progressively increasing T-index values, reaching a value of ~1 by 150 μm from the probe. Microglia around control probes did not reach a “1” T-index value until 210 μm from the implant. This difference in T-index was reflected in T-tests, where the L1 group had statistically higher T-index values between 150-210 and 240-270 μm from the probe (Welch’s T-test; $p < 0.05$).

There were also differences between the control and L1 group in the D-Index values (Figure 3-6D). The sigmoidal function parameters for the control were $a = -0.79$, $d_1 = 10.54 \mu\text{m}$, $w_1 = 15.45 \mu\text{m}$, $d_2 = 186.03 \mu\text{m}$, and $w_2 = 25.06$, and for the L1 group were $a = -0.82$, $d_1 = 43.45 \mu\text{m}$, $w_1 = 14.54 \mu\text{m}$, $d_2 = 141.28 \mu\text{m}$, and $w_2 = 9.65 \mu\text{m}$. Microglia within 60 μm of L1 coated probes had significantly lower D-Index values when compared to microglia around control probes (Welch’s T-Test; $p < 0.05$). Beyond 60 μm , D-Index values continued to rise without any significant differences between groups, reaching a “1” D-index value around 180 μm from the probe. The D-Index for the L1 group was significantly higher than the control group between 270-300 μm (Welch’s T-test; $p < 0.05$).

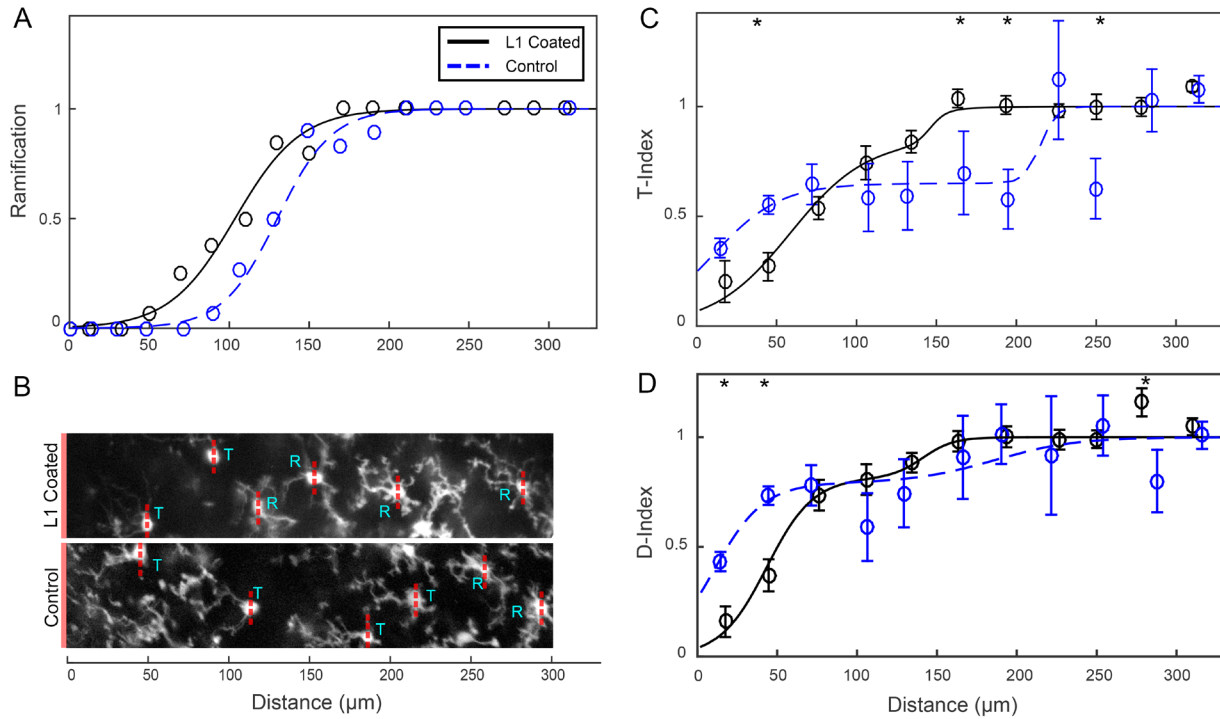


Figure 3-6 L1 coating alters morphological features at 6 h post implant.

(A) Probability of cell ramification (1 is ramified, 0 is T-stage) over distance show that the L1 group (black, solid line) has ramified cells closer to the probe than the control group (blue dotted line) in a logistic regression of probability data. Note: as this is a Bernolli Probability Distribution error bars cannot be calculated. **(B)** A sample image of microglia labeled as T-stage or ramified. A solid red bar at the left of each image indicates the surface of the probe. Red dotted lines indicate the axis that was used to distinguish the hemispheres facing toward the probe (left side of line) v. away from the probe (right side of line). **(C)** The T-stage index (T-Index) compares the length of the longest probe-facing process to the longest non-probe facing process, with 0 indicating no non-probe facing processes and 1 indicating fully ramified microglia. **(D)** The directionality index (D-Index) compares number of probe facing processes to number of non-probe facing processes, with 0 indicating all probe-facing processes and 1 indicating totally ramified microglia. Data are presented as means \pm SEM; all comparisons are made by Welch's T-tests. * denotes significance, $p < 0.05$.

3.5 DISCUSSION

The value of implantable microelectrode technologies as basic-research tools and substrates for brain-computer interfaces is well established, however, their clinical implementation has been stifled by their high failure rate in pre-clinical models. Covalently linking neural adhesion molecule L1 to the neural probe's surface is a promising strategy to improve biocompatibility. *In vitro*, substrate-bound L1 can selectively encourage neuronal attachment while deterring astrocyte and fibroblast attachment [95, 108, 299]. *In vivo*, we have previously shown that L1 coatings on probes implanted in the cortex, spinal cord, and dorsal root ganglia improve neuronal survivability, axonal regeneration, and even neuronal attachment to probe's surface for at least 8 weeks post-implant [86, 104, 105]. This is distinct from other coating strategies (laminin, Parylene-C, PDMS, PEG/polyurethane) which may attenuate some neuronal cell death, but do not improve regeneration [101, 106, 116]. Further, the microglial and astrocytic responses are attenuated in the region immediately surrounding the probe. These results were obtained via postmortem histology at discrete chronic time-points, while the specific interaction between the L1 coating and the host cells that leads to these effects remains unclear. Towards this end, the current experiment assessed the acute microglial response to L1-coated substrates in cortex immediately after implantation, providing mechanistic clues to describe L1's therapeutic effects.

3.5.1 Microglial process extension and probe surface coverage

As in our previous work, within 5 min after implantation of L1 or control probes, most microglia within 100 μm became polarized, extending processes toward the implantation site while retracting processes that were initially facing away from the probe [40]. Polarization and process

extension indicate microglia activation, and are often followed by cell body movement toward the source of activation (12+ hours to days) [51, 67, 149, 151, 303]. These processes extended until they reached the edge or surface of the probe, approximately 30-45 min post-implant, dependent upon the initial position of the process. There were no significant differences in the process extension velocities between the groups. This suggests that process extension is mediated by factors that are independent of the covalently attached L1 surface coating. The most likely factors are soluble chemokines or debris released from damaged cells, mechanically stimulated release of soluble chemokines, and blood plasma proteins release from the mechanically damaged BBB. Chemokines such ATP, UDP, and glutamate are known to incite directed microglial process extension along the chemokine gradient [56, 304-307]. Upon mechanical trauma, astrocytes and neurons release ATP and glutamate into the extracellular space, serving as chemokines for surrounding microglia [308-310]. This effect is conserved across many paradigms of mechanical trauma, including deep-brain stimulator implantation in humans [311]. It is not known if abrupt mechanical distortions directly affect microglial phenotype, though recent studies have shown that microglial behavior is modulated by at least some mechanical cues. Namely, if placed on a substrate with a gradient of stiffness, cultured microglia will migrate toward the stiffer areas [91].

In addition to mechanically stimulated release of chemokines, probe implantation will also mechanically rupture blood vessels, causing release of blood plasma proteins such as immunoglobulins, serine proteases, and albumin into injury site [37]. Diffusing through cortex at $\sim 137 \mu\text{m min}^{-1}$, these proteins—which are known to perpetuate microglial responses and contribute to neuronal death—will have spread through the volume of the entire viewing area of this study within the first 5 min post-implant [59, 66, 312-315]. These plasma proteins can also

physically adsorb to the surface of the probe, which may affect the phenotype of cells that contact the probe's surface [55, 95].

Most processes stopped extension once they reached the surface of the probe. The percent of the probe's surface that was covered in these processes increased over the 6 hour experiment for both groups. There was, however, significantly less coverage of the L1 probes as early as 8 min post-implant. At all points between 8 min and 6 h post-implant, there was a 75-83% reduction in surface coverage of the L1 group. There was a slight drop in surface coverage between 2 and 6 h post-implant for both the L1 and control groups, but it is not clear if that is due to microglial process retraction, or dimming of the image quality due to spontaneous bleeding or gradual photobleaching. However, the drop was not statistically significant, and the reduction in surface coverage was the same (83%) at both 2 and 6 h post-implant. We postulated that there were two possible mechanisms to explain the reduction in microglial surface coverage of the L1 group: the endfeet that were contacting or immediately adjacent to the L1 probe were smaller and covered a smaller area of the probe, or activated, T-stage microglia were projecting fewer processes to the surface of the L1 probe. To investigate these possibilities, we examined how the amount of microglial signal changed with distance from the probe's surface. If the first possibility was true, we would expect that the decrease in microglial signal for L1 probes would be confined to the region immediately adjacent to the surface of the probe, and there would be no difference between groups further away from the probe. In the second scenario, there would be fewer processes and therefore less microglial signal for the L1 group throughout the radius of microglial activation ($< 175 \mu\text{m}$ from probe, as seen in Figure 3-6A). Our evidence points to the former—there were a similar number of microglial processes directed toward both types of probes, but within $20 \mu\text{m}$ of the L1 probe, there was a decrease in microglial signal. This

suggests that L1's effect modulated the endfeet and processes contacting or immediately adjacent to the coating. Qualitative observations of the microglial surface coverage tissue corroborate this mechanisms, in which coverage tissue often appeared as flattened, contiguous swathes of tissue on control probes, but easily discernable 1-2 μ m diameter endfeet on L1 probes (Figure 3-3A).

While it is likely that microglial processes are guided to the probe along a chemotactic gradient generated by implantation trauma, it is unclear why microglial processes attach to the surface of the probe. It is believed that microglia make prolonged contacts with injury sites to uptake neurotoxic or excitotoxic factors released from damaged cells or vasculature [58, 316, 317], reconstitute damaged barriers between the brain and the rest of the body [56, 132], and phagocytose damaged neurons, plaques, or invading neutrophils [318-320]. It is unclear how L1 is influencing these particular microglial functions. For NCAM, terminal sialic acid residues can suppress microglial phagocytosis through the SIGLEC-E receptor [318]. Though it has not been tested, it is possible the sialic acid residues on L1 could act similarly. Further, it is unclear how this surface coverage behavior would affect the longevity and long-term outcome for the implanted device.

3.5.2 Possible mechanisms of the L1-coating effect

Taken together, the process extension data and surface coverage data suggest that the L1 did not have an effect on the microglia until after they made physical contact with the coating or were within 25 μ m of the probe's surface. Interestingly, while many cells of hematopoietic origin express L1, to our knowledge microglia do not, and so cannot engage in the L1-L1 homophilic binding that neurons exploit [321]. L1, however, is known to make heterophilic interactions with the proteoglycans phosphacan and neurocan as well as the integrins α V β 3 in humans and rodents

and $\alpha 5\beta 1$ in mice [322-324]. Of these potential heterophilic binding sites, microglia at least express $\alpha 5\beta 1$, and expression increases upon cytokine activation [325-327]. While there are no specific studies on the interaction between microglial $\alpha 5\beta 1$ and L1, this could be a potential mechanism by which the L1 coating is attenuating microglial surface coverage behavior. Further, as described above, it is possible that L1's terminal polysialic acid residues could bind to the microglial SIGLEC-E receptor, which suppresses phagocytosis.

In support of direct interaction between L1 and adjacent microglia is the observation that morphological differences exist between the two groups at 6 h post-implant. To understand the microglial morphology, cells were first defined as either ramified or T-stage by qualitative assessment, and then the number (D-Index) and length (T-Index) of individual processes that were projecting toward the probe were compared to processes that were projecting away from the probe. This allowed the characterization of trends in microglial activation as well as the degree of microglial activation. While the qualitative ramification index shows that there were more ramified microglia closer to the L1 implants, both the T-Index and D-Indexes were lower for the L1 group at points within 60 μm of the probe. This indicates that microglia within 60 μm of the L1 probes had more processes and longer processes extending toward the probe compared to microglia within 60 μm of the control probes. While this may suggest that the microglia in the immediate vicinity of the L1 probes are more “activated”, the L1 probes had an 83% reduction in microglial surface coverage at this same time point. This data suggests that, while the microglia are more activated, the phenotype of activation is different. Many recent studies have suggested that there is a continuum of microglial activation states, often broadly stated in terms of M1, which is proinflammatory and can lead to scarring, or M2 activation, which is anti-inflammatory, and is important in phagocytosing cell debris and tissue regeneration [328-330]. While trauma

such as a neural probe implantation may drive M1 microglia activation, perhaps interacting with the L1 coating alters the activation state of microglia [328]. *In vitro* studies are conflicting as to whether M1 and M2 microglia have different morphologies [331] or not [332, 333], and thus future studies looking at early time-point immunohistochemical markers for microglia polarization will be necessary to address this. Importantly, microglial activation could have consequences for neuronal health. Activated microglia have been implicated in directly causing or exacerbating phagocytotic, excitotoxic, and apoptotic neuronal death [35, 54, 334, 335]. Interestingly, previous work has shown that tissue around L1 coated probes had both fewer activated microglia as well as an increase in neuronal processes after 8 weeks of implantation when compared to healthy tissue and uncoated probe [104]. This suggests that the L1 coating has a neuronal regeneration effect, unlike dexamethasone coatings, which can reduce microglial activation but don't lead to neuronal regeneration [277]. It is unclear whether this regenerative effect is due to L1's action on neurons, microglia, or both. Future experiments should be focused on isolating these effects to achieve a full understanding of L1's mechanisms.

The morphology index data also suggests that there is an indirect interaction between the L1 coating and microglia. At 6 h post-implant, the T-index for the L1 group was significantly higher at points between 150-270 μ m and the D-Index was higher between 240-270 μ m, areas with cells that had no direct contact with the probe. It is possible that cells contacting the L1 coating—either microglia, astrocytes, or neurons—are releasing molecules or changing expression of membrane proteins in such a way to affect the phenotype of cells in this distant region. Supporting this are *in vitro* and *in vivo* studies of peripheral macrophages show that surface chemistry can affect secreted cytokine profiles within 1 day of implant [336, 337]. The areas between 60 μ m and the distant regions were not different between coating groups. This may

indicate that this area was still affected by mechanical changes due to probe insertion or soluble factors from damaged cells and blood vessels. The distant region that had significant changes between groups may have been out of range of these mechanical and chemical changes, but still within the range of L1-related changes.

It is also possible that the difference in hydrophobicity between the control and the L1 probes affected the microglial response. In previous studies, we have shown that the water contact angle for the unmodified control and L1 coated probes are respectively $27.3 \pm 1.4^\circ$ and $69.8 \pm 1.7^\circ$ [95]. In these previous studies, however, we showed that L1 functionalized substrates had distinct effects on primary neuron and astrocyte adhesion when compared to L1-free substrates with similar hydrophobicity. Further, in an experiment with a probe that had a region of L1 functionalization and a region of silane + GMBS treatment, there was an observable reduction in microglial surface coverage for the L1 region when compared to the silane +GMBS side at 3 h post-implant (Figure 3-7). This corroborates that L1 has a distinct, bioactive effect when compared to a surface with comparable hydrophobicity (Water contact angle: L1: $69.8 \pm 1.7^\circ$, silane +GMBS: $58.5 \pm 1.6^\circ$ [99]). Nevertheless, hydrophobicity of the surface is expected to play a role in protein adsorption and the consequent cellular interaction. A separate study is ongoing to examine the microglia response to well-controlled non-bioactive surfaces with different hydrophobicity.

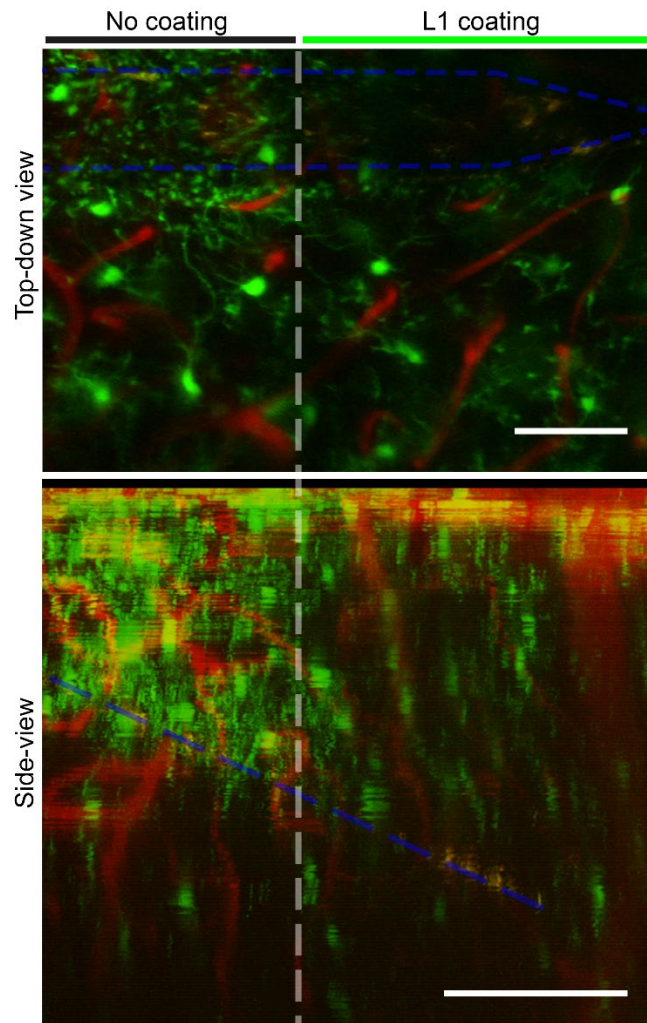


Figure 3-7 Partial L1 coatings show localized L1 effect.

The tip of a neural probe (profile shown by blue dotted line) was coated with L1 protein up to the dashed white line. After 3 h in vivo, the probe was imaged. There is a clear demarcation in microglial (green) response between the coated and uncoated portions of the probe. Vasculature is shown in red. Scale bars are 100 μm .

3.5.3 Long-term effects of L1 coatings and future directions

While the present study shows that the L1 coating is effective in reducing microglial surface coverage through 6 h post-implant, our previous work shows that the L1 coating is effective in reducing glial scarring and neuronal cell death to at least 8 weeks post implant [86, 105, 232]. It is unclear how these initial effects on microglial dynamics transition into the effects observed at late time points. Further, the present study demonstrates that while the L1 probes had less surface coverage, microglia around those probes had more morphological activation. Future studies will need to track these populations of activated microglia to study their long-term fate and role in glial scar formation. To address this, our group has also optimized cranial window techniques that enable longitudinal imaging from 12 h post-implant to at least 3 months post-implant [62].

While we have seen how microglia interact with the L1 coating, neurons, astrocytes, and oligodendrocytes also likely to interact with the coating [95, 108, 298, 299, 338, 339]. Animal models with transgenic labels in multiple cell types—such as neurons with expression of the calcium indicator GCaMP—could be crucial in understanding the complex effects the coating is playing [340]. Current efforts are underway to follow this work with chronic imaging studies of the long-term microglial and neuronal responses to L1 probes including microglial cell body migration and aggregation at the tissue-probe interface as well as changes in neuron distribution and electrophysiology over time.

In addition to L1, other cell-surface proteins implicated in modulating microglia-neuron or neuron-neuron interactions could be used alone or in synergy with L1 as a neural probe coating [299, 341-344]. Addressing these experiments will help to provide a framework for a broadly applicable bioactivity assay for novel neural technologies using longitudinal *in vivo* microscopy. Additionally, these experiments will improve our understanding of how surface

modification affect the integration of foreign bodies into host tissue, which is crucial for implantable stimulation and recording probes as well as microdialysis probes, neurochemical sensors, drug delivery devices, and other types of neural implants [165].

3.6 CONCLUSION

The current study has demonstrated an immediate and substantial reduction of microglial surface coverage of neural probes with an L1 protein coating. This effect remained significant through 6 h post-implant (the duration of the experiment), corroborating previous findings that L1 coatings provide long-lasting mitigation of gliosis and neuronal cell death (at least 8 weeks). The coating reduced surface adhesion-behavior of microglia that were contacting the probe, and also reduced morphological activation of distant microglia that had no direct contact with the probes. This work provides both a framework for a rapid bioactivity assay for implantable neural technologies, as well as identifies microglia as a possible key mediator of the L1-coating's long-lasting anti-gliosis effect. Ultimately, this study identifies novel pathways to improve the efficacy of implantable neural technologies and establishes two-photon microscopy techniques that can rapidly test and validate these novel pathways.

3.7 ACKNOWLEDGMENTS

This project was financially supported by NIH NINDS (Grant 5R01NS062019, 1R01NS094396, 1R01NS089688). The authors would like to thank Patrick Cody, and Bin Cao for assistance with the coating procedures.

4.0 MENINGEAL INFLAMMATORY RESPONSE AND FIBROUS TISSUE GROWTH AROUND INTRACORTICAL IMPLANTS: AN IN VIVO TWO-PHOTON IMAGING STUDY

4.1 ABSTRACT

Meningeal inflammation and encapsulation of neural electrode arrays is a leading cause of device failure, yet little is known about how it develops over time or what triggers it. This present work characterizes dynamic changes of meningeal inflammatory cells and collagen-I in order to understand the meningeal tissue response to implants. We use longitudinal in vivo two-photon microscopy of CX3CR1-GFP mice over the first month after electrode implantation to quantify changes in inflammatory cell behavior as well as meningeal collagen-I remodeling. We define a migratory window during the first day after electrode implantation hallmarked by robust inflammatory cell migration along electrodes in the meninges as well as cell trafficking through meningeal venules. This migratory window closes by 2 days after implant, but over the next month, the meningeal collagen-I doubles in thickness. Meningeal thickness occurs with and without a silicone craniotomy sealant. We show that there are distinct time courses for initial meningeal inflammatory cell infiltration and meningeal collagen-I thickening. This may indicate a therapeutic window early after implantation for modulation and mitigation of meningeal inflammation. This chapter has been reprinted from work published in *Biomaterials* [345].

4.2 INTRODUCTION

Penetrating neural electrodes are essential tools for electrophysiological monitoring of neural signals to enable brain-computer interfaces as well as longitudinal neuroscience research [12, 167-170]. Despite their clinical promise, neural electrodes have limited long-term performance due to their poor integration into host tissue. [35, 50, 53, 54, 171-174]. As a consequence, electrode recording failure within months to years after implantation has been reported in rodent [20, 176], cat[23], and primate models [25, 27] for chronically implanted electrode devices.

Many strategies have been pursued to improve the longevity of neural electrodes, with most focused on alleviating glial scarring and neurodegeneration within the brain parenchyma [204]. The neural tissue response, however, is not the only biological source of failure. The fibrous meningeal tissue at the surface of the brain can proliferate and encapsulate aspects of the electrode array that reside at the surface of the brain (commonly referred to as the “platform” or “base” of an electrode array). The meninges consists of layers of fibrous tissue at the brain’s surface (Figure 4-1A) that provide mechanical protection to the brain [126], harbor the major arteriole and venule inputs and outputs of the brain [128], and is essential in controlling brain inflammation and waste clearance [131, 133, 136, 346]. After injury, however, inflammatory cell influx and increased collagen synthesis can create thickening of the meningeal tissues [132-134]. In the context of neural implants, meningeal tissue and collagen-I progressively grows around and under the electrode device and can lead to ejection of the device from the cortex [23]. In their landmark studies analyzing failure modes of 78 Utah style electrode arrays implanted in non-human primates, Barrese et al. show that 53% of chronic device failures occur due to meningeal encapsulation and ejection of devices, with more arrays displaying some degree of meningeal encapsulation [27, 113]. Similar or greater rates of this phenomena have been

observed for Utah array implants in rodent [52, 65] and cat [23] models.. Meningeal encapsulation mirrors the foreign body response to implanted devices in other non-CNS tissues, which ultimately results in fibrous encapsulation of the device [347, 348]. Interestingly, meningeal encapsulation of neural devices is prevalent for chronically implanted sub- and epidural electrocorticographic electrode grids as well [140-142, 206]. This suggests that the encapsulation response does not require traumatic penetration to proceed.

Nonetheless, several studies have also reported cellular exchange between the meningeal and intracortical compartments adjacent to penetrating electrode arrays. Suspected fibroblast migration from the meninges along the electrode shank can occur in implants that protrude through the meninges, but not in implants that are fully embedded in the cortex [70-72, 349]. A similar cell migration route may be partly responsible for the large population of blood-borne macrophage at the intracortical tissue-electrode interface. Previous studies have shown that over 60% of monocytes at the interface come from outside instead of migration of resident brain microglia [50].

The current, limited solutions for preventing meningeal encapsulation of device extend to creating physical barriers between the device and meningeal tissue [350, 351] and pharmacologically inhibiting fibroblast proliferation [352], but these solutions have not changed the narrative on meningeal encapsulation [27, 62]. To create targeted prevention and mitigation strategies for meningeal encapsulation, we must understand the triggers and control switches for the fibrous growth. In the present work, we use *in vivo* two-photon microscopy in a mouse model for chronically implanted intracranial electrodes to quantify meningeal inflammatory cell response and meningeal collagen-I remodeling over the first month post-implantation. We build on our previous results showing rapid dynamic cell behavior at the meningeal surface [62] to

define a migratory window for meningeal inflammatory cells. Over the first day after implant, meningeal inflammatory cells show rapid migration along the surface of the electrode at the meningeal-electrode interface and through pial vessels. Over the next weeks, there is low cell migration in these compartments and stable, but variable, inflammatory cell densities in the tissue surrounding the electrode. By the first month after implant, meningeal collagen doubles in thickness with or without a silicone elastomer sealant in the craniotomy. These findings ultimately suggest that there is a rapid meningeal response in the early period after implantation that may present a therapeutic window to alter the long-term outlook for meningeal encapsulation of neural electrodes arrays.

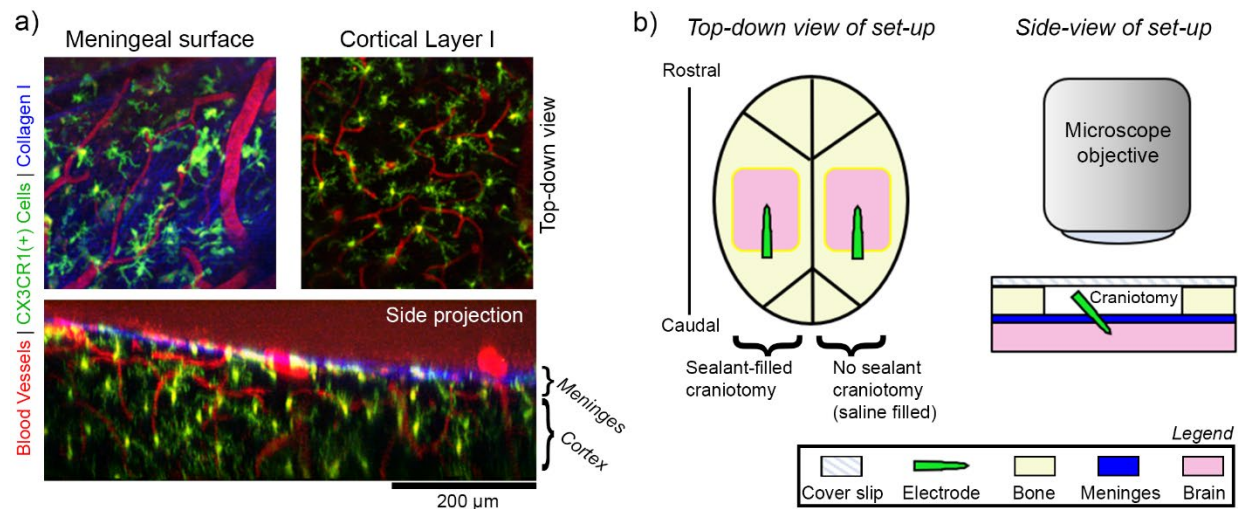


Figure 4-1 In vivo imaging of meningeal response to chronically implanted electrode arrays.

(A) Example two-photon microscope images of pre-implant meningeal biology in CX3CR1-GFP mice. Top-down images of the meninges (top left) and underlying cortex (top right) show distinct collagen I (blue), vascular (red), and CX3CR1(+) cellular morphologies (green). A side projection of the same region shows the spatial relationship between the meningeal and cortical compartments (bottom). The boundary between the meninges and cortex can be defined by the bright blue collagen trace along the surface of the brain. **(B)** Schematic of the in vivo implantation set-up. Left: Bilateral cranial windows are prepared for each mouse. Craniotomies are either filled a sealant material (silicone elastomer or PEG gel) or saline (no sealant) prior to being covered with a glass cover slip. Right: A cross-section of the set-up highlights that implants are fully underneath the glass coverslip. A two-photon microscope objective can be lowered over the glass coverslip to enable longitudinal imaging.

4.3 MATERIALS AND METHODS

4.3.1 Animals and surgery

This study used a total of 7 CX3CR1-GFP transgenic mice with GFP expression in brain microglia and macrophage as well as circulating leukocytes such as myeloid cells, NK cells, dendritic cells, and neutrophils controlled by the CX3CR1 promotor (Jackson Laboratories, Bar Harbor, ME)[353]. Implantation was based on previous surgical optimization[62]. Briefly, animals were anesthetized with 75mg/kg ketamine and 10mg/kg xylazine and head-fixed with ear bars. Animals' temperature and respiration was maintained with a heating pad and oxygen line. After cleaning with isopropyl alcohol and betadine, the animals' scalps were resected and bilateral craniotomies (~4x3mm) over visual, motor, and somatosensory cortices were drilled with a high-speed dental drill. Non-functional, 3mm single shank silicon planar electrode arrays (NeuroNexus, Ann Arbor, Michigan) were manually implanted in the center of the craniotomy (Figure 4-1B, *left*). The tab of the electrode was broken off with surgical microscissors such that the broken end was level with the top of the skull (Figure 4-1B, *right*). Craniotomies were either filled with sterile saline, *in situ* forming silicone elastomer sealant (Kwik-Sil, World Precision Instruments, Sarasota, FL), or a novel *in situ* forming hydrogel sealant (described below) and covered with a glass coverglass. The cranial window was secured with light-curable cement (Composite Flowable; Henry Schein, NY, USA), and animals were allowed to recover. All procedures and experimental protocols were approved by the University of Pittsburgh, Division of Laboratory Animal Resources and Institutional Animal Care and Use Committee in accordance with the standards for humane animal care as set by the Animal Welfare Act and the National Institutes of Health Guide for the Care and Use of Laboratory Animals.

4.3.2 Hydrogel preparation and validation

For one animal, the craniotomy was sealed with <10 μ L of a novel *in situ* forming hydrogel (referred to as PEG/PEI hydrogel). The gel was prepared by mixing 10% w/v 4-arm poly(ethylene) glycol (10 kDa, JenKem Technology USA, Plano, TX, USA) with 10% v/v branched polyethylenimine (25 kDa, Sigma-Aldrich) in a 10:1 ratio in sterile saline. The biocompatibility of the hydrogel was determined by a conditioned media study on a Highly Aggressive Proliferating Immortalized (HAPI) microglial cell line (provided by Dr. Xiaoping Hu, University of Pittsburgh) as previously described [273, 354, 355]. HAPI cells were plated in at 10⁵ cells/well in a 24-well plate. Cells were grown in control media (DMEM/F12 with 10% Fetal Bovine Serum and 1% penicillin-streptomycin, ThermoFisher Scientific) until 80% confluency. Media was replaced with either fresh control media, or control media that had been conditioned with a freshly crosslinked PEG/PEI hydrogel overnight. After 1 day of exposure, cells were stained with a Live/Dead Cell Viability Assay (ThermoFisher Scientific) and imaged with a fluorescence microscope. Cell viability was determined by comparing the area of each image occupied with live cells to the area of each image occupied with dead cells (analysis completed on the NIH software ImageJ).

4.3.3 *In vivo* two-photon imaging

At 0.5, 0.75, 1, 2, 4, 7, 14, 21, and 28 days post implant (dpi), animals were sedated with 1-1.5% isoflurane and head-fixed with ear bars for imaging. For vascular contrast, animals received intraperitoneal injections of sulforhodamine 101 (SR101) (~0.05 cc; 1 mg/ml). Animals were placed under a two-photon laser scanning microscope with a Bruker scan head (Prairie

Technologies, Madison, WI), Ti:sapphire laser tuned to 920 nm (Mai Tai DS; Spectra-Physics, Menlo Park, CA), light collection through non-descanned photomultiplier tubes (Hamamatsu Photonics KK, Hamamatsu, Shizuoka, Japan), and a 16x, 0.8 numerical aperture water immersion objective (Nikon Inc., Milville, NY) as previously described [62, 166, 177]. Laser power was maintained between 20-40 mW. All images were collected through Prairie View software. For each imaging session, “Z-stack” tissue volumes from each craniotomy (410 x 410 x 82 μ m XYZ at a resolution of 0.8 X 0.8 X 2 μ m) were scanned at 1 minute intervals (frame scan rate: 0.69Hz; line scan rate: 357 Hz) for 15-30 minutes. Additional Z-stacks were collected with filters to resolve second harmonic generation (SHG) at half the laser wavelength (~460nm), which enables intrinsic imaging of collagen-I (shown in blue in Figure 4-1A, *top left*). For a subset of animals (3 from the silicone sealant group and 2 from the saline sealant group), devices were explanted at the experimental endpoint and imaged under two-photon microscopy.

4.3.4 Non-human primate explant analysis

To compare and contrast these murine findings with higher order animals, we examined the ex vivo meningeal collagen around a 10x10 shank Utah style array (Blackrock Microsystems, Salt Lake City, UT) that had been implanted in the motor cortex of a rhesus macaque for ~2.5 years. Following transcardial perfusion with 4% paraformaldehyde, the brain was removed with the Utah array and surrounding bone left intact. After post-fixation in 10% paraformaldehyde, micro computed tomography (microCT) was performed with a multi-modal Siemens Inveon micro-CT/SPECT/PET system (Inveon, Siemens Inc., Knoxville, TN, USA) as previously described[52]. The Utah array and surrounding tissue (>5mm margin) was dissected out of the brain. Brain tissue adjacent to one side of the Utah array was sectioned away with a Vibratome

until the shanks of one edge of the device were visible. These shanks were imaged for second harmonic generation imaging as described in section 4.3.3.

4.3.5 Cell velocity analysis

CX3CR1(+) cellular element migration along the electrode's surface at the meningeal-electrode interface was estimated by a "cell migration index". First, time-series z-stacks of the silicone sealant group were preprocessed by a median filter (3x3 pixel kernel). For each time frame, images along the Z-axis were summed to project the 3D Z-stack into a single 2D plane. Motion between frames was corrected by a recursive rigid body transformation (StackReg plugin for ImageJ software[302]). A region of interest (ROI) around the meningeal-electrode interface was manually-defined based on the boundary between the electrode's surface and the SHG signal of the meningeal collagen-I. A custom Matlab script (MathWorks, Boston, MA) was used to determine the "cell migration index" for the CX3CR1(+) cellular elements in each time-series. First, to determine which pixels were part of CX3CR1(+) cellular elements, images were binarized based on an image intensity threshold (mean pixel intensity + the standard deviation of pixel intensities for each frame). The difference in number of CX3CR1(+) cellular elements within the ROI between consecutive frames was used to estimate the amount of migration during each frame. This number was normalized to the total number of CX3CR1(+) cellular elements to produce the cell migration index, where a "0" value indicates no migration and a "1" value indicates that all CX3CR1(+) cellular elements showed movement. The cell migration index was averaged across frames for each time-point to enable statistical comparisons across time-points. Four animals were used for this analysis as one animal died prematurely and two additional

animals did have a silicone sealed craniotomy. Statistical comparisons over time were performed with one-way ANOVA and Bonferonni post-tests (Matlab; significance: $p < 0.05$).

Individual cell velocities were also calculated by manual tracking at 0.5-1dpi in ImageJ. Velocities are presented as mean velocity over 5-30min windows. Cell diameters were based on the major axis of ellipses fitted to each migrating cell. Migratory direction preference was calculated by defining movement “toward interface” as negative X-direction movement and “away from the interface” as positive X-direction movement, where the X-direction is along the length of the electrode. Preference was defined by net movement/ absolute value of total movement for each cell, where a “-1” value would indicated that a cell moved exclusively toward the interface, a “+1” value would indicate that a cell moved exclusively away from the interface, and a value of “0” would indicate that the cell moved equal distance toward and away from the interface.

4.3.6 Cell density analysis

Density of meningeal CX3CR1(+) cellular elements within 100 μ m of the implanted electrode was determined for silicone sealed craniotomies over time. A custom Matlab script was used to automatically segment meningeal cells from cortical cells based on the SHG collagen-I signal. A maximum intensity projection of the SHG z-stack was used to find the Z-location with the most intensity collagen-I signal for each XY coordinates. This information was used to fit a cubic polynomial surface over the surface of the brain using the “fit” function in Matlab’s Curve Fitting Toolbox. Each fit was manually inspected. To determine meningeal density, the number of pixels with CX3CR1(+) cellular elements (defined by a threshold set to the mean pixel intensity plus the standard deviation of image intensity of the maximum intensity z-projection

image) within $\pm 10\mu\text{m}$ of the fitted meningeal surface were summed. The sample region was confined to within $100\mu\text{m}$ of the implanted electrode as defined by the distance transform (“bwdist” function in Matlab). The total area of the meningeal CX3CR1(+) signal was normalized to the total area of sampled meningeal surface. Statistical analysis of changes in density over time was carried out with a one-way ANOVA (Matlab).

4.3.7 Blood vessel trafficking analysis

To determine the extent of leukocyte trafficking through large pial vessels in silicone sealed craniotomies, vessels labeled with SR101 were first identified as either venule or arteriole by measuring vessel dilation over 0.5 to 2dpi, where venules showed $>10\mu\text{m}$ dilation as previously described [68]. A total of 3 venules and 3 arterioles over 5 animals were identified (two animals were excluded that did not have a silicone sealed craniotomy). To track the amount of cellular trafficking, images were preprocessed with a median filter (3x3 pixel kernel). The maximum intensity projection of Z-stack slices that contained the center of the pial vessels along the XY plane was taken and motion was corrected by recursive rigid body transformation (StackReg plugin for ImageJ). For image series with low SR101 leakage, vessel ROIs could be segmented by creating a binary mask of vessels in the SR101 channel 3D Z-stacks to exclude all non-vessel pixels (example images shown in Figure 4-4A, *right*). Following definition of the vessel ROIs, the CX3CR1 channel was binarized using the IsoData threshold technique[191], and the number of CX3CR1(+) cells were counted for each frame using ImageJ Particle Analysis particles (particles $<10\mu\text{m}^2$ in area were discounted as noise). The average number of CX3CR1(+) cells over each image session was quantified. The number of trafficking cells in venules and arterioles

at 0.5-1dpi and 2-4dpi were compared by two-way ANOVA with Tukey's HSD post-hoc tests (Matlab; significance: $p < 0.05$).

4.3.8 Meningeal thickness analysis

A custom Matlab script was used to automate the measurement of meningeal thickness in 3D Z-stacks with SHG images for both the silicone and saline sealed craniotomies. Following a 3D median filter (5x5x5 pixel kernel), a maximum intensity projection along the Z-axis was taken of the SHG signal. The 2D projection was used to manually defined an ROI drawn around the SHG(+) collagen-I signal surrounding the implants. The 3D z-stacks were then binarized based on a threshold of 0.5*mean pixel intensity of the maximum intensity projection ROI. Holes were filled in the binarized 3D stack with the "imfill" function in Matlab. Binarized images were manually inspected to ensure that a mask of the SHG(+) collagen-I was extracted. The thickness of the meninges was determined by taking the sum of pixels along the Z-axis at each XY location in the ROI. Sums were multiplied by Z-axis resolution (2 μ m). Any XY location in which the SHG(+) signal exceeded the depth of the Z-stack was automatically removed. To compare the thickness at 1dpi and the experimental endpoint (21-28dpi, depending on the animal) for the silicone and saline sealant groups, two-way ANOVA analysis with Tukey's HSD post-hoc tests were used (Matlab; significance: $p < 0.05$).

4.4 RESULTS

Fibrous meningeal encapsulation and ejection of chronically implanted electrode arrays is one of the most common causes for electrode recording failure. To understand the progression of meningeal inflammation that can lead to fibrous encapsulation, we implanted 7 CX3CR1-GFP mice with single shank Michigan-style silicon electrode devices and used two-photon microscopy to quantify changes in inflammatory leukocyte behavior and meningeal collagen from 12h to 28 days post implant (dpi).

4.4.1 A migratory window for rapid CX3CR1(+) cell movement along electrode shanks in the meninges

By 0.5 dpi, we noted robust migration on the implanted electrode device's surface that largely subsided by the end of the first week post implant (Figure 4-2A). Between 7-28dpi, cells on the probe appeared to aggregate and spread along the surface of the device, with unclear boundaries between cells. Due to the ambiguous boundaries of individual cells, quantification of cell movement from 0.5-28dpi relied on counting the changes in number of CX3CR1(+) pixels (determined by a threshold) during each imaging session. Electrodes implanted in craniotomies that were filled with saline became buried in tissue by 7-14dpi, and were not included in cell migration quantification (see section 4.4.5). Consistent with our qualitative assessment, there was significantly greater cell migration along the surface of the device at 0.5 - 0.75dpi compared to 4-28dpi (Figure 4-2B; one-way ANOVA $p < 0.001$; Bonferonni post-hoc tests $p < 0.05$). The shapes of 30 migrating cells from 0.5-1dpi were measured by ellipse fitting and each cell's

position was tracked for at least 5 minutes to determine cell velocity (Figure 4-2C). Due the tight clumping of cells at time points after 1dpi, it was not feasible to track cell velocities on the electrode's surface. Nonetheless, our migration index results (Figure 4-2A) suggest that there is little migration during this period. From 0.5-1 dpi, cells had a mean diameter of $10.31 \pm 3.46 \mu\text{m}$ velocity of $3.04 \pm 2.31 \mu\text{m}/\text{min}$ (mean \pm SEM), with no apparent correlation between these two parameters (linear regression $r^2 = 0.02$). These speeds are >60-fold greater than microglial cell body migration toward electrode implants at the same time points [68]. Migration direction preference was determined by normalizing the net distance traveled along the length of the implant (where “-” is toward the interface and “+” is away from the interface) to the absolute value of the total distance traveled along the length of the implant (Figure 4-2D). Individual cells show preference for going toward the interface, away from the interface, or neither, but without a discernable average preference (-0.14 ± 0.70 , mean \pm std. dev.), suggesting that cells are potentially responding to a multitude of chemotactic and other environmental cues.

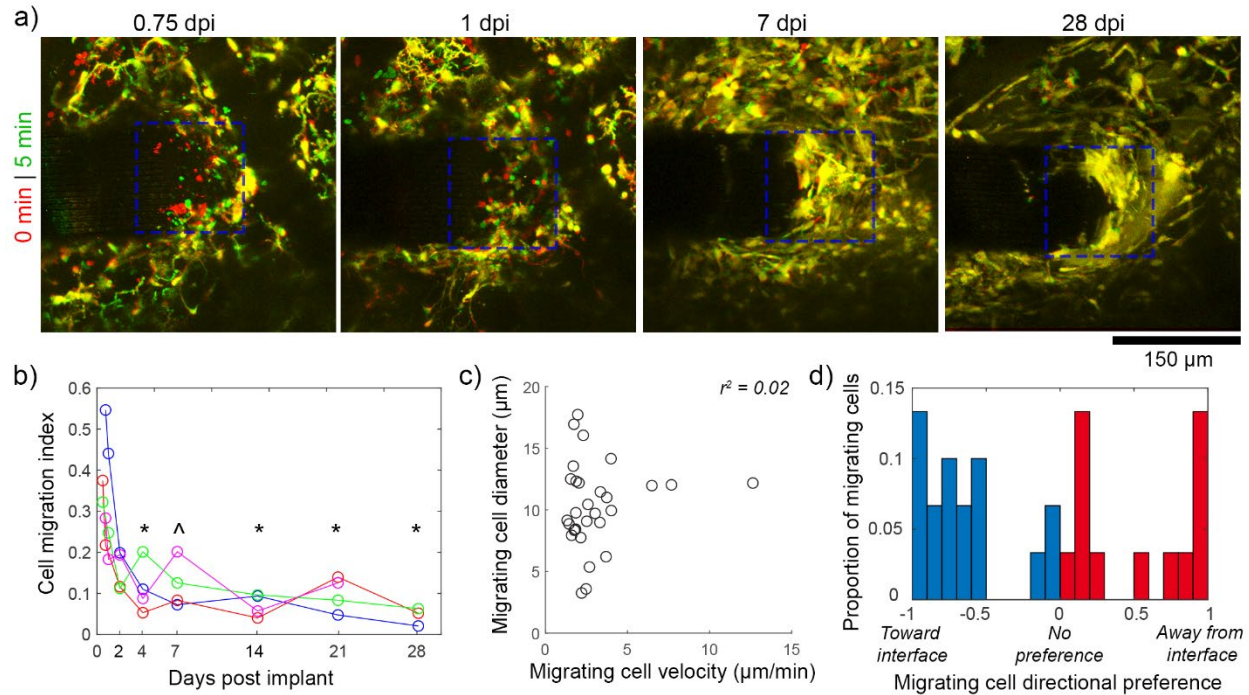


Figure 4-2 Meningeal CX3CR1(+) cells migrate along the electrode's surface during the first days post-implant.

(A) Superimposed images of the meningeal-electrode interface (ROI denoted by blue dashed box) at earlier (red) and later (green) time points show CX3CR1(+) cell movement as green and red, while stable elements are yellow. Images are tracking the same animal over time. (B) A cell migration index (fraction of cells at the meningeal-electrode interface that are moving) shows that there is significantly greater migration at 0.5-0.75 dpi compared to 4-28dpi (one-way ANOVA, $p < 0.0001$; * denotes significant differences from both 0.5 and 0.75 dpi groups with Tukey's HSD post-hoc tests, ^ denotes significance relative to 0.5 dpi only; $p < 0.05$). Each line plot represents a different animal ($n = 4$). (C) Migrating cells at 0.5-1dpi have a velocity of $3.04 \pm 2.31 \mu\text{m}/\text{min}$ and a diameter of $10.31 \pm 3.46 \mu\text{m}$ with no apparent relationship between these parameters (mean \pm st. dev.) with a linear regression R-squared value of 0.02. Individual cells displayed in graph ($n = 30$). (D) Migrating cells show no clear preference (For each cell: net movement / total distance traveled) for migrating toward (blue bars) or away from (red bars) the interface.

4.4.2 Variable meningeal CX3CR1(+) cell densities around the implant over the first month

In addition to inflammatory cell migration along the device, another critical metric to understanding meningeal-electrode interactions is inflammatory cell density changes in the meningeal tissue surrounding the implant. To cleanly differentiate meningeal inflammatory cells from brain inflammatory cells, we defined the meningeal surface by meningeal collagen-I through second harmonic generation imaging (Figure 4-3A). Cellular density in ROIs along this boundary were quantified over time for silicone filled craniotomies in four animals (Figure 4-3B). Saline filled craniotomies could not be quantified over time as electrodes became buried in meningeal tissue by 7-14dpi (see section 4.4.5.). There was some fluctuation in cell density within 100 μ m of the implant between animals and over time, but no statistically significant change in cell density (one-way ANOVA $p = .234$). The variability over time may echo the high variability of the cortical response to implanted electrodes [92].

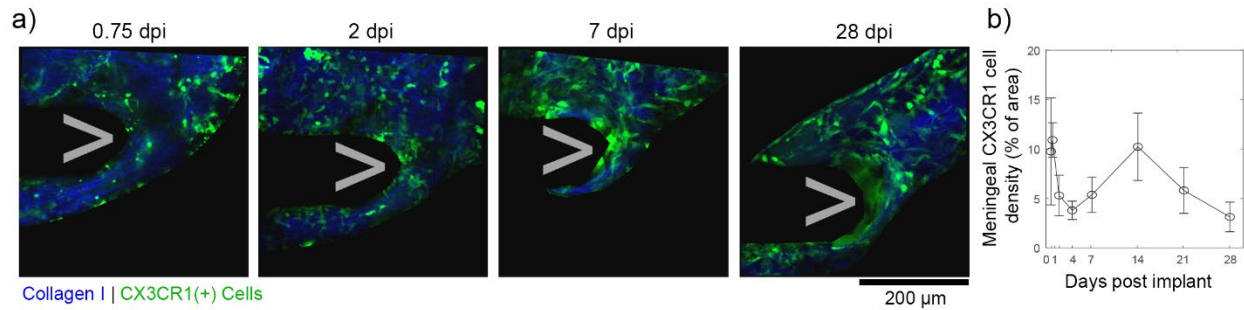


Figure 4-3 Meningeal CX3CR1(+) cell densities fluctuate, but are stable, over the first month post implant.

(A) Meningeal CX3CR1(+) cells (green) are automatically segmented from 3D image stacks if they are within or above the meninges (defined by continuous collagen I sheet; blue). These representative images track the same animal over the first month post implant. (B) The density of meningeal CX3CR1(+) cells (% of meningeal ROI that contains CX3CR1 signal) shows large fluctuations over time for each animal (Data presented as mean \pm SEM; One-way ANOVA $p > 0.05$; $n = 4$).

4.4.3 Robust CX3CR1(+) cell trafficking through venules at ≤ 1 dpi decreases by 2-4 dpi

To understand potential sources of the inflammatory cells that migrate along the surface of the device and fluctuate in the surrounding meningeal tissue, we quantified CX3CR1(+) cellular trafficking through blood vessels. Venules could be differentiated from arterioles based on a dilatory response over the first days after implantation (Figure 4-4A *left*, 4-4B) as previously described [68]. Venule dilation began to subside by 4dpi, which is consistent with other reports [160]. ROIs confined to vasculature could be defined (Figure 4-4A, *right*) and the number of CX3CR1(+) cells in these ROIs over each imaging session could be quantified by automated particle analysis. Over the first 4 days, we quantified 361 trafficking cells with a mean diameter

of $9.48 \pm 4.42 \mu\text{m}$ (mean \pm std. dev.). We noted that most detected cell trafficking was confined to venules within the first day after implantation (Figure 4-4C). Due to our relatively slow image acquisition rate (frame rate: 0.69Hz), it is likely that we only captured trafficking of leukocytes that were adhered to the surface of blood vessels [356]. In this case, the lack of leukocyte adhesion to arterioles is consistent with previous findings [357, 358]. To confirm these observations, we statistically compared the number of trafficking cells in venules and arterioles at the 0.5-1dpi period and 2-4dpi period (Figure 4-4D). There were significant effects both over time and between vessel types (two-way ANOVA: $p < 0.01$), with Tukey's post-hoc tests confirming that there were significantly more leukocytes trafficked through venules at 0.5-1dpi compared to all other groups.

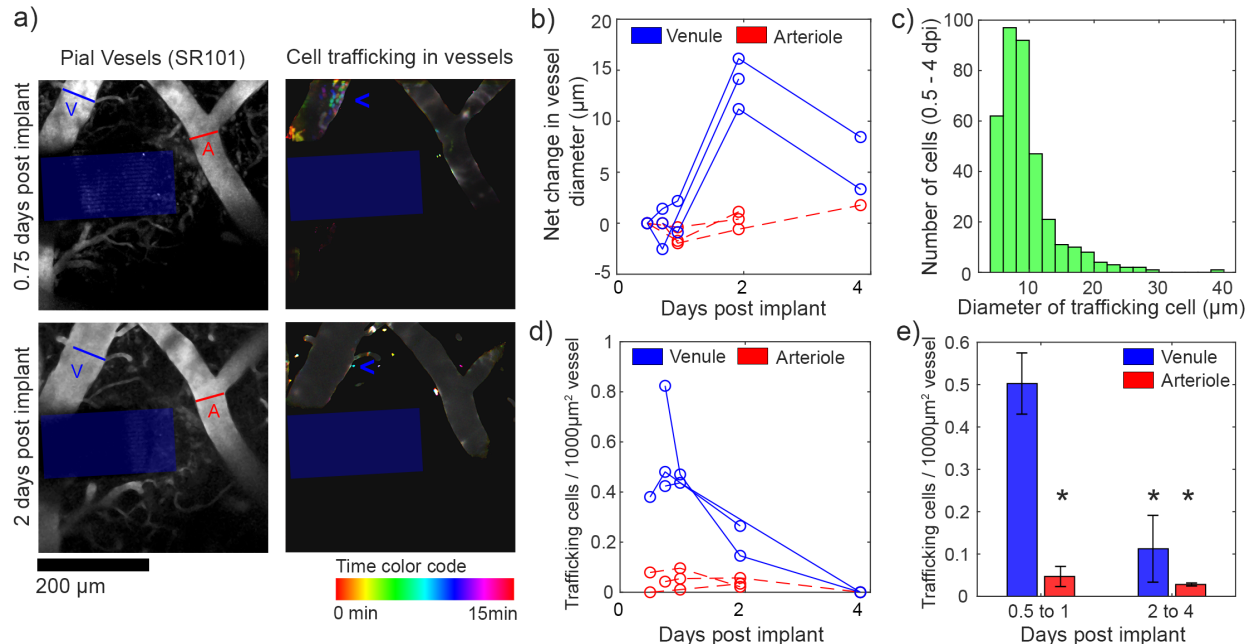


Figure 4-4 CX3CR1(+) cell trafficking through pial venules during the first 4 dpi.

(A) Left: Representative images of pial vessels labeled by SR101 at 18h (top) and 48h (bottom) post-implant adjacent to the electrode (blue box). An arteriole (red “A”) and a venule (blue “V”) were identified based on dilation response after implantation. **Right:** CX3CR1(+) cells within vessels were quantified over time. Frames over 15 minutes of imaging were superimposed, with each frame displaying a unique color defined by the “Time color code”. Cells that migrate during the course of a single frame retain the color of that frame, whereas cells that are stable over the imaging period appear as white. A region of high cell migration is seen in the venule (blue “<”) at 18h, but not at 48h. **(B)** Large pial vessel diameters (6 vessels from 5 animals) were measured over time. Vessels that showed $>10\mu\text{m}$ dilations were considered venules (blue). Each line represents an individual vessel over time. **(C)** Particle analysis of migration cells show a mean diameter of $9.48 \pm 4.42 \mu\text{m}$ (361 cells; mean \pm st. dev.). **(D)** Particle analysis detected robust migration through venules (blue), but not arterioles (red). Each line represents an individual vessel over time. **(E)** There are significantly more cells migrating through venules at 0.5 to 1 dpi compared to arterioles at the same time as well as venules and arterioles at 2 to 4 dpi (two-way ANOVA, $p < 0.01$ for main and interaction effects; * denotes significant differences from both 0.5 and 0.75 dpi groups with Tukey’s HSD post-hoc test; $p < 0.01$). Data presented as mean \pm SEM.

4.4.4 Meningeal collagen-I thickens over the first month post-implant, regardless of sealant

While CX3CR1(+) cell migration along implanted electrodes and through venules peaks within the first day after implantation, collagen-I remodeling occurred over a period of weeks (Figure 4-5A). Meningeal thickness could be quantified through automated measurements of the second harmonic signal of collagen-I (Figure 4-5B). Within 1dpi, meningeal thickness consistent between animals, regardless of the craniotomy being filled with silicone or saline (silicone: $19.36 \pm 1.4 \mu\text{m}$; saline: $19.36 \pm 1.84 \mu\text{m}$; mean \pm SEM). By the endpoint (21-28dpi), the meninges had thickened for both groups (silicone: $40.20 \pm 7.84 \mu\text{m}$; saline: $37.26 \pm 7.44 \mu\text{m}$; mean \pm SEM). In statistical comparisons, there was a statistically significant effect for time, but not craniotomy sealant for meningeal thickness (two-way ANOVA: $p < 0.01$) with statistically significant pairwise comparisons between the silicone filled craniotomies at 1dpi to both the silicone and saline filled groups at the experimental endpoint (Tukey's HSD post-hoc test: $p < 0.05$). As a note, the implants in saline filled craniotomies were buried in meningeal tissue by 7-14dpi, and so their locations could not always be identified. Meningeal thickness measurements for these animals were based on estimates of their last known location based on vascular landmarks and implant location.

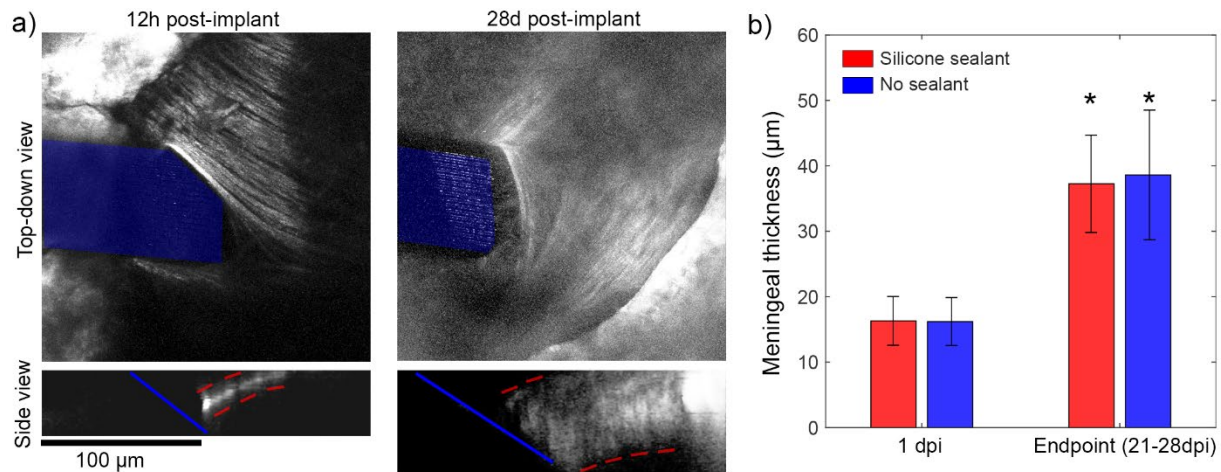


Figure 4-5 The meninges thicken over the first month post-implant.

(A) Top-down and side views of meningeal collagen I from the same animal (silicone sealant) at 12h and 28 days post implant reveals significant meningeal remodeling in the tissue surrounding the electrode (highlighted in blue). Namely, the meninges thicken over the first month (boundaries of collagen are shown by red dotted lines) (b) Automated quantification of meningeal thickness within 1 dpi and at the experimental endpoint (between 21-28 dpi) shows statistically significant elevation in meningeal thickness over time (two-way ANOVA $p < 0.01$ for time effect; * denotes significant differences from the 1dpi silicone sealant group with Tukey's HSD post hoc tests; $p < 0.05$). Sealant condition did not affect meningeal thickness over time, suggesting that the thickening was not in response to the presence of silicone.

4.4.5 Implants in saline-filled craniotomies become buried in meningeal tissue by 14dpi

In animals with saline-filled craniotomies and without the silicone sealant to fix the implant in place, electrodes were progressively buried in the meningeal tissue (Figure 4-6A). For each time-point, we determined if the meningeal-facing end of the implanted device was fully buried in

CX3CR1(+) cells or not (n = 5; Figure 4-6B). By 7-14dpi, all implants were found submerged in meningeal tissue. For some animals, we could still locate the implant after it was fully buried in tissue and confirmed that the electrode was indeed under remodeled meningeal collagen-I (Figure 4-6C). After sacrifice, we explanted devices (2 from saline filled craniotomies and 3 from silicone filled craniotomies) and qualitatively examined them with two-photon microscopy (Figure 4-6D). While it is unclear how many adherent cells were removed during the explantation process, we noted that the remaining cells had distinct morphologies between the saline and silicone craniotomies. Namely, CX3CR1(+) cells adhered to devices in silicone-filled craniotomies were larger and more densely distributed along the device than cells adhered to devices in saline-filled craniotomies. The latter devices were completely buried in tissue by 7-14dpi, and so many not have been subjected to micromotion-related strain or diffusive exchange with the meninges [349] [72].

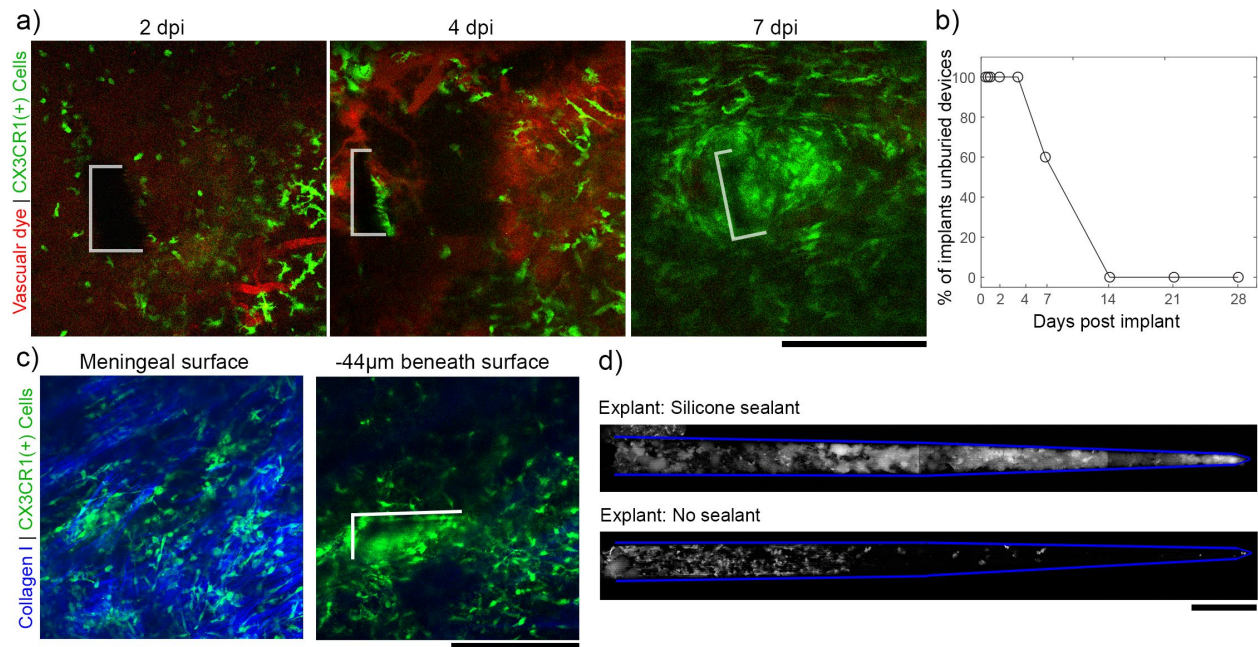


Figure 4-6 Without the silicone sealant to fix the devices in place, electrodes were buried under the meninges by 14 dpi.

(A) Representative images tracking the meningeal-electrode interface from the same animal over the first week post-implant (the electrode boundary is outlined in white). By 7 days post implant, the device is almost entirely buried in tissue. (B) For 5 devices implanted in craniotomies without silicone, 100% were completely buried in in tissue by 14 days post-implant. (C) Representative images from 21 dpi to confirm that, after being buried, electrodes are fully underneath meningeal collagen (left panel) and within the underlying cortex (right panel; the electrode is outlined in white). (D) CX3CR1(+) cells adhered to devices explanted at 28dpi from the silicone group (top) are morphologically distinct from those adhered to saline sealed devices (bottom). All scale bars are 200 μ m.

4.4.6 Material dependent response: meningeal CX3CR1(+) cells migrate within a hydrogel sealant

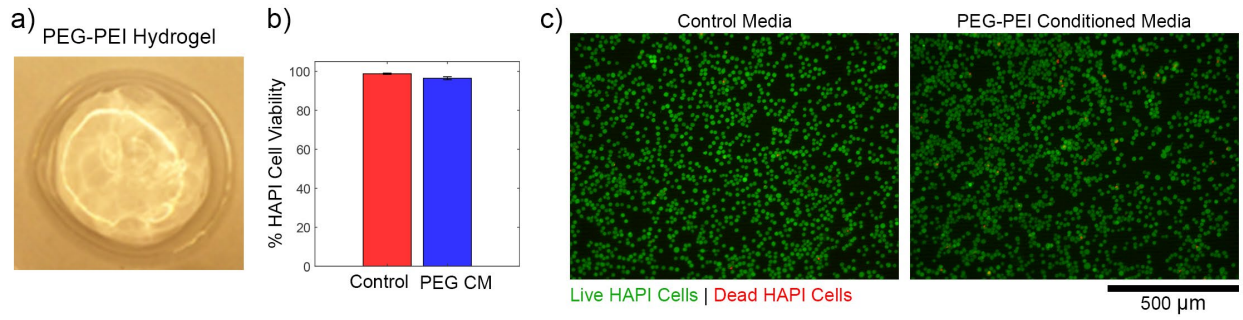


Figure 4-7 Validation of PEG/PEI hydrogel biocompatibility.

(A) Representative image of optically transparent hydrogel after cross linking. (B) Live/Dead viability assay results from HAPI cells exposed to either control media or media conditioned with PEG/PEI hydrogel over night shows no >95% survivability for both groups. Data presented as mean \pm SEM with 3 and 2 samples, respectively. (C) Representative images of live (green) and dead (red) HAPI cells exposed to control media (left) or PEG/PEI conditioned media (left).

Silicone sealants offer mechanical support to implants, but the silicone chemistry can also generate a foreign body response as previously described [62, 206]. In order to investigate how meningeal inflammatory cells interact with different materials, we filled one craniotomy with a novel *in situ* forming hydrogel composed of poly(ethylene) glycol and polyethyleneimine (PEG/PEI gel). The gel showed no significant cytotoxicity issues *in vitro* (Figure 4-7). *In vivo*, meningeal CX3CR1(+) cells showed robust migration within the hydrogel matrix, which was not observed with the silicone sealant (Figure 4-8A, migrating cells denoted by white “*”). Side projection images of this craniotomy confirm that cell migration is occurring within the PEG/PEI

gel (Figure 4-8B). These side projection also confirm that there is not a significant degree of swelling for this gel as compared to previous reports 30% PEG/PEG cross-linked gels [62]. The size and velocity of cells migrating through the gel between 1-14dpi were quantified (Figure 4-8C-D). Cells appear to have slightly elevated velocity compared to cell migration along the electrode's surface at 0.5-1dpi, but similar diameter (Figure 4-2C).

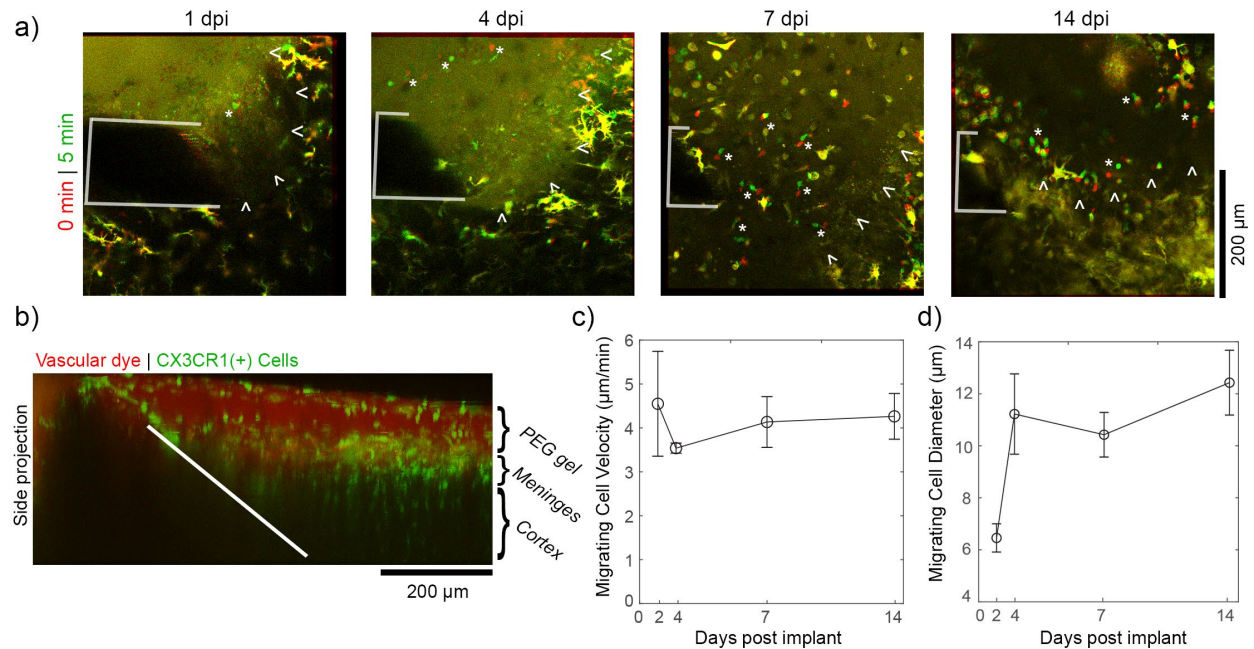


Figure 4-8 *In situ* forming PEG/PEI hydrogels elicit a unique meningeal inflammatory response.

(A) Meningeal CX3CR1(+) cells show robust migration through the PEG/PEI gel for at least 1 to 14 days post implant. Superimposed images at earlier time points (red) and later timepoints (green) show migrating cells as distinct red and green elements (denoted by white “*”), while stable elements are in yellow. The electrode is outlined in white. The boundary between the meninges and the hydrogel is denoted by white arrowheads.

(B) Side projections of the PEG/PEI sealant *in vivo* at 7 days post implant confirms that meningeal CX3CR1(+) cells (green) are within the hydrogel.

(C) The velocity of cells migrating within the PEG/PEI gel are stable over 14 days.

(D) The diameter of cells migrating within the PEG/PEI may increase after implantation (3-5 cells per time point, data presented as mean ± SEM).

4.5 DISCUSSION

4.5.1 The meningeal inflammation timeline

A critical step in designing prevention and mitigation strategies for meningeal encapsulation is to understand its time course and progression. We used in vivo microscopy to track both CX3CR1(+) meningeal inflammatory cell dynamics as well as meningeal tissue growth. We show that there is a meningeal reaction to implanted electrodes within the first hours after implantation. This initial reaction consists of rapid cell migration along the surface of the device, as well as cell migration through or along the inner wall of pial venules. Meningeal cell migration speeds along the electrode are >60X faster than microglial migration rates toward the probe, potentially providing a fast attack mechanism to the implant [68]. This is not surprising, as cell migration along a planar surface (such as the meninges) can proceed at much faster rates than through a volume (such as the brain parenchyma)[359]. Interestingly, this migration is transient, and drastically decreases after the first day post-implant. Others have reported that leukocyte migration through venules occurs within the first hour after cortical injury [358]. While their work did not follow leukocyte migration past 16h post-implant, a separate study found that there are normal levels of circulating leukocyte counts by 2 weeks after intracortical electrode implantation, but it is unclear how much earlier normalization could have occurred [50]. This early migratory window likely represents inflammatory mobilization to the craniotomy and implant site as the initiation of wound healing [132]. It is also possible that some of the cells migrating along the electrode's surface are entering the brain. Ravikumar et al., have reported that by 2 weeks post implant, over 60% of macrophage at the intracortical tissue-electrode interface are from peripheral sources [50]. Future studies should focus on determining if the

migrating cell population identified in the current study is contributing to intracortical macrophage aggregation.

While the initial migratory window subsided within the first day after implant, meningeal inflammation continued to progress over the next weeks. We observed stable, but variable, cell densities in the meningeal tissue surrounding the device throughout the implantation period. The high variability may be on account to variable vascular damage due to implantation [37]. While we did note variable amounts of vascular dye leakage after implantation, we were unable to clearly visualize vascular damage around the implant due to lack of dye perfusion into damaged vessels. There was consistent remodeling of the meninges over the first 2 weeks. Implants in craniotomies with silicone sealant were held in place and remained protruding through the meninges for the duration of the experiment. This was not the case for implants in craniotomies without a silicone sealant to fix the implants in place. These implants were encapsulated and buried in CX3CR1(+) cells by 7-14 days post-implant. It is unclear whether this is due to meningeal cell proliferation, sinking of the brain's surface after surgical edema subsided, or both. Nonetheless, this finding draws concern for probe migration for floating or anchored electrodes that are not fixed in place.

By one month post-implant, the meningeal collagen-I tissue had doubled in thickness for craniotomies with and without a silicone sealant. This is roughly on par with the time course of encapsulation and ejection of 4x4 Utah arrays in rats, which can happen within 3 months post-implant [52, 65]. In the present study, we show that fibrous tissue growth and meningeal thickening occurs between 1 and 28 dpi, which is after peak inflammatory cell invasion and adhesion to the electrode shan. Interestingly, macrophage presence on foreign bodies is a necessary precursor to fibrous encapsulation [145]. While CX3CR1-GFP expresses in multiple

cell types (macrophage, NK cells, dendritic cells, and neutrophils), the immobile, irregularly shaped cells at the meningeal-electrode interface by 7dpi are morphologically consistent with Iba-1(+) macrophage found on foreign bodies in the meninges [62, 206]. This may suggest that the inflammatory immobilization during the migratory window is instrumental for the meningeal thickening observed at later time points.

4.5.2 Disambiguating effects of implant, sealant, and craniotomy

During the migratory window in the first days after implantation, the electrode is targeted by meningeal inflammation. The craniotomy may be an underappreciated contributor to the inflammatory response when compared to the implantation injury and the foreign body response. It is possible that the electrode is merely a bystander during the broader wound healing response of bone healing. In support of this, craniotomy alone has been implicated in cognitive impairment as well as transient elevation of inflammatory cytokines, astrocyte markers, phagocytosis markers, and antigen presenting cells to a similar degree as traumatic brain injury in a mouse model [360-362]. Craniotomy can also lead to significant meningeal thickening in both rabbit and dog models [137, 138]. These effects can also be modulated by the size of the craniotomy [363, 364]. In aggregate, these studies may implicate craniotomy as a trigger for meningeal encapsulation. Future studies can probe this by examining meningeal encapsulation in craniotomies of varying sizes or by allowing the craniotomy to heal to before device implantation.

Surgical preparation may also have an impact on the formation of fibrous tissue. In this study as in other mouse studies, the electrode was implanted through the very thin dura (~20 μm

thick, see Figure 4-5) [20]. Larger animals typically have thicker dura (>300 μm in rhesus macaque) that is typically reflected prior to insertion and then sutured back in place [27, 206]. This additional intervention in the meninges may lead to exacerbated meningeal encapsulation as hemorrhage [133, 134] and mechanical trauma [132] in the meninges are both known to increase inflammatory mobilization and collagen synthesis within the meninges. Despite this, epi-durally implanted ECoG grids also generate a significant encapsulation response, suggesting that the effects from craniotomy and/or chronic foreign body placement are sufficient to generate a response [140, 141].

We have also previously noted that the silicone sealant material can generate its own foreign body response [62]. We controlled for this by tracking meningeal thickness in a cohort of implantations into craniotomies with no sealant. There were similar levels meningeal thickening with or without the sealant. Without the sealant to fix the implant in place, however, the device became buried in meningeal tissue. As an alternative to a “no-sealant” condition, choosing a different sealant or dural graft material can impact the degree of fibrotic response [137, 138, 365]. We examined the meningeal inflammatory response to a novel non-degradable PEG/PEI gel that is similar to commercially available resorbable PEG-based gels [138, 139]. The PEG/PEI gel had rapid inflammatory cell infiltration within the gel, which was not observed in the silicone sealant. This may be due to the hydrophilicity and high pore size of low-molecular weight PEG-based hydrogels, which promotes infiltration [366]. Previous reports have shown that cellular infiltration may promote more rapid wound healing, but it is unclear how rapid wound healing would interact with meningeal encapsulation of neural implants [367]. Future studies should explore this, as well as optimizing pore size, hydrophilicity, and degradation to identify a superior sealant material [368, 369].

4.5.3 Relevance for fibrous implant ejection in higher order animals

These results show that there is a consistent meningeal response in the first month of implantation for mice. There is a similarly consistent, fibrous reaction to implants in rats and cats [23, 52, 65]. In non-human primates, however, there are no studies that track progression of meningeal encapsulation, only reports on when devices have failed from meningeal encapsulation (21-261 days post implant for 9 devices) [27, 113]. It is likely that there is progressive increase of encapsulation leading to that failure point. Electrical impedance spectroscopy may provide some *in vivo* monitoring of encapsulation. Some groups have reported trends of decreasing electrical impedance for Utah style electrodes that are encapsulated and ejected from the brain [52, 113]. This may be due to the cone-shape of the Utah array shank. As the electrode site is pushed up through the cone-shaped tract, there would be an increasing gap between the electrode surface and the surrounding tissue that could lead to lower impedance. Decreasing impedance could also be explained by electrode insulation delamination, and so cannot be considered a unique signature for meningeal encapsulation and ejection [49, 52].

The meningeal thickening observed in the current study appears to be uniform throughout the craniotomy. In 10x10 Utah arrays in non-human primates, fibrous growth appears to tightly conform to the device platform and shanks (NHP at 2.5 years post-implant: Figure 4-9) [113]. The discrepancy between these encapsulation patterns may be due to the 2D platform that is present on the Utah array. The presence of a large 2D platform without penetrating shanks—such as an ECoG grid—is sufficient to elicit a meningeal encapsulation response [140-142, 206]. Notably, in the Utah array, the gold wire that bridge the connector and the platform are potted with medical-grade silicone, and may generate a similar meningeal reaction as the silicone sealant [62] or silicone platform ECoG grids [142, 206]. To interrogate the role of the platform

footprint and material as well as the non-human primate meningeal response, controlled histological studies with discrete end-points should be conducted.

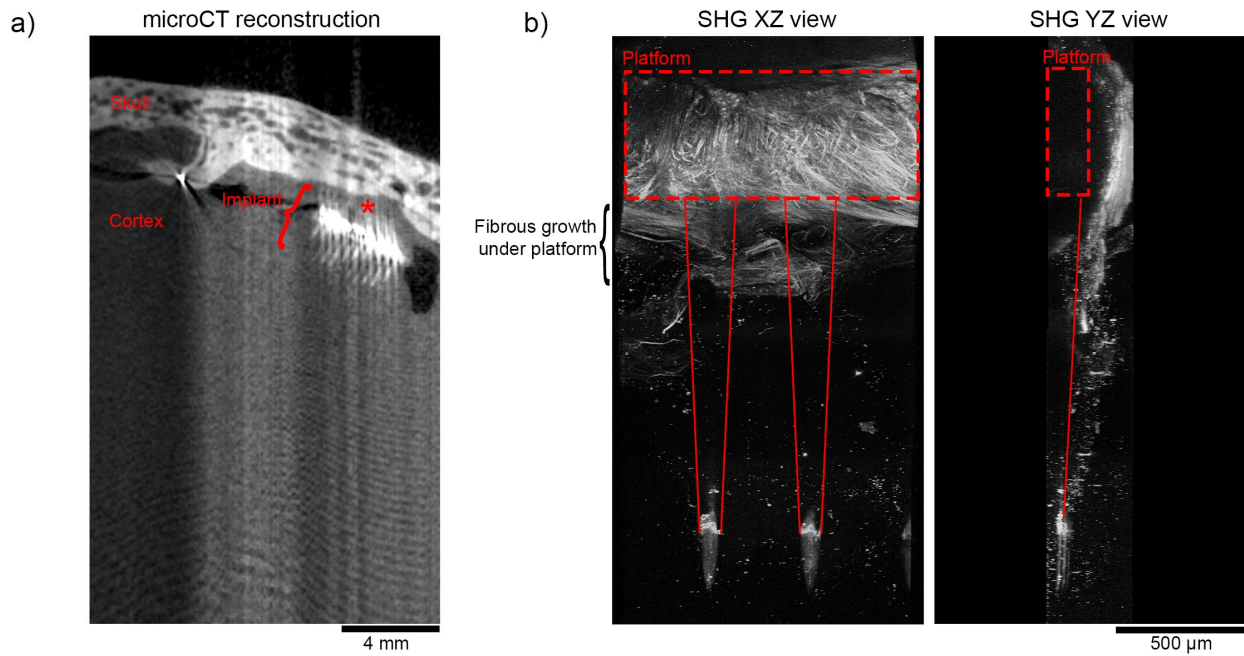


Figure 4-9 *Ex vivo* imaging of fibrous encapsulation of Utah array platform implanted in a rhesus macaque for 2.5 years.

(A) MicroCT reconstruction of the cortex and skull surrounding the implanted Utah array suggests that the array is still within the brain. Notably, soft tissues such as brain parenchyma and collagen I do not have sufficient contrast to be segmented in these images. Thick meningeal tissue is found above the device (red “*”). Optical aberrations are due to a metal artifact caused by the gold wiring at the array’s platform. (B) Second harmonic imaging along the length of shanks shows significant fibrous collagen growth around the platform of the device (red dotted box). Importantly, The XZ plane image (left) shows that the fibrous growth extends beyond the platform to the shanks (outlined by solid red lines). A YZ side view (right) shows that that the meningeal collagen I has remodeled to curve around the device’s platform.

4.5.4 Mitigation strategies and future directions

Preventing meningeal fibrosis is a major obstacle to wide-spread translation of brain-computer interface technologies. We have shown that there is a migratory window in the first days after implant that precedes meningeal fibrosis. One way to elucidate the relationship between these phenomena is to modulate that initial migratory window. Roth et al. have shown that anti-inflammatory therapeutics as well as purinergic signaling inhibitors are viable routes to modulate acute meningeal inflammation [132]. Cell adhesion to the electrode shanks, electrode array platforms, and dural sealants and grafts may also serve as a critical precursor to encapsulation. Macrophage and fibroblast adhesion to substrates can be modulated by surface treatments of L1 cell adhesion molecule [95, 104, 105, 108, 177] as well as different polymeric surfaces [370]. Inflammatory macrophage behavior can also be modulated with controlled-drug release from meningeal-interfacing domains of implants (see Appendix A.1.2) [233, 234, 271, 277, 352, 371]. Anti-fibrotic medication may also be a viable target [372].

On a macroscale, the surgical preparation and device design may also have critical repercussions for meningeal inflammation and encapsulation. The precision and size of craniotomies affects the amount of post-operative inflammation [361, 363] and choice of dural repair method and material can have an impact on the amount of meningeal fibrosis [137, 365]. To our knowledge, there have been no controlled optimization studies for these parameters. The presence of a 2D platform in the meninges may also govern the fibrotic response. Advances in ECoG devices can be emulated to pursue mesh style platforms [140] and flexible platforms [373-375] to reduce meningeal encapsulation of neural electrodes.

4.6 CONCLUSIONS

With cell migration speeds 60X faster than the cortex, the meningeal response to implanted electrode devices may be a “fast attack” mechanism. A transient, migratory window of cell infiltration to the electrode precedes meningeal thickening at later timepoints. This migratory window may provide a critical therapeutic target for reducing long-term meningeal encapsulation.

4.7 ACKNOWLEDGMENTS

This project was financially supported by NIH NINDS (Grant R01NS062019, R01NS094396, R01NS089688, R01NS094404). The authors thank Dr. Yijen Wu, director of the Animal Imaging Core at Rangos Research Center at Children's Hospital of Pittsburgh of UPMC, for assistance in microCT imaging.

5.0 HISTOLOGICAL EVALUATION OF A CHRONICALLY-IMPLANTED ELECTROCORTICOGRAPHIC ELECTRODE GRID IN A NON-HUMAN PRIMATE

5.1 NOTE ON AUTHORSHIP

This chapter is adapted from a published manuscript [206]. The work was completed as a collaboration between multiple laboratories, with primary authorship shared between James R. Eles and Alan D. Degenhart. James R. Eles led post-mortem histological and explant electrochemical data collection and analysis while Alan D. Degenhart led *in vivo* electrophysiological data collection and analysis. All work was completed with contributions from X. Tracy Cui, Aaron P. Batista, Wei Wang, Richard Dum, Jessica L. Mischel, Ivan Smalianchuk, Bridget Endler, Robin C. Ashmore, Elizabeth C. Tyler-Kabara, and Nicholas G. Hatsopoulos.

5.2 ABSTRACT

Electrocorticography (ECoG), used as a neural recording modality for brain-computer interfaces (BCIs), potentially allows for field potentials to be recorded from the surface of the cerebral cortex for long durations without suffering the host-tissue reaction to the extent that it is common with intracortical microelectrodes. Though the stability of signals obtained from chronically-

implanted ECoG electrodes has begun receiving attention, to date little work has characterized the effects of long-term implantation of ECoG electrodes on underlying cortical tissue. We implanted a high-density ECoG electrode grid subdurally over cortical motor areas of a Rhesus macaque for 666 days. Histological analysis revealed minimal damage to the cortex underneath the implant, though the grid itself was encapsulated in collagenous tissue. We observed macrophages and foreign body giant cells at the tissue-array interface, indicative of a stereotypical foreign body response. Despite this encapsulation, we recorded reach-related neural activity sessions 562 days post-implantation. These results suggest that ECoG may indeed provide a means by which stable chronic cortical recordings can be obtained with comparatively little tissue damage, facilitating the development of clinically-viable brain-computer interface systems.

5.3 INTRODUCTION

Brain-computer interfaces (BCIs) use cortical signals to directly control external devices for restoration of motor function in individuals with disabilities [12, 376-378]. A critical component of a BCI system is the neural recording modality used to extract meaningful information from the brain. The primary modalities used in clinical BCI systems, in order of spatial scale, are electroencephalography, electrocorticography (ECoG), local field potential, and single/multi-unit activity. These methods can be characterized by factors such as performance, decoding stability, longevity, and invasiveness. The choice of a neural recording modality for a particular BCI application must appropriately weigh these factors.

Penetrating intracortical electrode arrays offer the highest spatial and temporal resolution in neural recording. However, the implantation of these arrays inevitably disrupts brain tissue and vasculature, and leads to a chronic inflammatory response hallmarked by an aggregation of astrocytes and microglia in a glial scar around the probe, as well as progressive neuronal degeneration at the vicinity of the implanted electrodes [35, 54, 379]. This ultimately leads to recorded signal deterioration, manifested as a reduction in the number of electrodes recording individual neurons, or as a decrease in signal amplitude [8, 11, 12, 25, 27, 167, 376, 380]. Further, meningeal tissue proliferation and fibrous encapsulation have the potential to dislodge the implanted intracortical devices [27].

ECoG is a recording modality where electrodes are placed either subdurally (below the dura) or epidurally (on the surface of the dura) to record electrical field potentials generated by aggregate cortical activity. Since ECoG arrays do not penetrate the cortex, they avoid blood-brain barrier disruption and mechanical strain between the brittle electrode and soft neural tissue, which are common for intracortical electrodes. This potentially mitigates some inflammatory burden on the brain. ECoG signals have been found to encode information about arm and hand movements [9, 242, 381-392], as well as auditory [393, 394], visual [395], language [383, 396-399], and attentional processes [400-402]. Encouraged by these findings, researchers have begun to investigate ECoG as a potential source of control signals for BCI devices. Human and non-human primate subjects have controlled up to three-dimensional movement of cursors or a prosthetic limb [381, 382, 403-407].

Despite the promise of ECoG in BCI and neuroscience applications, very few studies have evaluated the long-term host-tissue response to either epidural or subdural grids. In humans and non-human primates, subdural and epidural arrays have been implanted for over one year

with viable neural recording, however these studies did not report end-term tissue health [391, 408]. Additionally, electrode grids are frequently implanted subdurally for up to 30 days in humans for purposes of epilepsy monitoring. While limited incidents of bleeding, infection, infarction, and functional deficits have been reported in association with these implants, no macroscopic fibrotic growth has been reported in otherwise uncomplicated surgeries [409-411]. Some longer-term studies (> 1 year) of sub-dural spinal and cortical stimulators and probes reported encapsulation or dural thickening in the vicinity of the implants [412-415]. In rats, just one week after an epidural implantation, connective tissue overgrowth was observed [140, 141]. These studies followed tissue growth around epidural ECoG grids implanted in rats for up to 419 days, showing dural thickening under the arrays and tissue encapsulation over the top of the array as early as one month following implantation [140]. These findings are corroborated by findings of dural thickening at 6 months post subdural implant. Tissue proliferation was correlated with a rise in 1kHz electrical impedance as early as 1 week, with stabilization at 18 weeks post implant [142]. This would presumably reduce the quality of any neural signal recorded by the ECoG array, though no study has correlated long-term tissue reaction with neural signal quality. While Schendel et al. and Henle et al. investigated possible glial reaction to epidural and subdural implantation in the superficial layers of cortex, few studies explore the impact of subdural grids on deeper layers of the cortical tissue, particularly on neuronal health.

The current study explores the host-tissue response to a subdural ECoG grid implanted for 666 days, focusing on both cortical tissue health as well as fibrosis at the implant site, while also validating device performance by recording reach-related neural activity. We found that cortical thickness and neuronal density was unaffected by array implantation. While microglial density was increased in superficial cortical layers, they were in a resting morphology, and

astrocyte activation was consistent with tissue not under the implant. The grid itself was encapsulated in a fibrous envelope, though it was still able to record reach-related neural activity 562 days post-implantation.

5.4 MATERIALS AND METHODS

All experimental procedures were approved by the Institutional Animal Care and Use Committee of the University of Pittsburgh and were in accordance with the National Institutes of Health's Guidelines for the Care and Use of Laboratory Animals.

5.4.1 ECoG grid implantation surgery

An adult male Rhesus monkey (*macaca mulatta*) was anesthetized, and a craniotomy was performed to expose the left motor and premotor cortex. The dura was retracted to expose an area approximately 2x2 cm between the arcuate and central sulci. A custom-built 15-channel, 1.01 mm thick silicone ECoG grid with 2mm (diameter) platinum electrode sites (Figure 5-1A, PMT Corp, Chanhassen, MN, USA) was placed directly on the exposed brain surface (Figure 5-1B-C). The material composition and sizing of this device is comparable to FDA approved devices commonly used in the clinic. After positioning was confirmed, the dura and the bone were reapproximated. Wires from the grid were connected to a Cereport pedestal connector (Blackrock Microsystems, Salt Lake City, UT, USA) affixed to the skull.

5.4.2 Neural recording and task control

Signals from the ECoG grid were recorded with a g.USBamp Biosignal Amplifier (g.tec Medical Engineering), and sampled at 1200 Hz. All recording, online processing, task control and presentation was performed using the Craniux Brain Computer Interface system [416]. Dura-facing electrodes 4 and 13 were used as reference and ground electrodes, respectively, for all recordings (Figure 5-1A). Visual stimuli were presented on a 22-inch computer monitor placed approximately 0.8 meters from the monkey.

5.4.3 Hand control task

In order to validate device performance and ECoG signal modulation at long-term time points, we analyzed data from all available behavior task sessions (15 sessions from day 542 to day 562 post-implant). This task was a standard center-out reaching task. During these experiments, the animal performed a standard 2D center-out task in a virtual environment, with the position of the hand controlling the location of a computer cursor in a two-dimensional plane. Hand position was tracked in real-time using an optical tracking system (Phasespace, San Leandro, CA) and rendered on a computer screen as a sphere in a virtual workspace. Trials began with the appearance of the cursor and central target; the animal was then required to move the cursor to the central target, and hold it there for 400–600 ms. One of eight peripheral targets would then appear, to which the animal was required to reach. A target hold time of 200 ms was enforced. The animal was provided a water reward immediately following successful completion of a trial.

Prior to offline analysis, hand control trials were visually examined for artifacts in both the time and time-frequency domains; all trials exhibiting artifacts during the central hold or

target acquisition periods were excluded from further analysis. These artifacts were characterized by large-amplitude, broadband transients across the majority of recording electrodes are believed to be the result of jaw movements based on their consistent appearance during the reward period of each trial. Time domain data from the remaining trials were transformed into the time-frequency domain using the Burg autoregressive method (0 - 200Hz range, 2Hz frequency bands, 100th order, 100ms non-causal window, 33ms step size), log-transformed, then normalized to pseudo Z-scores relative to the spectral power during the central target hold period. Trials were then manually aligned to movement onset using the cursor speed profile for each trial.

5.4.4 Electrical impedance measurement

Electrode impedances were measured both over the course of electrode implantation (in-vivo) and after explantation (ex-vivo). Impedance was measured at 20Hz using the g.USBamp biosignal amplifier (g.tec Medical Engineering). Two separate measurement configurations were used. In-vivo impedance measurements were made with respect to the recording ground and reference (electrodes e4 and e13, respectively), which were internally shorted together by the amplifier. After explantation of the electrode grid, ex-vivo impedance was measured in saline with two separate ground and reference configurations: electrode e4 (reference) and electrode e13 (ground), and a calomel electrode (reference) and a platinum sheet (ground). The first configuration attempted to mimic in-vivo impedance measurements as closely as possible, while the second configuration was used to measure the impedance of the encapsulating tissue. For both ex-vivo configurations, impedance was measured with the grid in the encapsulating tissue envelope and after removal from the encapsulation. Analysis of impedance measurements were

restricted to those 2mm-diameter electrodes which retained electrical connectivity throughout the course of the experiment.

5.4.5 RMS amplitude analysis

To assess changes in electrophysiological recordings over the course of the study, root-mean-squared (RMS) amplitudes were calculated for selected datasets. For each dataset analyzed, 10-minute long segments at the beginning of the recording session were inspected for the presence of movement artifacts; these were excluded from subsequent analyses. ECoG signals were then re-referenced with respect to the common-mode average, notch-filtered to remove power-line contamination, segmented into 1-second epochs, and band-pass filtered in 5Hz frequency bands over the 5Hz-195Hz range using 4th-order Butterworth filters. RMS values were computed for the resultant band-pass-filtered segments for each frequency band.

5.4.6 Explant

Electrodes remained implanted for a total of 666 days, after which the animal was sacrificed and the electrode grid removed. Surgical complications unrelated to the ECoG grid negated the possibility of perfusing the animal before removing the brain. After exposure of the skull, the original bone flap was removed to expose the dura. The skull proximal to the connector, the dura, and the encapsulated electrode grid were then removed as a single piece and the entire brain was extracted. The brain and the encapsulated array were then placed in a 10% formalin + 10% glycerin solution for 8 days followed by 10% formalin + 20% glycerin for 26 days to fixate the tissue. The brain was bisected along the midline and 3D renderings of each hemisphere were

generated with a 3D scanner (Faro Platinum Arm, Faro). Surface topography of the implanted hemisphere was quantitatively compared to the mirror image of the non-implanted hemisphere using Geomagic Studio (Geomagic). Fixated tissue was then frozen and sectioned into 50 μ m sections for staining. Sections were cut perpendicular to the central sulcus. The electrode grid was carefully removed from the encapsulation “envelope,” which was similarly fixed for 6 days and then stored in phosphate tris azide (PTA) solution until it was cut into 50 μ m sections for staining. Encapsulation tissue was cut perpendicular to the placement of the grid.

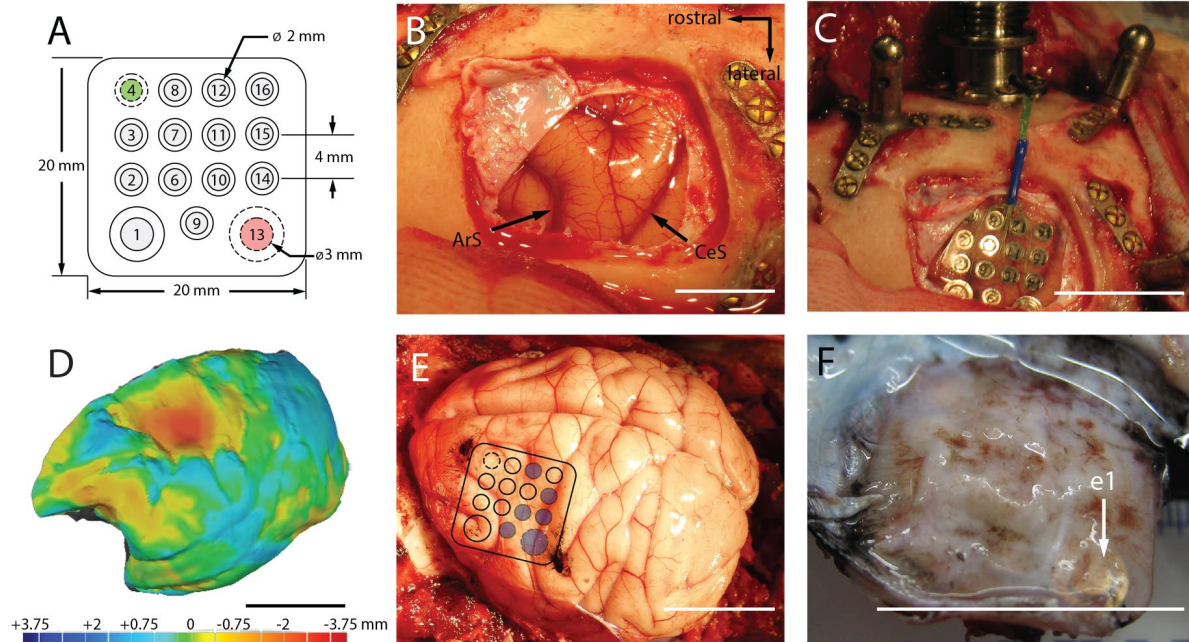


Figure 5-1 Gross anatomical disposition at implant and explant.

(A) Top view of the electrode grid. The neural recording electrodes (gray) face the cortical surface. The reference (#4, green) and ground (#13, red) electrodes face the dura. (B) Exposure of the left motor cortex prior to implantation (ArS: arcuate sulcus, CeS: central sulcus). (C) Placement of the electrode grid. (D) 3D rendering of the left-hemisphere superimposed on the mirror image of the right-hemisphere. Heat map denotes difference in surface topography between hemispheres in mm. (E) ECoG grid location superimposed on the postmortem brain. Blue circles indicate electrode sites targeted for histological analysis. Black ink marks the observed location of the rostral-medial and caudal-lateral corners of the grid. (F) Underside of the encapsulated grid following explantation. The location of electrode 1 (e1) is indicated by the white arrow. All scale bars are approximately 2cm unless otherwise indicated.

5.4.7 Immunohistochemistry

Cortical sections from implanted (left) and non-implanted (control, right) hemispheres were mounted on the same slide for comparison, and all slides were processed in the same session to minimize variability. A sample of dura mater distant from the edges of the tissue encapsulation (> 2cm) served as control dura mater for analysis of the encapsulation tissue.

Antibodies for cortical tissue were directed to neurons (NeuN, 1:200, Millipore), astrocytes (GFAP, 1:200, SeroTec), or microglia (Iba-1, 1:500, Fisher); antibodies for encapsulation/dura mater tissue were directed to macrophages (Iba-1, 1:500, Fisher) or fibroblasts/macrophages (Vimentin, 1:250, Millipore). Tissue was first blocked for 30 minutes in sodium citrate buffer (0.1M citric acid, 0.1M sodium citrate, pH 6.0) in room temperature followed by a peroxidase block (10% methanol, 3% hydrogen peroxide) for 20 minutes in room temperature on a shaker. Then, tissue was blocked in a serum containing blocking buffer (5% normal goat serum, Jackson Labs; 0.1% Triton X-100, Sigma) for one hour. Tissue was incubated in primary antibody for 12-24 hours. Following washes in phosphate buffer saline (PBS), tissue was incubated in 1:250 Alexa Fluor 488 and/or 633 (Invitrogen) for 2 hours in room temperature, followed by more PBS washes, 10 minute incubation in Hoescht 33342 (1 μ L/1mL; Invitrogen) stain, PBS washes, and coverslips were mounted with Fluoromount-G (Southern-Biotech).

5.4.8 Confocal imaging

All confocal imaging was performed with an Olympus Fluoview 1000 confocal scanning microscope. All images were taken with a 20X or 40X objective to optimize cellular resolution and image frame size. Images were taken at multiple focal depths for each frame in order to image the full depth of a tissue slice. This ensured that image analysis was not biased by choice of a single image depth. Confocal laser power, photomultiplier tube voltage (the sensitivity of the image detector), and photomultiplier offset (background level of image detector) were selected to ensure that image pixels did not exceed upper or lower detection limits. Images (n = 5 tissue sections per stain) were collected from cortical regions directly under electrode sites in Brodmann Area 4 (specific sites denoted by blue circles in Figure 5-1E) on the ECoG array or from the thickest region of both the dorsal and ventral sides of the center of the tissue encapsulation. Images collected were only discounted from analysis on grounds of poor quality of signal, photobleaching, or severe tissue tears during processing. For cortical tissue imaging, images from the contralateral hemisphere were collected for comparison. Images were matched to the same sagittal slice depth and anterior-posterior region of interest as the ipsilateral hemisphere. Tissue encapsulation images were compared to images from random regions of interest of control dura mater retrieved from > 2cm from the tissue encapsulation.

To determine cortical layers and cortical thickness, disconnected images of cortex were stitched to create continuous high-resolution images of the entire cortical depth using Fiji, an Image-J (NIH) plug-in [417]. Layers I/II-III were discerned from layer V by the location of layer V giant pyramidal cells [418]. Stitched images were used to measure cortical depth (n = 5) between conditions. Neuronal and microglial cell densities were determined for layers I/II-III and V with manual counting facilitated by Image J Cell Counter (n = 5). Layer I microglia

morphology was assessed as previously described [40, 149, 151]. Microglia were deemed to be ‘Unresponsive’ if they were ramified (resting) or activated but not extending processes to the cortical surface, and ‘Surface Directed’ if they had activated or amoeboid morphology, with processes extended to or along the cortical surface. Because GFAP labels extensive networks of astrocytic processes, discerning individual cell bodies for cell counting was inconclusive. Instead, the proportion of cortex occupied by reactive astrocytic signal (% GFAP signal) was determined by first setting a pixel intensity threshold to the mean pixel value of layer I/II-III, where the most intense signal was localized. Because the majority of pixels in a given image are not GFAP-signal, the pixels below the mean can be discounted as noise. Once thresholded, the GFAP signal was determined by automating a count of the non-zero pixels ($n = 5$). Implanted cortex and contralateral cortex were compared for all metrics by t-tests with significance level of $\alpha = 0.05$.

We identified cell-types in the encapsulation tissue based on morphology and antibody staining. Vimentin(+)/Iba-1(+) and vimentin(-)/Iba-1(+) cells were considered to be macrophages if found in the meninges, microglia if found in the parenchyma. Vimentin(+)/Iba-1(-) cells were considered to be fibroblasts. Multi-nucleated cells were considered cells that contained more than one Hoescht 33342 labeled nuclei in a single cell body. These cells are often found in pathological inflammatory conditions or in the presence of chronically implanted foreign bodies [347, 419, 420].

5.4.9 Collagen-I imaging

Collagen I, a key component of tissue encapsulation, can be visualized using second-harmonic generation (SHG) imaging. SHG imaging takes advantage of a second-order nonlinear optical

property of collagen type I to visualize an intrinsically-generated optical signal that can be used to locate and quantify collagen I in tissue. This is preferred to traditional histological staining protocols, which have been shown to have less signal specificity and require chemical processing that may alter the tissue quality [421, 422].

SHG images of tissue encapsulation and dura mater were captured using a laser with a Nikon A1Plus multiphoton scanning confocal microscope and Nikon NIS-Elements Microscope Imaging Software. SHG was generated at an 830nm wavelength, and signal was collected via a bandpass filter that isolated tissue auto-fluorescence (435 – 700nm) and a low-pass filter that isolated SHG signal (<492nm). Images were taken with a 25X objective to maximize signal resolution and imaging frame; stitching software (NIS-Elements Microscope Imaging Software, Nikon) was used to consolidate disconnected images to make a seamless, high-resolution image of the encapsulation through the dorsal-ventral plane.

Encapsulation and dura mater thickness were determined by measuring average thickness of tissue extent as denoted by auto-fluorescence. Because SHG signal was confined within an uninterrupted, fibrous area, percent SHG-signal was measured by dividing the average thickness of SHG area by the total tissue thickness. Such measures were generated for encapsulation tissue from the ventral and dorsal sides, as well as for control dura mater (n = 5 tissue sections for all groups). Encapsulation and dura mater thickness and percent SHG signal were compared between cortex-facing encapsulation, skull-facing encapsulation, and control dura mater groups by one-way ANOVA tests with Tukey's post-hoc tests. Significance for all comparisons was defined to be $\alpha = 0.05$.

In sum, we will examine the cortex for cortical thickness and neuron, microglia and astrocyte density. We examine the meningeal/encapsulation tissue for thickness as well as cellular and structural protein composition.

5.5 RESULTS

Our findings focus on three aspects of the tissue response to the implant: cortical architecture, encapsulation, and physiological signal quality.

5.5.1 Cortical architecture

We found that the brain was mechanically depressed under the ECoG array. We assessed the extent of this depression by generating a 3D rendering of the brain's surface topography. Then, the image of the implanted hemisphere was superimposed onto the non-implanted hemisphere. This allowed us to create a heatmap of topographic differences between the two hemispheres (Figure 5-1E). We found that the brain region under the ECoG grid was mechanically depressed by as much as 3.63 mm relative to the same region of the non-implanted hemisphere.

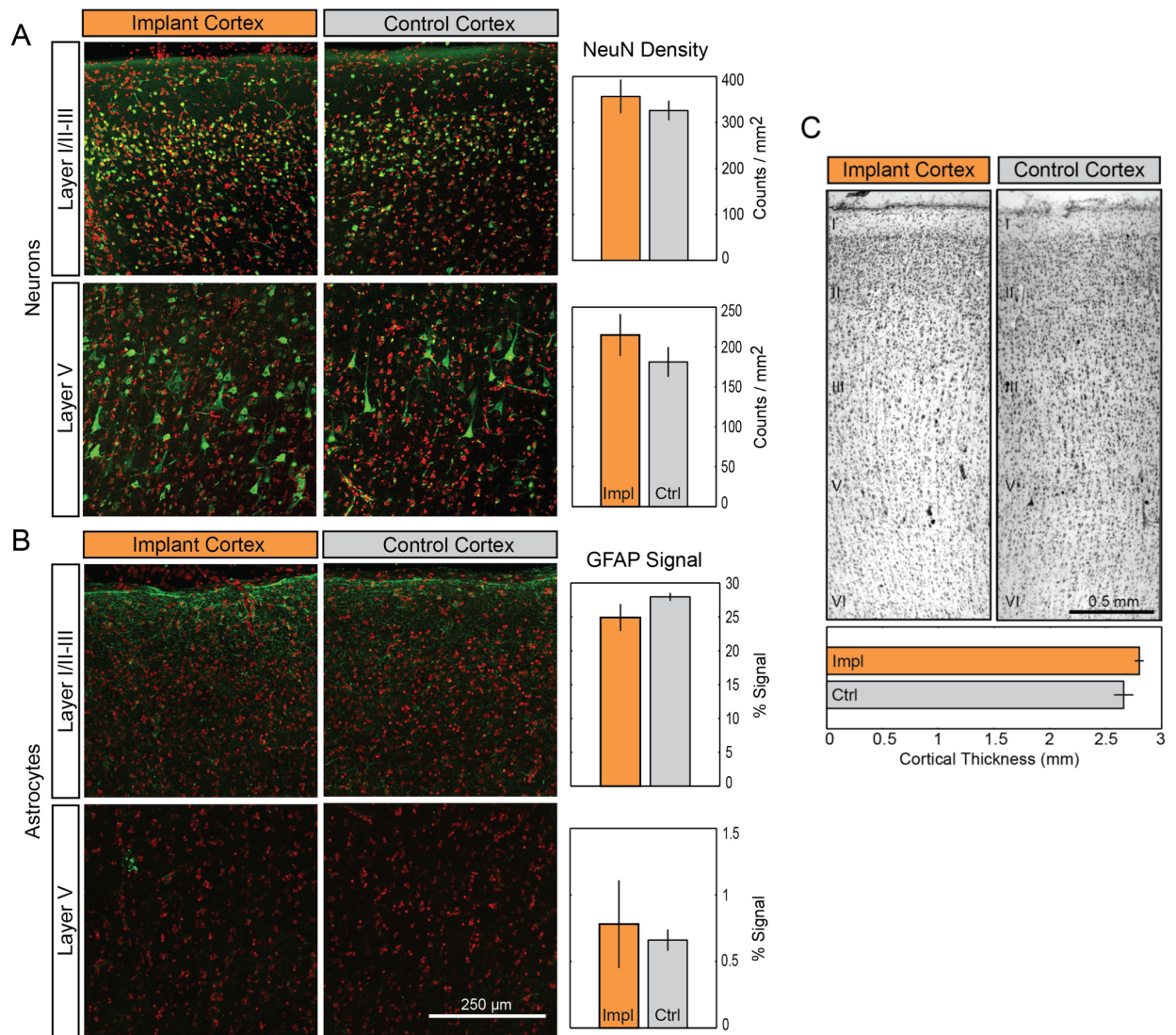


Figure 5-2 Long-term ECoG grid implantation causes minimal changes in cortical cytoarchitecture.

(A-B) Neither the density of NeuN-labeled neurons (A; green) nor the signal intensity of GFAP-labeling in astrocytes (B; green) located in layers I/II-III or layer V were significantly affected by implantation. Cell nuclei (red) counterstained with Hoescht 33342. Data presented as mean \pm SEM; * denotes significant difference from control ($p < 0.05$). (C) Impl: implanted cortex. Ctrl: control cortex. Comparison of Nissl-stained motor cortex between implanted and control hemispheres. Cortical layers are indicated by roman numerals I- VI.

To determine if this gross morphological change resulted in alterations of cortical cytoarchitecture, we evaluated neuronal and glial density as well as cortical thickness under the grid. We compared it to the corresponding cortex in the opposite hemisphere (Figure 5-2). The density of neurons labeled with the NeuN antibody in layers I/II-III or layer V not significantly higher (Student's t-test, $p = 0.5$ and 0.32 , respectively), in the cortex under the grid versus the contralateral cortex (Figure 5-2A). Similarly, the signal intensity of GFAP antibody labeling of reactive astrocytes in layers I/II-III or layer V was not significantly different between the two hemispheres (Figure 5-2B; 0.18 and 0.73 , respectively). Only the density of microglia labeled with the Iba-1 antibody and located in the superficial layers (I/II-III) exhibited a significant increase under the array (Figure 5-3A; t-test $p = 0.027$ for layers I/II-III; 0.24 for layer V). The microglia both under the array and in the contralateral cortex exhibited a qualitatively similar morphology, with only cell density along dorsal surface of the cortex of either hemisphere (7.6 ± 1.6 versus 6.6 ± 1.8 cells/mm for the implanted and control cortical surface, respectively) showing Surface Directed morphology (defined in Methods) (Figure 5-3B). These cells typically had processes polarized parallel to the cortical surface. Finally, the thickness of the Nissl stained cortex tissue under the grid (Figure 5-2C, top; 2.8 ± 0.04 mm) was not statistically different from that of the contralateral cortex (Figure 5-2C, bottom; 2.7 ± 0.09 mm; t-test: $p = 0.34$). These findings were qualitatively corroborated by observing the transition region of tissue at the edge of the ECoG array and tissue immediate adjacent to the implanted region, where limited changes were observed (Figure 5-4). Taken together, these tests provide little evidence of significant cytological changes in the cortex underlying the ECoG array.

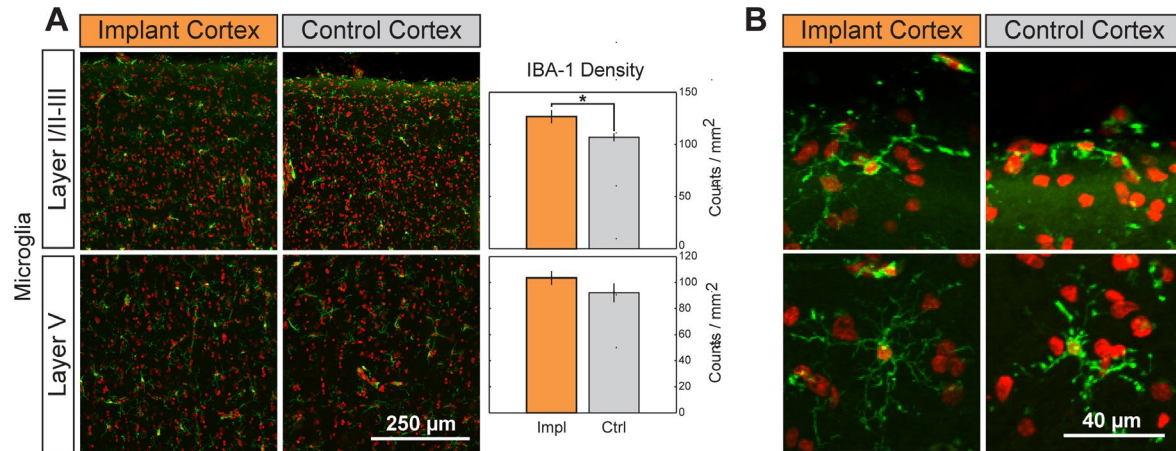


Figure 5-3 Chronic implantation yields higher microglial density with no change in cell morphology.

(A) The density of microglia (green; nuclei in red) was significantly increased in layers I/II-III but not in layer V following implantation. Data presented as mean \pm SEM; * denotes significant difference from control ($P < 0.05$). **(B)** Layer I microglia show no morphological indication of inflammatory response. A small population at the cortical surface of implant and control cortices are polarized along the curvature of the brain, all microglia beneath the surface are unresponsive.

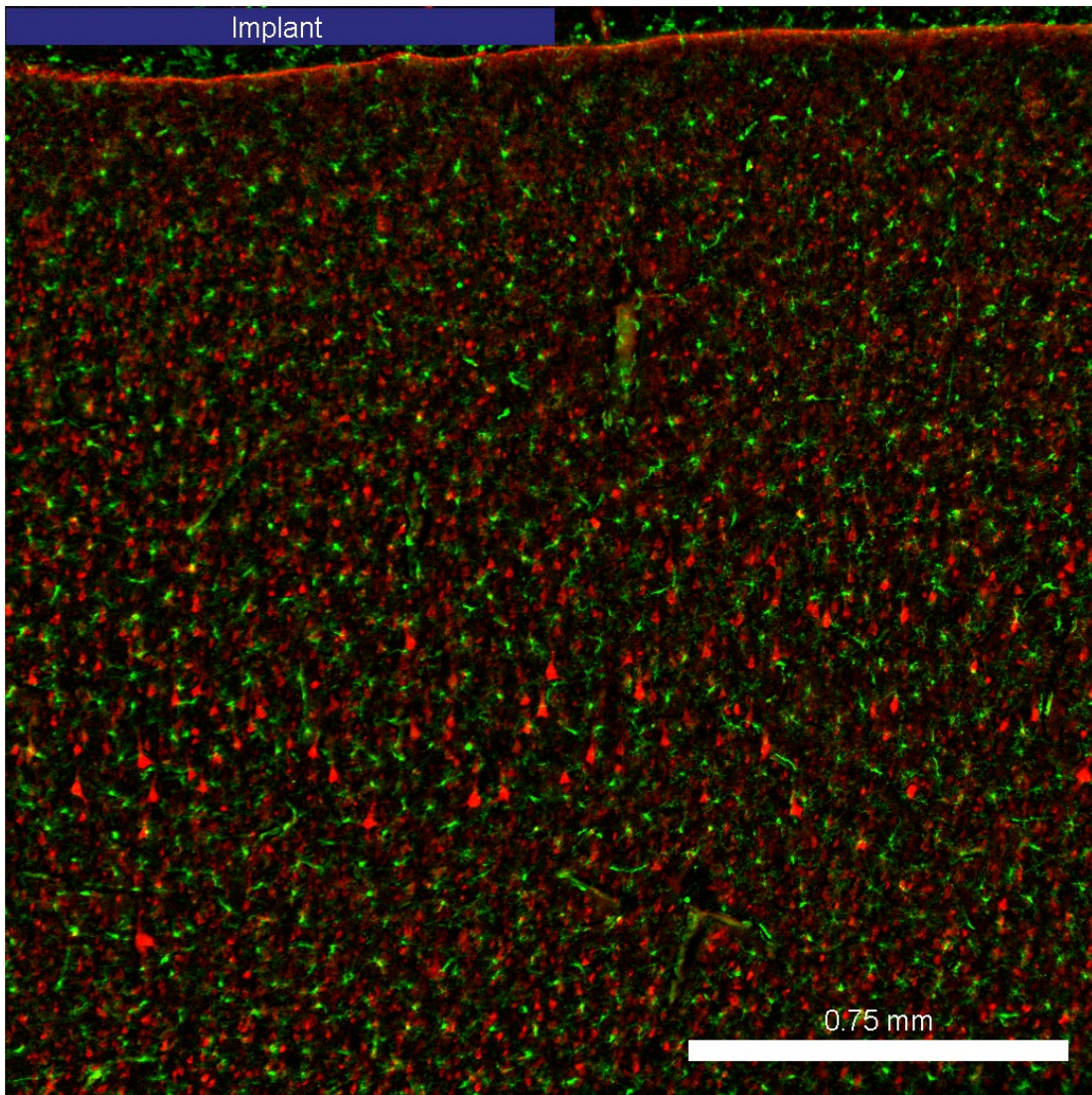


Figure 5-4 Wide-field image of implant margin.

Fluorescence microscopy of neural tissue under the edge of the ECoG array (blue box) and the adjacent tissue. No observable changes in cortical architecture as determined by neuronal morphology (red). Microglia in green.

5.5.2 Fibrous encapsulation

Chronic subdural ECoG implantation resulted in fibrous encapsulation of the grid. The grid was removed by making an incision along the anterior portion of the encapsulation and pulling the grid with forceps. Surprisingly, the grid offered little mechanical resistance to removal, indicating that adhesion between the grid and encapsulation tissue was minimal. Using second-harmonic generation (SHG) imaging, we detected collagen I in sections of the tissue encapsulation and control dura mater (> 2cm from implantation site). Using filters to image second-harmonic signals and tissue autofluorescence simultaneously, we quantified both the thickness of encapsulation tissue and the percentage of encapsulation tissue that was collagen I-positive (Figure 5-5). Because the dorsal portion of the encapsulation emerged from the original, autografted dura mater, we analyzed it separately from the ventral portion of the encapsulation, which grew *de novo* following initial implantation. Both sides of the tissue encapsulation were compared to control dura mater taken more than 2cm from the implantation site. There were statistically significant differences in the thicknesses of the tissues (one-way ANOVA: $F(2, 14) = 136.13, p < 0.001$), with both dorsal encapsulation ($0.82 \pm 0.04\text{mm}$) and ventral encapsulation ($1.76 \pm 0.09\text{mm}$) being thicker than control dura mater ($0.36 \pm 0.03\text{mm}$; Tukey's post-test: $p = 0.001$). The ventral encapsulation was also significantly thicker than dorsal encapsulation ($p < 0.001$). The encapsulation was presumably the cause of the visible depression of the cortex under the grid.

SHG imaging revealed encapsulation tissue to be comprised of a cellular region that did not express strong SHG signal and a collagenous region that was strongly SHG(+) (schematic: Figure 5-5B-E). Using the tissue thickness derived above, we were able to assess the relative proportions of cellular and collagenous regions by measuring the area of collagenous region

(SHG(+)) region) and dividing it by tissue thickness. This showed that the proportion of collagenous region was significantly different between the tissues (one-way ANOVA: $F(2, 14) = 44.33$; $p < 0.001$). Control dura mater had a significantly higher percentage of collagenous tissue ($96.4 \pm 0.33\%$) than either ventral encapsulation ($82.5 \pm 2.3\%$; Tukey's post-test: $p < 0.01$) or dorsal encapsulation ($58.9 \pm 4.5\%$; $p < 0.001$). The percentage of collagenous tissue in the ventral encapsulation was also significantly greater than that of the dorsal encapsulation ($p < 0.001$).

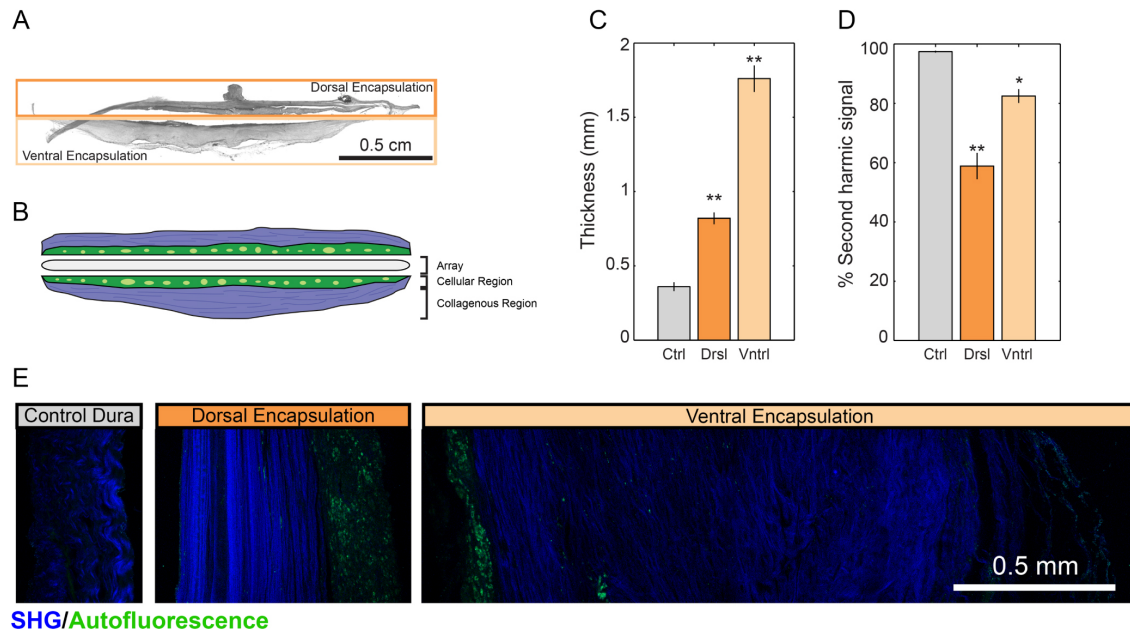


Figure 5-5 Second-harmonic imaging of fibrous encapsulation reveals fibrous, cell-sparse region and cell dense regions in both dorsal and ventral aspects of encapsulation.

(A) Sample image of full tissue encapsulation slice. (B) Schematic representation of encapsulation components. (C) Comparison of thickness of dorsal and ventral aspects of encapsulation tissue to control dura. (D) Percentage of SHG(+) tissue was significantly reduced in encapsulation tissue. (E) Sample images of dorsal encapsulation, central encapsulation, and control dura with SHG signal shown in blue and tissue autofluorescence shown in green. Data presented as mean \pm SEM. Asterisks * and ** denote significant differences from control at $p < 0.01$ and $p < 0.001$, respectively.

In order to determine the cellular composition of the encapsulation we used immunohistochemistry. We identified fibroblasts and macrophages in all tissue groups. Control dura mater was largely composed of fibroblasts, many of which exhibited elongated nuclei (Figure 6-C), consistent with previous literature [423]. Macrophages were sparsely distributed. This resembled the “collagenous” region ($>300\mu\text{m}$ from the array; Figure 5-6B) of the tissue

encapsulation, which also contained elongated fibroblasts and macrophages. The “cellular” region of encapsulation (< 300µm from the array; Figure 5-6A) was highly cell dense with round, mononuclear macrophages as well as multinuclear, foreign body giant cells (vimentin(+)/Iba-1(+)). Mononuclear/multinuclear distinction was based on nuclei count (Figure 5-6A *inset*). The encapsulation was organized as a gradient, with “cellular” tissue closest to the array exhibiting more inflammatory cell activity, and “collagenous” tissue more distal to the array more closely resembling healthy dura mater.

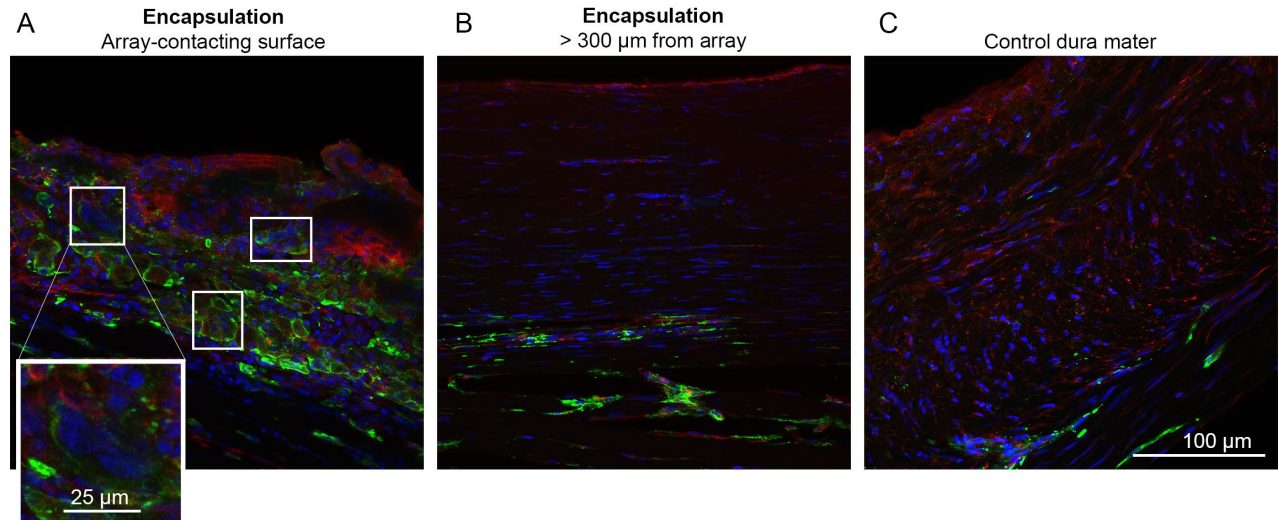


Figure 5-6 Immunohistochemical staining of encapsulation tissue.

Tissue was stained for nuclei (blue; Hoescht 33342) and antibodies directed to macrophages (green; Iba-1) or macrophages/fibroblasts (red; vimentin). (A). Array-contacting aspects of the encapsulation were highly cell dense, populated with macrophages (vimentin(+ or -)/ Iba-1(+)) as well as fibroblasts (vimentin(+)/Iba-1(-)). Boxes indicate multi-nucleated giant cells. Inset. Magnification of a multinucleated giant cell. (B). Distal portions of encapsulation were hallmarked by elongated fibroblasts and macrophages (vimentin(-)/Iba-1(+)). (C). Control dura mater is largely elongated fibroblasts with infrequent macrophages.

5.5.3 Physiological recordings

In order to validate long-term signal modulation, we examined ECoG signals during all available behavioral task recording sessions—reaching task trials conducted between day 542 to 562 post implantation. Signals exhibited clear modulation with target direction (Figure 5-7). Characteristic decreases in the mu and beta frequency bands (10-30 Hz), in conjunction with increases in the high gamma band (> 60 Hz), were observed. High gamma band modulation was found to be the

strongest over the 70 – 100 Hz frequency range, and was tightly locked to movement onset. Thirteen of the fifteen electrodes exhibited reach-modulated signals (Figure 5-8). Of the two electrodes not exhibiting reach-related activity, one was a reference (dura-facing) electrode and the other an electrically intact electrode that was not recording due to a failure in the cabling connecting the Cereport adapter and neural recording amplifier.

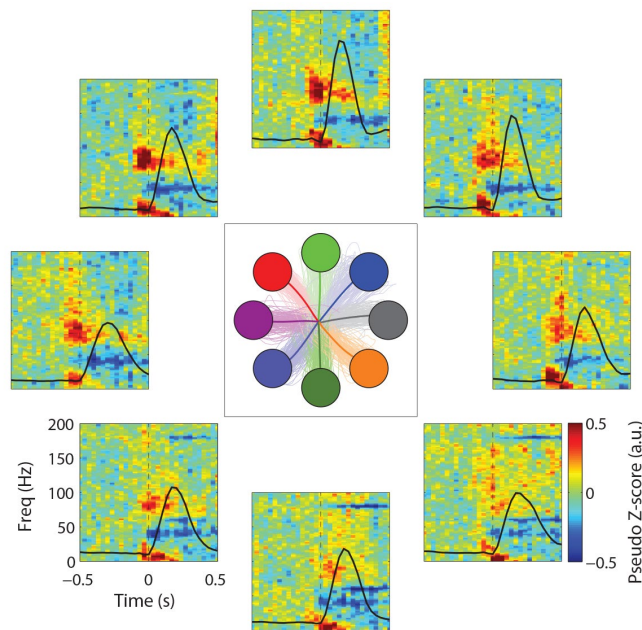


Figure 5-7 ECoG signal modulation during 8-target center-out reach tasks.

Average time-frequency data are shown for a single electrode (e10) for all reach directions. Averaged (thick lines) and individual trajectories (thin lines) for each target are shown in the center panel. Time-frequency data were normalized with respect to the spectral data during a central hold period preceding each trial. Black lines show average speed profiles for each target.

Prior to hand control experiments, a number of recording sessions devoted to BCI control experiments were conducted. However, during post-hoc analysis of these data we discovered that the animal had developed a strategy of using artifacts, possibly the result of jaw movement, to generate directionally-modulated broadband increases in spectral power. We now believe that our earlier report of stable multi-day BCI control was due in part to this strategy [424]. The presence of these artifacts precludes further analysis of the brain control data, apart from a baseline confirmation of the stability and robustness of the ECoG recordings.

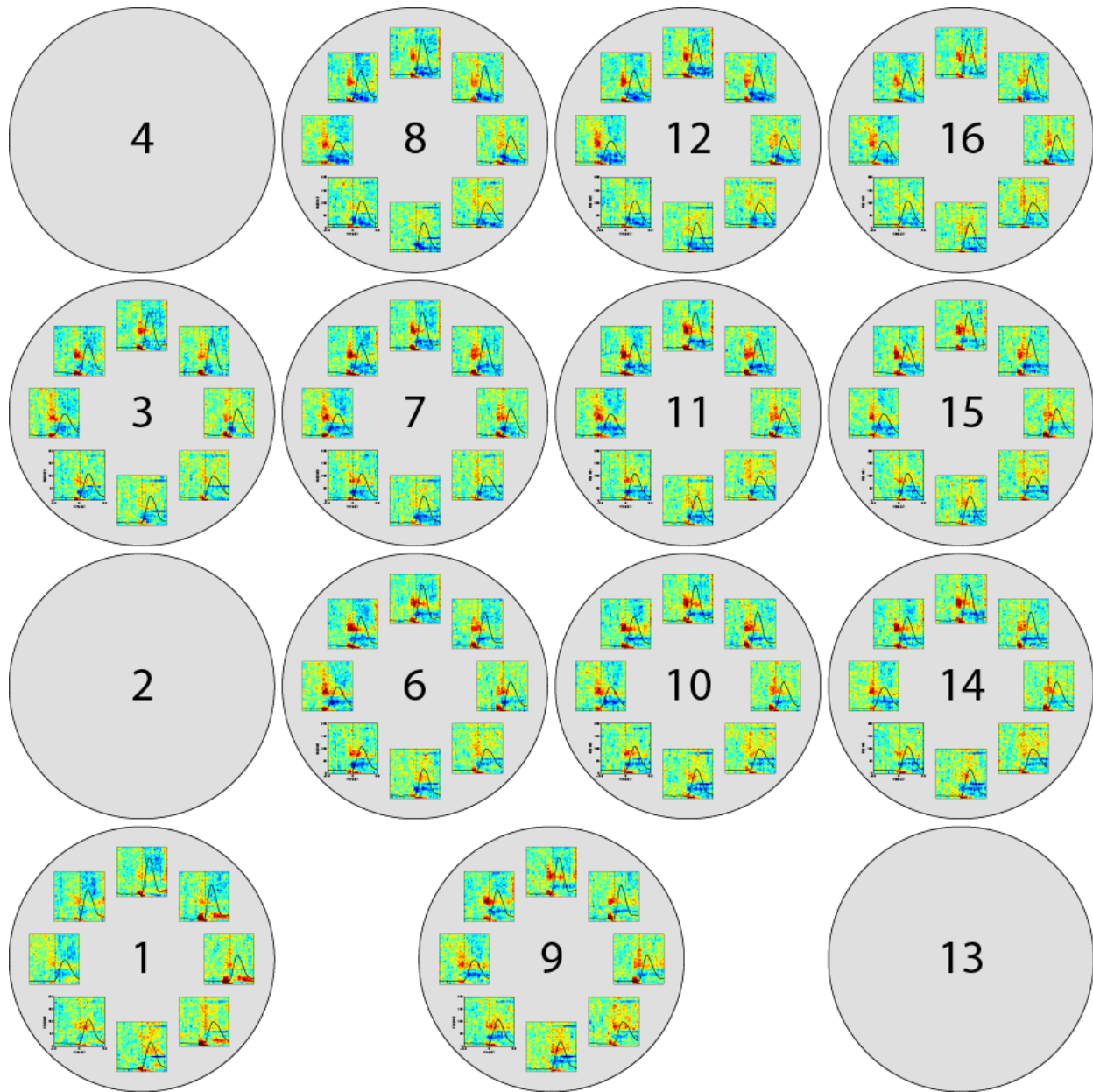


Figure 5-8 Directional modulation of ECoG signals during reaching.

Data are shown for all successful reaching trials (N = 1, 145). Movement onset is indicated by the dashed black line for each plot. Data for electrodes 4 and 13 are not available on account of these electrodes serving as ground and reference electrodes, respectively. Data for electrode 2 is not available on account of connectivity of this electrode being lost shortly after grid implantation.

We tracked 20Hz impedance at all functional electrode sites during recording sessions from day 52-562 post-implant (Figure 5-9). Impedance was relatively stable through the course of implantation, though it fluctuated following surgical interventions (Figure 5-9A). The encapsulation tissue's contribution to impedance was tested by comparing the impedance of the ECoG grid before and after removing it from the encapsulation. Impedance dropped 6-36kOhms after removal, dependent upon impedance measurement method (Figure 5-9B). Device performance was corroborated by representative root-mean speed (RMS) amplitude measurements of ECoG signals, which initially dropped, but stabilized by day 300 post implant (Figure 5-9C-D). The gradual decrease in signal amplitude observed is consistent with the development of encapsulation tissue over time. This development would increase the distance between the electrodes and cortex, which based on volume conductor models would be expected to reduce measured electrical potentials [425].

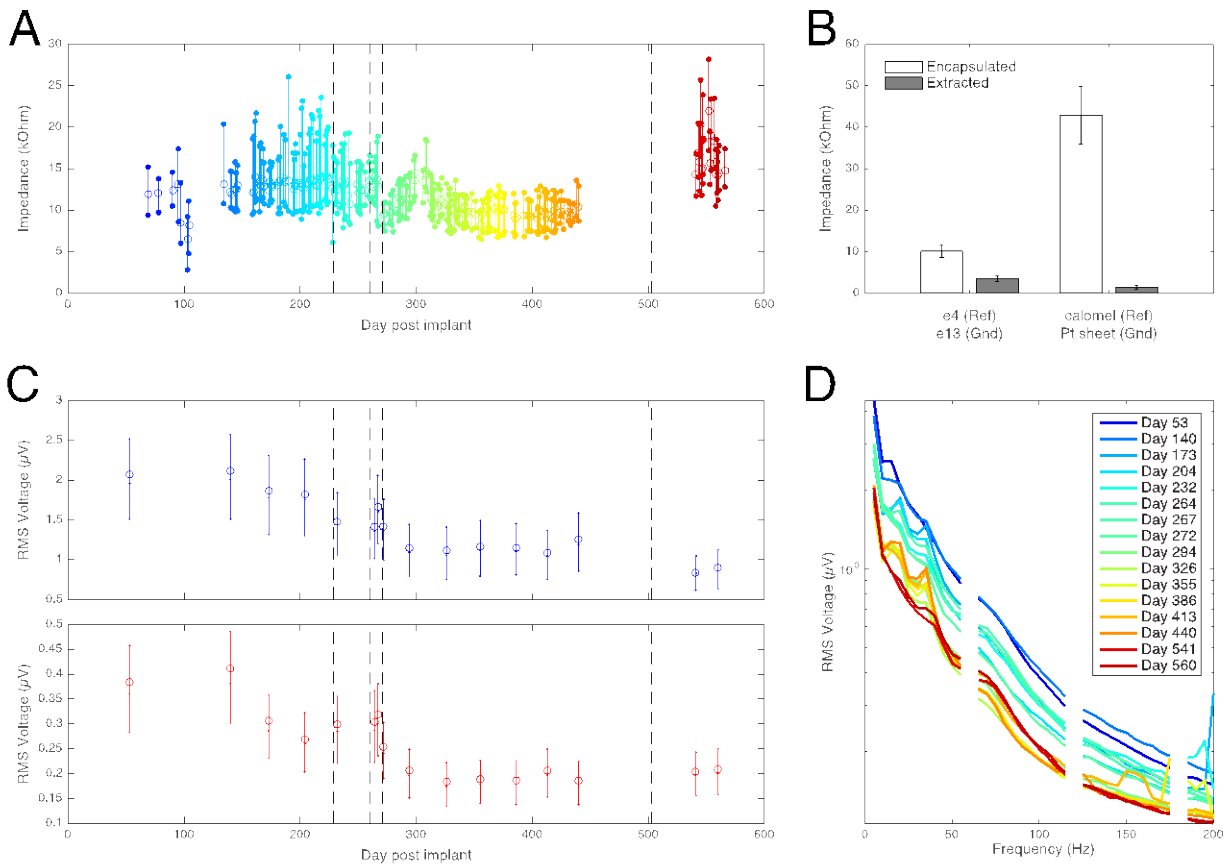


Figure 5-9 Electrode impedance and RMS amplitude of electrophysiological recordings.

(A) In vivo electrode impedance values (measured at 20Hz) over the course of electrode grid implantation. For each day impedance was measured, the range of impedance values is indicated by colored vertical lines, while the mean impedance is indicated by open circles. Dashed black lines indicate days on which surgical interventions were performed. **(B)** Ex-vivo electrode impedance values. Impedance data are shown for both ‘e4 + e13’ and ‘calomel + Pt’ measurement configurations for the electrode grid during encapsulated (white) and extracted (gray) conditions. Error bars indicate standard deviations from the mean impedance values for each condition. **(C)** RMS amplitude over the course of electrode implantation. RMS amplitude at 20Hz (blue) and 100Hz (red) is shown for selected recording sessions. Solid vertical lines indicate the [25th – 75th] quantile range of RMS amplitudes, with filled circles indicating the 25th, 50th, and 75th quantile values. Open circles indicate the mean RMS amplitude. **(D)** RMS amplitude spectra for selected recording sessions.

Mean RMS spectra are provided for the same recording days shown in (C). Individual spectra colors correspond to those of the in-vivo impedance data in (A).

5.6 DISCUSSION

5.6.1 Histological findings

We examined the foreign-body response to a subdural ECoG electrode grid nearly two years after implantation. There was fibrotic growth around the electrode grid, resulting in a shallow mechanical depression of the cortex under the array. Despite this, the cellular characteristics of the cerebral cortex underneath the ECoG grid were consistent with that of the tissue of the control contralateral hemisphere. Most importantly, cortical thickness and neuronal density of the tissue under the array were statistically indistinguishable from the contralateral tissue, with no morphological differences apparent at any spatial scale. After accounting for discrepancies in methods, measurements of thickness and neuronal density for both hemispheres agreed with those of previous anatomical studies of primate frontal cortex [418, 426]. Noting that cortical thickness and layering was unaffected by the gross mechanical deformation of the brain's surface, it is plausible that the displaced brain was merely pushed into the ventricles as in cerebral edema and subdural hematoma [427]. Only the microglial density of the superficial cortical layers was significantly different between the implanted and non-implanted hemispheres. It is possible that the persistent, unactivated microglia population was part of the foreign body

response to the implanted ECoG array, where increased macrophage density persists in the vicinity of the implant for its lifetime [76, 348]. It is also conceivable that this activation was not in response to a foreign body, but rather from pervasive mechanical stress caused by the fibrous encapsulation compressing the brain [132, 428]. With the exception of a population of cells at the cortical surface of both hemispheres, layer I microglia were either ramified or polarized but without processes that extended to the cortical surface, which indicates that these microglia were not actively responding to trauma or other noxious stimuli at the surface of the brain [40, 132, 149, 151]. The microglia at the surface of the brain were polarized with processes extending parallel to the cortical surface, similar to a cell type that has been described in healthy mouse cerebellum and rat prefrontal cortex, suggesting the observed cell type is not a result of pathology [429, 430]. The astrocytic GFAP expression between control and implanted hemispheres was not different. For both hemispheres, we observed low GFAP expression in the gray matter and relatively strong expression in the glia limitans. This expression pattern has been well documented in healthy macaque brain, with gray matter GFAP expression increasing only in response to trauma or chronic foreign body implantation [431-433]. Qualitatively, our finding of low levels of gray-matter GFAP(+) cells under the array suggests that the array was not actively causing trauma to the cortex.

During the grid implantation surgery, we resected the dura mater, replaced it over the ECoG array, and sutured it in place. After the 666 days of implantation, dura mater/fibrous encapsulation tissue was found in a contiguous piece surrounding both the top and bottom of the ECoG. Since there were only leptomeninges separating the brain and array at the time of the implant, we assume that the ventral encapsulation grew *de novo* post-implantation. This is similar to recent findings by Schendel et al., who reported progressive fibrous overgrowth of

epidural ECoG grids, with complete encapsulation as early as one month post implantation [140, 141]. The cellular distribution in the dorsal and ventral tissue encapsulation was distinct from dura mater elsewhere in the brain, and implied that the wound-healing response to implantation consisted of a stereotypic foreign body response, which involves aggregation of mononuclear macrophages and multinucleated foreign body giant cells to the implant site and encapsulation of the device in a collagenous envelope. Aggregated cells and tissue encapsulation generally persist through the lifetime of an implant, with pro-inflammatory cytokine expression diminishing within the first month as anti-inflammatory/pro-wound healing cytokines are expressed [347, 419, 420]. The fibrous encapsulation demarcates the final stage of wound healing in which the tissue disrupted by implantation is either regenerated from cells of the original cell type, or replaced with fibrous connective tissue. Given that dura mater is already largely fibrous connective tissue and mesenchymally derived fibroblasts, it was not clear to us the extent to which the tissue encapsulation was fibrous encapsulation or remodeled/regrown dura mater [347, 348, 423]. We observed a gradient where tissue proximal to the implant more closely resembled fibrous encapsulation, and tissue distal to the implant more closely resembled control dura mater.

Both the dorsal encapsulation and ventral encapsulation were thicker than the control dura mater, which would be expected of a foreign body tissue encapsulation. In the case of autografted, dorsal encapsulation, dural thickening may have also been an inevitable consequence of craniotomy and/or durotomy that was simply exacerbated by the presence of a foreign body. This is seen in epidural ECoG implants, where encapsulation with ventral and/or dorsal dural thickening has been reported in long-term implants [140]. Merely performing a craniotomy triggered a 3.8 fold increase in dural thickness at 3 weeks, with a reduction to a 2.6 fold increase at 3 months in New Zealand white rabbits [137]. Replacing dura with an alginate

hydrogel resulted in a 2.8 fold increase of dural thickness of regrown dura at 3 weeks and a 3.1 fold increase at 3 months. Dural thickening of 2mm 8 weeks after a 2cm dural incision has been observed in coonhound dogs; following application of a poly(ethylene) glycol based dural sealant, the healed dura was found to have thickened as much as 4mm [138]. Meningeal cells almost double collagen production following sub-arachnoid hemorrhage in rats [134]. Computational models of collagen I fibrosis following biomaterial implantation corroborate this [434]. In these experiment-validated models, increasing numbers of fibroblasts at the implant site results in significantly increased collagen deposition. Since the predominating cell type of dura mater is the fibroblast, it is plausible that we might expect pronounced collagen I production following implantation.

Despite the degree of encapsulation, the ECoG grid was extracted from the fibrous tissue with little effort, indicating relatively minor adhesions between the encapsulation and device. This is not surprising given the lack of porosity and surface features on the silicone grid. Previous studies have demonstrated smooth, non-porous dural substitutes are less susceptible to fibrosis and adhesion formation [365, 435].

While we have shown that the foreign body response to chronic ECoG grid implantation can result in grid encapsulation after ~22 months, we were unable to determine its exact time course. It is unclear whether the encapsulation was stable or still growing, or perhaps shrinking, at the time we observed it. Subdural ECoG electrodes implanted up to 30 days clinically for epilepsy monitoring do not exhibit such encapsulation [407, 409-411], so it is likely that the subdural implant encapsulation response occurs on the order of months rather than weeks. Meningeal thickening—but no encapsulation—has been observed micro-ECoG arrays in rats at 6 months post-implant, though no other time-points were assessed [142]. In contrast, epidural

implant encapsulation has been observed as soon as one month post implant [140, 141]. The same group also reported dramatically slower tissue encapsulation under an epidural array that had torn the dura mater during implantation. This suggests that there may be different foreign body response mechanisms for implants with different degrees of invasiveness. To our knowledge, there is no study directly comparing implantation depth to explore possible foreign body response mechanisms.

5.6.2 ECoG recording quality

ECoG electrodes provided recordings of physiological signals for nearly two years. Health issues with the animal that were unrelated to the ECoG grid determined the termination date of the study, but we believe that signal quality may have persisted past two years. Of the fifteen electrodes on the array, only one lost recording capability during the course of our study. Post-explantation, we determined that failure was on account of a faulty wire connecting the Cereport adapter to the neural amplifier, and not due to a tissue response. We found that all functional electrodes showed signals that were temporally modulated and spatially tuned during a reaching task.

We conducted extensive BCI control tasks as part of this study. By the time we detected that the animal had developed a strategy of generating an electromyographic artifact (presumably by contracting jaw or face muscles) to control the cursor, we were unable to train him to abandon this strategy. This made it very difficult to study the tuning properties of ECoG signals during the BCI control sessions. Future studies using a simple stereotypical task, such as the center-out task, will likely be able to better characterize changes in ECoG signal tuning properties throughout the entire lifespan of an ECoG implant.

Our earliest impedance and RMS amplitude measurements were at 56 days post implantation. Both metrics were relatively stable from this initial time-point to day 562 post implantation, though impedance slightly rose over time, and RMS amplitude slightly declined. The ECoG grid's mean impedance was $< 5\text{k}\Omega$ after being removed from the encapsulation tissue. This value is less than any impedance measured *in vivo*, suggesting that the encapsulation tissue could have been established our earliest measurement (day 56 post implantation).

5.6.3 Implications and future directions

We believe our results have implications for the viability of ECoG for long-term high-resolution brain recording. In addition to its use as a recording modality for brain-computer interfaces, ECoG has increasingly become a neuroimaging method of choice in a variety of neuroscience fields and non-BCI neural recording and neuromodulation applications. The potential for subdural ECoG grids to remain implanted for extended periods of time without damaging the cortex could facilitate the study of cognitive processes over long timescales. Lack of cortical damage combined with the ease of removal of the ECoG grid from encapsulation tissue may provide the possibility for repeated implants in case of failure. This is not as practical for intracortical electrodes, which typically damage neural tissue [27]. While ECoG grid encapsulation presents as a potentially detrimental consequence of implantation, many strategies can and have been pursued to minimize the foreign body response to ECoG electrodes. These include altering the shape of array substrate [140, 141, 373], increasing array flexibility [374, 375, 436], applying anti-fouling or biomimetic surface treatments [105, 420], and releasing anti-inflammatory drugs from the array substrate or electrodes [235, 437]. Use of such strategies may

help to further increase the stability of long-term ECoG recordings by eliminating changes in recording quality resulting from the foreign body response to sub-dural ECoG grids.

As this work is a case study in a single animal, additional studies will be required to fully assess the effects of chronic, sub-dural ECoG grid implantation. Nevertheless, the present's findings on meningeal thickening, encapsulation, and fibrosis echo studies on sub-dural and epidural implants in rats [140-142] as well as in long-term (> 1 year) sub-dural and epidural implants in humans [412-415]. There are fewer studies on the health of neural tissue underlying these implants. The present has provided indications that the underlying tissue is minimally affected, urging future studies to visit this premise and providing the analytical tools with which to do it.

This study is an important first step toward fully assessing the long-term use of chronically-implanted ECoG electrode grids. Minimal cortical tissue damage from chronic electrode implantation suggests that ECoG may provide the capability to record physiological signals from the cortex for extended periods of time. Ultimately, this highlights the utility of ECoG as a valuable tool for long-term BCI, clinical, and neuroscientific studies.

5.7 ACKNOWLEDGMENTS

The authors would like to thank Dr. Jason Godlove and Melissa Faulkner for their help in training the animal used in this study; Dr. Douglas Weber and Erin Gaia for their assistance in the explantation surgery; Darina Sipula and the Systems Neuroscience Institute for their assistance in the histological analysis; Dr. Simon Watkins, Dr. Gregory Gibson, and the Center

for Biological Imaging for their assistance in SHG and confocal imaging; and Dr. J. Andrew Holmes and the Swanson Center for Product Innovation for their assistance in 3D scanning. The work was supported by NIH Grants 2R01NS062019, 3R01NS050256-05S1, R01 NS065065, R01 RHD071686A, KL2TR000146, and P30 NS076405. The work was also supported by the National Science Foundation, the Burroughs Wellcome Fund, the UPMC Rehabilitation Institute, and the Craig H. Neilsen Foundation. The content is solely the responsibility of the authors and does not necessarily represent the official views of the National Institutes of Health.

6.0 CONCLUSION

6.1 SUMMARY OF RESULTS

Chapters 2 and 3 of the dissertation focused on the tissue reaction to implanted devices within the cortex. In Chapter 2, we used two-photon imaging to study how neurons are damaged during electrode implantation. Using transgenic mice with neuronal expression of calcium indicators, we demonstrated that neuronal calcium within 120 μm of the electrode is immediately disrupted by implantation, with changes evident for weeks after insert. We further provided evidence that axonal degeneration occurs after implant, and manifests as early as 1 hour after implantation. At 3-6h after implantation, cells with membrane disruption were largely confined to the first 20 μm of the implant, suggesting that only the cells closest to the device were mortally wounded by implantation. This is supported by the observation of progressively increasing calcium activity around the implanted devices over the first month after implant, which may be due to neuron repair and remodeling or attenuation of inflammation. This work suggests that alterations to neuron membrane permeability and calcium levels may be a viable target to prevent neuronal injury after implant.

Chapter 3 changed focus to examine the microglial reaction to implanted electrodes with differing surface chemistries. While our previous work has established that microglia immediately polarize in the direction of implanted electrodes, in Chapter 3 we used two-photon

microscopy to show that microglial behavior can be modulated by immobilizing L1 cell adhesion molecule onto the surface of electrode devices. After implantation, microglia endfeet processes extended toward both the control, silicon device as well as the L1-coated device at similar rates. Once the microglial processes reached the surface of the different devices, they began to adhere to and encapsulate the control device, while L1-coated devices showed an 83% reduction in encapsulation for at least 6 hours post implantation. Further, radius of activated microglia decreased by 26.5 μm . This study compounds previous research to show that L1 coatings have a beneficial effect in preventing cellular inflammation at the tissue-electrode interface. More generally, this work shows that microglia are immediately sensitive to surface chemistry of implanted devices, highlighting opportunities for thin films to improve electrode performance.

The subsequent chapters focused on the meningeal response to implanted electrodes. In Chapter 4, we used two-photon imaging of leukocytes and meningeal collagen to track the progression of meningeal inflammation and fibrous tissue growth over the first month after implantation. We found that there is a period of rapid meningeal cell migration through pial venules and along the electrode shank over the first day after implantation. This migration subsided, but there were fluctuating levels of meningeal leukocytes over the first month. By the end of the experiment, the meningeal tissue had doubled in thickness. This thickening was not affected by the presence of a silicone craniotomy sealant, but without the sealant, electrodes were buried in the growing meningeal tissue. Chapter 4 ultimately shows that there is a potential migratory window in the first day after implant that may be critical to the establishment of meningeal inflammation and encapsulation.

In Chapter 5, we deviated from *in vivo* imaging to examine meningeal encapsulation of an ECoG grid that had been implanted in a non-human primate for 666 days. We showed that

even non-penetrating devices can elicit significant meningeal encapsulation, while leaving the underlying cortical tissue largely unperturbed. The device's encapsulation tissue was 7.16X thicker than the subject's endogenous dura mater tissue. The electrical impedance was only consistently higher in the last months of the study, while signal amplitude progressively decreased over this time. These electrochemical and electrophysiological results give conflicting ideas of when the encapsulation tissue developed. Nonetheless, at the end of the implantation period, the device was still able to record reach-related activity. These results further the insights gained in Chapter 4 regarding the triggers of meningeal encapsulation, suggesting that meningeal encapsulation can occur independent of device penetration.

6.2 FUTURE DIRECTIONS

6.2.1 Directions to further understand and modulate the CNS tissue response

Chapters 2 and 3 have three primary conclusions: neural electrode implantation causes prolonged calcium elevation in neurons, neural electrode implantation causes cell membrane disruption, and microglial encapsulation behavior can be modulated by electrode's surface chemistry and biochemistry. The conclusions on neuronal damage suggest several future experiments. Firstly, it has been well established that electrode shape, size, insertion speed, and material hydrophobicity have effects on insertion force and potentially acute tissue damage [30, 36, 41-43, 45]. While many of these studies have shown that smaller, less densely spaced devices lead to less tissue damage, the verdict on insertion speed and surface chemistry's impact on acute damage is still out. Electrode tip shape, insertion speed and surface chemistry parameters should

be examined with the experimental set-up described in Chapter 2 to determine the optimal insertion strategy to minimize acute neuronal damage. The effect of prolonged calcium exposure and membrane disruption can also be examined by using calcium chelators or calcium channel blockers to reduce calcium after implantation [180, 182, 202] or polymer-based membrane “sealants” to mitigate membrane disruption [225-227] after implantation. These experiments could be used both further understand the mechanisms of implantation as well as to evaluate the efficacy calcium and sealant therapeutics, as many of these agents already have FDA approval. Finally, the long-term significance of early neuronal damage has yet to be established. Longitudinal experiments should be pursued that can track the long-term activity of neurons and neurites affected by implantation. The link between acute injury and long-term electrode failure is still largely theoretical. The scope of these experiments could be improved by achieving simultaneous imaging of neuronal activity and electrophysiology. In connecting spatial localization of active neurons through imaging with corresponding electrophysiological activity, the links between neuronal health, localization, and device performance could be determined. This paradigm could be expanded to include transgenic animals with expression of fluorophores in different cell types further correlate glial dynamics with neuronal behavior and device performance [438-440]. While simultaneous laser scanning imaging and electrophysiology is confounded by a photoelectric recording artifact produced by the laser, this may be addressed by rapid switching between imaging and recording [241]. These experiments could drastically improve the field’s understanding of the CNS tissue reaction to implanted electrodes. [441, 442]

The major conclusion that microglial encapsulation behavior is modulated by surface chemistry opens a wide door of new potential coating strategies for electrode devices. While other bioactive protein coatings like immobilized neural cell adhesion molecules [281, 290],

cytokine ligands [63], and anti-inflammatory enzymes [109] can be pursued to determine what pathways microglia are sensitive to, simply modulating hydrophobicity could be impactful in reducing fouling and subsequent cell attachment [97, 98, 420, 443]. [271, 277, 279, 444, 445] [234, 235, 446] Each of these strategies can be evaluated in a high-throughput format through the methods outlined in Chapter 3. However, while acute experiments are insightful in determining bioactivity of coatings, long-term experiments for L1 as well as the novel coatings suggested above should be carried out to determine if there is lasting improvement in microglial encapsulation. These experiments could be accomplished with animals that co-express fluorophores in neurons and microglia to explore dynamic interactions between each cell type and coatings.

6.2.2 Directions to further understand and modulate the meningeal response

In Chapters 4 and 5, we determined that there is a window of high leukocyte activity in the meninges after implantation and that meningeal encapsulation can proceed without any electrode penetration. The role of the migratory window can be dissected by acute administration of different anti-inflammatory agents to subdue this initial migration [132, 237, 447]. The long-term effect of this perturbation can be assessed with follow-up imaging or electrophysiological recording. We also noted that the meningeal tissue thickened after this initial inflammatory influx. This thickening extended to both penetrating (Chapter 4) and non-penetrating (Chapter 5) electrode arrays in non-human primate. This could be potentially modulated by using different sealant or electrode platform materials [137, 138, 365], pharmaceuticals [352, 448], surface coatings on sealants or electrode platforms [145, 449], or using open architecture platforms for

devices [140]. One interesting strategy to modulate the inflammatory response is to incorporate controlled drug-release platforms into the sealant or platform material. This is explored in Appendix A.1.2 of this dissertation. Each of these strategies is ripe for investigation under two-photon microscopy. These could also be examined in a rat or higher order animal model, which may not have the same array of genetic tools as mice but may have a more robust fibrous response that is more indicative of the clinical scenario [52].

Surprisingly, Chapter 5 presents one of the few studies to evaluate long-term biocompatibility of ECoG grids in non-human primates. While the results of Chapter 5 are promising in suggesting that ECoG grid implantation leads to little damage of the underlying cortex, a larger, controlled study should be launched to more convincingly demonstrate safety and efficacy of chronically implanted ECoG grids.

While these future directions provide logical next steps for understanding the interaction of the meninges and neural implants, it is worth noting that the basic biology and physiological roles of the meninges are still actively being uncovered. Future research should also be directed at uncovering the interactions between these newly discovered roles and neural implants. Namely, the meningeal role in clearing parenchymal waste after injury through the “glymphatic” system could play a large role in damage and recovery after electrode implantation [450, 451]. This could be explored by experiments to test the rate of clearance of large, fluorescent solutes injected cisternally. Additionally, the meninges have been implicated as a staging ground for innate and adaptive immune responses in the brain [133, 346]. While multiple studies have confirmed that there is invasion of peripheral immune cells into the tissue-electrode interface, no studies have conclusively demonstrated if these cells can invade from the meningeal space [50, 66]. This could be studied by additional longitudinal two-photon studies of meningeal cell

dynamics around electrodes implanted in chimera mouse models with fluorophore expression exclusively in peripheral immune cells. Through these studies, more insight can be gathered about the basic biology of the meninges and how implants can interact with these functions.

APPENDIX A

A.1 PRELIMINARY DATA FOR CONTROLLED DRUG RELEASE PLATFORMS TO MODULATE THE TISSUE ELECTRODE INTERFACE

While the content of this dissertation is largely concerned with characterizing biological pathways within the tissue-electrode interface, in the course of this work methods for modulating the tissue-electrode interface through controlled drug release systems were also innovated. These extend to drug release systems that are integrated into the surface chemistry of the device and drug release systems that are integrated into dural sealants that could modulate the meningeal response to implanted electrodes.

A.1.1 Electrically controlled plasmid release from polymer films

Electrically stimulated release of therapeutics from neural electrodes has previously been achieved through conductive polymer films loaded with both small [234, 273, 446, 452, 453] and large molecules [454, 455]. In the latter case, large molecules extend to growth factor proteins, that are approximately 1-2 nm in size [456]. While growth factors represent an important drug delivery target, yet larger molecules such as DNA plasmids, which are 20-40nm in size [457], could present unique opportunities as a drug release target. Namely, targeted gene delivery through viral vectors and plasmids can push reprogramming of reactive astrocytes to functional

neurons [458, 459]. Such reprogramming could have profound implications in the context of modulating the tissue-electrode interface and rescuing device performance after glial scar formation has matured.

In order to test if electrically-addressable polymer films could successfully incorporate and release DNA plasmids, we electrically deposited polyethylenedioxythiophene (PEDOT), along with acid-functionalized carbon nanotube (CNT), and either DNA plasmid (Lonza eGFPmax plasmid, 0.5 $\mu\text{g}/\mu\text{L}$) or albumin-fluorescein isothiocyanate conjugate (FITC-albumin, Sigma) on electrode surfaces as previously described [273, 446]. Briefly, 1 mg/mL CNTs were mixed into distilled water and bath sonicated for 1 hr. Next, 2 $\mu\text{L}/\text{mL}$ EDOT and either polyethylenimine (PEI, 25kDa, Sigma) / plasmid polyplex solution consisting of 8 μL plasmid, 21 μL of $1 \times 10^{-4}\text{X}$ PEI, and 20 μL sterile PBS, or 1-5mg/mL FITC-albumin were mixed via pipette and allowed to passively mix for an additional hour. Following this, the polymer solution was electrodeposited onto either 3mm glassy carbon, 3mm gold disk electrodes, or custom build interdigitated gold electrode sensor chips to a density of 80 mC (3mm electrodes) or 4 mC (interdigitated electrodes) at +1.0V via chronocoulometry with a platinum counter electrode and Ag/AgCl reference electrode (Gamry Potentiostat). Sensor chips consisted of 16-wells (0.33 cm² plate area per well) with independent working electrode, counter electrode, and reference electrode contacts for each well. Following which, plasmid could be released from sensor to transfect cells by 1h cycles of 20Hz -0.5 to +0.5V square waves for 200ms every 1s. To test drug release from 3mm electrodes without transfecting cells, FITC-Albumin was released by monophasic negative square wave deflections that lasted 1s and plasmid was released by square waves of 5s 0V and 5s 1V as previously described with a platinum counter electrode [273]. Released FITC-Albumin was detected by fluorescence microscopy and released DNA was

measured by Hoescht stain and a spectrophotometer [460]. To test plasmid transfection of cells, HAPI cells were cultured on sensor chips following methods outlined in section 4.3.2. Once 70% cell confluence was reached, plasmid was released for 1h and cell transfection was assessed with fluorescence microscopy after 24h.

First, we assessed whether it was possible to release large molecules with our PEDOT-CNT composite. PEDOT-CNT-FITC-Albumin coatings were generated on glassy carbon electrodes to test this. High amplitude, 1s monophasic pulses were delivered to the electrodes and FITC-Albumin release was monitored by fluorescence microscope as seen in Figure A6-1.

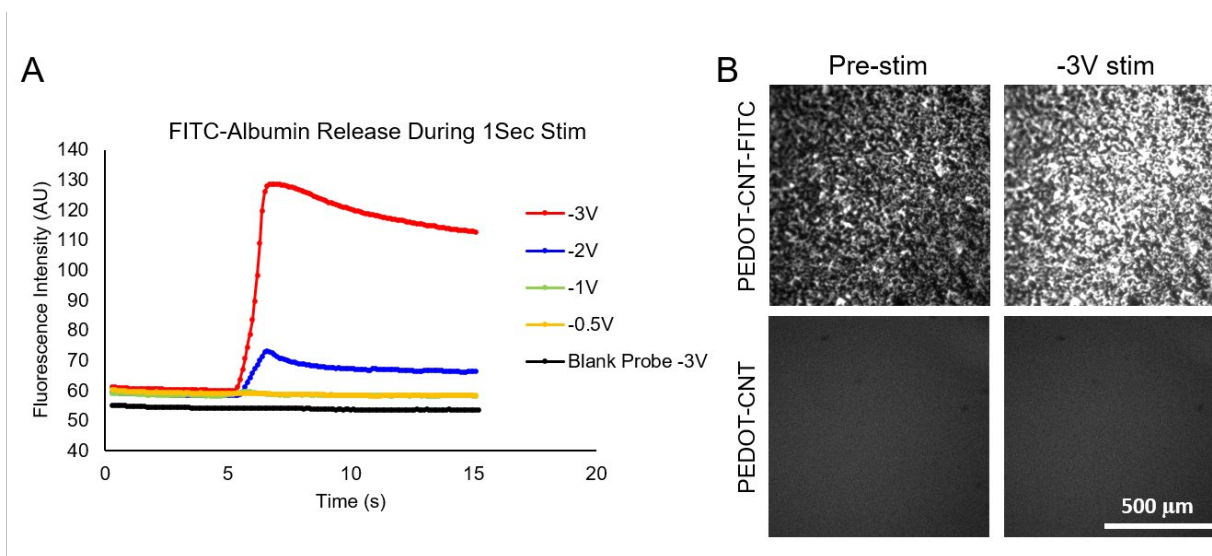


Figure A6-1 FITC Albumin release from PEDOT-CNT film.

(A) Mean intensity of FITC fluorescence is plotted for stimulations of different amplitudes. Stimulation begins at 5s. Small increases in fluorescence are visible with -0.5 and -1V stimulations, but drug release is **(B)** readily visible at high amplitude stimulations. All images generated with the same exposure time.

To determine if large molecule release extend to release of plasmids, we loaded PEDOT-CNT films with plasmid on glassy carbon electrodes and released with an hour of 5s 0V, 5s 1V square waves. Release was detected by Hoechst dye and a spectrophotometer and normalized to Hoechst fluorescence without any DNA present as shown in Figure A6-2.

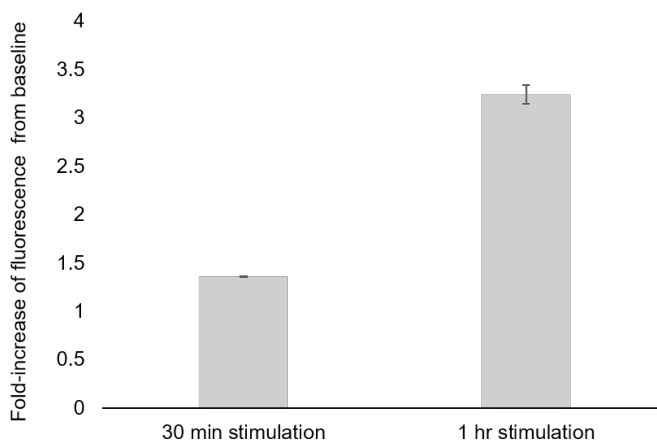


Figure A6-2 Fold increase of DNA signal after electrically stimulated release from PEDOT-CNT films.

Release over time shows gradual increase of released plasmid. By 1h, released plasmid concentration correlates to 0.1 $\mu\text{g}/\text{mL}$ under standard curve.

Plasmid concentration increases with longer durations of stimulation, showing approximately 0.1 $\mu\text{g}/\text{mL}$ release by 1h with respect to a standard curve. Finally, in order to test if released GFP-Plasmid can successfully transfect cells, HAPI cells were cultured on sensor chips (Figure A6-3A) and 1h of square wave stimulation was carried out. Stimulation either used a platinum foil counter electrode that was lowered into the sensor well (Figure A6-3C) or the

gold counter electrode that is part of the device on the device (Figure A6-3D). In the latter case, we observed that the conductive polymer degraded by the end of stimulation. This may be due to the closer proximity of the working and counter/reference electrode in this set-up, which would result lower solution resistance and therefore higher current output in voltage-controlled stimulation. Cell transfection was assessed by observing cells that showed GFP expression after 24h of stimulated plasmid release. Due to high autofluorescence of the cells (shown in the red channel), successfully transfected cells appeared yellow. Compared to unstimulated (Figure A6-3B) and external ground stimulated wells, the internally grounded wells showed pronounced HAPI cell GFP transfection. This led us to conclude that, while plasmid release in effective doses is possible through PEDOT-CNT films, it may require degradation of the film. Alternatively, it is possible that by generating larger features in the film, released plasmid diffusion can be improved. This is possible by co-doping films with particles during electropolymerization that can later be dissolved [461].

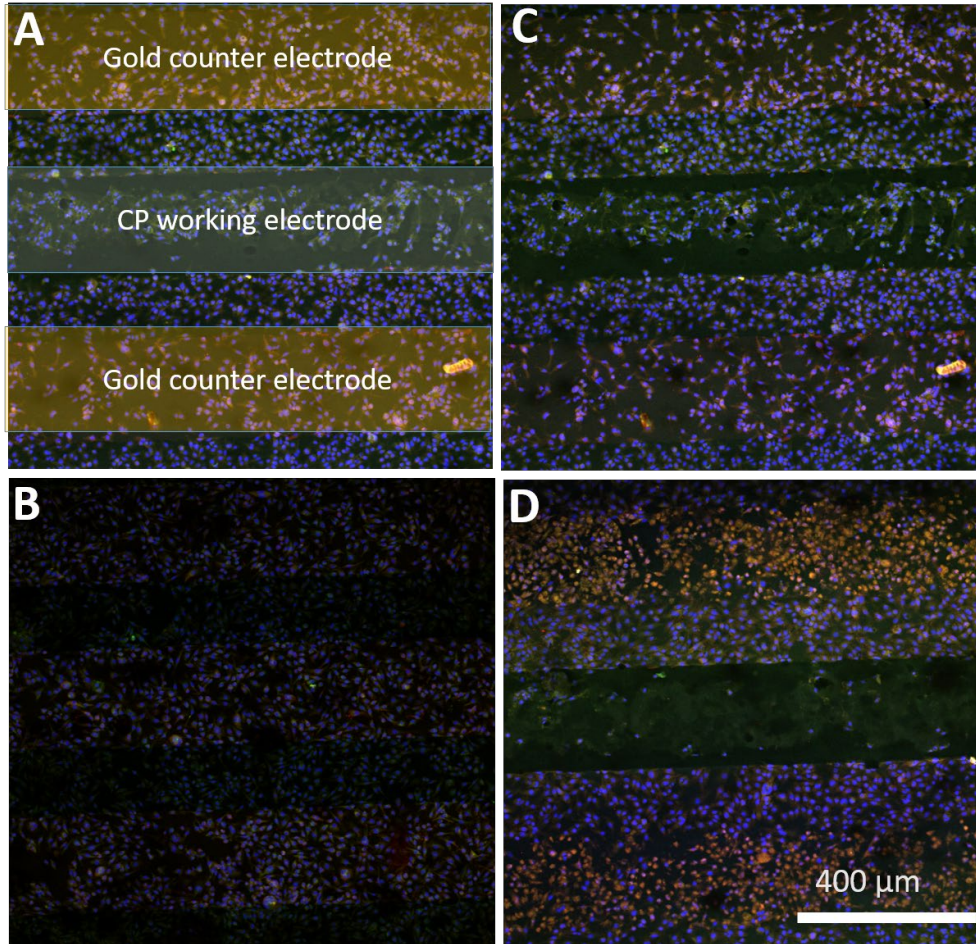


Figure A6-3 Transfection of HAPI cells through electrically released GFP-Plasmid from PEDOT-CNT films. (A) HAPI cells were plated on sensor chips with interdigitated working and counter electrodes. PEDOT-CNT-Plasmid was deposited at the CP working electrode. (B) Without electrical stimulation, there is no evidence of HAPI cell transfection. (C) After stimulation using a platinum foil counter electrode lowered into the well, there is little evidence of HAPI cell transfection. (D) After stimulation using the internal gold counter electrodes as stimulation counter electrodes, there is robust transfection apparent at the counter electrodes. Interestingly, there are few remaining cells at the conductive polymer working electrodes, which appear to have been damaged during stimulation.

A.1.2 Controlled drug release from *in situ* forming hydrogel

Controlled drug release strategies could also be effective in modulating meningeal inflammation and fibrosis. Namely, drug eluting dural sealants present as a convenient point of intervention. In bulk administration, groups have shown that drugs such as 5-fluorouracil [352], glutathione [132], and resveratrol [462] are effective in culling meningeal inflammation and fibrosis. In this section, the PEG/PEI based hydrogel described in Chapter 4 of this dissertation is tested for its efficacy in controlled drug release of resveratrol.

Prior to mixing PEG and PEI to form hydrogel, 5mg/mL resveratrol (Sigma) was mixed into the PEI solution. Solubility of resveratrol in water is poor ($\sim 100\mu\text{M}$), therefore, resveratrol largely mixed as a slurry into the gel precursor. Once mixed, the gel formed within 30s. While the gel precursor is alkaline (determined by pH strips; data not shown), we noted that PBS conditioned freshly crosslinked gel overnight was pH neutral. Neutral pH is a critical factor to the biocompatibility of the gel. Resveratrol release was detected into PBS solution via the molecule's absorbance peak (304 nm) over 7 days (Figure A6-4). PBS was collected daily and replenished with fresh PBS.

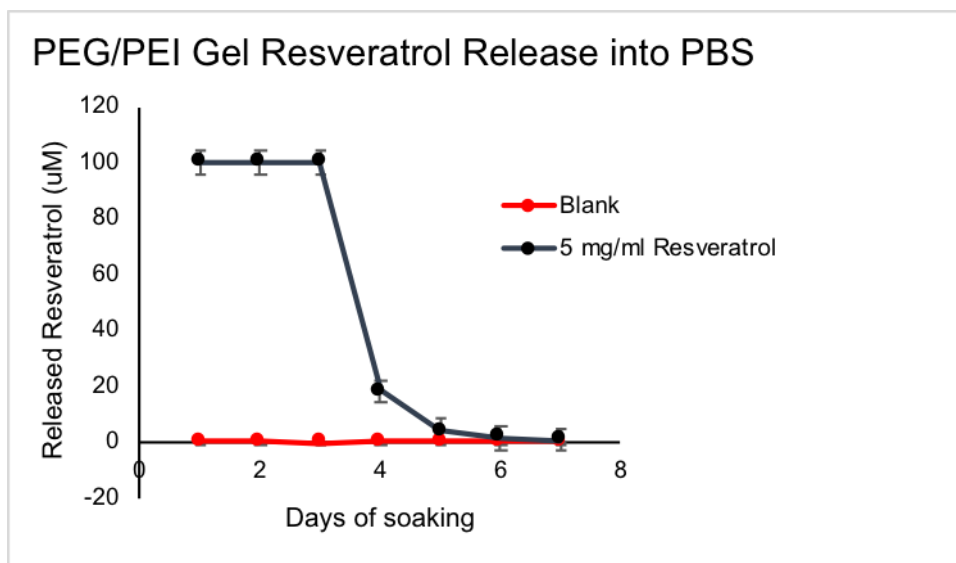


Figure A6-4 Resveratrol release from a PEG-PEI Gel into PBS.

Resveratrol release into PBS was measured from 2 gels over 1 week of soaking via spectrophotometry at 304nm absorbance. Peak detection was at 100µM. Gels saturated PBS solution for the first 3 days of release, following which release rapidly subsided. Data presented as mean ± SEM.

Released resveratrol saturated the PBS solution (100 µM) for the first 3 days of soaking and then subsided to baseline levels by 7 days. This release profile closely followed the sequence of meningeal cellular inflammation seen in Figure 4-2 of this dissertation. This suggests that release from this gel would be well matched for this application. Next, in order to test bioreactivity of released resveratrol, we conditioned cell media with resveratrol loaded PEG-PEI gels before treating HAPI cells with conditioned media for 24h. Gels were soaked for either 1, 3, or 6 days before being used to condition media. HAPI cells stimulated with lipopolysaccharide and interferon gamma prior to conditioned media treatment. We then used a live/dead cell assay to measure cell viability relative to unstimulated, untreated HAPI cells (Figure A6-5).

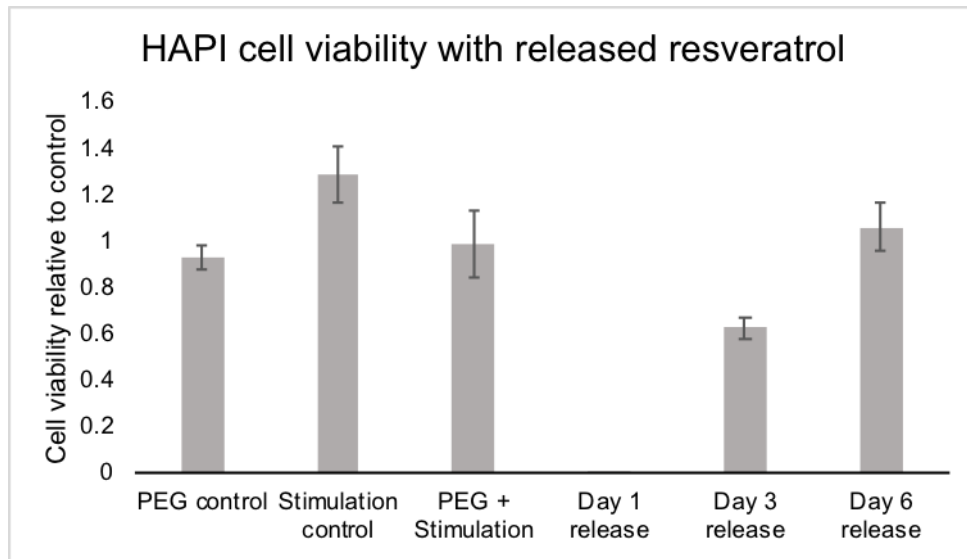


Figure A6-5 Viability of stimulated HAPI cells after treatment with released resveratrol.

HAPI cells were stimulated with lipopolysaccharide and interferon gamma and treated with PEG/PEI hydrogel treated media. Media was either conditioned with gels after 1, 3, or 6 days of soaking before HAPI cell treatment. Cell viability was measured after 24h of treatment with a live/dead assay. Low cell viability for Day 1 and Day 3 release conditions is likely due to high resveratrol dose. All data presented as mean \pm SEM; n = 3.

Media conditioned with fresh gels (Day 1 release) resulted in a high degree of cell detachment. Thus, we registered very low viability for these gels. Viability progressively increased for gels that soaked for 3 and 6 days before being used to condition media. This is not unexpected, as high doses of resveratrol have been shown to negatively affect cell survival [463]. Future studies should focus on finding the proper dosage of resveratrol for PEG/PEI gel loading, as this release system could be effective in modulating meningeal inflammation around neural electrode implants.

BIBLIOGRAPHY

- [1] E.D. Adrian, *The basis of sensation*, W W Norton & Co, New York, NY, US, 1928.
- [2] A. Djourno, C. Eyries, B. Vallancien, Electric excitation of the cochlear nerve in man by induction at a distance with the aid of micro-coil included in the fixture, *Comptes rendus des seances de la Societe de biologie et de ses filiales* 151(3) (1957) 423-5.
- [3] G.S. Brindley, W.S. Lewin, The sensations produced by electrical stimulation of the visual cortex, *The Journal of physiology* 196(2) (1968) 479-493.
- [4] C.N. Shealy, J.T. Mortimer, J.B. Reswick, Electrical inhibition of pain by stimulation of the dorsal columns: preliminary clinical report, *Anesthesia and analgesia* 46(4) (1967) 489-91.
- [5] J. Gardner, A history of deep brain stimulation: Technological innovation and the role of clinical assessment tools, *Social Studies of Science* 43(5) (2013) 707-728.
- [6] D.R. Humphrey, E.M. Schmidt, W.D. Thompson, Predicting measures of motor performance from multiple cortical spike trains, *Science* 170(3959) (1970) 758-62.
- [7] J.K. Chapin, K.A. Moxon, R.S. Markowitz, M.A. Nicolelis, Real-time control of a robot arm using simultaneously recorded neurons in the motor cortex, *Nat Neurosci* 2(7) (1999) 664-70.
- [8] J.L. Collinger, B. Wodlinger, J.E. Downey, W. Wang, E.C. Tyler-Kabara, D.J. Weber, A.J. McMorland, M. Velliste, M.L. Boninger, A.B. Schwartz, High-performance neuroprosthetic control by an individual with tetraplegia, *Lancet* 381(9866) (2012) 557-64.
- [9] W. Wang, A.D. Degenhart, J.L. Collinger, R. Vinjamuri, G.P. Sudre, P.D. Adelson, D.L. Holder, E.C. Leuthardt, D.W. Moran, M.L. Boninger, A.B. Schwartz, D.J. Crammond, E.C. Tyler-Kabara, D.J. Weber, Human motor cortical activity recorded with Micro-ECoG electrodes, during individual finger movements, *Conference proceedings : ... Annual International Conference of the IEEE Engineering in Medicine and Biology Society. IEEE Engineering in Medicine and Biology Society. Annual Conference 2009* (2009) 586-9.
- [10] L.R. Hochberg, D. Bacher, B. Jarosiewicz, N.Y. Masse, J.D. Simeral, J. Vogel, S. Haddadin, J. Liu, S.S. Cash, P. van der Smagt, J.P. Donoghue, Reach and grasp by people with tetraplegia using a neurally controlled robotic arm, *Nature* 485 (2012) 372-375.

- [11] J.D. Simeral, S.P. Kim, M.J. Black, J.P. Donoghue, L.R. Hochberg, Neural control of cursor trajectory and click by a human with tetraplegia 1000 days after implant of an intracortical microelectrode array, *J Neural Eng* 8(2) (2011) 025027.
- [12] A.B. Schwartz, X.T. Cui, D.J. Weber, D.W. Moran, Brain-controlled interfaces: movement restoration with neural prosthetics., *Neuron* 52 (2006) 205-20.
- [13] G. Buzsáki, C.A. Anastassiou, C. Koch, The origin of extracellular fields and currents — EEG, ECoG, LFP and spikes, *Nature Reviews Neuroscience* 13 (2012) 407-420.
- [14] D.T. Bundy, M. Pahwa, N. Szrama, E.C. Leuthardt, Decoding three-dimensional reaching movements using electrocorticographic signals in humans, *J Neural Eng* 13(2) (2016) 026021.
- [15] B. Wodlinger, J.E. Downey, E.C. Tyler-Kabara, A.B. Schwartz, M.L. Boninger, J.L. Collinger, Ten-dimensional anthropomorphic arm control in a human brain-machine interface: difficulties, solutions, and limitations, *J Neural Eng* 12(1) (2015) 016011.
- [16] G. Buzsáki, Large-scale recording of neuronal ensembles, *Nature Neuroscience* 7 (2004) 446-451.
- [17] K.E. Jones, P.K. Campbell, R.A. Normann, A glass/silicon composite intracortical electrode array, *Ann Biomed Eng* 20(4) (1992) 423-37.
- [18] A.C. Hoogerwerf, K.D. Wise, A three-dimensional microelectrode array for chronic neural recording, *IEEE Trans Biomed Eng* 41(12) (1994) 1136-46.
- [19] K.D. Wise, J.B. Angell, A. Starr, An integrated-circuit approach to extracellular microelectrodes, *IEEE Trans Biomed Eng* 17(3) (1970) 238-47.
- [20] T.D.Y. Kozai, X. Li, L.M. Bodily, E.M. Caparosa, G.A. Zenonos, D.L. Carlisle, R.M. Friedlander, X.T. Cui, Effects of caspase-1 knockout on chronic neural recording quality and longevity: insight into cellular and molecular mechanisms of the reactive tissue response., *Biomaterials* 35 (2014) 9620-34.
- [21] A. Prasad, Q.-S. Xue, R. Dieme, V. Sankar, R.C. Mayrand, T. Nishida, W.J. Streit, J.C. Sanchez, Abiotic-biotic characterization of Pt/Ir microelectrode arrays in chronic implants., *Frontiers in neuroengineering* 7 (2014) 2.
- [22] J.C. Williams, R.L. Rennaker, D.R. Kipke, Long-term neural recording characteristics of wire microelectrode arrays implanted in cerebral cortex, *Brain Research Protocols* 4 (1999) 303-313.
- [23] P.J. Rousche, R.A. Normann, Chronic recording capability of the Utah Intracortical Electrode Array in cat sensory cortex, *J Neurosci Methods* 82(1) (1998) 1-15.
- [24] M.A.L. Nicolelis, D. Dimitrov, J.M. Carmena, R. Crist, G. Lehew, J.D. Kralik, S.P. Wise, Chronic, multisite, multielectrode recordings in macaque monkeys, *Proceedings of the National Academy of Sciences* 100(19) (2003) 11041.

- [25] C.A. Chestek, V. Gilja, P. Nuyujukian, J.D. Foster, J.M. Fan, M.T. Kaufman, M.M. Churchland, Z. Rivera-Alvidrez, J.P. Cunningham, S.I. Ryu, K.V. Shenoy, Long-term stability of neural prosthetic control signals from silicon cortical arrays in rhesus macaque motor cortex., *Journal of neural engineering* 8 (2011) 045005.
- [26] X. Liu, D.B. McCreery, L.A. Bullara, W.F. Agnew, Evaluation of the Stability of Intracortical Microelectrode Arrays, *IEEE Transactions on Neural Systems and Rehabilitation Engineering* 14 (2006) 91-100.
- [27] J.C. Barrese, N. Rao, K. Paroo, C. Triebwasser, C. Vargas-Irwin, L. Franquemont, J.P. Donoghue, Failure mode analysis of silicon-based intracortical microelectrode arrays in non-human primates., *Journal of neural engineering* 10 (2013) 066014.
- [28] N.J. Michelson, A.L. Vazquez, J.R. Eles, J.W. Salatino, E.K. Purcell, J.J. Williams, X.T. Cui, T.D.Y. Kozai, Multi-scale, multi-modal analysis uncovers complex relationship at the brain tissue-implant neural interface: New Emphasis on the Biological Interface, *Journal of Neural Engineering* 15(033001) (2018).
- [29] O.A. Shergold, N.A. Fleck, Experimental investigation into the deep penetration of soft solids by sharp and blunt punches, with application to the piercing of skin, *J Biomech Eng* 127(5) (2005) 838-48.
- [30] A.A. Sharp, A.M. Ortega, D. Restrepo, D. Curran-Everett, K. Gall, In Vivo Penetration Mechanics and Mechanical Properties of Mouse Brain Tissue at Micrometer Scales, *IEEE Transactions on Biomedical Engineering* 56 (2009) 45-53.
- [31] B. Morrison, H.L. Cater, C.D. Benham, L.E. Sundstrom, An in vitro model of traumatic brain injury utilising two-dimensional stretch of organotypic hippocampal slice cultures, *Journal of Neuroscience Methods* 150 (2006) 192-201.
- [32] B. Morrison, H.L. Cater, C.C.-B. Wang, F.C. Thomas, C.T. Hung, G.A. Ateshian, L.E. Sundstrom, A tissue level tolerance criterion for living brain developed with an in vitro model of traumatic mechanical loading., *Stapp car crash journal* 47 (2003) 93-105.
- [33] E. Bar-Kochba, M.T. Scimone, J.B. Estrada, C. Franck, Strain and rate-dependent neuronal injury in a 3D in vitro compression model of traumatic brain injury, *Scientific Reports* 6 (2016) 30550.
- [34] D.M. Geddes, R.S. Cargill, 2nd, M.C. LaPlaca, Mechanical stretch to neurons results in a strain rate and magnitude-dependent increase in plasma membrane permeability, *J Neurotrauma* 20(10) (2003) 1039-49.
- [35] G.C. McConnell, H.D. Rees, A.I. Levey, C.-A. Gutekunst, R.E. Gross, R.V. Bellamkonda, Implanted neural electrodes cause chronic, local inflammation that is correlated with local neurodegeneration., *Journal of neural engineering* 6 (2009) 056003.

- [36] C.S. Bjornsson, S.J. Oh, Y.A. Al-Kofahi, Y.J. Lim, K.L. Smith, J.N. Turner, S. De, B. Roysam, W. Shain, S.J. Kim, Effects of insertion conditions on tissue strain and vascular damage during neuroprosthetic device insertion., *Journal of neural engineering* 3 (2006) 196-207.
- [37] T.D.Y. Kozai, T.C. Marzullo, F. Hooi, N.B. Langhals, A.K. Majewska, E.B. Brown, D.R. Kipke, Reduction of neurovascular damage resulting from microelectrode insertion into the cerebral cortex using in vivo two-photon mapping., *Journal of neural engineering* 7 (2010) 046011.
- [38] P.A. House, J.D. MacDonald, P.A. Tresco, R.A. Normann, Acute microelectrode array implantation into human neocortex: preliminary technique and histological considerations., *Neurosurgical focus* 20 (2006) E4.
- [39] A.Y. Shih, P. Blinder, P.S. Tsai, B. Friedman, G. Stanley, P.D. Lyden, D. Kleinfeld, The smallest stroke: occlusion of one penetrating vessel leads to infarction and a cognitive deficit, *Nature Neuroscience* 16 (2012) 55-63.
- [40] T.D.Y. Kozai, A.L. Vazquez, C.L. Weaver, In vivo two-photon microscopy reveals immediate microglial reaction to implantation of microelectrode through, *Journal of neural engineering* 9 (2012).
- [41] A. Andrei, M. Welkenhuysen, B. Nuttin, W. Eberle, A response surface model predicting the in vivo insertion behavior of micromachined neural implants, *Journal of Neural Engineering* 9 (2012) 016005.
- [42] F. Casanova, P.R. Carney, M. Sarntinoranont, In vivo evaluation of needle force and friction stress during insertion at varying insertion speed into the brain, *Journal of Neuroscience Methods* 237 (2014) 79-89.
- [43] N. Haj Hosseini, R. Hoffmann, S. Kisban, T. Stieglitz, O. Paul, P. Ruther, Comparative study on the insertion behavior of cerebral microprobes, 2007 29th Annual International Conference of the IEEE Engineering in Medicine and Biology Society, IEEE, 2007, pp. 4711-4714.
- [44] P.J. Rousche, R.A. Normann, A method for pneumatically inserting an array of penetrating electrodes into cortical tissue., *Annals of biomedical engineering* 20 (1992) 413-22.
- [45] W. Jensen, K. Yoshida, U.G. Hofmann, In-vivo implant mechanics of flexible, silicon-based ACREO microelectrode arrays in rat cerebral cortex, *IEEE Transactions on Biomedical Engineering* 53 (2006) 934-940.
- [46] S.M. Wellman, J.R. Eles, K.A. Ludwig, J.P. Seymour, N.J. Michelson, W.E. McFadden, A.L. Vazquez, T.D.Y. Kozai, A Materials Roadmap to Functional Neural Interface Design, *Adv Funct Mater* 28(12) (2018).
- [47] S. Singh, M.-C. Lo, V. Damodaran, H. Kaplan, J. Kohn, J. Zahn, D. Shreiber, Modeling the Insertion Mechanics of Flexible Neural Probes Coated with Sacrificial Polymers for Optimizing Probe Design, *Sensors* 16 (2016) 330.

- [48] P.R. Patel, K. Na, H. Zhang, T.D.Y. Kozai, N.A. Kotov, E. Yoon, C.A. Chestek, Insertion of linear 8.4 μm diameter 16 channel carbon fiber electrode arrays for single unit recordings., *Journal of neural engineering* 12 (2015) 046009.
- [49] T.D.Y. Kozai, K. Catt, X. Li, Z.V. Gugel, V.T. Olafsson, A.L. Vazquez, X.T. Cui, Mechanical failure modes of chronically implanted planar silicon-based neural probes for laminar recording, *Biomaterials* 37 (2015) 25-39.
- [50] M. Ravikumar, S. Sunil, J. Black, D.S. Barkauskas, A.Y. Haung, R.H. Miller, S.M. Selkirk, J.R. Capadona, The roles of blood-derived macrophages and resident microglia in the neuroinflammatory response to implanted intracortical microelectrodes., *Biomaterials* 35 (2014) 8049-64.
- [51] D.H. Szarowski, M.D. Andersen, S. Retterer, A.J. Spence, M. Isaacson, H.G. Craighead, J.N. Turner, W. Shain, Brain responses to micro-machined silicon devices., *Brain research* 983 (2003) 23-35.
- [52] P.A. Cody, J.R. Eles, C.F. Lagenaur, T.D.Y. Kozai, X.T. Cui, Unique electrophysiological and impedance signatures between encapsulation types: An analysis of biological Utah array failure and benefit of a biomimetic coating in a rat model, *Biomaterials* 161 (2018) 117-128.
- [53] K.A. Potter, A.C. Buck, W.K. Self, J.R. Capadona, Stab injury and device implantation within the brain results in inversely multiphasic neuroinflammatory and neurodegenerative responses, *J Neural Eng* 9(4) (2012) 046020.
- [54] R. Biran, D.C. Martin, P.A. Tresco, Neuronal cell loss accompanies the brain tissue response to chronically implanted silicon microelectrode arrays, *Experimental Neurology* 195 (2005) 115-126.
- [55] T.D. Kozai, N.B. Langhals, P.R. Patel, X. Deng, H. Zhang, K.L. Smith, J. Lahann, N.A. Kotov, D.R. Kipke, Ultrasmall implantable composite microelectrodes with bioactive surfaces for chronic neural interfaces, *Nat Mater* 11(12) (2012) 1065-73.
- [56] D. Davalos, J. Grutzendler, G. Yang, J.V. Kim, Y. Zuo, S. Jung, D.R. Littman, M.L. Dustin, W.-B. Gan, ATP mediates rapid microglial response to local brain injury in vivo., *Nature neuroscience* 8 (2005) 752-8.
- [57] E. Ulvestad, K. Williams, R. Matre, H. Nyland, A. Olivier, J. Antel, Fc receptors for IgG on cultured human microglia mediate cytotoxicity and phagocytosis of antibody-coated targets, *J Neuropathol Exp Neurol* 53(1) (1994) 27-36.
- [58] D. Davalos, J. Kyu Ryu, M. Merlini, K.M. Baeten, N. Le Moan, M.A. Petersen, T.J. Deerinck, D.S. Smirnoff, C. Bedard, H. Hakozaki, S. Gonias Murray, J.B. Ling, H. Lassmann, J.L. Degen, M.H. Ellisman, K. Akassoglou, Fibrinogen-induced perivascular microglial clustering is required for the development of axonal damage in neuroinflammation, *Nature Communications* 3 (2012) 1227.

- [59] A. Nadal, E. Fuentes, J. Pastor, P.A. McNaughton, Plasma albumin is a potent trigger of calcium signals and DNA synthesis in astrocytes., *Proceedings of the National Academy of Sciences of the United States of America* 92 (1995) 1426-30.
- [60] H.R. Ranaivo, M.S. Wainwright, Albumin activates astrocytes and microglia through mitogen-activated protein kinase pathways, *Brain research* 1313C (2010) 222-231.
- [61] Z. Liu, J. Liu, S. Wang, S. Liu, Y. Zhao, Neuronal uptake of serum albumin is associated with neuron damage during the development of epilepsy, *Experimental and Therapeutic Medicine* 12(2) (2016) 695-701.
- [62] T.D.Y. Kozai, J.R. Eles, A.L. Vazquez, X.T. Cui, Two-photon imaging of chronically implanted neural electrodes: Sealing methods and new insights, *Journal of Neuroscience Methods* 258 (2016) 46-55.
- [63] J.D. Falcone, S.L. Carroll, T. Saxena, D. Mandavia, A. Clark, V. Yarabarla, R.V. Bellamkonda, Correlation of mRNA Expression and Signal Variability in Chronic Intracortical Electrodes, *Frontiers in Bioengineering and Biotechnology* 6(26) (2018).
- [64] L. Karumbaiah, T. Saxena, D. Carlson, K. Patil, R. Patkar, E.A. Gaupp, M. Betancur, G.B. Stanley, L. Carin, R.V. Bellamkonda, Relationship between intracortical electrode design and chronic recording function, *Biomaterials* 34 (2013) 8061-8074.
- [65] N.F. Nolte, M.B. Christensen, P.D. Crane, J.L. Skousen, P.A. Tresco, BBB leakage, astrogliosis, and tissue loss correlate with silicon microelectrode array recording performance, *Biomaterials* 53 (2015) 753-762.
- [66] T. Saxena, L. Karumbaiah, E.A. Gaupp, R. Patkar, K. Patil, M. Betancur, G.B. Stanley, R.V. Bellamkonda, The impact of chronic blood-brain barrier breach on intracortical electrode function, *Biomaterials* 34 (2013) 4703-4713.
- [67] E.K. Purcell, J.P. Seymour, S. Yandamuri, D.R. Kipke, In vivo evaluation of a neural stem cell-seeded prosthesis., *Journal of neural engineering* 6 (2009) 026005.
- [68] S.M. Wellman, T.D.Y. Kozai, In vivo spatiotemporal dynamics of NG2 glia activity caused by neural electrode implantation, *Biomaterials* 164 (2018) 121-133.
- [69] J.N. Turner, W. Shain, D.H. Szarowski, M. Andersen, S. Martins, M. Isaacson, H. Craighead, Cerebral astrocyte response to micromachined silicon implants, *Exp Neurol* 156(1) (1999) 33-49.
- [70] R. Biran, D.C. Martin, P.A. Tresco, The brain tissue response to implanted silicon microelectrode arrays is increased when the device is tethered to the skull, *Journal of Biomedical Materials Research Part A* 82A (2007) 169-178.
- [71] A.J. Woolley, H.A. Desai, K.J. Otto, Chronic intracortical microelectrode arrays induce non-uniform, depth-related tissue responses., *Journal of neural engineering* 10 (2013) 026007.

- [72] Y.-T. Kim, R.W. Hitchcock, M.J. Bridge, P.A. Tresco, Chronic response of adult rat brain tissue to implants anchored to the skull., *Biomaterials* 25 (2004) 2229-37.
- [73] J. Thelin, H. Jörntell, E. Psouni, M. Garwicz, J. Schouenborg, N. Danielsen, C.E. Linsmeier, Implant Size and Fixation Mode Strongly Influence Tissue Reactions in the CNS, *PLoS ONE* 6 (2011) e16267.
- [74] J.P. Seymour, D.R. Kipke, Neural probe design for reduced tissue encapsulation in CNS., *Biomaterials* 28 (2007) 3594-607.
- [75] S.F. Bernatchez, P.J. Parks, D.F. Gibbons, Interaction of macrophages with fibrous materials in vitro, *Biomaterials* 17(21) (1996) 2077-2086.
- [76] J.E. Sanders, C.E. Stiles, C.L. Hayes, Tissue response to single-polymer fibers of varying diameters: Evaluation of fibrous encapsulation and macrophage density, *Journal of Biomedical Materials Research* 52 (2000) 231-237.
- [77] L. Luan, X. Wei, Z. Zhao, J.J. Siegel, O. Potnis, C.A. Tuppen, S. Lin, S. Kazmi, R.A. Fowler, S. Holloway, A.K. Dunn, R.A. Chitwood, C. Xie, Ultraflexible nanoelectronic probes form reliable, glial scar-free neural integration, *Science Advances* 3(2) (2017).
- [78] E. Fernández, B. Greger, P.A. House, I. Aranda, C. Botella, J. Albiñá, C. Soto-Sánchez, A. Alfaro, R.A. Normann, Acute human brain responses to intracortical microelectrode arrays: challenges and future prospects, *Frontiers in Neuroengineering* 7 (2014) 24.
- [79] G. Lind, L. Gällentoft, N. Danielsen, J. Schouenborg, L.M.E. Pettersson, Multiple Implants Do Not Aggravate the Tissue Reaction in Rat Brain, *PLoS ONE* 7 (2012) e47509.
- [80] A. Gilletti, J. Muthuswamy, Brain micromotion around implants in the rodent somatosensory cortex., *Journal of neural engineering* 3 (2006) 189-95.
- [81] H. Lee, R.V. Bellamkonda, W. Sun, M.E. Levenston, Biomechanical analysis of silicon microelectrode-induced strain in the brain., *Journal of neural engineering* 2 (2005) 81-9.
- [82] J. Subbaroyan, D.C. Martin, D.R. Kipke, A finite-element model of the mechanical effects of implantable microelectrodes in the cerebral cortex., *Journal of neural engineering* 2 (2005) 103-13.
- [83] Z.J. Du, C.L. Kolarcik, T.D.Y. Kozai, S.D. Luebben, S.A. Sapp, X.S. Zheng, J.A. Nabity, X.T. Cui, Ultrasoft microwire neural electrodes improve chronic tissue integration, *Acta Biomater* 53 (2017) 46-58.
- [84] S.P. Lacour, S. Benmerah, E. Tarte, J. FitzGerald, J. Serra, S. McMahon, J. Fawcett, O. Graudejus, Z. Yu, B. Morrison, Flexible and stretchable micro-electrodes for in vitro and in vivo neural interfaces., *Medical & biological engineering & computing* 48 (2010) 945-54.

- [85] T. Zhou, G. Hong, T.-M. Fu, X. Yang, T.G. Schuhmann, R.D. Viveros, C.M. Lieber, Syringe-injectable mesh electronics integrate seamlessly with minimal chronic immune response in the brain, *Proceedings of the National Academy of Sciences* 114(23) (2017) 5894.
- [86] C.L. Kolarcik, S.D. Luebben, S.A. Sapp, J. Hanner, N. Snyder, T.D.Y. Kozai, E. Chang, J.A. Nabity, S.T. Nabity, C.F. Lagenaur, X.T. Cui, Elastomeric and soft conducting microwires for implantable neural interfaces., *Soft matter* 11 (2015) 4847-61.
- [87] H.C. Lee, F. Ejserholm, J. Gaire, S. Currilin, J. Schouenborg, L. Wallman, M. Bengtsson, K. Park, K.J. Otto, Histological evaluation of flexible neural implants; flexibility limit for reducing the tissue response?, *J Neural Eng* 14(3) (2017) 036026.
- [88] T.D.Y. Kozai, Z. Gugel, X. Li, P.J. Gilgunn, R. Khilwani, O.B. Ozdoganlar, G.K. Fedder, D.J. Weber, X.T. Cui, Chronic tissue response to carboxymethyl cellulose based dissolvable insertion needle for ultra-small neural probes., *Biomaterials* 35 (2014) 9255-68.
- [89] T.D.Y. Kozai, D.R. Kipke, Insertion shuttle with carboxyl terminated self-assembled monolayer coatings for implanting flexible polymer neural probes in the brain., *Journal of neuroscience methods* 184 (2009) 199-205.
- [90] G. Lind, C.E. Linsmeier, J. Schouenborg, The density difference between tissue and neural probes is a key factor for glial scarring, *Scientific Reports* 3 (2013) 11830-11838.
- [91] L. Bollmann, D.E. Koser, R. Shahapure, H.O.B. Gautier, G.A. Holzapfel, G. Scarcelli, M.C. Gather, E. Ulbricht, K. Franze, Microglia mechanics: immune activation alters traction forces and durotaxis., *Frontiers in cellular neuroscience* 9 (2015) 363.
- [92] T.D.Y. Kozai, A.S. Jaquins-Gerstl, A.L. Vazquez, A.C. Michael, X.T. Cui, Brain Tissue Responses to Neural Implants Impact Signal Sensitivity and Intervention Strategies, *ACS Chemical Neuroscience* 6 (2015) 48-67.
- [93] A.W. Bridges, A.J. García, Anti-inflammatory polymeric coatings for implantable biomaterials and devices., *Journal of diabetes science and technology* 2 (2008) 984-94.
- [94] B.K. Leung, R. Biran, C.J. Underwood, P.A. Tresco, Characterization of microglial attachment and cytokine release on biomaterials of differing surface chemistry, *Biomaterials* 29 (2008) 3289-3297.
- [95] E. Azemi, W.R. Stauffer, M.S. Gostock, C.F. Lagenaur, X.T. Cui, Surface immobilization of neural adhesion molecule L1 for improving the biocompatibility of chronic neural probes: In vitro characterization., *Acta biomaterialia* 4 (2008) 1208-17.
- [96] J.Y. Lee, Z.Z. Khaing, J.J. Siegel, C.E. Schmidt, Surface modification of neural electrodes with a pyrrole-hyaluronic acid conjugate to attenuate reactive astrogliosis in vivo, *RSC Adv.* 5 (2015) 39228-39231.

- [97] H. Zhao, B. Zhu, S.-C. Luo, H.-A. Lin, A. Nakao, Y. Yamashita, H.-h. Yu, Controlled Protein Absorption and Cell Adhesion on Polymer-Brush-Grafted Poly(3,4-ethylenedioxythiophene) Films, *ACS Applied Materials & Interfaces* 5 (2013) 4536-4543.
- [98] Y. Hu, G. Yang, B. Liang, L. Fang, G. Ma, Q. Zhu, S. Chen, X. Ye, The fabrication of superlow protein absorption zwitterionic coating by electrochemically mediated atom transfer radical polymerization and its application, *Acta Biomaterialia* 13 (2015) 142-149.
- [99] H. Zhang, M. Chiao, Anti-fouling Coatings of Poly(dimethylsiloxane) Devices for Biological and Biomedical Applications., *Journal of medical and biological engineering* 35 (2015) 143-155.
- [100] A.W. Bridges, R.E. Whitmire, N. Singh, K.L. Templeman, J.E. Babensee, L.A. Lyon, A.J. García, Chronic inflammatory responses to microgel-based implant coatings, *Journal of Biomedical Materials Research Part A* 94A (2010) 252-258.
- [101] L. Rao, H. Zhou, T. Li, C. Li, Y.Y. Duan, Polyethylene glycol-containing polyurethane hydrogel coatings for improving the biocompatibility of neural electrodes, *Acta Biomaterialia* 8 (2012) 2233-2242.
- [102] H.C. Lee, J. Gaire, S.W. Currilin, M.D. McDermott, K. Park, K.J. Otto, Foreign Body Response to Intracortical Microelectrodes Is Not Altered with Dip-Coating of Polyethylene Glycol (PEG), *Frontiers in Neuroscience* 11 (2017) 513.
- [103] K.C. Spencer, J.C. Sy, K.B. Ramadi, A.M. Graybiel, R. Langer, M.J. Cima, Characterization of Mechanically Matched Hydrogel Coatings to Improve the Biocompatibility of Neural Implants, *Sci Rep* 7(1) (2017) 1952.
- [104] E. Azemi, C.F. Lagenaur, X.T. Cui, The surface immobilization of the neural adhesion molecule L1 on neural probes and its effect on neuronal density and gliosis at the probe/tissue interface., *Biomaterials* 32 (2011) 681-92.
- [105] C.L. Kolarcik, D. Bourbeau, E. Azemi, E. Rost, L. Zhang, C.F. Lagenaur, D.J. Weber, X.T. Cui, In vivo effects of L1 coating on inflammation and neuronal health at the electrode-tissue interface in rat spinal cord and dorsal root ganglion., *Acta biomaterialia* 8 (2012) 3561-75.
- [106] W. He, G.C. McConnell, R.V. Bellamkonda, Nanoscale laminin coating modulates cortical scarring response around implanted silicon microelectrode arrays., *Journal of neural engineering* 3 (2006) 316-26.
- [107] W.R. Stauffer, X.T. Cui, Polypyrrole doped with 2 peptide sequences from laminin, *Biomaterials* 27 (2006) 2405-2413.
- [108] K. Webb, E. Budko, T.J. Neuberger, S. Chen, M. Schachner, P.A. Tresco, Substrate-bound human recombinant L1 selectively promotes neuronal attachment and outgrowth in the presence of astrocytes and fibroblasts., *Biomaterials* 22 (2001) 1017-28.

- [109] K.A. Potter-Baker, J.K. Nguyen, K.M. Kovach, M.M. Gitomer, T.W. Srail, W.G. Stewart, J.L. Skousen, J.R. Capadona, Development of superoxide dismutase mimetic surfaces to reduce accumulation of reactive oxygen species for neural interfacing applications, *J. Mater. Chem. B* 2 (2014) 2248-2258.
- [110] J.C. Williams, J.A. Hippensteel, J. Dilgen, W. Shain, D.R. Kipke, Complex impedance spectroscopy for monitoring tissue responses to inserted neural implants., *Journal of neural engineering* 4 (2007) 410-23.
- [111] K.A. Malaga, K.E. Schroeder, P.R. Patel, Z.T. Irwin, D.E. Thompson, J. Nicole Bentley, S.F. Lempka, C.A. Chestek, P.G. Patil, Data-driven model comparing the effects of glial scarring and interface interactions on chronic neural recordings in non-human primates, *J Neural Eng* 13(1) (2016) 016010.
- [112] A. Prasad, J.C. Sanchez, Quantifying long-term microelectrode array functionality using chronic in vivo impedance testing, *J Neural Eng* 9(2) (2012) 026028.
- [113] J.C. Barrese, J. Aceros, J.P. Donoghue, Scanning electron microscopy of chronically implanted intracortical microelectrode arrays in non-human primates, *J Neural Eng* 13(2) (2016) 026003.
- [114] K.A. Potter-Baker, W.G. Stewart, W.H. Tomaszewski, C.T. Wong, W.D. Meador, N.P. Ziats, J.R. Capadona, Implications of chronic daily anti-oxidant administration on the inflammatory response to intracortical microelectrodes, *Journal of Neural Engineering* 12 (2015) 046002.
- [115] B.D.S. Clarkson, R.J. Kahoud, C.B. McCarthy, C.L. Howe, Inflammatory cytokine-induced changes in neural network activity measured by waveform analysis of high-content calcium imaging in murine cortical neurons, *Scientific Reports* 7(1) (2017) 9037.
- [116] B.D. Winslow, M.B. Christensen, W.-K. Yang, F. Solzbacher, P.A. Tresco, A comparison of the tissue response to chronically implanted Parylene-C-coated and uncoated planar silicon microelectrode arrays in rat cortex, *Biomaterials* 31 (2010) 9163-9172.
- [117] J.W. Salatino, K.A. Ludwig, T.D.Y. Kozai, E.K. Purcell, Glial responses to implanted electrodes in the brain, *Nature Biomedical Engineering* 1(11) (2017) 862-877.
- [118] J.W. Salatino, B.M. Winter, M.H. Drazin, E.K. Purcell, Functional remodeling of subtype-specific markers surrounding implanted neuroprostheses, *J Neurophysiol* 118(1) (2017) 194-202.
- [119] P. Takmakov, K. Ruda, K. Scott Phillips, I.S. Isayeva, V. Krauthamer, C.G. Welle, Rapid evaluation of the durability of cortical neural implants using accelerated aging with reactive oxygen species, *Journal of Neural Engineering* 12 (2015) 026003.
- [120] R. Caldwell, R. Sharma, P. Takmakov, M.G. Street, F. Solzbacher, P. Tathireddy, L. Rieth, Neural electrode resilience against dielectric damage may be improved by use of highly doped silicon as a conductive material, *J Neurosci Methods* 293 (2018) 210-225.

- [121] E. Patrick, M.E. Orazem, J.C. Sanchez, T. Nishida, Corrosion of tungsten microelectrodes used in neural recording applications, *Journal of Neuroscience Methods* 198 (2011) 158-171.
- [122] N.J. Michelson, A.L. Vazquez, J.R. Eles, J.W. Salatino, E.K. Purcell, J.J. Williams, X.T. Cui, T.D.Y. Kozai, Multi-scale, multi-modal analysis uncovers complex relationship at the brain tissue-implant neural interface: new emphasis on the biological interface, *J Neural Eng* 15(3) (2018) 033001.
- [123] M. Jorfi, J.L. Skousen, C. Weder, J.R. Capadona, Progress towards biocompatible intracortical microelectrodes for neural interfacing applications, *J Neural Eng* 12(1) (2015) 011001.
- [124] J.E. Downey, N. Schwed, S.M. Chase, A.B. Schwartz, J.L. Collinger, Intracortical recording stability in human brain-computer interface users, *J Neural Eng* 15(4) (2018) 046016.
- [125] J. Mestas, C.C. Hughes, Of mice and not men: differences between mouse and human immunology, *J Immunol* 172(5) (2004) 2731-8.
- [126] B.L. Wright, J.T. Lai, A.J. Sinclair, Cerebrospinal fluid and lumbar puncture: a practical review, *Journal of neurology* 259(8) (2012) 1530-45.
- [127] M. Marín-Padilla, D.S. Knopman, Developmental aspects of the intracerebral microvasculature and perivascular spaces: insights into brain response to late-life diseases., *Journal of neuropathology and experimental neurology* 70 (2011) 1060-9.
- [128] E.T. Zhang, C.B. Inman, R.O. Weller, Interrelationships of the pia mater and the perivascular (Virchow-Robin) spaces in the human cerebrum., *Journal of anatomy* 170 (1990) 111-23.
- [129] F. Bifari, V. Berton, A. Pino, M. Kusalo, G. Malpeli, M. Di Chio, E. Bersan, E. Amato, A. Scarpa, M. Krampera, G. Fumagalli, I. Decimo, Meninges harbor cells expressing neural precursor markers during development and adulthood, *Frontiers in Cellular Neuroscience* 9 (2015).
- [130] I. Decimo, G. Fumagalli, V. Berton, M. Krampera, F. Bifari, Meninges: from protective membrane to stem cell niche., *American journal of stem cells* 1 (2012) 92-105.
- [131] J.-H. Cha, H.-J. Wee, J.H. Seo, B.J. Ahn, J.-H. Park, J.-M. Yang, S.-W. Lee, O.-H. Lee, H.-J. Lee, I.H. Gelman, K. Arai, E.H. Lo, K.-W. Kim, Prompt meningeal reconstruction mediated by oxygen-sensitive AKAP12 scaffolding protein after central nervous system injury., *Nature communications* 5 (2014) 4952.
- [132] T.L. Roth, D. Nayak, T. Atanasijevic, A.P. Koretsky, L.L. Latour, D.B. McGavern, Transcranial amelioration of inflammation and cell death after brain injury., *Nature* 505 (2014) 223-8.
- [133] P.J. Lindsberg, D. Strbian, M.-L. Karjalainen-Lindsberg, Mast cells as early responders in the regulation of acute blood-brain barrier changes after cerebral ischemia and hemorrhage.,

Journal of cerebral blood flow and metabolism : official journal of the International Society of Cerebral Blood Flow and Metabolism 30 (2010) 689-702.

[134] J. Sajanti, A.S. Bjorkstrand, S. Finnila, E. Heikkinen, J. Peltonen, K. Majamaa, Increase of collagen synthesis and deposition in the arachnoid and the dura following subarachnoid hemorrhage in the rat, *Biochimica et biophysica acta* 1454(3) (1999) 209-16.

[135] P. Kivisakk, J. Imitola, S. Rasmussen, W. Elyaman, B. Zhu, R.M. Ransohoff, S.J. Khoury, Localizing central nervous system immune surveillance: Meningeal antigen-presenting cells activate T cells during experimental autoimmune encephalomyelitis, *Annals of Neurology* 65 (2009) 457-469.

[136] B.A. Plog, M. Nedergaard, The glymphatic system in CNS health and disease: past, present and future, *Annual review of pathology* 13 (2018) 379-394.

[137] E.A. Nunamaker, D.R. Kipke, An alginate hydrogel dura mater replacement for use with intracortical electrodes, *J Biomed Mater Res B Appl Biomater* 95(2) (2010) 421-9.

[138] M.C. Preul, W.D. Bichard, T.R. Muench, R.F. Spetzler, Toward Optimal Tissue Sealants for Neurosurgery: Use of a Novel Hydrogel Sealant in a Canine Durotomy Repair Model, *Neurosurgery* 53(5) (2003) 1189-1199.

[139] C. Zoia, D. Bongetta, F. Lombardi, V.M. Custodi, R. Pugliese, P. Gaetani, First Impressions about Adherus, a New Dural Sealant, *Journal of Applied Biomaterials & Functional Materials* 13(4) (2015) 372-375.

[140] A.a. Schendel, M.W. Nonte, C. Vokoun, T.J. Richner, S.K. Brodnick, F. Atry, S. Frye, P. Bostrom, R. Pashaie, S. Thongpang, K.W. Eliceiri, J.C. Williams, The effect of micro-ECoG substrate footprint on the meningeal tissue response., *Journal of neural engineering* 11 (2014) 046011.

[141] A.A. Schendel, S. Thongpang, S.K. Brodnick, T.J. Richner, B.D.B. Lindevig, L. Krugner-Higby, J.C. Williams, A cranial window imaging method for monitoring vascular growth around chronically implanted micro-ECoG devices, *Journal of Neuroscience Methods* 218 (2013) 121-130.

[142] C. Henle, M. Raab, J.G. Cordeiro, S. Doostkam, A. Schulze-Bonhage, T. Stieglitz, J. Rickert, First long term in vivo study on subdurally implanted Micro-ECoG electrodes, manufactured with a novel laser technology, *Biomedical Microdevices* 13(1) (2011) 59-68.

[143] J. Liu, W. Yu, Y. Liu, S. Chen, Y. Huang, X. Li, C. Liu, Y. Zhang, Z. Li, J. Du, C. Tang, J. Du, H. Jin, Mechanical stretching stimulates collagen synthesis via down-regulating SO(2)/AAT1 pathway, *Scientific Reports* 6 (2016) 21112.

[144] S. Van Linthout, K. Miteva, C. Tschape, Crosstalk between fibroblasts and inflammatory cells, *Cardiovascular Research* 102 (2014) 258-269.

- [145] J.C. Doloff, O. Veiseh, A.J. Vegas, H.H. Tam, S. Farah, M. Ma, J. Li, A. Bader, A. Chiu, A. Sadraei, S. Aresta-Dasilva, M. Griffin, S. Jhunjhunwala, M. Webber, S. Siebert, K. Tang, M. Chen, E. Langan, N. Dholokia, R. Thakrar, M. Qi, J. Oberholzer, D.L. Greiner, R. Langer, D.G. Anderson, Colony stimulating factor-1 receptor is a central component of the foreign body response to biomaterial implants in rodents and non-human primates, *Nature Materials* 16 (2017) 671.
- [146] V.V. Gusel'nikova, D.E. Korzhevskiy, NeuN As a Neuronal Nuclear Antigen and Neuron Differentiation Marker, *Acta Naturae* 7(2) (2015) 42-47.
- [147] G.E. Hoffman, M.S. Smith, J.G. Verbalis, c-Fos and related immediate early gene products as markers of activity in neuroendocrine systems, *Frontiers in neuroendocrinology* 14(3) (1993) 173-213.
- [148] J. Moss, T. Ryder, T.Z. Aziz, M.B. Graeber, P.G. Bain, Electron microscopy of tissue adherent to explanted electrodes in dystonia and Parkinson's disease, *Brain* 127(Pt 12) (2004) 2755-63.
- [149] A. Nimmerjahn, F. Kirchhoff, F. Helmchen, Resting microglial cells are highly dynamic surveillants of brain parenchyma in vivo., *Science (New York, N.Y.)* 308 (2005) 1314-8.
- [150] L. Fourgeaud, P.G. Través, Y. Tufail, H. Leal-Bailey, E.D. Lew, P.G. Burrola, P. Callaway, A. Zagórska, C.V. Rothlin, A. Nimmerjahn, G. Lemke, TAM receptors regulate multiple features of microglial physiology, *Nature* 532 (2016) 240-244.
- [151] N. Stence, M. Waite, M.E. Dailey, Dynamics of microglial activation: a confocal time-lapse analysis in hippocampal slices, *Glia* 33(3) (2001) 256-66.
- [152] S. Bardehle, M. Kruger, F. Buggenthin, J. Schwausch, J. Ninkovic, H. Clevers, H.J. Snippert, F.J. Theis, M. Meyer-Luehmann, I. Bechmann, L. Dimou, M. Gotz, Live imaging of astrocyte responses to acute injury reveals selective juxtavascular proliferation, *Nat Neurosci* 16(5) (2013) 580-6.
- [153] D.S. Richardson, J.W. Lichtman, Clarifying Tissue Clearing, *Cell* 162(2) (2015) 246-257.
- [154] M.L. Berlanga, S. Phan, E.A. Bushong, S. Wu, O. Kwon, B.S. Phung, S. Lamont, M. Terada, T. Tasdizen, M.E. Martone, M.H. Ellisman, Three-Dimensional Reconstruction of Serial Mouse Brain Sections: Solution for Flattening High-Resolution Large-Scale Mosaics, *Frontiers in Neuroanatomy* 5 (2011) 17.
- [155] Mikael J. Pittet, R. Weissleder, Intravital Imaging, *Cell* 147(5) (2011) 983-991.
- [156] D.W. Carmichael, J.S. Thornton, R. Rodionov, R. Thornton, A. McEvoy, P.J. Allen, L. Lemieux, Safety of localizing epilepsy monitoring intracranial electroencephalograph electrodes using MRI: Radiofrequency-induced heating, *Journal of Magnetic Resonance Imaging* 28(5) (2008) 1233-1244.

- [157] J.D. Weiland, B. Faraji, R.J. Greenberg, M.S. Humayun, F.G. Shellock, Assessment of MRI issues for the Argus II retinal prosthesis, *Magnetic resonance imaging* 30(3) (2012) 382-9.
- [158] Q. Zeng, Q. Wang, J. Zheng, W. Kainz, J. Chen, Evaluation of MRI RF electromagnetic field induced heating near leads of cochlear implants, *Physics in medicine and biology* 63(13) (2018) 135020.
- [159] Y. Xie, N. Martini, C. Hassler, R.D. Kirch, T. Stieglitz, A. Seifert, U.G. Hofmann, In vivo monitoring of glial scar proliferation on chronically implanted neural electrodes by fiber optical coherence tomography, *Front Neuroeng* 7 (2014) 34.
- [160] D.X. Hammer, A. Lozzi, E. Abliz, N. Greenbaum, A. Agrawal, V. Krauthamer, C.G. Welle, Longitudinal vascular dynamics following cranial window and electrode implantation measured with speckle variance optical coherence angiography, *Biomedical Optics Express* 5(8) (2014) 2823-2836.
- [161] W. Denk, J.H. Strickler, W.W. Webb, Two-photon laser scanning fluorescence microscopy, *Science* 248(4951) (1990) 73.
- [162] N.G. Horton, K. Wang, D. Kobat, C.G. Clark, F.W. Wise, C.B. Schaffer, C. Xu, In vivo three-photon microscopy of subcortical structures within an intact mouse brain, *Nature Photonics* 7 (2013) 205.
- [163] H.T. Xu, F. Pan, G. Yang, W.B. Gan, Choice of cranial window type for in vivo imaging affects dendritic spine turnover in the cortex, *Nat Neurosci* 10(5) (2007) 549-51.
- [164] G. Yang, F. Pan, C.N. Parkhurst, J. Grutzendler, W.-B. Gan, Thinned-skull cranial window technique for long-term imaging of the cortex in live mice, *Nature protocols* 5(2) (2010) 201-208.
- [165] T.D.Y. Kozai, A.S. Jaquins-gerstl, A.L. Vazquez, A.C. Michael, X.T. Cui, Dexamethasone retrodialysis attenuates microglial response to implanted probes in vivo, *Biomaterials* 87 (2016) 157-169.
- [166] J.R. Eles, A.L. Vazquez, T.D.Y. Kozai, X.T. Cui, In vivo imaging of neuronal calcium during electrode implantation: Spatial and temporal mapping of damage and recovery, *Biomaterials* 174 (2018) 79-94.
- [167] A.B. Schwartz, Cortical neural prosthetics., *Annual review of neuroscience* 27 (2004) 487-507.
- [168] D.R. Kipke, W. Shain, G. Buzsaki, E. Fetz, J.M. Henderson, J.F. Hetke, G. Schalk, Advanced Neurotechnologies for Chronic Neural Interfaces: New Horizons and Clinical Opportunities, *Journal of Neuroscience* 28 (2008) 11830-11838.
- [169] D.M. Brandman, S.S. Cash, L.R. Hochberg, Review: Human Intracortical recording and neural decoding for brain-computer interfaces, *IEEE Trans Neural Syst Rehabil Eng* (2017).

- [170] B. Iordanova, A.L. Vazquez, T.D.Y. Kozai, M. Fukuda, S.G. Kim, Optogenetic investigation of the variable neurovascular coupling along the interhemispheric circuits *Journal of Cerebral Blood Flow & Metabolism* 38(4) (2018) 627-640.
- [171] S.M. Wellman, T.D.Y. Kozai, Understanding the Inflammatory Tissue Reaction to Brain Implants To Improve Neurochemical Sensing Performance, *ACS Chemical Neuroscience* (2017).
- [172] T.D.Y. Kozai, A. Jaquins-Gerstl, A.L. Vazquez, A.C. Michael, X.T. Cui, Brain Tissue Responses to Neural Implants Impact Signal Sensitivity and Intervention Strategies, *ACS Chemical Neuroscience* 6(1) (2015) 48-67.
- [173] T.D.Y. Kozai, Z. Gugel, X. Li, P.J. Gilgunn, R. Khilwani, O.B. Ozdoganlar, G.K. Fedder, D.J. Weber, X.T. Cui, Chronic tissue response to carboxymethyl cellulose based dissolvable insertion needle for ultra-small neural probes, *Biomaterials* 35(34) (2014) 9255-68.
- [174] S.M. Wellman, T.D.Y. Kozai, In vivo spatiotemporal dynamics of NG2 glia activity caused by neural electrode implantation, *Biomaterials* 164 (2018) 121-133.
- [175] D.A. Henze, Z. Borhegyi, J. Csicsvari, A. Mamiya, K.D. Harris, G. Buzsáki, Intracellular Features Predicted by Extracellular Recordings in the Hippocampus In Vivo, *Journal of Neurophysiology* 84 (2000).
- [176] T.D.Y. Kozai, Z. Du, Z.V. Gugel, M.A. Smith, S.M. Chase, L.M. Bodily, E.M. Caparosa, R.M. Friedlander, X.T. Cui, Comprehensive chronic laminar single-unit, multi-unit, and local field potential recording performance with planar single shank electrode arrays, *Journal of Neuroscience Methods* 242(1) (2015) 15-40.
- [177] J.R. Eles, A.L. Vazquez, N.R. Snyder, C.F. Lagenaur, M.C. Murphy, T.D.Y. Kozai, X.T. Cui, Neuroadhesive L1 coating attenuates acute microglial attachment to neural electrodes as revealed by live two-photon microscopy, *Biomaterials* 113 (2017) 279-292.
- [178] H. Dana, T.W. Chen, A. Hu, B.C. Shields, C. Guo, L.L. Looger, D.S. Kim, K. Svoboda, Thy1-GCaMP6 transgenic mice for neuronal population imaging in vivo, *PLoS One* 9(9) (2014) e108697.
- [179] G. Zündorf, G. Reiser, Calcium Dysregulation and Homeostasis of Neural Calcium in the Molecular Mechanisms of Neurodegenerative Diseases Provide Multiple Targets for Neuroprotection, *Antioxidants & Redox Signaling* 14(7) (2011) 1275-1288.
- [180] P.R. Williams, B.N. Marincu, C.D. Sorbara, C.F. Mahler, A.M. Schumacher, O. Griesbeck, M. Kerschensteiner, T. Misgeld, A recoverable state of axon injury persists for hours after spinal cord contusion in vivo, *Nat Commun* 5 (2014) 5683.
- [181] W.L. Maxwell, J.T. Povlishock, D.L. Graham, A mechanistic analysis of nondisruptive axonal injury: a review, *J Neurotrauma* 14(7) (1997) 419-40.

- [182] J.A. Wolf, P.K. Stys, T. Lusardi, D. Meaney, D.H. Smith, Traumatic axonal injury induces calcium influx modulated by tetrodotoxin-sensitive sodium channels, *J Neurosci* 21(6) (2001) 1923-30.
- [183] Y. Deng, B. Kim, X. He, S. Kim, C. Lu, H. Wang, S.-G. Cho, Y. Hou, J. Li, X. Zhao, Q.R. Lu, Direct Visualization of Membrane Architecture of Myelinating Cells in Transgenic Mice Expressing Membrane-Anchored EGFP, *Genesis (New York, N.Y. : 2000)* 52(4) (2014) 341-349.
- [184] G. Feng, R.H. Mellor, M. Bernstein, C. Keller-Peck, Q.T. Nguyen, M. Wallace, J.M. Nerbonne, J.W. Lichtman, J.R. Sanes, Imaging neuronal subsets in transgenic mice expressing multiple spectral variants of GFP, *Neuron* 28(1) (2000) 41-51.
- [185] B. Iordanova, A.L. Vazquez, A.J. Poplawsky, M. Fukuda, S.G. Kim, Neural and hemodynamic responses to optogenetic and sensory stimulation in the rat somatosensory cortex, *J Cereb Blood Flow Metab* 35(6) (2015) 922-32.
- [186] K.J. Otto, M.D. Johnson, D.R. Kipke, Voltage pulses change neural interface properties and improve unit recordings with chronically implanted microelectrodes, *Ieee T Bio-Med Eng* 53(2) (2006) 333-340.
- [187] M.D. Johnson, K.J. Otto, D.R. Kipke, Repeated Voltage Biasing Improves Unit Recordings by Reducing Resistive Tissue Impedances, *IEEE Transactions on Neural Systems and Rehabilitation Engineering* 13(2) (2005) 160-165.
- [188] S. Saalfeld, *Interactive Stack Rotation*, 2010.
- [189] A.J. Canty, L.M. Teles-Grilo Ruivo, C. Nesarajah, S. Song, J.S. Jackson, G.E. Little, V. De Paola, Synaptic elimination and protection after minimal injury depend on cell type and their prelesion structural dynamics in the adult cerebral cortex, *J Neurosci* 33(25) (2013) 10374-83.
- [190] N.J. Michelson, A.L. Vazquez, J.R. Eles, J.W. Salatino, E.K. Purcell, J.J. Williams, X.T. Cui, T.D.Y. Kozai, Multi-scale, multi-modal analysis uncovers complex relationship at the brain tissue-implant neural interface: New Emphasis on the Biological Interface, *Journal of Neural Engineering* (2017).
- [191] T. Ridler, S. Calvard, Picture Thresholding Using an Iterative Selection Method, *IEEE Transactions on Systems, Man, and Cybernetics* 8 (1978) 630-632.
- [192] E. Tibau, M. Valencia, J. Soriano, Identification of neuronal network properties from the spectral analysis of calcium imaging signals in neuronal cultures, *Frontiers in Neural Circuits* 7 (2013) 199.
- [193] P. Uhlen, Spectral analysis of calcium oscillations, *Science's STKE : signal transduction knowledge environment* 2004(258) (2004) p115.

- [194] E. Farkas, R. Pratt, F. Sengpiel, T.P. Obrenovitch, Direct, live imaging of cortical spreading depression and anoxic depolarisation using a fluorescent, voltage-sensitive dye, *J Cereb Blood Flow Metab* 28(2) (2008) 251-62.
- [195] T.P. Patel, S.C. Ventre, D.F. Meaney, Dynamic changes in neural circuit topology following mild mechanical injury in vitro, *Ann Biomed Eng* 40(1) (2012) 23-36.
- [196] G.R. Prado, J.D. Ross, S.P. DeWeerth, M.C. LaPlaca, Mechanical trauma induces immediate changes in neuronal network activity, *J Neural Eng* 2(4) (2005) 148-58.
- [197] Q. Chen, J. Cichon, W. Wang, L. Qiu, S.-Jin R. Lee, Nolan R. Campbell, N. DeStefino, Michael J. Goard, Z. Fu, R. Yasuda, Loren L. Looger, Benjamin R. Arenkiel, W.-B. Gan, G. Feng, Imaging Neural Activity Using Thy1-GCaMP Transgenic Mice, *Neuron* 76(2) (2012) 297-308.
- [198] L. Tian, S.A. Hires, T. Mao, D. Huber, M.E. Chiappe, S.H. Chalasani, L. Petreanu, J. Akerboom, S.A. McKinney, E.R. Schreiter, C.I. Bargmann, V. Jayaraman, K. Svoboda, L.L. Looger, Imaging neural activity in worms, flies and mice with improved GCaMP calcium indicators, *Nature methods* 6(12) (2009) 875-881.
- [199] M.J. Whalen, T. Dalkara, Z. You, J. Qiu, D. Bempohl, N. Mehta, B. Suter, P.G. Bhide, E.H. Lo, M. Ericsson, M.A. Moskowitz, Acute plasmalemma permeability and protracted clearance of injured cells after controlled cortical impact in mice, *Journal of cerebral blood flow and metabolism : official journal of the International Society of Cerebral Blood Flow and Metabolism* 28(3) (2008) 490-505.
- [200] M.D. Tang-Schomer, V.E. Johnson, P.W. Baas, W. Stewart, D.H. Smith, Partial interruption of axonal transport due to microtubule breakage accounts for the formation of periodic varicosities after traumatic axonal injury, *Experimental neurology* 213 (2012) 364--372.
- [201] M.D. Tang-Schomer, A.R. Patel, P.W. Baas, D.H. Smith, Mechanical breaking of microtubules in axons during dynamic stretch injury underlies delayed elasticity, microtubule disassembly, and axon degeneration, *The FASEB Journal* 24 (2010) 1401-1410.
- [202] T.P. Patel, S.C. Ventre, D. Geddes-Klein, P.K. Singh, D.F. Meaney, Single-Neuron NMDA Receptor Phenotype Influences Neuronal Rewiring and Reintegration following Traumatic Injury, *The Journal of Neuroscience* 34(12) (2014) 4200-4213.
- [203] V.E. Johnson, W. Stewart, D.H. Smith, Axonal Pathology in Traumatic Brain Injury, *Experimental neurology* 246 (2013) 35-43.
- [204] S.M. Wellman, J.R. Eles, K.A. Ludwig, J.P. Seymour, N.J. Michelson, W.E. McFadden, A.L. Vazquez, T.D.Y. Kozai, A Materials Roadmap to Functional Neural Interface Design, *Advanced Functional Materials* 1701269-n/a.
- [205] D.R. Kramer, T. Fujii, I. Ohiorhenuan, C.Y. Liu, Cortical spreading depolarization: Pathophysiology, implications, and future directions, *Journal of clinical neuroscience : official journal of the Neurosurgical Society of Australasia* 24 (2016) 22-7.

- [206] A.D. Degenhart, J. Eles, R. Dum, J.L. Mischel, I. Smalianchuk, B. Endler, R.C. Ashmore, E.C. Tyler-Kabara, N.G. Hatsopoulos, W. Wang, A.P. Batista, X.T. Cui, Histological evaluation of a chronically-implanted electrocorticographic electrode grid in a non-human primate., *Journal of neural engineering* 13 (2016) 046019.
- [207] P.A. Cody, J.R. Eles, C.F. Lagenaur, T.D. Kozai, X.T. Cui, Unique electrophysiological and impedance signatures between encapsulation types: An analysis of biological Utah array failure and benefit of a biomimetic coating in a rat model, *Biomaterials* 161 (2018) 117-128.
- [208] S.M. Wellman, J.R. Eles, K.A. Ludwig, J.P. Seymour, N.J. Michelson, W.E. McFadden, A.L. Vazquez, T.D. Kozai, A Materials Roadmap to Functional Neural Interface Design, *Advanced Functional Materials* 28(12) (2018) 201701269.
- [209] J.E. Greer, J.T. Povlishock, K.M. Jacobs, Electrophysiological Abnormalities in both Axotomized and Nonaxotomized Pyramidal Neurons following Mild Traumatic Brain Injury, *The Journal of Neuroscience* 32(12) (2012) 6682-6687.
- [210] P.W. Wright, L.M. Brier, A.Q. Bauer, G.A. Baxter, A.W. Kraft, M.D. Reisman, A.R. Bice, A.Z. Snyder, J.M. Lee, J.P. Culver, Functional connectivity structure of cortical calcium dynamics in anesthetized and awake mice, *PLoS One* 12(10) (2017) e0185759.
- [211] D.S. Alwis, E.B. Yan, M.C. Morganti-Kossmann, R. Rajan, Sensory cortex underpinnings of traumatic brain injury deficits, *PLoS One* 7(12) (2012) e52169.
- [212] D. Cantu, K. Walker, L. Andresen, A. Taylor-Weiner, D. Hampton, G. Tesco, C.G. Dulla, Traumatic Brain Injury Increases Cortical Glutamate Network Activity by Compromising GABAergic Control, *Cerebral cortex (New York, N.Y. : 1991)* 25(8) (2015) 2306-20.
- [213] S.F. Carron, D.S. Alwis, R. Rajan, Traumatic Brain Injury and Neuronal Functionality Changes in Sensory Cortex, *Frontiers in Systems Neuroscience* 10(47) (2016).
- [214] K.D. Hall, J. Lifshitz, Diffuse traumatic brain injury initially attenuates and later expands activation of the rat somatosensory whisker circuit concomitant with neuroplastic responses, *Brain Res* 1323 (2010) 161-73.
- [215] A. Sridharan, S.D. Rajan, J. Muthuswamy, Long-term changes in the material properties of brain tissue at the implant–tissue interface, *Journal of Neural Engineering* 10 (2013) 066001.
- [216] T.D.Y. Kozai, A.L. Vazquez, Photoelectric artefact from optogenetics and imaging on microelectrodes and bioelectronics: New Challenges and Opportunities, *Journal of Materials Chemistry B* 3 (2015) 4965-4978.
- [217] T.D.Y. Kozai, N.A. Alba, H. Zhang, N.A. Kotov, R.A. Gaunt, X.T. Cui, Nanostructured Coatings for Improved Charge Delivery to Neurons, in: M. De Vittorio, L. Martiradonna, J. Assad (Eds.), *Nanotechnology and Neuroscience: Nano-electronic, Photonic and Mechanical Neuronal Interfacing*, Springer New York, New York, NY, 2014, pp. 71-134.

- [218] S.F. Cogan, K.A. Ludwig, C.G. Welle, P. Takmakov, Tissue damage thresholds during therapeutic electrical stimulation, *Journal of Neural Engineering* 13(2) (2016) 021001.
- [219] D.R. Merrill, M. Bikson, J.G. Jefferys, Electrical stimulation of excitable tissue: design of efficacious and safe protocols, *Journal of Neuroscience Methods* 141(2) (2005) 171-98.
- [220] S.F. Cogan, A.A. Guzelian, W.F. Agnew, T.G. Yuen, D.B. McCreery, Over-pulsing degrades activated iridium oxide films used for intracortical neural stimulation, *Journal of Neuroscience Methods* 137(2) (2004) 141-50.
- [221] C.Q. Huang, P.M. Carter, R.K. Shepherd, Stimulus induced pH changes in cochlear implants: an in vitro and in vivo study, *Ann Biomed Eng* 29(9) (2001) 791-802.
- [222] D.R. Merrill, M. Bikson, J.G. Jefferys, Electrical stimulation of excitable tissue: design of efficacious and safe protocols, *J Neurosci Methods* 141(2) (2005) 171-98.
- [223] M.H. Histed, V. Bonin, R.C. Reid, Direct activation of sparse, distributed populations of cortical neurons by electrical microstimulation, *Neuron* 63(4) (2009) 508-22.
- [224] A. Sinning, C.A. Hubner, Minireview: pH and synaptic transmission, *FEBS letters* 587(13) (2013) 1923-8.
- [225] R. Shi, Polyethylene glycol repairs membrane damage and enhances functional recovery: a tissue engineering approach to spinal cord injury, *Neuroscience Bulletin* 29(4) (2013) 460-466.
- [226] P. Smucker, S.K. Hekmatyar, N. Bansal, R.B. Rodgers, S.A. Shapiro, R.B. Borgens, Intravenous polyethylene glycol successfully treats severe acceleration-induced brain injury in rats as assessed by magnetic resonance imaging, *Neurosurgery* 64(5) (2009) 984-90; discussion 990.
- [227] J.G. Moloughney, N. Weisleder, Poloxamer 188 (P188) as a Membrane Resealing Reagent in Biomedical Applications, *Recent patents on biotechnology* 6(3) (2012) 200-211.
- [228] T.D.Y. Kozai, K. Catt, Z. Du, K. Na, O. Srivannavit, R.-U.M. Haque, J. Seymour, K.D. Wise, E. Yoon, X.T. Cui, Chronic In Vivo Evaluation of PEDOT/CNT for Stable Neural Recordings., *IEEE transactions on bio-medical engineering* 63 (2016) 111-9.
- [229] T.D.Y. Kozai, N.B. Langhals, P.R. Patel, X. Deng, H. Zhang, K.L. Smith, J. Lahann, N.A. Kotov, D.R. Kipke, Ultrasmall implantable composite microelectrodes with bioactive surfaces for chronic neural interfaces, *Nat Mater* 11(12) (2012) 1065-73.
- [230] P.R. Patel, H. Zhang, M.T. Robbins, J.B. Nofar, S.P. Marshall, M.J. Kobylarek, T.D.Y. Kozai, N.A. Kotov, C.A. Chestek, Chronic In Vivo Stability Assessment of Carbon Fiber Microelectrode Arrays, *J Neural Eng* 13(6) (2016) 066002.
- [231] P.R. Patel, K. Na, H. Zhang, T.D.Y. Kozai, N.A. Kotov, E. Yoon, C.A. Chestek, Insertion of linear 8.4 μ m diameter 16 channel carbon fiber electrode arrays for single unit recordings, *Journal of Neural Engineering* 12(4) (2015).

- [232] E. Azemi, G.T. Gobbel, X.T. Cui, Seeding neural progenitor cells on silicon-based neural probes, *J Neurosurg* 113(3) (2010) 673-81.
- [233] X. Luo, C. Matranga, S. Tan, N. Alba, X.T. Cui, Carbon nanotube nanoreservoir for controlled release of anti-inflammatory dexamethasone, *Biomaterials* 32(26) (2011) 6316-23.
- [234] R. Wadhwa, C.F. Lagenaur, X.T. Cui, Electrochemically controlled release of dexamethasone from conducting polymer polypyrrole coated electrode, *Journal of Controlled Release* 110 (2006) 531-541.
- [235] C.L. Weaver, J.M. LaRosa, X. Luo, X.T. Cui, Electrically Controlled Drug Delivery from Graphene Oxide Nanocomposite Films, *ACS Nano* 8(2) (2014) 1834-1843.
- [236] R.L. Rennaker, J. Miller, H. Tang, D.A. Wilson, Minocycline increases quality and longevity of chronic neural recordings, *J Neural Eng* 4(2) (2007) L1-5.
- [237] K.A. Potter, A.C. Buck, W.K. Self, M.E. Callanan, S. Sunil, J.R. Capadona, The effect of resveratrol on neurodegeneration and blood brain barrier stability surrounding intracortical microelectrodes, *Biomaterials* 34(29) (2013) 7001-15.
- [238] Y. Zhong, R.V. Bellamkonda, Controlled release of anti-inflammatory agent alpha-MSH from neural implants, *J Control Release* 106(3) (2005) 309-18.
- [239] K. Birmingham, V. Gradinaru, P. Anikeeva, W.M. Grill, V. Piskov, B. McLaughlin, P. Pasricha, D. Weber, K. Ludwig, K. Famm, Bioelectronic medicines: a research roadmap, *Nat Rev Drug Discov* 13 (2014) 399-400.
- [240] S.F. Cogan, K.A. Ludwig, C.G. Welle, P. Takmakov, Tissue damage thresholds during therapeutic electrical stimulation, *Journal of Neural Engineering* 13 (2016) 021001.
- [241] T.D.Y. Kozai, A.L. Vazquez, Photoelectric artefact from optogenetics and imaging on microelectrodes and bioelectronics: new challenges and opportunities, *J. Mater. Chem. B* 3 (2015) 4965-4978.
- [242] C.A. Chestek, V. Gilja, C.H. Blabe, B.L. Foster, K.V. Shenoy, J. Parvizi, J.M. Henderson, Hand posture classification using electrocorticography signals in the gamma band over human sensorimotor brain areas., *Journal of neural engineering* 10 (2013) 026002.
- [243] G.W. Fraser, S.M. Chase, A. Whitford, A.B. Schwartz, Control of a brain-computer interface without spike sorting., *Journal of neural engineering* 6 (2009) 055004.
- [244] X. Jia, M.A. Smith, A. Kohn, Stimulus selectivity and spatial coherence of gamma components of the local field potential., *The Journal of neuroscience : the official journal of the Society for Neuroscience* 31 (2011) 9390-403.
- [245] T.D.Y. Kozai, Z. Du, Z.V. Gugel, M.A. Smith, S.M. Chase, L.M. Bodily, E.M. Caparosa, R.M. Friedlander, X.T. Cui, Comprehensive chronic laminar single-unit, multi-unit, and local

field potential recording performance with planar single shank electrode arrays, *Journal of Neuroscience Methods* 242 (2015) 15-40.

[246] K. Mizuseki, S. Royer, K. Diba, G. Buzsáki, Activity dynamics and behavioral correlates of CA3 and CA1 hippocampal pyramidal neurons., *Hippocampus* 22 (2012) 1659-80.

[247] D.R. Kipke, R.J. Vetter, J.C. Williams, J.F. Hetke, Silicon-substrate intracortical microelectrode arrays for long-term recording of neuronal spike activity in cerebral cortex, *IEEE Transactions on Neural Systems and Rehabilitation Engineering* 11 (2003) 151-155.

[248] S.F. Cogan, A.A. Guzelian, W.F. Agnew, T.G.H. Yuen, D.B. McCreery, Over-pulsing degrades activated iridium oxide films used for intracortical neural stimulation, *Journal of Neuroscience Methods* 137 (2004) 141-150.

[249] P.J. Gilgunn, X.C. Ong, S.N. Flesher, A.B. Schwartz, R.A. Gaunt, Structural analysis of explanted microelectrode arrays, 2013 6th International IEEE/EMBS Conference on Neural Engineering (NER), IEEE, 2013, pp. 719-722.

[250] E. Jan, J.L. Hendricks, V. Husaini, S.M. Richardson-Burns, A. Sereno, D.C. Martin, N.A. Kotov, Layered carbon nanotube-polyelectrolyte electrodes outperform traditional neural interface materials., *Nano letters* 9 (2009) 4012-8.

[251] T.D.Y. Kozai, N.A. Alba, H. Zhang, N.A. Kotov, R.A. Gaunt, X.T. Cui, Nanostructured Coatings for Improved Charge Delivery to Neurons, *Nanotechnology and Neuroscience: Nano-electronic, Photonic and Mechanical Neuronal Interfacing*, Springer New York, New York, NY, 2014, pp. 71-134.

[252] X. Luo, C.L. Weaver, D.D. Zhou, R. Greenberg, X.T. Cui, Highly stable carbon nanotube doped poly(3,4-ethylenedioxythiophene) for chronic neural stimulation., *Biomaterials* 32 (2011) 5551-7.

[253] C.C. McIntyre, W.M. Grill, Selective microstimulation of central nervous system neurons., *Annals of biomedical engineering* 28 (2000) 219-33.

[254] T. Ware, D. Simon, C. Liu, T. Musa, S. Vasudevan, A. Sloan, E.W. Keefer, R.L. Rennaker, W. Voit, Thiol-ene/acrylate substrates for softening intracortical electrodes., *Journal of biomedical materials research. Part B, Applied biomaterials* 102 (2014) 1-11.

[255] B.J. Kim, E.P. Washabaugh, E. Meng, Annealing effects on flexible multi-layered parylene-based sensors, 2014 IEEE 27th International Conference on Micro Electro Mechanical Systems (MEMS), IEEE, 2014, pp. 825-828.

[256] J.P. Seymour, Y.M. Elkasabi, H.-Y. Chen, J. Lahann, D.R. Kipke, The insulation performance of reactive parylene films in implantable electronic devices., *Biomaterials* 30 (2009) 6158-67.

[257] L. Karumbaiah, S.E. Norman, N.B. Rajan, S. Anand, T. Saxena, M. Betancur, R. Patkar, R.V. Bellamkonda, The upregulation of specific interleukin (IL) receptor antagonists and

paradoxical enhancement of neuronal apoptosis due to electrode induced strain and brain micromotion., *Biomaterials* 33 (2012) 5983-96.

[258] K.A. Ludwig, N.B. Langhals, M.D. Joseph, S.M. Richardson-Burns, J.L. Hendricks, D.R. Kipke, Poly(3,4-ethylenedioxythiophene) (PEDOT) polymer coatings facilitate smaller neural recording electrodes., *Journal of neural engineering* 8 (2011) 014001.

[259] J.P. Seymour, N.B. Langhals, D.J. Anderson, D.R. Kipke, Novel multi-sided, microelectrode arrays for implantable neural applications, *Biomedical microdevices* 13(3) (2011) 441-451.

[260] N.A. Alba, Z.J. Du, K.A. Catt, T.D.Y. Kozai, X.T. Cui, In vivo electrochemical analysis of a PEDOT/MWCNT neural electrode coating, *Biosensors* 5 (2015) 618-646.

[261] X. Cui, J.F. Hetke, J.A. Wiler, D.J. Anderson, D.C. Martin, Electrochemical deposition and characterization of conducting polymer polypyrrole/PSS on multichannel neural probes, *Sensors and Actuators A: Physical* 93 (2001) 8-18.

[262] X. Cui, D.C. Martin, Electrochemical deposition and characterization of poly(3,4-ethylenedioxythiophene) on neural microelectrode arrays, *Sensors and Actuators B: Chemical* 89 (2003) 92-102.

[263] X. Cui, D.C. Martin, Fuzzy gold electrodes for lowering impedance and improving adhesion with electrodeposited conducting polymer films, *Sensors and Actuators A: Physical* 103 (2003) 384-394.

[264] X. Cui, J. Wiler, M. Dzaman, R.A. Altschuler, D.C. Martin, In vivo studies of polypyrrole/peptide coated neural probes., *Biomaterials* 24 (2003) 777-87.

[265] C.L. Kolarcik, K. Catt, E. Rost, I.N. Albrecht, D. Bourbeau, Z. Du, T.D.Y. Kozai, X. Luo, D.J. Weber, X.T. Cui, Evaluation of poly(3,4-ethylenedioxythiophene)/carbon nanotube neural electrode coatings for stimulation in the dorsal root ganglion., *Journal of neural engineering* 12 (2015) 016008.

[266] P.J. Gilgunn, R. Khilwani, T.D.Y. Kozai, D.J. Weber, X.T. Cui, G. Erdos, O.B. Ozdoganlar, G.K. Fedder, An ultra-compliant, scalable neural probe with molded biodissolvable delivery vehicle, 2012 IEEE 25th International Conference on Micro Electro Mechanical Systems (MEMS), IEEE, 2012, pp. 56-59.

[267] J.P. Harris, A.E. Hess, S.J. Rowan, C. Weder, C.A. Zorman, D.J. Tyler, J.R. Capadona, In vivo deployment of mechanically adaptive nanocomposites for intracortical microelectrodes., *Journal of neural engineering* 8 (2011) 046010.

[268] H. Zhang, P.R. Patel, Z. Xie, S.D. Swanson, X. Wang, N.A. Kotov, Tissue-Compliant Neural Implants from Microfabricated Carbon Nanotube Multilayer Composite, *ACS Nano* 7 (2013) 7619-7629.

- [269] C.D. Hue, F.S. Cho, S. Cao, C.R. Dale Bass, D.F. Meaney, B. Morrison, Dexamethasone potentiates in vitro blood-brain barrier recovery after primary blast injury by glucocorticoid receptor-mediated upregulation of ZO-1 tight junction protein., *Journal of cerebral blood flow and metabolism : official journal of the International Society of Cerebral Blood Flow and Metabolism* 35 (2015) 1191-8.
- [270] A. Jaquins-Gerstl, Z. Shu, J. Zhang, Y. Liu, S.G. Weber, A.C. Michael, Effect of Dexamethasone on Gliosis, Ischemia, and Dopamine Extraction during Microdialysis Sampling in Brain Tissue, *Analytical Chemistry* 83 (2011) 7662-7667.
- [271] D.-H. Kim, D.C. Martin, Sustained release of dexamethasone from hydrophilic matrices using PLGA nanoparticles for neural drug delivery., *Biomaterials* 27 (2006) 3031-7.
- [272] L. Leprince, A. Dogimont, D. Magnin, S. Demoustier-Champagne, Dexamethasone electrically controlled release from polypyrrole-coated nanostructured electrodes., *Journal of materials science. Materials in medicine* 21 (2010) 925-30.
- [273] X. Luo, C. Matranga, S. Tan, N. Alba, X.T. Cui, Carbon nanotube nanoreservoir for controlled release of anti-inflammatory dexamethasone., *Biomaterials* 32 (2011) 6316-23.
- [274] K.M. Nesbitt, E.L. Varner, A. Jaquins-Gerstl, A.C. Michael, Microdialysis in the rat striatum: effects of 24 h dexamethasone retrodialysis on evoked dopamine release and penetration injury., *ACS chemical neuroscience* 6 (2015) 163-73.
- [275] W. Shain, L. Spataro, J. Dilgen, K. Haverstick, S. Retterer, M. Isaacson, M. Saltzman, J.N. Turner, Controlling cellular reactive responses around neural prosthetic devices using peripheral and local intervention strategies., *IEEE transactions on neural systems and rehabilitation engineering : a publication of the IEEE Engineering in Medicine and Biology Society* 11 (2003) 186-8.
- [276] L. Spataro, J. Dilgen, S. Retterer, A.J. Spence, M. Isaacson, J.N. Turner, W. Shain, Dexamethasone treatment reduces astroglia responses to inserted neuroprosthetic devices in rat neocortex., *Experimental neurology* 194 (2005) 289-300.
- [277] Y. Zhong, R.V. Bellamkonda, Dexamethasone-coated neural probes elicit attenuated inflammatory response and neuronal loss compared to uncoated neural probes., *Brain research* 1148 (2007) 15-27.
- [278] K.M. Nesbitt, A. Jaquins-Gerstl, E.M. Skoda, P. Wipf, A.C. Michael, Pharmacological Mitigation of Tissue Damage during Brain Microdialysis, *Analytical Chemistry* 85 (2013) 8173-8179.
- [279] Y. Zhong, R.V. Bellamkonda, Controlled release of anti-inflammatory agent alpha-MSH from neural implants., *Journal of controlled release : official journal of the Controlled Release Society* 106 (2005) 309-18.

- [280] C. Figge, G. Loers, M. Schachner, T. Tilling, Neurite outgrowth triggered by the cell adhesion molecule L1 requires activation and inactivation of the cytoskeletal protein cofilin., *Molecular and cellular neurosciences* 49 (2012) 196-204.
- [281] P.F. Maness, M. Schachner, Neural recognition molecules of the immunoglobulin superfamily: signaling transducers of axon guidance and neuronal migration., *Nature neuroscience* 10 (2007) 19-26.
- [282] M. Dihné, C. Bernreuther, M. Sibbe, W. Paulus, M. Schachner, A new role for the cell adhesion molecule L1 in neural precursor cell proliferation, differentiation, and transmitter-specific subtype generation., *The Journal of neuroscience : the official journal of the Society for Neuroscience* 23 (2003) 6638-50.
- [283] P. Hulley, M. Schachner, H. Lübbert, L1 neural cell adhesion molecule is a survival factor for fetal dopaminergic neurons., *Journal of neuroscience research* 53 (1998) 129-34.
- [284] S. Kenwrick, A. Watkins, E. De Angelis, Neural cell recognition molecule L1: relating biological complexity to human disease mutations., *Human molecular genetics* 9 (2000) 879-86.
- [285] C. Lagenaur, V. Lemmon, An L1-like molecule, the 8D9 antigen, is a potent substrate for neurite extension., *Proceedings of the National Academy of Sciences of the United States of America* 84 (1987) 7753-7.
- [286] V. Lemmon, K.L. Farr, C. Lagenaur, L1-mediated axon outgrowth occurs via a homophilic binding mechanism., *Neuron* 2 (1989) 1597-603.
- [287] H. Nishimune, C. Bernreuther, P. Carroll, S. Chen, M. Schachner, C.E. Henderson, Neural adhesion molecules L1 and CHL1 are survival factors for motoneurons., *Journal of neuroscience research* 80 (2005) 593-9.
- [288] F.G. Rathjen, M. Schachner, Immunocytological and biochemical characterization of a new neuronal cell surface component (L1 antigen) which is involved in cell adhesion., *The EMBO journal* 3 (1984) 1-10.
- [289] Y. Takeda, Y. Murakami, H. Asou, K. Uyemura, The roles of cell adhesion molecules on the formation of peripheral myelin., *The Keio journal of medicine* 50 (2001) 240-8.
- [290] L. Vutskits, Z. Djebbara-Hannas, H. Zhang, J.P. Paccard, P. Durbec, G. Rougon, D. Muller, J.Z. Kiss, PSA-NCAM modulates BDNF-dependent survival and differentiation of cortical neurons., *The European journal of neuroscience* 13 (2001) 1391-402.
- [291] I. Aubert, J.L. Ridet, F.H. Gage, Regeneration in the adult mammalian CNS: guided by development., *Current opinion in neurobiology* 5 (1995) 625-35.
- [292] J. Chen, C. Bernreuther, M. Dihné, M. Schachner, Cell adhesion molecule 11-transfected embryonic stem cells with enhanced survival support regrowth of corticospinal tract axons in mice after spinal cord injury., *Journal of neurotrauma* 22 (2005) 896-906.

- [293] J. Chen, J. Wu, I. Apostolova, M. Skup, A. Irintchev, S. Kügler, M. Schachner, Adeno-associated virus-mediated L1 expression promotes functional recovery after spinal cord injury., *Brain : a journal of neurology* 130 (2007) 954-69.
- [294] Y.-F. Cui, J.-C. Xu, G. Hargus, I. Jakovcevski, M. Schachner, C. Bernreuther, Embryonic stem cell-derived L1 overexpressing neural aggregates enhance recovery after spinal cord injury in mice., *PloS one* 6 (2011) e17126.
- [295] D. Guseva, D.N. Angelov, A. Irintchev, M. Schachner, Ablation of adhesion molecule L1 in mice favours Schwann cell proliferation and functional recovery after peripheral nerve injury., *Brain : a journal of neurology* 132 (2009) 2180-95.
- [296] A.A. Lavdas, J. Chen, F. Papastefanaki, S. Chen, M. Schachner, R. Matsas, D. Thomaidou, Schwann cells engineered to express the cell adhesion molecule L1 accelerate myelination and motor recovery after spinal cord injury., *Experimental neurology* 221 (2010) 206-16.
- [297] C. Roonprapunt, W. Huang, R. Grill, D. Friedlander, M. Grumet, S. Chen, M. Schachner, W. Young, Soluble cell adhesion molecule L1-Fc promotes locomotor recovery in rats after spinal cord injury., *Journal of neurotrauma* 20 (2003) 871-82.
- [298] J.-C. Xu, C. Bernreuther, Y.-F. Cui, I. Jakovcevski, G. Hargus, M.-F. Xiao, M. Schachner, Transplanted L1 expressing radial glia and astrocytes enhance recovery after spinal cord injury., *Journal of neurotrauma* 28 (2011) 1921-37.
- [299] J.E. Collazos-Castro, G.R. Hernández-Labrado, J.L. Polo, C. García-Rama, N-Cadherin- and L1-functionalised conducting polymers for synergistic stimulation and guidance of neural cell growth., *Biomaterials* 34 (2013) 3603-17.
- [300] J.C.M. Vega L., M.K. Lee, J.H. Jeong, C.E. Smith, K.Y. Lee, H.J. Chung, D.E. Leckband, H. Kong, Recapitulating Cell-Cell Adhesion Using N-Cadherin Biologically Tethered to Substrates, *Biomacromolecules* 15 (2014) 2172-2179.
- [301] H. Labit, A. Goldar, G. Guilbaud, C. Douarche, O. Hyrien, K. Marheineke, A simple and optimized method of producing silanized surfaces for FISH and replication mapping on combed DNA fibers., *BioTechniques* 45 (2008) 649-52, 654, 656-8.
- [302] P. Thevenaz, U.E. Ruttimann, M. Unser, A pyramid approach to subpixel registration based on intensity, *IEEE Transactions on Image Processing* 7 (1998) 27-41.
- [303] N.L. Rosidi, J. Zhou, S. Pattanaik, P. Wang, W. Jin, M. Brophy, W.L. Olbricht, N. Nishimura, C.B. Schaffer, Cortical Microhemorrhages Cause Local Inflammation but Do Not Trigger Widespread Dendrite Degeneration, *PLoS ONE* 6 (2011) e26612.
- [304] H. Cho, T. Hashimoto, E. Wong, Y. Hori, L.B. Wood, L. Zhao, K.M. Haigis, B.T. Hyman, D. Irimia, Microfluidic Chemotaxis Platform for Differentiating the Roles of Soluble and Bound Amyloid- β on Microglial Accumulation, *Scientific Reports* 3 (2013) 169-175.

- [305] G.J. Liu, R. Nagarajah, R.B. Banati, M.R. Bennett, Glutamate induces directed chemotaxis of microglia., *The European journal of neuroscience* 29 (2009) 1108-18.
- [306] J.J. Neher, U. Neniskyte, T. Hornik, G.C. Brown, Inhibition of UDP/P2Y6 purinergic signaling prevents phagocytosis of viable neurons by activated microglia in vitro and in vivo., *Glia* 62 (2014) 1463-75.
- [307] P. Swiatkowski, M. Murugan, U.B. Eyo, Y. Wang, S. Rangaraju, S.B. Oh, L.-J. Wu, Activation of microglial P2Y12 receptor is required for outward potassium currents in response to neuronal injury., *Neuroscience* 318 (2016) 22-33.
- [308] P.B. Guthrie, J. Knappenberger, M. Segal, M.V. Bennett, A.C. Charles, S.B. Kater, ATP released from astrocytes mediates glial calcium waves., *The Journal of neuroscience : the official journal of the Society for Neuroscience* 19 (1999) 520-8.
- [309] A.E. Ross, M.D. Nguyen, E. Privman, B.J. Venton, Mechanical stimulation evokes rapid increases in extracellular adenosine concentration in the prefrontal cortex., *Journal of neurochemistry* 130 (2014) 50-60.
- [310] K. Shahlaie, B.G. Lyeth, G.G. Gurkoff, J.P. Muizelaar, R.F. Berman, Neuroprotective effects of selective N-type VGCC blockade on stretch-injury-induced calcium dynamics in cortical neurons., *Journal of neurotrauma* 27 (2010) 175-87.
- [311] S.-Y. Chang, I. Kim, M.P. Marsh, D.P. Jang, S.-C. Hwang, J.J. Van Gompel, S.J. Goerss, C.J. Kimble, K.E. Bennet, P.A. Garris, C.D. Blaha, K.H. Lee, Wireless fast-scan cyclic voltammetry to monitor adenosine in patients with essential tremor during deep brain stimulation., *Mayo Clinic proceedings* 87 (2012) 760-5.
- [312] J.J. Bernstein, L.A. Willingham, W.J. Goldberg, Sequestering of immunoglobulins by astrocytes after cortical lesion and homografting of fetal cortex., *International journal of developmental neuroscience : the official journal of the International Society for Developmental Neuroscience* 11 (1993) 117-24.
- [313] M.B. Gingrich, C.E. Junge, P. Lyuboslavsky, S.F. Traynelis, Potentiation of NMDA receptor function by the serine protease thrombin., *The Journal of neuroscience : the official journal of the Society for Neuroscience* 20 (2000) 4582-95.
- [314] C. Nicholson, L. Tao, Hindered diffusion of high molecular weight compounds in brain extracellular microenvironment measured with integrative optical imaging., *Biophysical journal* 65 (1993) 2277-90.
- [315] A.J. Sawyer, T.R. Kyriakides, Nanoparticle-based evaluation of blood-brain barrier leakage during the foreign body response., *Journal of neural engineering* 10 (2013) 016013.
- [316] D.J. Hines, R.M. Hines, S.J. Mulligan, B.A. Macvicar, Microglia processes block the spread of damage in the brain and require functional chloride channels., *Glia* 57 (2009) 1610-8.

- [317] Y. Li, X.-F. Du, C.-S. Liu, Z.-L. Wen, J.-L. Du, Reciprocal regulation between resting microglial dynamics and neuronal activity in vivo., *Developmental cell* 23 (2012) 1189-202.
- [318] G.C. Brown, J.J. Neher, Microglial phagocytosis of live neurons, *Nature Publishing Group* 15 (2014).
- [319] Z. Liu, C. Condello, A. Schain, R. Harb, J. Grutzendler, CX3CR1 in Microglia Regulates Brain Amyloid Deposition through Selective Protofibrillar Amyloid- β Phagocytosis, *Journal of Neuroscience* 30 (2010).
- [320] J. Neumann, S. Sauerzweig, R. Rönicke, F. Gunzer, K. Dinkel, O. Ullrich, M. Gunzer, K.G. Reymann, Microglia cells protect neurons by direct engulfment of invading neutrophil granulocytes: a new mechanism of CNS immune privilege., *The Journal of neuroscience : the official journal of the Society for Neuroscience* 28 (2008) 5965-75.
- [321] A. Kowitz, G. Kadmon, M. Eckert, V. Schirmacher, M. Schachner, P. Altevogt, Expression and function of the neural cell adhesion molecule L1 in mouse leukocytes, *European Journal of Immunology* 22 (1992) 1199-1205.
- [322] G. Kadmon, P. Altevogt, A. The, M. Sams, The cell adhesion molecule L1 : species- and cell-type-dependent multiple binding mechanisms, *Differentiation* 61 (1997) 143-150.
- [323] A.M. Montgomery, J.C. Becker, C.H. Siu, V.P. Lemmon, D.A. Cheresh, J.D. Pancook, X. Zhao, R.A. Reisfeld, Human neural cell adhesion molecule L1 and rat homologue NILE are ligands for integrin alpha v beta 3, *The Journal of Cell Biology* 132 (1996) 475-485.
- [324] M. Oleszewski, S. Beer, S. Katich, C. Geiger, Y. Zeller, U. Rauch, P. Altevogt, Integrin and Neurocan Binding to L1 Involves Distinct Ig Domains *, *The Journal of Biological Chemistry* 274 (1999) 24602-24610.
- [325] N.P. Hailer, J.D. Jarhult, R. Nitsch, Resting microglial cells in vitro: analysis of morphology and adhesion molecule expression in organotypic hippocampal slice cultures., *Glia* 18 (1996) 319-31.
- [326] R. Milner, I.L. Campbell, The Extracellular Matrix and Cytokines Regulate Microglial Integrin Expression and Activation, *The Journal of Immunology* 170 (2003) 3850-3858.
- [327] K. Nasu-Tada, S. Koizumi, K. Inoue, Involvement of β 1 integrin in microglial chemotaxis and proliferation on fibronectin: Different regulations by ADP through PKA, *Glia* 52 (2005) 98-107.
- [328] J.D. Cherry, J.A. Olschowka, M.K. O'Banion, Neuroinflammation and M2 microglia: the good, the bad, and the inflamed., *Journal of neuroinflammation* 11 (2014) 98.
- [329] A. Kumar, B.A. Stoica, B. Sabirzhanov, M.P. Burns, A.I. Faden, D.J. Loane, Traumatic brain injury in aged animals increases lesion size and chronically alters microglial/macrophage classical and alternative activation states., *Neurobiology of aging* 34 (2013) 1397-411.

- [330] W.Y. Tam, C.H. Ma, Bipolar/rod-shaped microglia are proliferating microglia with distinct M1/M2 phenotypes, *Sci Rep* 4 (2014) 7279.
- [331] X.-M. Zhang, H. Lund, S. Mia, R. Parsa, R.A. Harris, Adoptive transfer of cytokine-induced immunomodulatory adult microglia attenuates experimental autoimmune encephalomyelitis in DBA/1 mice., *Glia* 62 (2014) 804-17.
- [332] B.A. Durafour, C.S. Moore, D.A. Zammit, T.A. Johnson, F. Zaguia, M.-C. Guiot, A. Bar-Or, J.P. Antel, Comparison of polarization properties of human adult microglia and blood-derived macrophages., *Glia* 60 (2012) 717-27.
- [333] L.A.N. Peferoen, D.Y.S. Vogel, K. Ummenthum, M. Breur, P.D.A.M. Heijnen, W.H. Gerritsen, R.M.B. Peferoen-Baert, P. van der Valk, C.D. Dijkstra, S. Amor, Activation status of human microglia is dependent on lesion formation stage and remyelination in multiple sclerosis., *Journal of neuropathology and experimental neurology* 74 (2015) 48-63.
- [334] A. Bal-Price, G.C. Brown, Inflammatory neurodegeneration mediated by nitric oxide from activated glia-inhibiting neuronal respiration, causing glutamate release and excitotoxicity., *The Journal of neuroscience : the official journal of the Society for Neuroscience* 21 (2001) 6480-91.
- [335] J.J. Neher, U. Neniskyte, J.-W. Zhao, A. Bal-Price, A.M. Tolkovsky, G.C. Brown, Inhibition of microglial phagocytosis is sufficient to prevent inflammatory neuronal death., *Journal of immunology (Baltimore, Md. : 1950)* 186 (2011) 4973-83.
- [336] D.-H. Kim, J.T. Smith, A. Chilkoti, W.M. Reichert, The effect of covalently immobilized rhIL-1ra-ELP fusion protein on the inflammatory profile of LPS-stimulated human monocytes., *Biomaterials* 28 (2007) 3369-77.
- [337] R.J. Schutte, L. Xie, B. Klitzman, W.M. Reichert, In vivo cytokine-associated responses to biomaterials, *Biomaterials* 30 (2009) 160-168.
- [338] G. Barbin, M.S. Aigrot, P. Charles, A. Foucher, M. Grumet, M. Schachner, B. Zalc, C. Lubetzki, Axonal cell-adhesion molecule L1 in CNS myelination., *Neuron glia biology* 1 (2004) 65-72.
- [339] J.F. Cherry, N.K. Bennett, M. Schachner, P.V. Moghe, Engineered N-cadherin and L1 biomimetic substrates concertedly promote neuronal differentiation, neurite extension and neuroprotection of human neural stem cells., *Acta biomaterialia* 10 (2014) 4113-26.
- [340] J. Akerboom, T.-W. Chen, T.J. Wardill, L. Tian, J.S. Marvin, S. Mutlu, N.C. Calderon, F. Esposti, B.G. Borghuis, X.R. Sun, A. Gordus, M.B. Orger, R. Portugues, F. Engert, J.J. Macklin, A. Filosa, A. Aggarwal, R.A. Kerr, R. Takagi, S. Kracun, E. Shigetomi, B.S. Khakh, H. Baier, L. Lagnado, S.S.-H. Wang, C.I. Bargmann, B.E. Kimmel, V. Jayaraman, K. Svoboda, D.S. Kim, E.R. Schreier, L.L. Looger, Optimization of a GCaMP Calcium Indicator for Neural Activity Imaging, *Journal of Neuroscience* 32 (2012) 13819-13840.

- [341] T. Araki, M. Yamada, H. Ohnishi, S.I. Sano, H. Hatanaka, BIT/SHPS-1 enhances brain-derived neurotrophic factor-promoted neuronal survival in cultured cerebral cortical neurons., *Journal of neurochemistry* 75 (2000) 1502-10.
- [342] J.K. Harrison, Y. Jiang, S. Chen, Y. Xia, D. Maciejewski, R.K. McNamara, W.J. Streit, M.N. Salafranca, S. Adhikari, D.A. Thompson, P. Botti, K.B. Bacon, L. Feng, Role for neuronally derived fractalkine in mediating interactions between neurons and CX3CR1-expressing microglia., *Proceedings of the National Academy of Sciences of the United States of America* 95 (1998) 10896-901.
- [343] R.M. Hoek, S.R. Ruuls, C.A. Murphy, G.J. Wright, R. Goddard, S.M. Zurawski, B. Blom, M.E. Homola, W.J. Streit, M.H. Brown, A.N. Barclay, J.D. Sedgwick, Down-regulation of the macrophage lineage through interaction with OX2 (CD200). *Science (New York, N.Y.)* 290 (2000) 1768-71.
- [344] A. Junker, M. Krumbholz, S. Eisele, H. Mohan, F. Augstein, R. Bittner, H. Lassmann, H. Wekerle, R. Hohlfeld, E. Meinl, MicroRNA profiling of multiple sclerosis lesions identifies modulators of the regulatory protein CD47., *Brain : a journal of neurology* 132 (2009) 3342-52.
- [345] J.R. Eles, A.L. Vazquez, T.D.Y. Kozai, X.T. Cui, Meningeal inflammatory response and fibrous tissue remodeling around intracortical implants: An in vivo two-photon imaging study, *Biomaterials* 195 (2019) 111-123.
- [346] I. Bartholomäus, N. Kawakami, F. Odoardi, C. Schläger, D. Miljkovic, J.W. Ellwart, W.E.F. Klinkert, C. Flügel-Koch, T.B. Issekutz, H. Wekerle, A. Flügel, Effector T cell interactions with meningeal vascular structures in nascent autoimmune CNS lesions., *Nature* 462 (2009) 94-98.
- [347] J.M. Anderson, A. Rodriguez, D.T. Chang, Foreign body reaction to biomaterials, *Seminars in Immunology* 20 (2008) 86-100.
- [348] J.M. Anderson, Biological Responses to Materials, *Annual Review of Materials Research* 31(1) (2001) 81-110.
- [349] N.T. Markwardt, J. Stokol, R.L. Rennaker, II, Sub-meninges implantation reduces immune response to neural implants., *Journal of neuroscience methods* 214 (2013) 119-25.
- [350] E.M. Maynard, E. Fernandez, R.A. Normann, A technique to prevent dural adhesions to chronically implanted microelectrode arrays, *Journal of Neuroscience Methods* 97(2) (2000) 93-101.
- [351] K.M. Spitler, K.M. Gothard, A removable silicone elastomer seal reduces granulation tissue growth and maintains the sterility of recording chambers for primate neurophysiology, *Journal of Neuroscience Methods* 169(1) (2008) 23-26.
- [352] R.L. Spinks, S.N. Baker, A. Jackson, P.T. Khaw, R.N. Lemon, Problem of dural scarring in recording from awake, behaving monkeys: a solution using 5-fluorouracil, *J Neurophysiol* 90(2) (2003) 1324-32.

- [353] S. Jung, J. Aliberti, P. Graemmel, M.J. Sunshine, G.W. Kreutzberg, A. Sher, D.R. Littman, Analysis of Fractalkine Receptor CX(3)CR1 Function by Targeted Deletion and Green Fluorescent Protein Reporter Gene Insertion, *Molecular and Cellular Biology* 20(11) (2000) 4106-4114.
- [354] K. Catt, H. Li, X.T. Cui, Poly (3,4-ethylenedioxythiophene) graphene oxide composite coatings for controlling magnesium implant corrosion, *Acta Biomaterialia* 48 (2017) 530-540.
- [355] K. Catt, H. Li, V. Hoang, R. Beard, X.T. Cui, Self-powered therapeutic release from conducting polymer/graphene oxide films on magnesium, *Nanomedicine: Nanotechnology, Biology and Medicine* (2017).
- [356] C.M. Rovainen, T.A. Woolsey, N.C. Blocher, D.-B. Wang, O.F. Robinson, Blood Flow in Single Surface Arterioles and Venules on the Mouse Somatosensory Cortex Measured with Videomicroscopy, Fluorescent Dextran, Nonoccluding Fluorescent Beads, and Computer-Assisted Image Analysis, *Journal of Cerebral Blood Flow & Metabolism* 13(3) (1993) 359-371.
- [357] L.S. Ritter, J.A. Orozco, B.M. Coull, P.F. McDonagh, W.I. Rosenblum, Leukocyte accumulation and hemodynamic changes in the cerebral microcirculation during early reperfusion after stroke, *Stroke* 31(5) (2000) 1153-61.
- [358] S.M. Schwarzmaier, R. Zimmermann, N.B. McGarry, R. Trabold, S.W. Kim, N. Plesnila, In vivo temporal and spatial profile of leukocyte adhesion and migration after experimental traumatic brain injury in mice, *J Neuroinflammation* 10 (2013) 32.
- [359] L.T. Vu, G. Jain, B.D. Veres, P. Rajagopalan, Cell Migration on Planar and Three-Dimensional Matrices: A Hydrogel-Based Perspective, *Tissue Engineering. Part B, Reviews* 21(1) (2015) 67-74.
- [360] M. Lagraoui, J.R. Latoche, N.G. Cartwright, G. Sukumar, C.L. Dalgard, B.C. Schaefer, Controlled Cortical Impact and Craniotomy Induce Strikingly Similar Profiles of Inflammatory Gene Expression, but with Distinct Kinetics, *Frontiers in Neurology* 3 (2012) 155.
- [361] J.T. Cole, A. Yarnell, W.S. Kean, E. Gold, B. Lewis, M. Ren, D.C. McMullen, D.M. Jacobowitz, H.B. Pollard, J.T. O'Neill, N.E. Grunberg, C.L. Dalgard, J.A. Frank, W.D. Watson, Craniotomy: True Sham for Traumatic Brain Injury, or a Sham of a Sham?, *Journal of Neurotrauma* 28(3) (2011) 359-369.
- [362] M. Sashindranath, M. Daglas, R.L. Medcalf, Evaluation of gait impairment in mice subjected to craniotomy and traumatic brain injury, *Behavioural brain research* 286 (2015) 33-8.
- [363] P.A. Forcelli, D. Kalikhman, K. Gale, Delayed effect of craniotomy on experimental seizures in rats, *PLoS One* 8(12) (2013) e81401.
- [364] C. Szpalski, J. Barr, M. Wetterau, P.B. Saadeh, S.M. Warren, Cranial bone defects: current and future strategies, *Neurosurg Focus* 29(6) (2010) E8.

- [365] T.A. Barbolt, M. Odin, M. Leger, L. Kangas, J. Hoiste, S.H. Liu, Biocompatibility evaluation of dura mater substitutes in an animal model, *Neurological research* 23(8) (2001) 813-20.
- [366] A. Singh, S. Suri, K. Roy, In-situ crosslinking hydrogels for combinatorial delivery of chemokines and siRNA-DNA carrying microparticles to dendritic cells, *Biomaterials* 30(28) (2009) 5187.
- [367] X. Zhao, X. Sun, L. Yildirimer, Q. Lang, Z.Y.W. Lin, R. Zheng, Y. Zhang, W. Cui, N. Annabi, A. Khademhosseini, Cell infiltrative hydrogel fibrous scaffolds for accelerated wound healing, *Acta Biomater* 49 (2017) 66-77.
- [368] S. Jo, S.M. Kang, S.A. Park, W.D. Kim, J. Kwak, H. Lee, Enhanced adhesion of preosteoblasts inside 3D PCL scaffolds by polydopamine coating and mineralization, *Macromol Biosci* 13(10) (2013) 1389-95.
- [369] B.M. Baker, A.O. Gee, R.B. Metter, A.S. Nathan, R.A. Marklein, J.A. Burdick, R.L. Mauck, The potential to improve cell infiltration in composite fiber-aligned electrospun scaffolds by the selective removal of sacrificial fibers, *Biomaterials* 29(15) (2008) 2348-58.
- [370] M.E. Manwaring, R. Biran, P.A. Tresco, Characterization of rat meningeal cultures on materials of differing surface chemistry, *Biomaterials* 22(23) (2001) 3155-68.
- [371] T.D.Y. Kozai, A.S. Jaquins-gerstl, A.L. Vazquez, A.C. Michael, X.T. Cui, Biomaterials Dexamethasone retrodialysis attenuates microglial response to implanted probes in vivo, *Biomaterials* 87 (2016) 157-169.
- [372] J. Rosenbloom, F.A. Mendoza, S.A. Jimenez, Strategies for anti-fibrotic therapies, *Biochimica et biophysica acta* 1832(7) (2013) 1088-103.
- [373] T. Yamakawa, T. Yamakawa, S. Aou, S. Ishizuka, M. Suzuki, M. Fujii, Subdural electrode array manipulated by a shape memory alloy guidewire for minimally-invasive electrocorticogram recording, 2010 World Automation Congress, 2010, pp. 1-6.
- [374] J.D. Yeager, D.J. Phillips, D.M. Rector, D.F. Bahr, Characterization of flexible ECoG electrode arrays for chronic recording in awake rats, *J Neurosci Methods* 173(2) (2008) 279-85.
- [375] D.-H. Kim, J. Viventi, J.J. Amsden, J. Xiao, L. Vigeland, Y.-S. Kim, J.A. Blanco, B. Panilaitis, E.S. Frechette, D. Contreras, D.L. Kaplan, F.G. Omenetto, Y. Huang, K.-C. Hwang, M.R. Zakin, B. Litt, J.A. Rogers, Dissolvable films of silk fibroin for ultrathin conformal bio-integrated electronics, *Nature Materials* 9 (2010) 511.
- [376] D. Moran, Evolution of brain-computer interface: action potentials, local field potentials and electrocorticograms, *Curr Opin Neurobiol* 20(6) (2010) 741-5.
- [377] J.R. Wolpaw, N. Birbaumer, D.J. McFarland, G. Pfurtscheller, T.M. Vaughan, Brain-computer interfaces for communication and control, *Clinical neurophysiology : official journal of the International Federation of Clinical Neurophysiology* 113(6) (2002) 767-91.

- [378] E.C. Leuthardt, G. Schalk, D. Moran, J.G. Ojemann, The emerging world of motor neuroprosthetics: a neurosurgical perspective, *Neurosurgery* 59(1) (2006) 1-14; discussion 1-14.
- [379] V.S. Polikov, P.A. Tresco, W.M. Reichert, Response of brain tissue to chronically implanted neural electrodes, *J Neurosci Methods* 148(1) (2005) 1-18.
- [380] M.A. Freire, E. Morya, J. Faber, J.R. Santos, J.S. Guimaraes, N.A. Lemos, K. Sameshima, A. Pereira, S. Ribeiro, M.A. Nicolelis, Comprehensive analysis of tissue preservation and recording quality from chronic multielectrode implants, *PLoS One* 6(11) (2011) e27554.
- [381] E.C. Leuthardt, G. Schalk, J.R. Wolpaw, J.G. Ojemann, D.W. Moran, A brain-computer interface using electrocorticographic signals in humans, *J Neural Eng* 1(2) (2004) 63-71.
- [382] G. Schalk, K.J. Miller, N.R. Anderson, J.A. Wilson, M.D. Smyth, J.G. Ojemann, D.W. Moran, J.R. Wolpaw, E.C. Leuthardt, Two-dimensional movement control using electrocorticographic signals in humans, *J Neural Eng* 5(1) (2008) 75-84.
- [383] N.E. Crone, L. Hao, J. Hart, Jr., D. Boatman, R.P. Lesser, R. Irizarry, B. Gordon, Electrocorticographic gamma activity during word production in spoken and sign language, *Neurology* 57(11) (2001) 2045-53.
- [384] K.J. Miller, S. Zanos, E.E. Fetz, M. den Nijs, J.G. Ojemann, Decoupling the cortical power spectrum reveals real-time representation of individual finger movements in humans, *J Neurosci* 29(10) (2009) 3132-7.
- [385] T. Pistohl, T. Ball, A. Schulze-Bonhage, A. Aertsen, C. Mehring, Prediction of arm movement trajectories from ECoG-recordings in humans, *J Neurosci Methods* 167(1) (2008) 105-14.
- [386] J. Kubanek, K.J. Miller, J.G. Ojemann, J.R. Wolpaw, G. Schalk, Decoding flexion of individual fingers using electrocorticographic signals in humans, *J Neural Eng* 6(6) (2009) 066001.
- [387] T. Ball, A. Schulze-Bonhage, A. Aertsen, C. Mehring, Differential representation of arm movement direction in relation to cortical anatomy and function, *J Neural Eng* 6(1) (2009) 016006.
- [388] Z.C. Chao, Y. Nagasaka, N. Fujii, Long-term asynchronous decoding of arm motion using electrocorticographic signals in monkeys, *Front Neuroeng* 3 (2010) 3.
- [389] S. Acharya, M.S. Fifer, H.L. Benz, N.E. Crone, N.V. Thakor, Electrocorticographic amplitude predicts finger positions during slow grasping motions of the hand, *J Neural Eng* 7(4) (2010) 046002.
- [390] A.D. Degenhart, J.L. Collinger, R. Vinjamuri, J.W. Kelly, E.C. Tyler-Kabara, W. Wang, Classification of hand posture from electrocorticographic signals recorded during varying force conditions, Conference proceedings : ... Annual International Conference of the IEEE

Engineering in Medicine and Biology Society. IEEE Engineering in Medicine and Biology Society. Annual Conference 2011 (2011) 5782-5.

[391] K. Shimoda, Y. Nagasaka, Z.C. Chao, N. Fujii, Decoding continuous three-dimensional hand trajectories from epidural electrocorticographic signals in Japanese macaques, *J Neural Eng* 9(3) (2012) 036015.

[392] Y. Nakanishi, T. Yanagisawa, D. Shin, R. Fukuma, C. Chen, H. Kambara, N. Yoshimura, M. Hirata, T. Yoshimine, Y. Koike, Prediction of three-dimensional arm trajectories based on ECoG signals recorded from human sensorimotor cortex, *PLoS One* 8(8) (2013) e72085.

[393] E. Edwards, M. Soltani, L.Y. Deouell, M.S. Berger, R.T. Knight, High gamma activity in response to deviant auditory stimuli recorded directly from human cortex, *J Neurophysiol* 94(6) (2005) 4269-80.

[394] P. Trautner, T. Rosburg, T. Dietl, J. Fell, O.A. Korzyukov, M. Kurthen, C. Schaller, C.E. Elger, N.N. Boutros, Sensory gating of auditory evoked and induced gamma band activity in intracranial recordings, *NeuroImage* 32(2) (2006) 790-8.

[395] J.P. Lachaux, N. George, C. Tallon-Baudry, J. Martinerie, L. Hugueville, L. Minotti, P. Kahane, B. Renault, The many faces of the gamma band response to complex visual stimuli, *NeuroImage* 25(2) (2005) 491-501.

[396] N. Mainy, P. Kahane, L. Minotti, D. Hoffmann, O. Bertrand, J.P. Lachaux, Neural correlates of consolidation in working memory, *Human brain mapping* 28(3) (2007) 183-93.

[397] S. Kellis, K. Miller, K. Thomson, R. Brown, P. House, B. Greger, Decoding spoken words using local field potentials recorded from the cortical surface, *J Neural Eng* 7(5) (2010) 056007.

[398] W. Wang, A.D. Degenhart, G.P. Sudre, D.A. Pomerleau, E.C. Tyler-Kabara, Decoding semantic information from human electrocorticographic (ECoG) signals, *Conference proceedings : ... Annual International Conference of the IEEE Engineering in Medicine and Biology Society. IEEE Engineering in Medicine and Biology Society. Annual Conference 2011* (2011) 6294-8.

[399] X. Pei, D.L. Barbour, E.C. Leuthardt, G. Schalk, Decoding vowels and consonants in spoken and imagined words using electrocorticographic signals in humans, *J Neural Eng* 8(4) (2011) 046028.

[400] C. Tallon-Baudry, O. Bertrand, M.A. Henaff, J. Isnard, C. Fischer, Attention modulates gamma-band oscillations differently in the human lateral occipital cortex and fusiform gyrus, *Cerebral cortex* (New York, N.Y. : 1991) 15(5) (2005) 654-62.

[401] J. Jung, N. Mainy, P. Kahane, L. Minotti, D. Hoffmann, O. Bertrand, J.P. Lachaux, The neural bases of attentive reading, *Human brain mapping* 29(10) (2008) 1193-206.

[402] S. Ray, E. Niebur, S.S. Hsiao, A. Sinai, N.E. Crone, High-frequency gamma activity (80-150Hz) is increased in human cortex during selective attention, *Clinical neurophysiology :*

official journal of the International Federation of Clinical Neurophysiology 119(1) (2008) 116-33.

[403] E.C. Leuthardt, C. Gaona, M. Sharma, N. Szrama, J. Roland, Z. Freudenberg, J. Solis, J. Breshears, G. Schalk, Using the electrocorticographic speech network to control a brain-computer interface in humans, *J Neural Eng* 8(3) (2011) 036004.

[404] G. Schalk, E.C. Leuthardt, Brain-computer interfaces using electrocorticographic signals, *IEEE reviews in biomedical engineering* 4 (2011) 140-54.

[405] J.A. Wilson, E.A. Felton, P.C. Garell, G. Schalk, J.C. Williams, ECoG factors underlying multimodal control of a brain-computer interface, *IEEE Trans Neural Syst Rehabil Eng* 14(2) (2006) 246-50.

[406] T. Yanagisawa, M. Hirata, Y. Saitoh, H. Kishima, K. Matsushita, T. Goto, R. Fukuma, H. Yokoi, Y. Kamitani, T. Yoshimine, Electrocorticographic control of a prosthetic arm in paralyzed patients, *Ann Neurol* 71(3) (2012) 353-61.

[407] W. Wang, J.L. Collinger, A.D. Degenhart, E.C. Tyler-Kabara, A.B. Schwartz, D.W. Moran, D.J. Weber, B. Wodlinger, R.K. Vinjamuri, R.C. Ashmore, J.W. Kelly, M.L. Boninger, An electrocorticographic brain interface in an individual with tetraplegia, *PLoS One* 8(2) (2013) e55344.

[408] M.J. Morrell, Responsive cortical stimulation for the treatment of medically intractable partial epilepsy, *Neurology* 77(13) (2011) 1295-304.

[409] K.N. Fountas, J.R. Smith, Subdural electrode-associated complications: a 20-year experience, *Stereotactic and functional neurosurgery* 85(6) (2007) 264-72.

[410] J.J. Van Gompel, G.A. Worrell, M.L. Bell, T.A. Patrick, G.D. Cascino, C. Raffel, W.R. Marsh, F.B. Meyer, Intracranial electroencephalography with subdural grid electrodes: techniques, complications, and outcomes, *Neurosurgery* 63(3) (2008) 498-505; discussion 505-6.

[411] C.H. Wong, J. Birkett, K. Byth, M. Dexter, E. Somerville, D. Gill, R. Chaseling, M. Fearnside, A. Bleasel, Risk factors for complications during intracranial electrode recording in presurgical evaluation of drug resistant partial epilepsy, *Acta neurochirurgica* 151(1) (2009) 37-50.

[412] B.S. Nashold, Jr., H. Friedman, Dorsal column stimulation for control of pain. Preliminary report on 30 patients, *J Neurosurg* 36(5) (1972) 590-7.

[413] A. Pineda, Complications of dorsal column stimulation, *J Neurosurg* 48(1) (1978) 64-8.

[414] Y. Saitoh, M. Shibata, S. Hirano, M. Hirata, T. Mashimo, T. Yoshimine, Motor cortex stimulation for central and peripheral deafferentation pain. Report of eight cases, *J Neurosurg* 92(1) (2000) 150-5.

- [415] K.A. Sillay, P. Rutecki, K. Cicora, G. Worrell, J. Drazkowski, J.J. Shih, A.D. Sharan, M.J. Morrell, J. Williams, B. Wingeier, Long-term measurement of impedance in chronically implanted depth and subdural electrodes during responsive neurostimulation in humans, *Brain Stimul* 6(5) (2013) 718-26.
- [416] A.D. Degenhart, J.W. Kelly, R.C. Ashmore, J.L. Collinger, E.C. Tyler-Kabara, D.J. Weber, W. Wang, Craniux: a LabVIEW-based modular software framework for brain-machine interface research, *Computational intelligence and neuroscience* 2011 (2011) 363565.
- [417] S. Preibisch, S. Saalfeld, P. Tomancak, Globally optimal stitching of tiled 3D microscopic image acquisitions, *Bioinformatics (Oxford, England)* 25(11) (2009) 1463-5.
- [418] M. Matelli, G. Luppino, G. Rizzolatti, Architecture of superior and mesial area 6 and the adjacent cingulate cortex in the macaque monkey, *J Comp Neurol* 311(4) (1991) 445-62.
- [419] A.D. Lynn, A.K. Blakney, T.R. Kyriakides, S.J. Bryant, Temporal progression of the host response to implanted poly(ethylene glycol)-based hydrogels, *J Biomed Mater Res A* 96(4) (2011) 621-31.
- [420] T.O. Collier, J.M. Anderson, W.G. Brodbeck, T. Barber, K.E. Healy, Inhibition of macrophage development and foreign body giant cell formation by hydrophilic interpenetrating polymer network, *J Biomed Mater Res A* 69(4) (2004) 644-50.
- [421] M. Strupler, A.M. Pena, M. Hernest, P.L. Tharaux, J.L. Martin, E. Beaurepaire, M.C. Schanne-Klein, Second harmonic imaging and scoring of collagen in fibrotic tissues, *Optics express* 15(7) (2007) 4054-65.
- [422] G. Cox, E. Kable, A. Jones, I. Fraser, F. Manconi, M.D. Gorrell, 3-dimensional imaging of collagen using second harmonic generation, *Journal of structural biology* 141(1) (2003) 53-62.
- [423] N. Adeeb, M.M. Mortazavi, R.S. Tubbs, A.A. Cohen-Gadol, The cranial dura mater: a review of its history, embryology, and anatomy, *Child's nervous system : ChNS : official journal of the International Society for Pediatric Neurosurgery* 28(6) (2012) 827-37.
- [424] R.C. Ashmore, B.M. Endler, I. Smalianchuk, A.D. Degenhart, N.G. Hatsopoulos, E.C. Tyler-Kabara, A.P. Batista, W. Wang, Stable online control of an electrocorticographic brain-computer interface using a static decoder, *Conference proceedings : ... Annual International Conference of the IEEE Engineering in Medicine and Biology Society. IEEE Engineering in Medicine and Biology Society. Annual Conference 2012* (2012) 1740-4.
- [425] F. Rattay, Modeling the excitation of fibers under surface electrodes, *IEEE Transactions on Biomedical Engineering* 35(3) (1988) 199-202.
- [426] R. Gittins, P.J. Harrison, Neuronal density, size and shape in the human anterior cingulate cortex: a comparison of Nissl and NeuN staining, *Brain research bulletin* 63(2) (2004) 155-60.
- [427] J.J. Kim, A.D. Gean, Imaging for the diagnosis and management of traumatic brain injury, *Neurotherapeutics* 8(1) (2011) 39-53.

- [428] M.C. Ding, E.H. Lo, G.B. Stanley, Sustained focal cortical compression reduces electrically-induced seizure threshold, *Neuroscience* 154(2) (2008) 551-5.
- [429] J.M. Vela, I. Dalmau, B. González, B. Castellano, Morphology and distribution of microglial cells in the young and adult mouse cerebellum., *The Journal of comparative neurology* 361 (1995) 602-616.
- [430] R. Kongsui, S.B. Beynon, S.J. Johnson, F.R. Walker, Quantitative assessment of microglial morphology and density reveals remarkable consistency in the distribution and morphology of cells within the healthy prefrontal cortex of the rat, *J Neuroinflammation* 11 (2014) 182.
- [431] L.F. Eng, R.S. Ghirnikar, Y.L. Lee, Glial fibrillary acidic protein: GFAP-thirty-one years (1969-2000), *Neurochemical research* 25(9-10) (2000) 1439-51.
- [432] R.W. Griffith, D.R. Humphrey, Long-term gliosis around chronically implanted platinum electrodes in the Rhesus macaque motor cortex, *Neuroscience letters* 406(1-2) (2006) 81-6.
- [433] A. Peters, C. Sethares, The effects of age on the cells in layer 1 of primate cerebral cortex, *Cerebral cortex (New York, N.Y. : 1991)* 12(1) (2002) 27-36.
- [434] J. Su, M. Todorov, H.P. Gonzales, L. Perkins, H. Kojouharov, H. Weng, L. Tang, A Predictive Tool for Foreign Body Fibrotic Reactions Using 2-Dimensional Computational Model, *Open access bioinformatics* 2011(3) (2011) 19-35.
- [435] C.M. Sayama, M. Sorour, R.H. Schmidt, Dural adhesion to porous cranioplastic implant: A potential safety concern, *Surgical neurology international* 5 (2014) 19.
- [436] B. Rubehn, C. Bosman, R. Oostenveld, P. Fries, T. Stieglitz, A MEMS-based flexible multichannel ECoG-electrode array, *J Neural Eng* 6(3) (2009) 036003.
- [437] L.W. Norton, E. Tegnell, S.S. Toporek, W.M. Reichert, In vitro characterization of vascular endothelial growth factor and dexamethasone releasing hydrogels for implantable probe coatings, *Biomaterials* 26(16) (2005) 3285-97.
- [438] J. Gaire, H.C. Lee, R. Ward, S. Currllin, A.J. Woolley, J.E. Coleman, J.C. Williams, K.J. Otto, PrismPlus: a mouse line expressing distinct fluorophores in four different brain cell types, *Scientific Reports* 8(1) (2018) 7182.
- [439] M.-È. Tremblay, R.L. Lowery, A.K. Majewska, Microglial Interactions with Synapses Are Modulated by Visual Experience, *PLoS biology* 8(11) (2010) e1000527.
- [440] C. Ricard, E.D. Arroyo, C.X. He, C. Portera-Cailliau, G. Lepousez, M. Canepari, D. Fiole, Two-photon probes for in vivo multicolor microscopy of the structure and signals of brain cells, *Brain Structure and Function* 223(7) (2018) 3011-3043.

- [441] M.H. Mohajerani, A.W. Chan, M. Mohsenvand, J. LeDue, R. Liu, D.A. McVea, J.D. Boyd, Y.T. Wang, M. Reimers, T.H. Murphy, Spontaneous cortical activity alternates between motifs defined by regional axonal projections, *Nature neuroscience* 16(10) (2013) 1426-1435.
- [442] I.R. Winship, T.H. Murphy, Remapping the Somatosensory Cortex after Stroke: Insight from Imaging the Synapse to Network, *The Neuroscientist* 15(5) (2009) 507-524.
- [443] C.-H. Chen, H.-C. Su, S.-C. Chuang, S.-J. Yen, Y.-C. Chen, Y.-T. Lee, H. Chen, T.-R. Yew, Y.-C. Chang, S.-R. Yeh, D.-J. Yao, Hydrophilic modification of neural microelectrode arrays based on multi-walled carbon nanotubes, *Nanotechnology* 21 (2010) 485501.
- [444] K.A. Potter, M. Jorfi, K.T. Householder, E.J. Foster, C. Weder, J.R. Capadona, Curcumin-releasing mechanically adaptive intracortical implants improve the proximal neuronal density and blood–brain barrier stability, *Acta Biomaterialia* 10 (2014) 2209-2222.
- [445] X. Zhao, J.M. Harris, Novel degradable poly(ethylene glycol) hydrogels for controlled release of protein, *Journal of Pharmaceutical Sciences* 87 (1998) 1450-1458.
- [446] Z.J. Du, G.-Q. Bi, X.T. Cui, Electrically Controlled Neurochemical Release from Dual-Layer Conducting Polymer Films for Precise Modulation of Neural Network Activity in Rat Barrel Cortex, *Advanced Functional Materials* 28(12) (2017) 1703988.
- [447] A. Golabchi, B. Wu, X. Li, D.L. Carlisle, T.D.Y. Kozai, R.M. Friedlander, X.T. Cui, Melatonin improves quality and longevity of chronic neural recording, *Biomaterials* 180 (2018) 225-239.
- [448] B. Cemil, K. Tun, E. Kaptanoglu, B. Cevirgen, A.G. Gurcay, F. Kaymaz, I. Tekdemir, The effect of mitomycin C as fibrosis preventive agent during craniectomies, *British Journal of Neurosurgery* 23 (2009) 304-308.
- [449] M.E. Manwaring, R. Biran, P.A. Tresco, Characterization of rat meningeal cultures on materials of differing surface chemistry, *Biomaterials* 22 (2001) 3155-3168.
- [450] J.J. Iliff, M.J. Chen, B.A. Plog, D.M. Zeppenfeld, M. Soltero, L. Yang, I. Singh, R. Deane, M. Nedergaard, Impairment of glymphatic pathway function promotes tau pathology after traumatic brain injury, *The Journal of neuroscience : the official journal of the Society for Neuroscience* 34(49) (2014) 16180-16193.
- [451] M. Absinta, S.K. Ha, G. Nair, P. Sati, N.J. Luciano, M. Palisoc, A. Louveau, K.A. Zaghoul, S. Pittaluga, J. Kipnis, D.S. Reich, Human and nonhuman primate meninges harbor lymphatic vessels that can be visualized noninvasively by MRI, *eLife* 6 (2017).
- [452] F. Ding, X. Shi, Z. Jiang, L. Liu, J. Cai, Z. Li, S. Chen, Y. Du, Electrochemically stimulated drug release from dual stimuli responsive chitin hydrogel, *Journal of Materials Chemistry B* 1 (2013) 1729.

- [453] W.R. Stauffer, P.M. Lau, G.Q. Bi, X.T. Cui, Rapid modulation of local neural activity by controlled drug release from polymer-coated recording microelectrodes, *J Neural Eng* 8(4) (2011) 044001.
- [454] R.T. Richardson, A.K. Wise, B.C. Thompson, B.O. Flynn, P.J. Atkinson, N.J. Fretwell, J.B. Fallon, G.G. Wallace, R.K. Shepherd, G.M. Clark, S.J. O'Leary, Polypyrrole-coated electrodes for the delivery of charge and neurotrophins to cochlear neurons, *Biomaterials* 30(13) (2009) 2614-2624.
- [455] A.J. Evans, B.C. Thompson, G.G. Wallace, R. Millard, S.J. O'Leary, G.M. Clark, R.K. Shepherd, R.T. Richardson, Promoting neurite outgrowth from spiral ganglion neuron explants using polypyrrole/BDNF-coated electrodes, *Journal of Biomedical Materials Research Part A* 91A (2009) 241-250.
- [456] H.P. Erickson, Size and shape of protein molecules at the nanometer level determined by sedimentation, gel filtration, and electron microscopy, *Biological procedures online* 11 (2009) 32-51.
- [457] N.S. Bhise, R.B. Shmueli, J. Gonzalez, J.J. Green, A novel assay for quantifying the number of plasmids encapsulated by polymer nanoparticles, *Small (Weinheim an der Bergstrasse, Germany)* 8(3) (2012) 367-373.
- [458] Z. Guo, L. Zhang, Z. Wu, Y. Chen, F. Wang, G. Chen, In vivo direct reprogramming of reactive glial cells into functional neurons after brain injury and in an Alzheimer's disease model, *Cell stem cell* 14(2) (2014) 188-202.
- [459] A. Pataskar, J. Jung, P. Smialowski, F. Noack, F. Calegari, T. Straub, V.K. Tiwari, NeuroD1 reprograms chromatin and transcription factor landscapes to induce the neuronal program, *The EMBO journal* 35(1) (2016) 24-45.
- [460] S.R. Gallagher, P.R. Desjardins, Quantitation of DNA and RNA with absorption and fluorescence spectroscopy, *Current protocols in protein science Appendix 3* (2008) Appendix 4K.
- [461] X. Luo, X.T. Cui, Sponge-like nanostructured conducting polymers for electrically controlled drug release, *Electrochemistry Communications* 11(10) (2009) 1956-1959.
- [462] P. Sun, B. Miao, H. Xin, J. Zhao, G. Xia, P. Xu, J. Hu, Z. Li, J. Li, The Effect of Resveratrol on Surgery-Induced Epidural Fibrosis in Laminectomy Rats, *Evidence-Based Complementary and Alternative Medicine* 2014 (2014) 6.
- [463] D.H. Wong, J.A. Villanueva, A.B. Cress, A.J. Duleba, Effects of resveratrol on proliferation and apoptosis in rat ovarian theca-interstitial cells, *Molecular human reproduction* 16(4) (2010) 251-259.